# Magnetic and Thermal Phenomena in Topologically Constrained Systems Explored by Advanced Scanning Probe Microscopy Techniques

By

ROBERT PUTTOCK


Department of Physics
ROYAL HOLLOWAY UNIVERSITY OF LONDON

A Thesis for the Degree of Doctor of Philosophy

APRIL 8, 2021

## AUTHOR'S DECLARATION

I declare that the work in this dissertation was carried out in accordance with the requirements of the Royal Holloway University of London's Regulations and Code of Practice for Research Degree Programmes and that it has not been submitted for any other academic award. Except where indicated by specific reference in the text, the work is the candidate's own work. Work done in collaboration with, or with the assistance of, others, is indicated as such. Any views expressed in the dissertation are those of the author.

SIGNED:  DATE: APRIL 8, 2021

## ACKNOWLEDGEMENTS

The irony of studying frustration throughout my Ph.D. was never lost on me. However, frustration could have quickly turned to exasperation if I did not work alongside a large number of talented and supportive individuals. First and foremost, I must thank Olga and Vladimir for offering me the opportunity to study under their steady guidance. I particularly applaud their support for my (sometimes chaotic) ideas, and their patience in reviewing the resulting works.

I am indebted to my Nanomag/LLE colleagues at NPL, past and present: Craig; Héctor; Katherina; Mitsos; Murat; James; and Andrew. All have been great mentors or peers who have supported me considerably throughout this process with input, discussions and distractions. Héctor and Craig deserve a highlighted mention as the longest suffering colleagues of mine and for all their help in the work undertaken in Chapters 4 and 5, respectively.

A special thanks also goes to (in sort-of chronological order): Vish; Christos; Alex; Cristina; Eli; Tom (×2); David; Nate; Alessandro; and Miriam for *useful* discussions inside of NPL and *better* discussions outside of it. However, I must also blame many of those named for fuelling my poor coffee habits over the last four years.

I have been incredibly lucky to have collaborated with some incredibly helpful and supportive people outside of NPL. A lot of the output from these fruitful collaborations has made its way into the present thesis. It would not be possible to name everyone, but I would like to shout-out: Volker Neu; Alessandra Manzin; Petr Klapetek, Alex Fernandez-Scarioni, Mark Rosamond, and all those at CEMES.

I would like to thank all friends and family for their unwavering support. If any have politely asked to read my thesis, you are off the hook from here. Rest assured I am greatly looking-forward to answering the question "*So, have you submitted your thesis yet?*" with something other than "*Almost*" or "*Getting there*".

Finally, I should thank Katie. Without her unrelenting support and perseverance with my Ph.D. highs and lows ... this thesis would have been completed much sooner.

## Abstract

As “big-data” becomes the norm the demand for improved, energy-efficient storage and computation is valuable and never satisfied. Magnets and their properties are highly favourable for this problem and it has driven research into novel architectures and the resulting effects. Scanning-probe microscopy (SPM) is ideal for visualising physical properties of nanoscale systems as SPM is cheap, modular, and possess high spatial resolution ($\approx 20$ nm). Instrument modifications and image processing means complex architectures can be investigated. This thesis uses these techniques to explore nanomagnetic systems with promise in novel computation.

First, a patterned magnetic probe was designed for customised magnetic force microscopy (MFM) measurements and evaluated against commercial equivalents. The novel probes revealed advantageous properties for imaging heterogeneous samples. Subsequently, a novel SPM method was developed for characterising spin textures in a nanowire with high magnetic susceptibility by inducing spin caloritronic effects with a joule-heated SPM probe. Both methods give precedent for characterising challenging magnetic samples for applications including magnetic storage.

Following this, local behaviours in artificial spin ice (ASI) are investigated by advanced MFM and supplementary techniques. ASI are 2D systems that exhibit collective dynamics and emergent monopoles, which have application to reconfigurable magnonics and probabilistic computation. Here, the formation of non-Ising states in a novel ASI lattice were shown to form and randomly distribute across the array deterministically and their frequency was highly tunable. The stray-field of many frustrated vertices was examined by quantitative-MFM and electron holography, which revealed that even periodic configurations were energetically disparate and influences the non-Ising state properties. Finally, artificial defects in an ASI lattice were shown to influence neighbouring vertices by injecting monopoles into the lattice. Their characteristics are compared to those that form independently by *in situ* MFM and Lorentz microscopy. The described effects have implications for devices aimed towards energy-efficient storage and computation.

# Table of Contents

## List of Figures

**Figure** Page

# List of Publications

## First Author

- R. Puttock, H. Corte-Leon, V. Neu, D. Cox, A. Manzin, V. Antonov, P. Vavassori, and O. Kazakova, IEEE Trans. Magn. 53, 1 (2017).
- R. Puttock, A. Manzin, V. Neu, F. Garcia Sanchez, A. Fernandez Scarioni, H. W. Schumacher, and O. Kazakova, Small, 2003141, 1-8 (2020).

## Co-Author

- T. Wren, R. Puttock, B. Gribkov, S. Vdovichev, and O. Kazakova, Ultramicroscopy 179, 41 (2017).
- F. Moro, M. A. Bhuiyan, Z. R. Kudrynskyi, R. Puttock, O. Kazakova, O. Makarovsky, M. W. Fay, C. Parmenter, Z. D. Kovalyuk, A. J. Fielding, M. Kern, J. van Slageren, and A. Patanè, Adv. Sci. 5, 1800257 (2018).
- O. Kazakova, R. Puttock, C. Barton, H. Corte-Leon, M. Jaafar, V.Neu, and A. Asenjo, J. Appl. Phys. 125, 060901 (2019).
- D. Necas, P. Klapetek, V. Neu, M Havlicek, R. Puttock, O. Kazakova, X. Hu, and L. Zajickova, Sci. Rep., 9, 3880 (2019).
- X. Hu, G. Dai, S. Sievers, A. Fernández-Scarioni, H. Corte-León, R. Puttock, C. Barton, O. Kazakova, M. Ulvr, P. Klapetek, M. Havlíček, D. Nečas, Y. Tang, V. Neu, and H. Werner Schumacher, J. Magn. Magn. Mater. 511, 166947 (2020).
- E. Guen, P. Klapetek, R. Puttock, B. Hay, A. Allard, T. Maxwell, P. Chapuis, D. Renahy, G. Davee, M. Valtr, J. Martinek, O. Kazakova, S. Gomés, Int. J. Therm. Sci., 156, 106502 (2020).

# List of Symbols

**Abbreviations**

AFM Atomic Force Microscopy, page 41

AHE Anomalous Hall Effect, page 55

AMR Anisotropic magnetoresistance, page 57

AMSE Anisotropic Magneto-Seebeck Effect, page 58

ANE Anomalous Nernst Effect, page 55

ASI Artificial spin ice, page 28

bcc body-centered cubic, page 22

BM Bimodal, page 90

CCD Charge-coupled device, page 59

DW Domain Wall, page 24

DWCO Domain Wall Convolution Operator, page 51

EBID Electron beam induced deposition, page 45

ED Electrochemical deposition, page 45

EH Electron Holography, page 61

FIB Focused ion beam, page 45

HMP High-Moment Probe, page 67

IMA In-plane magnetic anisotropy, page 22

IQR Inter-quartile range, page 132

LLG Landau–Lifshitz–Gilbert, page 64

LMP Low-Moment Probe, page 67

LS Landau state, page 92

LTEM Lorentz Transmission Electron Microscopy, page 59

MFM Magnetic Force Microscopy, page 32

MFM Magnetic Force Microscopy, page 40

MM Multimodal, page 92

MSD root mean square difference, page 52

Nearest-Neighbour NN, page 130

Next Nearest-Neighbour NNN, page 130

NI Nanoisland, page 28

NW Nanowire, page 28

OOMMF Object-oriented micromagnetic framework, page 65

PHE Planar Hall Effect, page 57

PMA Perpendicular magnetic anisotropy, page 22

PMA perpendicular magnetic anisotropy, page 46

PMMA Polymethyl methacrylate, page 62

PNE Planar Nernst Effect, page 58

Py Permalloy, page 29

QH Quasi-Hexagonal, page 89

RIE Reactive-ion etching, page 44

S-W Stoner-Wahlfarth, page 23

SEM Scanning electron microscopy, page 44

SMP Standard-Moment Probe, page 67

SPM Scanning Probe Microscopy, page 41

SThEM Scanning thermoelectric microscopy, page 78

SThM Scanning thermal microscopy, page 78

$T_N$ Type 1-4, page 30

TEM Transmission Electron Microscopy, page 59

TTF Tip-transfer function, page 42

UF Under-focused, page 107

UM Unimodal, page 90

vdW van der Waals, page 41

VSM Vibrating sample magnetometry, page 48

**Mathematical Operators**

$\delta_w$ Domain wall width, page 51

$\mu$ orbital magnetic moment, page 17

$\mu_0$ permeability of free space, page 20

$\nabla T$ Temperature gradient, page 57

$\omega$ Frequency, page 43

$\phi$ Phase, page 43

$\rho$ Resistivity, page 55

$A$ Orbital area, page 17

$B$ Magnetic induction, page 20

$H$ Magnetic Field, page 20

$h$ Plank's constant, page 17

$I$ Current, page 17

$k$ Spring constant, page 43

$M$ Magnetisation, page 20

$m$ mass, page 17

$M_R$ remanent magnetisation, page 90

$Q$ Quality factor, page 43

$q$ Charge, page 17

$Q_s$ anomalous Nernst coefficient, page 57

$r$ orbital distance, page 17

$S_\perp/S_\parallel$ perpendicular/parallel Seebeck coefficients, page 58

$v$ Velocity, page 17

# Introduction

The rapid improvement of nanoscale lithography techniques has resulted in an equally rapid shrinking of feature sizes in patterned ferromagnetic nanostructures and devices. As a result, the application towards miniaturised sensing devices (such as lab-on-a-chip or positional sensing applications) and nanoscale logic devices for application in the information technology or computation sectors currently fall at the feet of the designer rather than a limitation of the technology.

When ferromagnets are lithographically defined on the nanometre length-scales, the typical formation of multi-domain structures becomes less likely due to the high energy cost. However, if the design allows, the inherent topology of the structure can result in domain formation with a coherent rotation of spins between the domains. These domain walls can be "trapped" at energy minima governed solely by the shape (in the absence of magneto-crystalline anisotropy). Depending on the depth of the energy minima, small perturbations from applied external fields, temperature or other mechanisms can be used to push the domain wall placement out of its current minima and into the next one. As such, the controlled propagation of domain walls through simple wires or complex arrays remains a hot-topic in subsets of the literature, including applied spin-electronics or "spintronics".

Spintronic devices typically consists of lithographically defined nanowires and nanoelements, either isolated or as constituent parts of an array. They are frequently studied by 2D imaging techniques in order to visualise the changes in magnetisation as a result of perturbing the state. These techniques can be divided into beam- and scanning probe-based techniques. The former involves a broad spectrum of physical principles of operation (i.e., polarised light, x-rays, and electrons) and includes both well-established and novel techniques such as magneto-optical microscopy based on Kerr and Faraday effects, Lorentz force microscopy, scanning electron microscopy with polarisation analysis, and photoemission electron microscopy specifically including x-ray magnetic linear and circular dichroism microscopy.

The latter group consists of a variety of magnetically sensitive scanning probe microscopy-based techniques. A recent exciting example includes the integration of nitrogen vacancy defect centres in high $Q$-factor diamond mechanical oscillators, allowing for the realisation of a quantum qubit system with highly coherent electron spin, narrow optical transitions, with nanometre scale resolution. These methods have both advantages and drawbacks, as well as a different degree of application in both research and industry. However, the most widely used scanning-probe

microscopy technique for the nanoscale characterisation of ferromagnetic nanostructures is magnetic force microscopy (MFM).

As the name suggests, MFM directly measures the magnetic force interaction between the stray-fields of an oscillating ferromagnetic probe and the stray-field emanating from the sample surface, thus providing a spatial map of the magnetic state of the sample. The long-ranged force gradients between the ferromagnetic probe and the magnetic sample are recorded and correlated from the resonance shifts in frequency/phase of the probe in the absence of van der Waal interactions.

The popularity of MFM stems from its high spatial resolution ($\approx 20$ nm), force interaction sensitivity ($\approx 10$ pN), relative simplicity in sample preparation, capability to apply *in situ* magnetic fields to study magnetisation processes, and its ability to operate in different environments. The MFM technique has been proven as an excellent characterisation tool in both fundamental research and industrial applications.

Within this thesis two lithographically defined material structures composed of different materials are investigated by the advanced SPM techniques. The first classification are ferromagnetic nanowires, which have been designed through shape to possess a single location where a domain wall will favourably pin. Away from the pinning site the magnetisation is uniform as governed by the anisotropy of the wire shape and composition. The first nanowire is L-shaped and is composed of permalloy, meaning the magnetisation naturally sits in-plane along the arms of the wire. At the corner where the arms meet, a head-to-head or head-to-tail domain-wall must exist, resulting in a large localised stray-field at the corner. The second nanowire is a straight, ultra-thin CoFeB nanowire with a notch in the middle. The wire magnetisation favourable aligns normal to the sample surface, possesses high magnetic susceptibility, and the notch traps the domain wall as the wire switches magnetisation. Both nanowire designs have been heavily researched in literature as spintronic sensing devices, which means they are useful test samples for means-testing experimental SPM methods.

The second material classification is artificial spin ice (ASI), which are lithographically defined 2D projections of geometrically frustrated materials. Each component of ASI is one of many Ising "macro-spins" that are geometrically arranged such that a singular ground-state is never truly realised due to competing neighbour interactions. The inability to find a singular ground-state at absolute zero violates the third law of thermodynamics, meaning the system has a residual entropy at 0 K. As ASI have reduced dimensions and the macro-spin placement can be controlled with nanoscale precision, ASI are often used to model more complex frustrated systems (e.g. spin ice); and also exhibit interesting properties in their own right, including collective dynamics and emergent monopole stabilisation. These behaviours can be applied to probabilistic computing, signal propagation, and logic devices. The capacity to design an almost infinite number of topologies to induce novel frustration-based effects, and the ability to probe these characteristics optically, electrically and by scanning probe techniques have made ASI an

exciting candidate for fundamental research.

In application to nanoscale patterned elements thus far described, MFM is a powerful imaging technique in its own right for the direct visualisation of the magnetisation through the emanating stray-field. However, the technique does possess its own limitations. The first example is generally true for all data acquisition methods across the sciences: which is that MFM is susceptible to artefacts that lead to the incorrect interpretation of the results. The second example is more specific to MFM: the measurement of the force interaction between the probe and the sample as a function of the probe's oscillation is a proxy for the stray-field of the sample being studied, making it a qualitative technique. The third example is the result of imaging a magnet with another magnet: the probe can induce changes in the magnetisation beneath its interaction area, and this effect can also be reciprocated, where the sample induces a change in the probe's magnetisation.

The first limitation is simply solved. MFM results cannot be taken in isolation and where possible should be correlated with other methods. Throughout the present thesis, MFM results are correlated with a number of different methods, including Lorentz transmission electron microscopy, electron holography, micromagnetic modelling. Including such a vast range of analytical tools for the analysis of the patterned material systems under study provides a greater certainty in the results and complement each other to provide a full picture of the micromagnetic processes.

The second limitation is addressed by the implementation of an advanced data processing technique to extract quantitative information from MFM measurements (quantitative-MFM, qMFM). The tip-transfer function (TTF) approach calculates the force on an MFM probe exerted by the stray field of a sample with perpendicular magnetic anisotropy in Fourier space. By performing a calibration measurement of a suitable reference sample, a model-independent and parameter-free description of the probe's imaging properties can be ascertained. This probe-calibration can be removed from other MFM images on an unknown sample performed with the same probe to extract quantitative information of the stray-field. This method throughout the thesis has been used as a tool to quantitatively correlate MFM datasets with micromagnetic modelling.

The third limitation is in some ways the least trivial to resolve as a consequence of the inevitable probe sample interaction required for the technique. The first point-of-call is careful probe selection based on the sample in question; and this simple method solves the majority of artefacts induced by unfavourable probe-sample interaction. However, sometimes this is not always possible, for example when imaging heterogeneous samples or when the probe-properties change as a function of the measurement. In the cases of measuring difficult samples, creative solutions are required to accurately sample the magnetisation.

One such solution to overcome perturbing magnetostatic effects from probe-sample interaction is by inducing spin caloritronic effects in the material, which is introduced in this thesis. Using a joule-heated AFM probe as a source of heat, which is raster-scanned over the sample under study, thermoelectric effects are induced and may be recorded as a function of the heat-spot

location by measuring the electrical response of the sample. By probing the magnetisation by a non-magnetic probe, the high magnetic susceptibility of the sample and other probe-induced artefacts are removed from the measurement sequence.

The thesis structure follows these three themes as motivations for the present work. **Chapters 1-2** introduce the relevant systems primarily under study throughout in the form of a theoretical background of relevant nanoscale magnetic phenomena; and a literature review on ASI, respectively. **Chapter 3** reviews the relevant physics and experimental methods for the techniques used throughout the thesis, including: an in-depth review of modern MFM techniques and quantitative-MFM, as well as more targeted descriptions of Lorentz transmission electron microscopy, electron holography and micromagnetic modelling.

The proceeding experimental chapters are loosely grouped to address the motivations described throughout this introduction. **Chapter 4** assesses the use of a custom-made V-shaped MFM probe for improved imaging properties when imaging heterogeneous samples of high and low magnetic coercivity. This probe is assessed by quantitative-MFM analysis alongside commercially available probes using the permalloy L-shaped nanowire with pinned domain wall at the wire apex as a test sample. **Chapter 5** studies a specific case for the notched CoFeB nanowire with perpendicular magnetic anisotropy that cannot be effectively measured by MFM because of its high magnetic susceptibility. As a result, the aforementioned new method using a Joule-heated probe is introduced to investigate the magnetisation of the wire through induced spin caloritronic effects.

The remaining chapters investigate novel artificial spin ice structures by a combination of MFM and additional complementary magnetic imaging methods. **Chapter 6** investigates the role of coupled nanomagnets built into an artificial spin ice lattice, which results in an energetically favourable disruption to the magnetic periodicity. A combination of MFM, quantitative-MFM and micromagnetic modelling is utilised to understand this unique periodicity breaking and resultant magnetic states. The results of which are directly compared to electron holography studies of the same lattice, which provides a richer understanding of the in-plane magnetic textures and flux-pathways that occur at the frustrated vertices in **Chapter 7**. The final experimental chapter investigates the role of magnetic defects on the properties of the surrounding lattice. **Chapter 8** correlates MFM measurements performed under applied in-plane field with Lorentz transmission electron microscopy measurements in order to ascertain the degree to which the defects influence the inherent frustration of the lattice.

The last chapter of the thesis, **Chapter 9**, summarises the key results from the experimental chapters and places its significance in the framework of the broader field of research and where it may develop in the future.

CHAPTER 1

# MAGNETIC BEHAVIOUR ON THE NANOSCALE

Ferromagnetism derives from the orbital and spin of electrons in atoms that possess unpaired electrons in either the $d$- of $f$-orbitals. In this chapter, the classifications of magnetism, energy contributions in ferromagnetic systems, and different types of domain walls are discussed.

## 1.1 Origins of magnetism

Magnetism derives from two sources: the orbital motion of an electron around the nucleus of an atom, and the electron's intrinsic spin. For the former, the mathematical description of the moment produced by an orbiting electron around a hydrogen nucleus is akin to the description of the magnetic field produced by a current-carrying wire.

$$\mu = IA = \pi r^2 \left(\frac{qv}{2\pi r}\right) = \frac{qvr}{2} \tag{1.1}$$

Here the term $\frac{qv}{2\pi r}$ describes the current, $I$, as the product of the electron's charge, $q$, and velocity, $v$ divided by the orbital distance $r$. By multiplying out the orbital area $A = \pi r^2$ the orbital magnetic moment of an electron in orbit, $\mu$, is described. The Bohr relationship, further defined by de Broglie, describes the angular momentum of an electron as $mvr = \frac{nh}{2\pi}$, where $h$ is the Plank's constant and $n$ is an integer multiple of the number of standing particle-waves [1, 2]. Thus by substituting this relation into Equation 1.1 a formal definition of the Bohr magneton ($\mu_B$) is reached as the lowest possible magnetic moment of an orbiting electron.

$$\mu_B = \frac{qh}{4\pi m} \tag{1.2}$$

For the second component of magnetic behaviour, the approximate intrinsic magnetic moment from the spin of an electron ($\mu_S$) is described as

$$\mu_S = g\frac{q}{2m}S = \gamma S \tag{1.3}$$

where the gyromagnetic ratio, $\gamma$, is the ratio of a particle's magnetic moment to its angular momentum. The Landé g-factor, $g$, is a proportionality constant defined for each given particle, which indicates whether the magnetic moment derives from spin ($g = -2$) or orbital motion ($g = -1$) of the electron.

The importance of this atomistic description of $\mu$ in the systems described throughout the thesis is how they all align in many-atom systems and in bulk materials. In magnetic materials there are three main spin ordered systems: *ferromagnetism*, where the nearest-neighbour spins are aligned along one direction; *antiferromagnetism*, where nearest neighbour spins are aligned anti-parallel to each other with no net moment; and *ferrimagnetism*, which has an antiparallel spin ordering akin to antiferromagnets but due to an imbalance of dipole moments possessed a net moment and spontaneous magnetisation[2]. These exist in addition to spin disordered systems, *paramagnetism* where dipole moments are randomly oriented across the material to yield a net magnetisation of zero when no field is applied. However, what governs whether a material is one of these magnetic configurations?

Starting with the spin-disordered system, the unpaired electrons are thermalised within paramagnetic materials according to Boltzmann statistics. In the absence of an applied field the spins will randomly orientate in order to occupy their ground state energy as there is no minimal interaction between spins compared to the thermal energy of the system. Their probability of occupying a spin-up or spin-down state is proportional to $P = \exp(\pm\mu_B B/k_B T)$, where $B$, $k_B$ and $T$ are the magnetic induction, Boltzmann constant and temperature, respectively. Although there is no coupling between spins within the material, under a magnetic induction the proportion of spins changes, meaning paramagnetic materials possess high magnetic susceptibility. This magnetic susceptibility, $\chi$, is related to the moment by the Curie Law [1]

$$\chi = \frac{n\mu_0\mu^2}{3k_B T}, \tag{1.4}$$

where $n$ is the total number of unpaired atomic spins per unit volume, and $\mu_0$ is the magnetic permeability in free space.

This model describes non-metallic paramagnetic materials well, however it does not describe metallic paramagnets whose susceptibility is independent of temperature [2]. This is because the Curie law assumes electrons are highly localised to the atom, which is not true in conductive materials. Instead, understanding $\chi$ requires a quantum mechanical description, i.e. the Pauli paramagnetism principle. Here the distribution of spins within conduction electrons is described as a density of states occupied by electrons up to the Fermi level ($E_\mathrm{f}$). Under application of a field

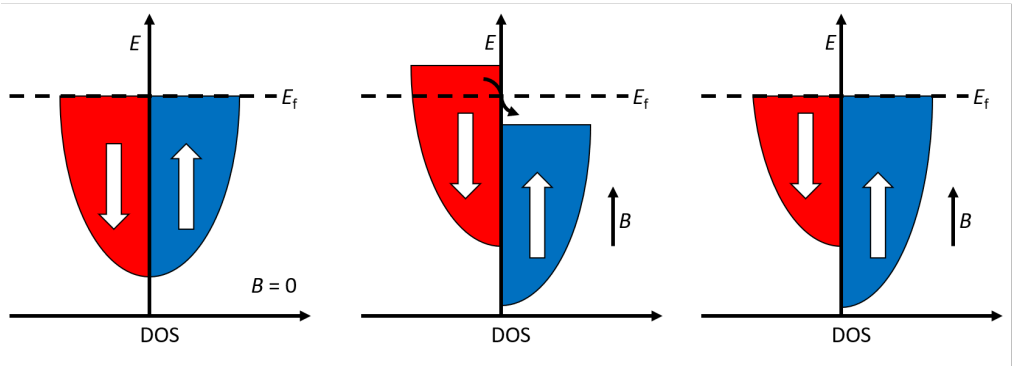


FIGURE 1.1. Density of states in a free electron gas under no field (left) and under applied field in the up direction. White arrows represent the magnetic moment.

the spins aligned parallel to the field reduce in energy and those aligned antiparallel increase in energy (Figure 1.1). As a result, it is energetically favourable for spins close to the Fermi surface flip to align parallel to the field [2, 3].

$$\chi_P = \frac{3}{2}\frac{n\mu_0\mu_B^2}{k_B T_\mathrm{f}} \tag{1.5}$$

Equation 1.5 describes the effects of Pauli paramagnetism, which is similar to the Curie Law from Equation 1.4. The difference is that the absolute temperature has been replaced with the Fermi temperature ($T_\mathrm{f} = E_\mathrm{f}/k_\mathrm{B}$) [2, 3]. As $T_\mathrm{f}$ is much greater than $T$, the Pauli paramagnetic contribution to $\chi$ is considered largely independent of temperature.

In spin-ordered systems, the spin alignment is governed by the exchange energy ($E_\mathrm{ex}$). This is the spin-spin interaction over short length-scales, defined within the Heisenberg Hamiltonian approximation,

$$e_\mathrm{ex} = -2J_\mathrm{ex}S_iS_j, \tag{1.6}$$

where $J_\mathrm{ex}$ is the exchange constant and $S_i$ and $S_j$ are neighbouring spin vectors. The sign of $J_\mathrm{ex}$ governs whether neighbouring spins align parallel or anti-parallel (i.e. ferro-or antiferromagnetically, respectively). This is visualised by the Bethe-Slater curve in Figure 1.2, which relates $J_\mathrm{ex}$ to the ratio of the inter-atomic distance ($r_a$) and the radius of the $3d$ shell of the electron ($r_{3d}$) for common magnetic materials [4]). The $E_\mathrm{ex}$ does not have a classical description, however in quantum mechanics it describes the strength of interaction between electrons $i$ and $j$ due to the Coulombic interaction between them [5].

In a system with more than two spins, the exchange energy is dominant over the material-defined exchange length. Assuming homogeneity across neighbouring spins, the exchange energy is the summation of spin-spin interactions, $E_\mathrm{ex} = -2J_\mathrm{ex}\sum_{i<j}^{nn} S_iS_j$. In the Heisenberg model $S$ encompasses the sum of interactions along all individual Cartesian components (i.e., $S_iS_j =$

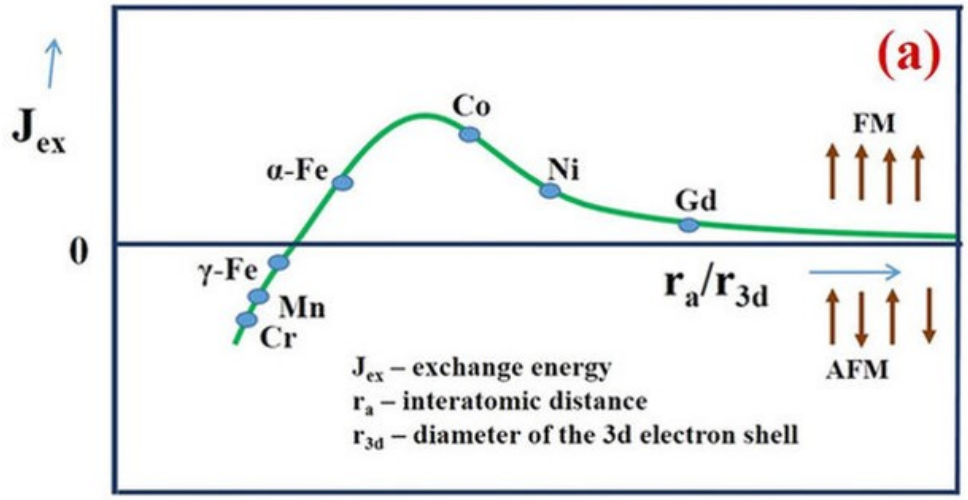


FIGURE 1.2. The Bethe-Slater curve (schematic) showing the dependence of the exchange interaction ($J_{ex}$) on the ratio of interatomic distance to the diameter of the $3d$ electron shell ($r_a/r_{3d}$). ©2016 Springer Nature. Reproduced, with permission, from Chaudhary *et al.* [4].

$s_i^x s_j^x + s_i^y s_j^y + s_i^z s_j^z$). However, 1- and 2D models of the spin-spin exchange interactions are frequently used [6, 7]. The exchange interaction across the whole volume is given by [5, 6]

$$E_{\text{ex}} = \frac{A}{M_s^2} \int_V [\nabla M]^2 \, dV, \tag{1.7}$$

where $A$ is the exchange stiffness, $M_s$ is the saturation magnetisation and $M$ is the magnetisation.

The introduction of the first energy term for nanoscale magnetic systems nicely provides a gateway into a review of the competing energy interactions within ferromagnetic materials and domain theory. These describe how a bulk material, thin film, or patterned structure will minimise its internal energy.

## 1.2 Ferromagnetism and domain theory

Before reviewing the energy terms, a brief introduction of the key terminology is required. Equation 1.8 relates $B$ to the magnetic field and magnetisation ($H$ and $M$, respectively),

$$B = \mu_0 (H + M), \tag{1.8}$$

where $\mu_0$ is the permeability of free space approximately defined as $4\pi \times 10^{-7}$ H/m [8]. The associated nomenclature for describing the magnetic properties of a material derives from its magnetic response within an applied field. The divergence of the magnetic induction ($\nabla B$) is

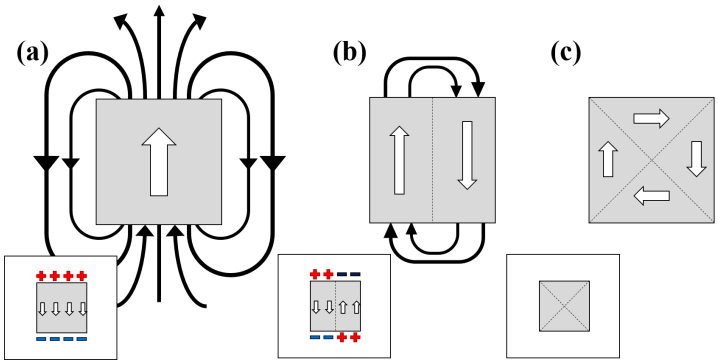


FIGURE 1.3. A magnetised body in single, double, and Landau domain structures (a-c, respectively) with magnetisation and stray demagnetising field represented by white and black arrows, respectively. *Inset* Representation of the magnetism as surface charges with demagnetising field vectors throughout the medium indicated.

described through one of Maxwell's famous equations as

$$\nabla \cdot B = \mu_0 \nabla \cdot (H + M) = 0. \tag{1.9}$$

By rearranging Equation 1.9 it is clear the divergence in magnetisation is accompanied by a nullifying divergence in magnetic field. For example, in a uniformly magnetised body stray-fields emanate from the two polar ends (Figure 1.3(a)). A magnetic stray-field arises from the non-zero divergence in $M$, creating a divergence in $H$ that acts in the opposite direction of the sample magnetisation. This field is referred to as the *demagnetising field* $H_d = -NM$, where $N$ is the demagnetisation tensor, and its mere existence is energetically expensive [2, 5]. The energy of the demagnetising field, i.e. the magnetostatic energy ($E_{ms}$), is defined as

$$E_{ms} = \frac{1}{2}\int_{V_\infty} \mu_0 H_d^2 dV = -\frac{1}{2}\int_{V} \mu_0 H_d \cdot M dV \tag{1.10}$$

where the first and second integrals are performed over all interaction space ($V_\infty$) and the material volume ($V$), respectively. These integrals are equivalent when substituting Equation 1.8 into the first integral of Equation 1.10, where $\int_{V\infty} B \cdot H_d dV = 0$ in the absence of conduction currents [6].

The magnetostatic energy competes against $E_{\text{ex}}$ in a ferromagnetic system, therefore the magnetism within an isotropic material whose volume extends beyond the exchange length fragments into *domains* of aligned magnetisation (Figure 1.3 (b-c)). The act of rearranging the spins into separate domains minimises the materials total energy ($E_{\text{tot}}$) by reducing $E_{ms}$. However, this spin rearrangement comes at the expense of other energy terms, some of which are discussed in the following section.

Another way to describe the phenomena that results from Equation 1.9 is the formation of effective magnetic charges at the surface ($\sigma$). The magnetisation is discontinuous at the material

boundary resulting in a non-zero divergence. Thus the surface charge density is equivalent to $\sigma \equiv n \cdot M$, where $n$ is a unit vector in the direction of the outwards surface normal [5, 9]. These surface charges are depicted in the insets of Figure 1.3 for each domain configuration.

It is evident that reviewing the orientation of individual atomic spins across the bulk of a ferromagnetic material is not trivial. In most samples of substantial size the spins will not align along one single direction without an external influence as this is energetically expensive [6]. In fact the magnetic state of ferromagnetic materials are a fine balancing act of different energy terms, which cumulatively must act to reduce the $E_{tot}$ of the system

$$E_{tot} = E_{ex} + E_{ms} + E_{mstr} + E_a + E_z. \tag{1.11}$$

$E_{tot}$ in Equation 1.11 encompasses the following energy terms: exchange ($E_{ex}$); magnetostatic/demagnetisation ($E_{ms}$); stress/magnetostriction ($E_{str}$); anisotropy ($E_a$); and response to an external applied field,i.e. Zeeman energy, ($E_z$) [6].

$E_{str}$ encompasses both the magnetic response within a material to an acting mechanical stress [10]; and the physical change in dimensions of a material in response to an applied magnetic field [11]. These energy contributions are comparatively smaller than the other energy terms [6] in the materials used throughout this thesis, thus will not be discussed further. The remainder of this section shall review the remaining energy contributions in Equation 1.11.

### 1.2.1 Magnetic Anisotropy

The anisotropy term, $E_a$, dictates a three-dimensional asymmetry with respect to the alignment of spins along any vector of the Cartesian coordinates. In a material with magnetic anisotropy, the energy is minimised when the spins align along a particular axis. This typically results in a magnetic *easy*- and *hard*-axis. These axes describe the direction within the crystal coordinate where the applied field/energy required to saturate the material is either small/large, respectively. The anisotropic energy is therefore quantified by measuring the field/energy required to rotate the magnetisation away from its easy axis. There are four primary components of magnetic anisotropy: magneto-crystalline, shape, surface and stress. For the purposes of this thesis, there will only be a discussion on the first two of these components.

*Magneto-crystalline* anisotropy is the intrinsic component of the anisotropy from the material, which couples the magnetisation direction to the crystal lattice (e.g. for body-centered cubic (bcc)-iron the magnetisation aligns along the edges of the cubic unit cell and in nickel the spins align along the cubic-diagonal) [2, 6, 12]. This form of anisotropy is a competition between the spin-orbit coupling and the favourable overlap of orbitals throughout the lattice due to crystal structure and composition. Under an external field the spins, and thus the orbitals, rotate. This in turn weakens the inter-lattice bonding through the material [2]. The magneto-crystalline anisotropy governs a film's magnetic anisotropic direction, which can however be altered by, for example, interfacial coupling to heavy metal spacer layers [6].

*Shape* anisotropy is the secondary component to the $E_a$ term. It governs the magnetisation in non-spherical objects, e.g. grains, nanoparticles or nanowires. Typically, the magnetisation within anisotropically-shaped materials aligns preferentially along the long-axis. This is due to $H_d$, which is stronger along the short-axis than the long axis of a structure [13]. As a result,"engineered" magnetic phenomena heavily rely on shape anisotropy for desirable properties such macro-spin degeneracy (see Section 2.2).

### 1.2.2 Zeeman energy

The Zeeman energy is the potential energy of the material in the presence of an external magnetic field.

$$E_z = -\mu_0 \int_V M \cdot H_{\text{ext}} dV. \tag{1.12}$$

Under an external field, $H_{\text{ext}}$, it is energetically favourable for the spins within the material to align along the applied field direction. Figure 1.4 analytically describes the energy of a uniaxial magnetised body as a function of angle ($\theta$) between the magnetisation and the $x$-axis, where a field ($B$) is applied at $\theta = \gamma = 45°$. The coherent rotation of magnetisation in the field follows the

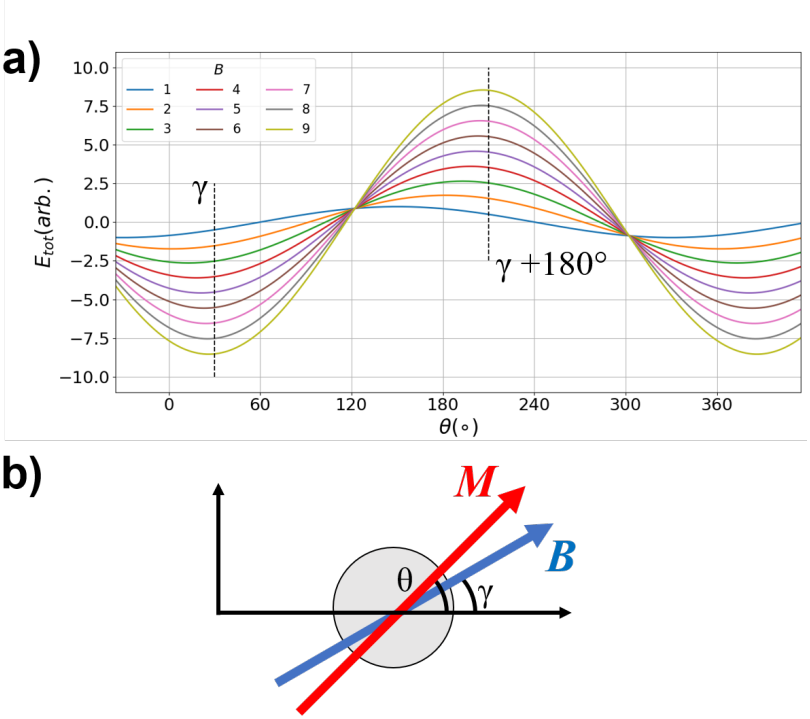


FIGURE 1.4. (a) Stoner-Wahlfarth Energy of a magnetised body with uniaxial anisotropy of unspecified origin for different values of $B$. (b) Coordinate system demonstrating $\theta$ and $\gamma$ as relative $M$ and $B$ angles, respectively. Upon increased field, the energy minima/maxima shift towards the $B$ direction

Stoner-Wahlfarth (S-W) model [14], which describes the change in magnetisation direction of a uniaxial material as a coherent rotation of the spins. Figure 1.4 shows that the energy minima and maxima are when the magnetisation is aligned parallel and antiparallel to the field direction, respectively.

In a material with anisotropy there is an asymmetry in the amount of field required to saturate the spins dependent on $\theta$. When $H_{\text{ext}}$ is aligned along an easy axis it requires relatively low-field to align the spins, whereas along the hard axis it requires more field. Along the easy axis, a material can also display a hysteresis where the material "resists" the realignment of spins when the energy-well with the predetermined spin arrangement must be overcome. This resistance is the magnetic coercivity ($H_c$), which is equal to the field applied to reduce the magnetisation to zero post-saturation [6]. Materials with a large $H_c$ are referred to as *hard* magnetic materials, whereas low- coercivity materials are magnetically soft.

## 1.3 Domain walls

As described in the previous sections, ferromagnetic materials break up into magnetic domains in order to reduce the total self-energy of the system. The uniform areas of aligned spins are separated by a higher energy rotation of spins called a domain wall (DW). This gradual rotation avoids abrupt changes in neighbouring spins, which would be very high energy at the domain boundary from the $E_{\text{ex}}$.

The arrangement of domains, and the DW configuration between them, is an intrinsic property

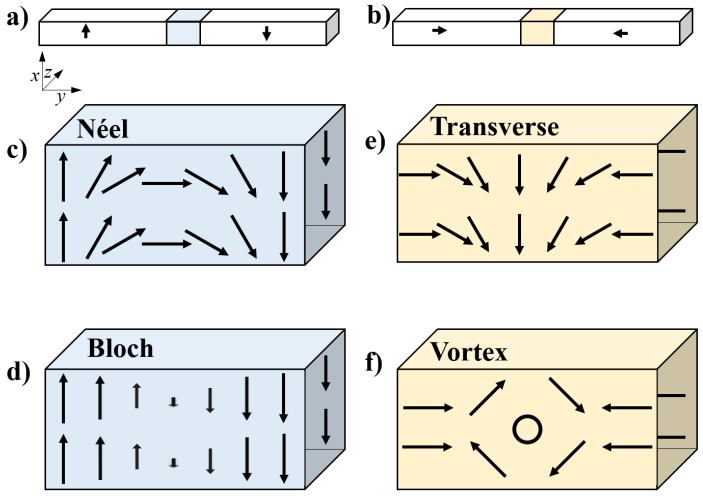


FIGURE 1.5. Schematic of IMA nanowire with two antiparallel (a) and transient (b) domains separated by a 180° domain wall. Néel (c) and Bloch (d) domain walls are associated with domain configuration depicted in (a). Transverse (e) and vortex (f) domain wall are associated with the domain configuration depicted in (b).

of the material. Tuning the dimensions or composition of the magnetic material can form many complex DWs and domain configurations. However, here only four of the most prevalent are discussed. Figure 1.5 schematically describes these common DWs for materials with anisotropy in-plane, thus descriptions are relative to this magnetisation geometry. Figure 1.5a-b are schematics of a magnetic "block" with two domains aligned 180° antiparallel and transient, respectively. Two of the most common 180° DWs between anti-parallel domains are the Néel [15] and Bloch [16] DWs (Figure 1.5 c-d, respectively). Néel DWs have smooth transitional spins which rotate within the plane of the magnetic domains ,which are most common in thin-films where the exchange length of the material is far greater than the film thickness [17]. Bloch walls, by comparison, are favourable in thicker films as a 3D rotation of the vector field is energetically preferred.

Figure 1.5 e-f demonstrates the DWs between transient 180° domains. Transverse DW is similar to the Néel DW as the spin rotates in the 2D plane of the domain magnetisation. Whereas the vortex state is an example of a more complex magnetic DW, characterised as a 2D-rotation of magnetisation around an out-of-plane core. It is stable in soft-magnetic structures with low shape-anisotropy, but larger than the coherence radius [6]. Although $E_{\text{ex}}$ is expensive, it effectively minimises $H_d$ as the surface charges are massively reduced.

## 1.4 Summary

This chapter introduced some specific concepts of magnetism that are most relevant to all of the following chapters of the thesis. Concepts such as the origins of magnetism, the competing energy-terms within magnetic systems, and domain theory provide a much needed background. Chapter 2 will apply these concepts to frustrated meta-material systems of artificial spin ice, which are the main features of interest throughout the Chapters 6-8.

CHAPTER 2

# LITERATURE REVIEW

## 2.1 Geometric Frustration

Frustration, the inability of a system to simultaneously achieve a minimum energy within its constitutive parts, yields reconfigurable behaviours from its classical ground-state degeneracy. This behaviour allows certain materials to exhibit a residual ground state entropy at zero-temperature [18]. Figure 2.1 gives three examples of geometric frustration: Ising spin placement on a triangular lattice; close-packing pentagons in 2D; and tetrahedrons in 3D (a-c, respectively). In all three examples, there exists two or more configurations that are equivalent in energy such that a single configuration is not preferred.

This phenomena is seen across numerous natural and synthetic systems. One famous example

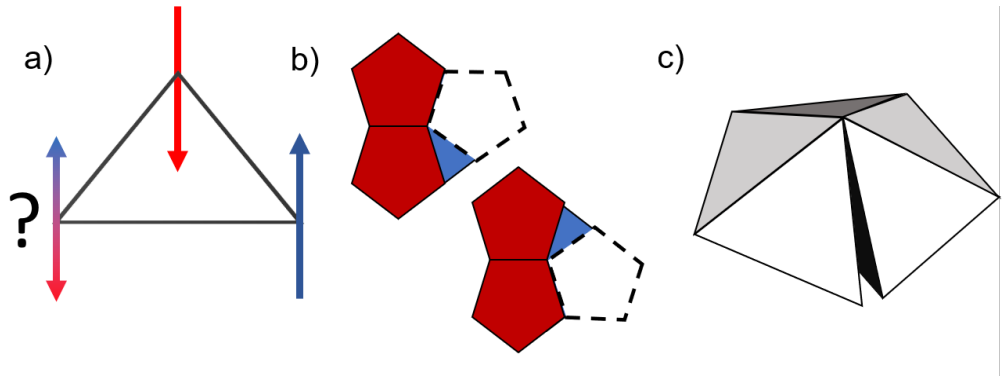


FIGURE 2.1. Schematic examples of geometric frustration, including: antiferromagnetically coupled spins fixed on a triangular lattice (a); 2D tiling of pentagons (b); and close-packing of tetrahedrons (c).

is water ice, which is geometrically frustrated (Figure 2.2) as each hydrogen atom is effectively bound to two oxygen atoms, but is not localised symmetrically between them. This creates statistically two positional minima for each hydrogen atom depending on the surrounding environment resulting in a residual entropy in the ground state [19, 20]. The purple displacement vector arrows in Figure 2.2a, demonstrates how the system obeys a "*two-in two-out*" structure; also known as the ice rule [19].

Another example is spin ice (e.g. $Dy_2Ti_2O_7$ or $Ho_2Ti_2O_7$), which are tetrahedral lattices that are corner-linked by ferromagnetic rare-earth ions [21] (e.g. $Dy^{3+}$ or $Ho^{3+}$). Due to the large intrinsic crystal field acting on the rare earth ions they demonstrate idealistic Ising spin, i.e. they can only orientate along the ⟨111⟩ easy-axis pointing towards or away from the centre of the unit cell (Figure 2.2b) [22]. From this, an energetically favourable ground-state is only realised when two spins point towards the centre of the tetrahedron. With this in mind, there are six possible ground-state configurations for each tetrahedron in a lattice, creating a ground-state degeneracy and a residual entropy equivalent to Pauling's originally derived entropy of water ice [18, 22, 23]. The comparison between water-ice and spin ice behaviour extends to the excited states where the two-in two-out degeneracy is violated. In frozen water a thermal equilibrium results in ionic "defects" from the existence of $H_3O^+$ and $OH^-$ ions in the solution. Likewise, a thermalised tetrahedral spin ice may possess "*three-in one-out*" (or *vice versa*) from a spin-flip within the unit cell, which is balanced by a "*one-in three-out*" (or *vice versa*) configuration elsewhere in the closed lattice [21]. This extends to highest energy metastable state in four-in or four-out double-defects

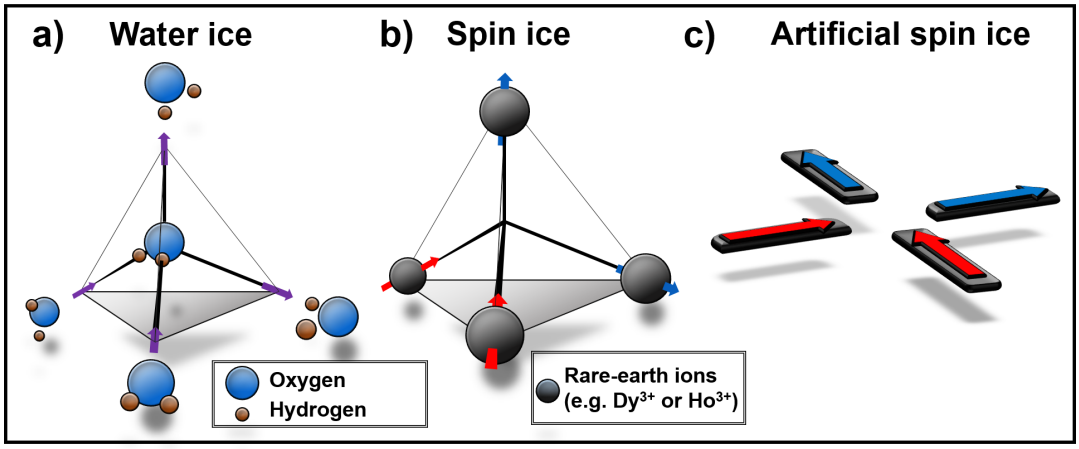


FIGURE 2.2. a) Schematic of frozen water, with displacement vector arrows (purple) demonstrating "two-in two-out" ground state ice rule. b) Example spin ice structure of four rare earth ions (e.g. $Dy^{3+}$ or $Ho^{3+}$) on tetrahedral corners with ice rule compliant magnetic moments orientated towards (red) and away (blue) from the tetrahedral center. c) Example of the square 2D ASI structure, composed of lithographically patterned ferromagnets, with magnetisation (red and blue arrows) indicated.

corresponding to unfavourable $H_4O^{2+}$ and $O^{2-}$ ionic defects in water.

A major interest in this branch of condensed matter physics is the formation and controllable dynamics of bound "magnetic monopoles" [24, 25]. These monopoles are magnetic quasi-particle pairs which arise in an otherwise ice-rule compliant frustrated lattice because of a flip of a spin to create ice-rule violated vertices. Upon numerous spin-flips, the distance between the monopoles effectively increases step-wise until an annihilation event occurs, and the energy between them can be understood as Coulombic with pair-wise interaction energy. The energy cost to host these bound monopoles is spent upon their initial formation (i.e. the first spin flip). Any further switching that extends the distance between the bound monopoles requires practically no additional energy. This is analogous with proposed magnetic monopoles bound together by a vector potential singularity named a Dirac string, as first described by Dirac in 1931 [26]. This importantly prevents a violation of the sacred Maxwell equation, $\nabla B = \mu\nabla(H + M) = 0$.

Therefore, the effective/emergent monopoles described herein are topologically protected defects that correspond to a localised source/sink in the magnetic moment, which is counterbalanced by its inverse monopole bound through a solenoid-like string of flux. Emergent monopoles in this regard are then a source of field-lines in magnetic field strength [24, 27, 28]. Unbinding these monopoles is a well sought out holy-grail for these materials as unbound magnetic monopoles could be used in magnetic-electricity (or "magnetricity") applications as an alternative to conventional electric current [24, 25, 29, 30].

## 2.2 Artificial spin ice

Artificial spin ice (ASI) are lithographically defined arrays of nanoscale single domain nanoelements that constitute as two-dimensional projections of spin ice. In this system frustration arises from the coupling between neighbouring ferromagnetic elements, which are specifically arranged to have frustrated junctions throughout the lattice where nanoelement vertices meet. The elements across the array may be disconnected nanoislands (NIs), where frustration arises from dipolar coupling; or connected nanowires (NWs), which couple through the exchange interaction across each junction [31]. The magnetisation in a four-vertex unit cell conforms to the two-in two-out spin degeneracy in its ground-states due to the intrinsic frustration at each junction (Figure 2.2c); with multiple ground- and excited-states possible by application of low-energy stimuli (e.g. field or temperature). The interest in ASI stems from the statistical mapping of elementary degrees of freedom across a system, and how they may be biased and manipulated by design. This research effort pushes towards realisations of ASI-based reprogrammable logic [32], reconfigurable magnonics [33, 34], as well as hardware realisations of more complex three-dimensional frustrated systems [35, 36].

A plethora of research has emanated from the analysis of these reconfigurable inter elemental interactions as they are easily probed through microscopic [37–41] and spectroscopic [34, 42–47]

techniques. They are studied through: their response to stimuli (e.g. magnetic fields or thermal activation); lattice topology and geometry; and the manipulation of bound emergent monopoles. Utilising nanomagnets such as ASI for low power computation is desirable as they are non-volatile and highly efficient for logic operations, which are performed at energies close to the thermodynamic limit of $kT\ln(2)$ [32]. This is highly applicable for smart energy technologies with application to scalable devices [48] or within military applications [49].

### 2.2.1 The Ising model and Dipole interactions

The fundamental concept for research in ASI systems revolves around the modelling of the magnetisation in the constituent parts as macro-spins, which converge on a vertex or a frustration centre. The model of choice for the orientation of the macro-spins is the Ising model, which limits the directions of the macro-spins to one of two possible directions along the long axis of the element, i,e, $S = \pm 1$. By considering the material properties and shape anisotropy of the constituent parts, the magnetisation within each NW or NI is forced to align along the long axis. Permalloy (Py), a nickel-iron alloy, is the most prominent material of choice for ASI across literature as its magnetocrystalline anisotropy is effectively zero, therefore the anisotropy of the material can be engineered through its shape. Py also exhibits a high Curie temperature allowing for athermal probing of the frustrated systems. Typically, the constituent NIs have a nominal thickness of the order of 10's nm and lateral dimensions ten-fold greater, with an oblong aspect ratio to ensure the magnetisation of the element remains compliant with the Ising model.

The magnetostatic coupling between islands in close proximity will influence the relative moment vector of the vertex and the greater structure of the many-body system [50]. The magnetostatic dipolar energies of the NIs can be approximated by modelling the islands as individual macro-spins. Thus the energy of an ASI system is primarily associated as the sum of pairwise interactions. In the simplest case this can be demonstrated in two dimensions through the orientation of two dipoles according to Equation 2.1 [51]

$$E_{ij} = \frac{\mu_0}{4\pi}\left[\frac{\mu_i\mu_j}{r_{ij}^3} - 3\frac{(\mu_i r_{ij})(\mu_j r_{ij})}{r_{ij}^3}\right] \times \left[2(\cos(\theta_{ij}) \times \cos(\theta_{ij} - \beta_j)) - \sin(\theta_{ij}) \times \sin(\theta_{ij} - \beta_j)\right] \tag{2.1}$$

where $\mu$ and $r_{ij}$ are the magnetic dipole moments of dipoles $i$ and $j$ and the distance between their centres, respectively. The second part of Equation 2.1 includes angular and rotational contributions between $i$ and $j$, where $\theta$ is the pairwise translational angle between the centres of dipoles $i$ and $j$, and $\beta$ is the rotation of the dipole $j$ with respect to dipole $i$.

Figure 2.3(a) plots the relative interaction energy for two dipoles as a function of $\beta$ according to the geometries denoted in Figure 2.3(b). In the first arrangement, the dipoles $i$ and $j_2$ are fixed such that the two dipoles lie on the $x$-axis (i.e. $\theta = 0°$). The red plot demonstrates that the dipoles experience the greatest interaction energy when dipole $j_2$ is aligned along dipole $i$'s long-axis ($\beta = 0°/\beta = 180°$) as the poles that are in closest proximity experience stronger repulsive or

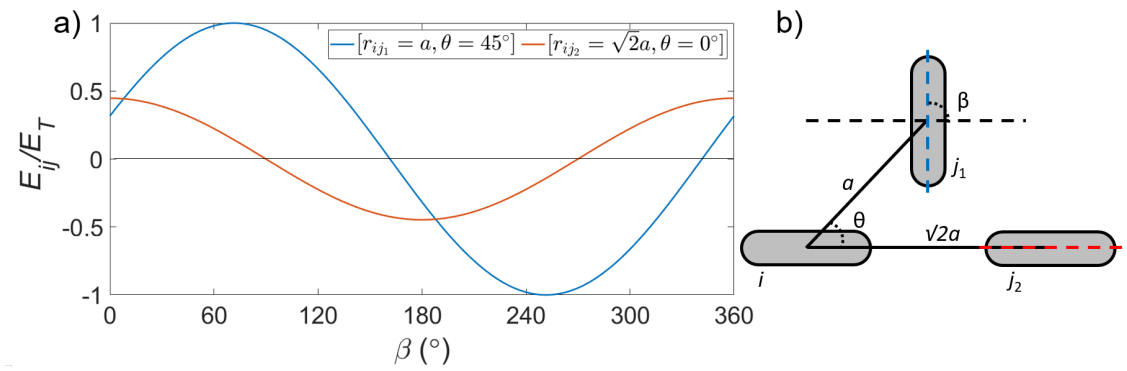


FIGURE 2.3. (a) Calculated dipolar interaction energies as a function of rotational angle for two configurations of "macro-spins" $i$ and $j_n$ depicted in (b) (from equation 2.1).

attractive effects, respectively. On the other hand, these attractive/repulsive effects are cancelled out when dipole $j_2$ is aligned perpendicular to $i$'s long axis.

The second geometry between $i$ and $j_1$ has a different symmetry as $\theta = 45°$, thus the energy maxima in figure 2.3a (blue) differs. The difference in $r$ between the two geometries accounts for the difference in the magnitude of the interaction energy, which decays as a function of $r^3$, which does constitute a non-equal pairwise degeneracy in square ASI.This is discussed in the following section. At frustrated vertices in ASI, more than one degree of freedom is necessary, therefore in, e.g., square ASI the interaction energy is a result of the summation of all possible interactions between NIs. Equation 2.1 must be summed over the number of interacting elements.

### 2.2.2 Lattice designs

#### Square

Square ASI originated from the seminal works of Wang et al. [37], and describes the arrangement of disconnected NIs is a square unit cell. This gives rise to the four-island frustration sites between each unit cell, and the 16-vertex model for frustration in ASI as is depicted in Fig. 2.4. This model represents all the possible magnetic moment configurations at each vertex, which increases in interaction energy as the figure is read from left to right. It is common to describe each energy type in terms of its moment and charge ($\mu$ and $q$, respectively).

Type I-II states ($T_1$ and $T_2$, respectively) represent the two energetically favourable magnetic moment configurations and match the ice rule described in Section 2.1. $T_1$ balances the magnetic charges at the frustration centre as poles of alike charge are distributed in opposite vertices. This results in a net moment $\mu = 0$ and charge $Q = 0q$. Instead, $T_2$ states exhibit a net moment as the charge distribution is unbalanced. Despite the presence of a moment the $Q = 0q$. Type III ($T_3$) vertices are again higher energy as they now disobey the ice-rule and conform to a three-in

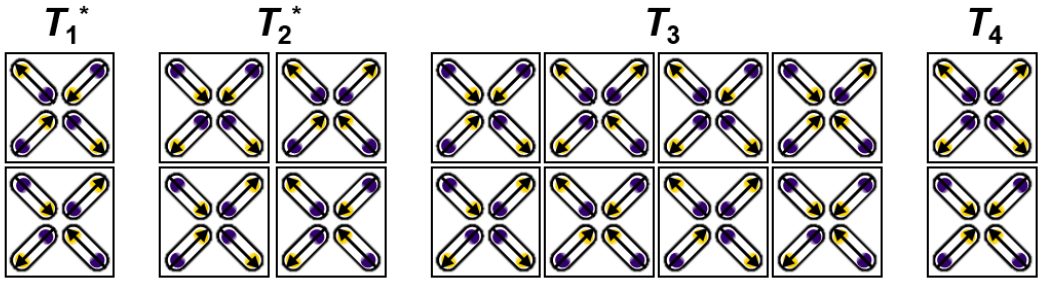


FIGURE 2.4. The sixteen magnetic types at vertices of square artificial spin ice and their degenerate multiplicities; where purple and yellow dots relate to the MFM contrast from the magnetic confinement at the ends of the nanoislands. Ice rule allowed states indicated by an asterisk.

one-out moment configuration (or *vice versa*). This results in a net magnetic charge ($Q = \pm 2q$) at the frustration centre. Finally, the highest vertex energy configuration is Type IV ($T_4$), which has a net charge $Q = \pm 4q$ and net moment of 0 as all alike poles cancel across the junction. A schematic of the charges and moments in terms of $q$ and $\mu$ is shown in Figure 2.5 for $T_1$-$T_4$ states.

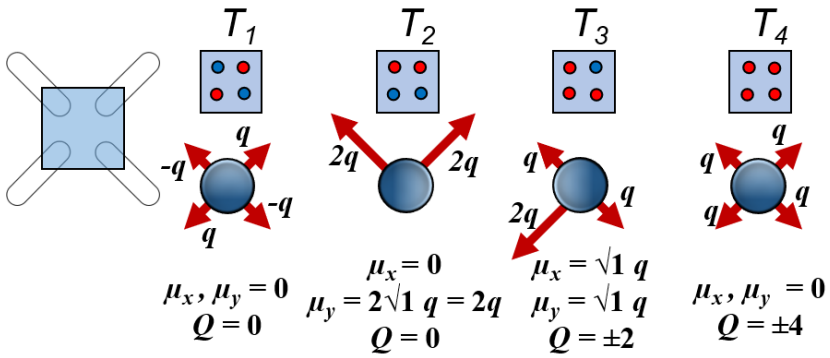


FIGURE 2.5. Schematic demonstrating the magnetic moments ($\mu$) and charges ($q$) for square lattice junctions.

The square design is considered one of the two classical architectures for ASI lattices, and remains frequently used in literature. However, a criticism of this design is that it does not have an extensive degenerate ground state. Instead the square ASI lattice is two-fold degenerate in the ground state as it forms an antiferromagnetic tiling of $T_1$ vertices. In addition, the 2D design results in unequal pairwise interactions across the vertex as the diagonal and parallel separations (as depicted in Figure 2.3(b)) are not equal. This deviates from the classical spin ice picture, which maintains this degeneracy. Möller and Moessner [52], proposed a modulation in

height of the islands in order to counteract this effect, which was later demonstrated in practice by Perrin *et al.* [53]. Implementation of the 3D- modulation of the square geometry normalises the pair-wise such that a larger degeneracy is possible in the lattice ground-state.

#### Kagomé

Kagomé, or "honeycomb", ASI differs from square ASI as there are just three moments confined at each vertex. Thus the ice rule is modified to a "one-in two-out", or vice versa, ground state configuration with a non-zero charge and moment. A benefit of this is that there is a much larger ground-state degeneracy than in the 2D square geometry. Higher energy states, or excitations, occur when three alike moments converge on the same vertex.

The Kagomé lattice is investigated in two forms: disconnected NIs and connected NWs (Figure 2.6a(i) and (ii), respectively). A primary strength of the disconnected lattice is ability to visualise the gross magnetic charges of each participating vertex by magnetic force microscopy (MFM). This contrasts the connected lattice, which shows the net moment at each vertex in MFM (Figure 2.6(b)). It is also challenging to isolate ice-rule forbidden states in a connected lattice, especially when composed of Py, as the increased nearest neighbour interactions in the connected vertex leads to an unfavourable increase in exchange and dipolar energies, which in turn push out the ice-rule forbidden state [54, 55]. Higher energy states have, however, been experimentally observed in connected lattices of other compositions, such as cobalt [55].

A huge advantage for connected lattices is that they allow for electrical connection and probing of the magnetisation dynamics within the connected Kagomé lattice by, e.g., magneto-transport [56, 57]. Therefore frustration based nucleation, pinning and annihilation processes throughout the structure can be electrically/spectroscopically monitored. In some special cases, specialised alterations to the disconnected lattice can be performed to fill the vacant vertex with non-magnetic material. This allows for some magnetotransport comparison between both connected and disconnected Kagomé structures, although with that comes added complications with interface effects [58, 59].

### Novel designs and lattice modifications

Lithography provides total control over the arrangement of magnetic material on the nanoscale in order to define complete novel designs. These structures can in turn inspire a better understanding of the frustration and degeneracy within both 2D and higher dimensional systems. This may be mapping atomic properties as macro-spins [60], or functional operations such as probabilistic logic [32, 61] or reconfigurable magnonics [34], or representing complex crystallographic structures [62–65].This subsection will briefly review a select few adapted and novel designs from literature that have both impacted the wider ASI field of research and has relevance to the experimental chapters.

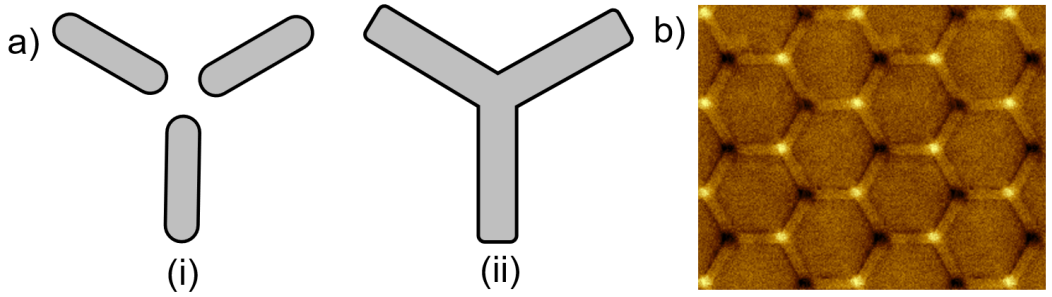


FIGURE 2.6. (a) Schematic of disconnected (i) and connected (ii) Kagomé primitive unit cells. (b) MFM image at remanence, after saturation along the $x$-axis, of connected Kagomé lattice where bright and dark contrast represents the stray-field resulting from the net magnetic moment at each vertex.

The Shakti lattice was designed to address the limitations of both the square and Kagomé lattices to have critical correlations in two-dimensions that better mimics the Coulomb phase in pyrochlore spin ice [66–68]. The design is displayed in Figure 2.7, starting from the original square lattice design (a), NIs highlighted red are periodically removed such that the coordination number in the Shakti lattice (b) is variable [31, 67]. This yields rectangular plaquette unit-cells where the energetic degeneracy does not manifest from the NI junctions, but rather from the plaquettes net charge. The intrinsic degeneracy derives from the inability to satisfy all the vertices within the plaquette, thus the higher energy vertices can be distributed across four potential junction sites [60, 69]. This lattice also demonstrates interesting magnetic charge screening properties by the nearest neighbours of a vertex junction hosting an emergent monopole [60, 69].

More recently, the thermally driven kinetics of the magnetic and topological ordering has been investigated for both this lattice and a modified version with two characteristic component sizes. In particular, Lao *et al* [70] demonstrated that the monopole excitations at the junctions are topologically protected and behave according to classical topological order. However, variation in length- and energy-scales between the two lattice designs impacts the magnetic ordering because of the presence of multiple blocking temperatures in the multi-component lattice [71].

The pinwheel lattice is obtained from a square lattice where each element is rotated on its mid-point such that each NI vertex terminates equidistant from all adjacent NI vertices (Figure 2.7(c)) [72, 73]. This produces a unidirectional dynamic chirality when it undergoes thermal relaxation, resulting in a 'ratchet effect' where the magnetisation rotates in one direction within the array governed by the symmetry-broken edge states [31, 72] and deviations from Ising behaviour in the ends of the constituent NIs [74]. It was shown that this chirality may be reversed by applying a small biasing field during relaxation. The pinwheel design also features "macro-ferromagnetic" behaviours where different macro-domains of uniform moments form depending on the array size [41, 73] similar to traditional ferromagnets. The lattice also demonstrated a tunable ground-state

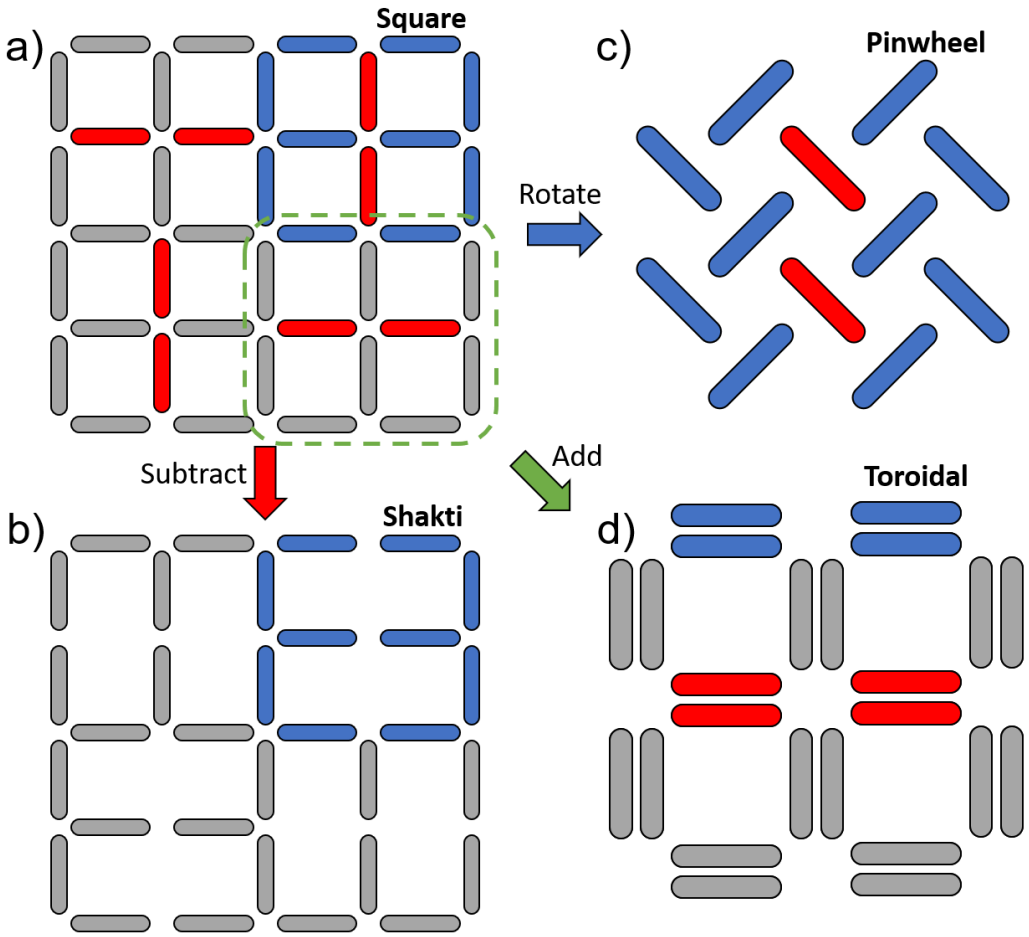


FIGURE 2.7. Starting from the Square geometry (a) other structures can be realised. Subtracting red elements from (a) produces the Shakti lattice (b). The pinwheel lattice is realised through a rotation of the elements within the structure (c). And th Torroidal lattice is formed by adding additional elements into each unit cell (d).

dependent on the degree of rotation, which in turn gives rise to phase competition at non-critical angles [75].

Designer meta-materials like ASI also allows for the mixing of competing effects to understand complex systems by coupling elements of the lattice together. By expanding the number of competing interactions the number of modes within the lattice increases [76]. One way to achieve this is to have coupled or throupled nanomagnets, where two or three parallel NIs replace single NIs in the square [76–78] or pinwheel [77, 79] geometries (Figure 2.7(d)). Such structures have competing geometric frustration as well as dipolar coupling between nearest neighbour parallel elements in ferro-/antiferromagnetic configurations, providing alternative mechanisms for tuning the degenerate ground state configurations. This may yield interesting effects, including the

formation of a mesoscopic magneto-toroidal field that may be manipulated by an MFM probe [78], or ground-state FM/AFM phase co-existence in-keeping with a generalised Potts model [79] tunable by annealing with field biases [79, 80]. Another way to couple two lattices together is by placing interaction modifiers at frustration sites, e.g. superimposed coupled square ASI and disk lattices [81].

This section has reviewed the influence of the design of the lattice on the frustration occurring at the vertex junctions. Numerous designs that are dotted about the literature have not been possible to discuss in this section in the efforts to keep this review concise. However, a number of themes from the structures selected have either influenced or neatly complimented the works in the later chapters on ASI (Chaps 6-8. With increasingly imaginative efforts, and the subsequent improvement of lithography techniques, it is a near certainty that novel designs of frustrated meta-materials will continue as the field develops.

### 2.2.3 Magnetic reversal mechanisms in ASI lattices

The dynamics and process of magnetisation reversal in ASI is one of the most prominent aspects of research. For the reasons described in subsection 2.2.2, the reversal mechanisms in connected and disconnected lattices are slightly different, thus this subsection will be divided into two parts.

#### Disconnected lattices

Figure 2.8 (reproduced from Skjærvø *et al.* in Ref. [31]) describes the reversal mechanism of Kagomé and square lattices (top and bottom, respectively) starting from saturation of spins towards the left of panel 1. Inset is a representation of the dumbbell model to represent the magnetic charges at each vertex, where the charge is represented by $\pm q$ depending on the direction of the NI. $Q_\alpha$ represents the net magnetic charge at each vertex ($\alpha$) as the sum of charges [42]. The energy landscape of the initial state across the vertices is as an alternating pattern of $\pm Q$. The application of a non-saturating field in the opposite direction triggers the start of the cascade event for magnetic reversal in panel two, with the Ising reversal of one NI. This results in a disruption to the periodicity of charge states as two energetically alike vertex charges of opposite sign form in neighbouring proximity. As a result, the net change at the highlighted vertices is $\Delta Q \pm 2q$, which is the definition of a monopole/antimonopole pair whilst their population is dilute [31, 42].

The chain of flipped islands between the monopole/antimonopole pairs are analogous to the singularities that bind Dirac monopoles [26]; These strings ensure that the monopole and antimonopole pair remain bound to each other, therefore conserving Maxwell's equation as described in Section 2.1. This Dirac string between the monopoles is essentially a thin solenoid, whose length governs the degree to which the monopoles are truly bound [25, 82, 83].

Dirac strings and bound monopole behaviour translates onto the effective monopole excitations observed in both spin ice and ASI systems. The monopole pairs here form as a consequence

of energetically-expensive spin flips that result in localised ice-rule violations. The flipped spin between the monopoles represent the Dirac string as the "flux pathway" between the opposing effective monopoles. As is the case in spin ice, it is energetically inexpensive to move the monopoles throughout the lattice as the vertices that are incorporated into the string pathway are energetically equivalent to the surrounding lattice (providing the ice-rule is predominantly conserved). Due to this, further spin flips result in non-determinate Dirac string lengths and pathways [25] between the magnetic monopoles. This does not hold if there are an excess of monopole-pairs that form in the lattice, as they do interact with a weak preferential charge ordering of monopole vertices during the reversal process [84, 85].

The remaining panels demonstrate the expansion of the Dirac string with increased applied field. This can result in the formation of ice-rule forbidden states $\pm 3q$ (panel 3). Ultimately, this state is still the result of a net change of $\Delta Q = \pm 2q$. Excluding annihilation events where non-associated monopole/anti-monopoles combine, these charges exist up to the point of reversed saturation, where they terminate at the lattice edges and energetic periodicity is restored across the lattice.

The mechanism for a square lattice in Figure 2.8 (bottom) is equivalent to the prior description for the Kagomé lattice. The initial configuration starts with a net vertex charge $Q = 0$ from the

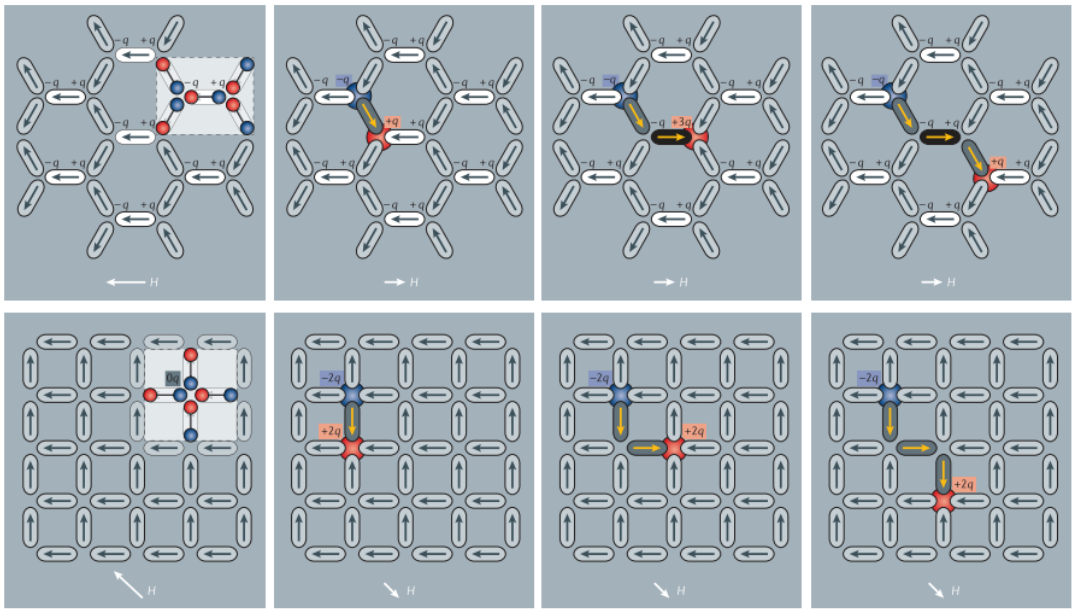

FIGURE 2.8. Magnetic reversal mechanism of Kagomé (top) and square (bottom) ASI under increasing applied field ($H$). $q$ notation represents the net vertex charges at each junction. Inset in the left panels represent a dumbbell model of the magnetic charges. Field directions are indicated by the white arrow at the bottom of each panel. ©2020 Nature Research. Reprinted, with permission, from Skjærvø *et al.* [31].

additional participating NI at each junction. This does provide an additional degree of freedom for the Dirac string expansion, as well as a simpler understanding of the topologically protected charge states as $\Delta Q = Q$, thus charge is also conserved [31]. For increasingly dense emergent monopole/antimonopole pairs this mechanism is slightly altered as the initial periodic state breaks up into smaller domains of alternated vertex order, until only short-range order remains [86].

### Connected lattices

In the connected Kagomé lattice, a dumbbell model at each junction is replaced with a slightly different mechanism during magnetisation reversal. Instead, we consider the gross point-charge at each junction as the coupling between connected NWs is too great. Figure 2.9, reproduced from Ref. [87], presents a schematic of the magnetic reversal mechanism of the connected Kagomé lattice. The magnetic reversal of connected wires is essentially DW propagation throughout the arms of the lattice. Prior to the switching event (a-b), the magnetisation in the NWs points along the respective long axes except at the junction, which exhibits a curl in the magnetisation (i.e. a DW) [87, 88]. Upon increasing the applied field, a transverse DW (or vortex DW, dependent on the constituent dimensions of the NWs in the lattice) nucleates and propagates along the length of the wire (c-f). Assuming the unit-cell extends without bounds, this can trigger another

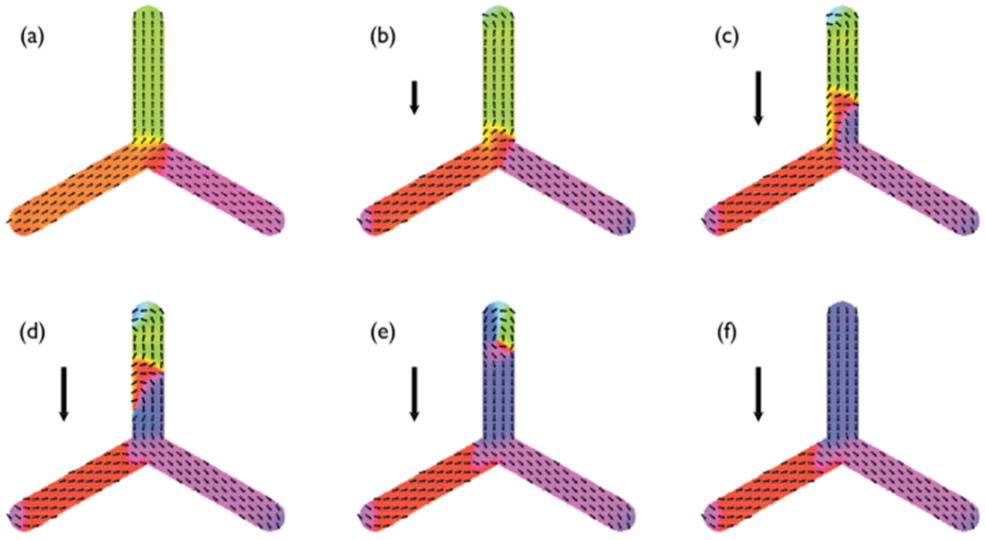


FIGURE 2.9. Magnetic simulations of the reversal in the primitive unit cell of the connected Kagomé lattice. Under no and field $H << H_c$ (a and b, respectively) a DW is pinned at the junction. (c-f) as field $H \approx H_c$ a DW detaches from the junction and propagates through the vertical leg. ©2012 Institute of Physics. Reprinted, with permission, from Shen *et al.* [87].

switching event at the next vertex junction, thus propagating along the lattice in long cascades.

A deviation from the idealised case is seen in connected lattices, which stems from symmetry breaking induced by the chirality of the transverse/vortex DW. This also results in a directional bias in the cascading reversal mechanism [89]. As such, the ability to control and fix the chirality of the DW can result in a preference in propagation direction, which may be used for deterministic logic operations [32]. However, this in practice is difficult as stochasticity in DW propagation may be reintroduced by Walker breakdown above a critical field. This describes precessions in the spin structure of the DW as it propagates that can cause its structure to change (e.g. inversion of chirality) [90–92].

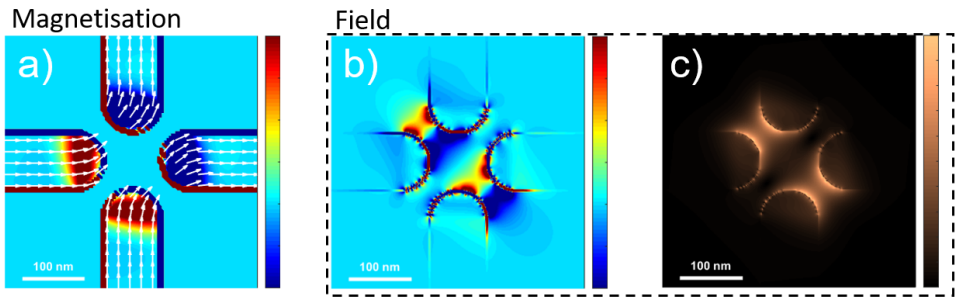


FIGURE 2.10. (a) Modelled magnetisation map of an X-shaped junction in the $T_2$ energy configuration; arrows represent the in-plane magnetisation vector and the colour-map represents the divergence of the magnetisation. (b-c) Stray-field maps of the same junction indicating the strong coupling between nearest-neighbour vertices of opposing magnitude; the maps represent the curl and the magnitude of the field vector, respectively.

One aspect where the distinction between connected and disconnected lattices is important is the propagation mechanism of the magnetic chain upon switching. Comparing with the disconnected lattice in the purely Ising mechanism, the probability of the Dirac string propagation direction should also be 50/50 down either leg of the junction (excluding the leg that has just switched). This is because the system would be perfectly symmetric, thus the propagation direction should have a random walk selectivity.

In reality, the NIs do deviate from this idealised case due to the inter-island coupling between neighbouring NIs at the junction. This results in a bending of the magnetisation at the NI vertices breaking the vertex symmetry and yielding $S$ and $C$-shaped magnetisation vectors across the NIs [93, 94]. This evidences a chiral nature to the bound monopoles at vertex junctions, which can be biased by field or cell geometry. A demonstration of the inter-island coupling, and resultant divergence from the Ising behaviour, is demonstrated in the modelled magnetisation map of a square vertex junction presented in Figure 2.10.

Thus, despite the slightly different mechanisms in magnetic reversal between connected and disconnected lattices, the use of connected lattices for integrated electrical devices (e.g.

nanomagnetic logic with an electrical read out) has an equivalence to the degrees of freedom within disconnected lattices. A comparison of connected and disconnected lattice is conducted in Chapter 8.

## 2.3 Summary

Throughout this chapter, geometric frustration and its application to two-dimensional lattices was introduced and associative energies demonstrated through dipolar interactions within the Ising model. A comprehensive review of the square and Kagomé lattices was conducted, discussing the uses and pitfall, as well as their magnetic reversal mechanisms. A review of unique lattice designs and their broader impact was also conducted, demonstrating how the finely tuning the topology of the unit-cells within the lattice impacts the energy landscape of the frustrated structures.

A number of these elements of ASI literature either influence or compliment the work undertaken throughout the presented thesis. Namely: the phenomena under study e.g. magnetic reversal and energy-states; tuning the frustration by design; and disrupting lattice periodicity.

CHAPTER 3

# METHODS

This chapter outlines the experimental descriptions applied in the data acquisition and analysis for the present work alongside their key concepts. Any additional experimental procedures will be specified in the proceeding chapters. Many of the methods used throughout the thesis have been a collaborative effort. Therefore, where appropriate, collaborators have been cited within the relevant sections.

## 3.1 Magnetic Force Microscopy

This section reviews the methodology of magnetic force microscopy (MFM), a technique to spatially resolve stray magnetic fields emanating from a sample surface, with nanoscale precision. Its immense popularity as a technique comes from its relative simplicity, as it does not require specialised equipment/facilities or complex sample preparation. However, the technique is largely qualitative as the resultant micrographs are a convolution of both the probe and the sample's magnetic stray-field properties. In addition, the method is susceptible to parasitic probe-sample interactions. Thus, the retrieval of quantitative information is an ill-posed problem [95]. The first section reviews the principles behind MFM as it is heavily used throughout the remainder of the thesis to visualise and understand the physical systems under study.

### 3.1.1 Background of Magnetic force microscopy

First demonstrated in 1987 [96, 97] MFM has become a widespread characterisation technique to measure stray magnetic field distributions on the nanoscale. The technique has high spatial resolution (approximately 50 nm), works in variable temperatures [98–102] and applied magnetic fields [39, 103–105], whilst remaining versatile and simple in operation. However, for most

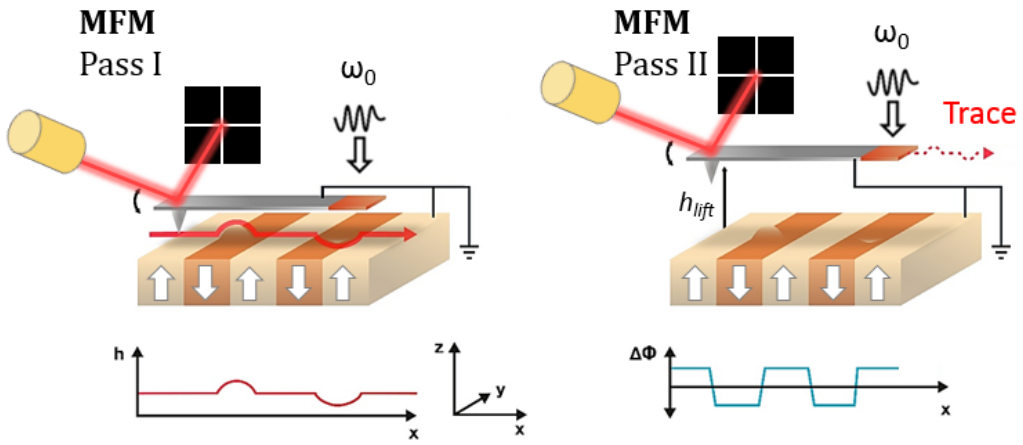


FIGURE 3.1. Standard two-pass MFM: In the first pass (*left*), the probe raster scans the surface, mapping the topography of the sample by "tapping" along the surface at its resonant frequency ($\omega_0$); in the second pass (*right*), the probe lifts a set distance away from the sample ($h_{\text{lift}}$) and maps the long-range interactions, via the phase change of the oscillating cantilever, at a constant probe–sample separation. Adapted from Kazakova *et al.* [106]

users, MFM provides only qualitative information and the number of modes is usually limited. Additionally, samples investigated by MFM are largely restricted to "classic" ferromagnetic samples (typically, thin films or patterned nanostructures) [106].

MFM is a dynamic scanning probe microscopy (SPM) technique. These techniques represent a class of measurements that use a microscale cantilever with a nanoscale sharpened tip grown on the free-end (typically a pyramidal or conic in shape). This probe is traditionally composed of silicon with a magnetic alloy (e.g. CoCr) coating of approximately 10-50 nm thickness [107]. The technique is performed using a semi-contact (or tapping) method, where the probe is vibrated at (or near) its resonant frequency (normally $10^1 - 10^2$ kHz range) with a piezoelectric actuator. An AC-voltage applied to the actuator produces its vibration normal to the surface plane, which in turn excites the probe's oscillation when in physical contact with the fixed end of the cantilever [108].

A typical MFM procedure involves the acquisition two concurrent raster-scans over a sample area: the first is in contact with the sample surface; and the second is performed at a set distance above it (Figure 3.1) such that the probe is no longer making physical contact with the sample while oscillating. The relative changes to the oscillation amplitude of the probe, monitored by a reflected laser focused on the end of the cantilever and detected by a photo-diode providing information of the probe-sample interactions which are indicative of the surface topography and stray-magnetic field, respectively. First, the topography of the surface is obtained by using the semi-contact mode atomic force microscopy (AFM) method, which measures the van der Waals

(vdW) interactions between the probe and sample. During the second pass, the probe is lifted away from the sample so that vdW interactions are negligible and the initial topography profile is repeated at the constant tip-sample separation and sensitive only to long-ranged forces [106].

Despite decades of advances in magnetic imaging [106, 109, 110] obtaining direct quantitative information with high spatial resolution and affordable equipment remains an outstanding challenge. Attempts to extract quantitative measurements from MFM images includes a deconvolution method of extracting the instrument calibration function (also referred to as the tip-transfer function (TTF)) from an MFM image of a reference magnetic thin-film [111, 112]. Similarly, a method for calibrated measurement using the stray-field from current-carrying micro-coils [113, 114] is also reported. The first of these calibration procedures will be discussed in Section 3.1.4, but first an introduction to the physical principles of probe-sample interactions in MFM is required.

### 3.1.2 Physical principles of magnetic force microscopy

The forces between the probe and the sample in SPM measurements can be separated into two categories: short- and long-range interactions. The first- and second-passes in MFM samples the short- and long-range interactions, respectively. Short-range interactions are defined through the Lennard-Jones potential ($W_{LJ}^{12-6}$), which describes the dominance of attractive (vdW) and repulsive (Coulombic) interactions as a function of distance between two neutral atoms

$$W_{\mathrm{LJ}}^{12\text{-}6} = 4\epsilon \left[ \left(\frac{\sigma}{r}\right)^{12} - \left(\frac{\sigma}{r}\right)^{6} \right] \tag{3.1}$$

where $\epsilon$ is the depth of the potential well, $\sigma$ is the distance at which the inter-atomic potential is zero and $r$ is the separation. The $r^{-12}$ and $r^{-6}$ terms describe the length-scales of the repulsive and attractive regimes, respectively [115]. Tip-sample interactions act over multiple atomic lengths, therefore the interaction is integrated across (relative) macroscopic bodies. Hence, Equation 3.2 describes the tip as a sphere approaching a flat sample (i.e. the sample) as depicted in Figure 3.2 [116].

$$W_{\mathrm{LJ}} = \frac{A_H R}{6\sigma} \left[ \frac{1}{210} \left(\frac{\sigma}{r_{\text{t-s}}}\right)^{7} - \frac{\sigma}{r_{\text{t-s}}} \right] \tag{3.2}$$

where $\frac{A_H R}{6\sigma}$ describes a macroscopic variation on $\epsilon$ in terms of the Hamaker constant ($A_H$) and the tip radius ($R$).

When tip-sample separation is greater than $\sim 5$ nm the attractive regime from Coulombic interactions become negligible, and long-range interactions dominate [117]. The long-range force interactions between the magnetic probe and the magnetic sample in MFM are measured in the second pass by the shift in frequency ($\Delta\omega$), amplitude ($\Delta A$), or phase ($\Delta\phi$) of the cantilever

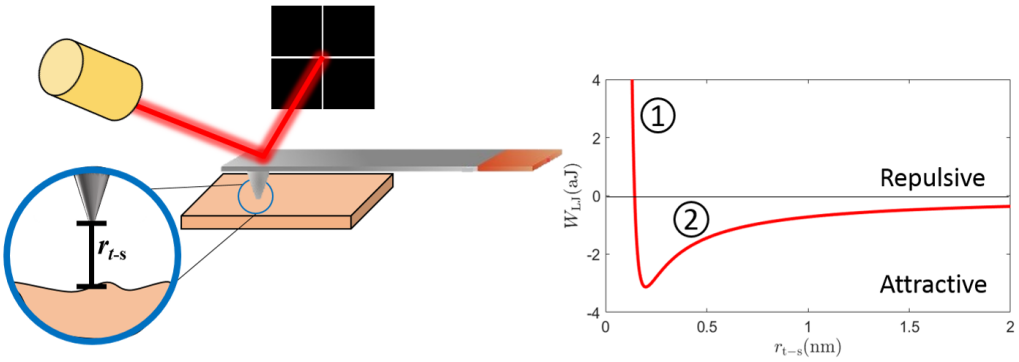


FIGURE 3.2. (a) Schematic of AFM with tip-sample separation defined inset. (b) plot of the Lennard-Jones potential as a function of tip-sample separation; regions 1 and 2 describe the contact and non-contact regions of the plot; negative values are in the attractive force regime.

from the initial driven parameters (i.e., $\omega_0$, $A_0$,and $\phi_0$, respectively). However, quantitatively describing the tip-sample interactions without prior knowledge of the probe magnetic and physical properties is not possible. For a quantitative understanding of MFM interactions it is important to initially describe the instrumentation in the absence of any tip-sample interactions. One way to do this is through a harmonic description of the system. The oscillating probe in the presence of damping can be approximated as a point-mass spring and thus the amplitude of the driving force ($F_0$) can be defined by a classic non-linear, second order differential Equation 3.3, i.e., from Newton's second law of motion [108]

$$F_0\cos(\omega t) = \underbrace{mz''(t)}_{\text{Newton's 2nd law}} + \overbrace{\frac{m\omega_0}{Q}}^{\text{Damping}} z'(t) + \underbrace{kz(t)}_{\text{Hooke's Law}}, \tag{3.3}$$

where $k$, $m$, $z$, $Q$, and $\omega_0$ are the spring constant, point mass, $z$-displacement, quality factor and resonant angular frequency of the cantilever, respectively. $\Delta\phi$ is the most common representation of magnetic contrast in the second-pass of MFM; hence equation relates the phase of the oscillating probe in free space ($\phi_f$) to the excitation frequency ($\omega$) in the absence of externally acting forces [118, 119]

$$\phi_f = \tan^{-1}\frac{m\omega\omega_0}{Q(k-m\omega^2)}, \tag{3.4}$$

$$k = m\omega_0^2 \tag{3.5}$$

where the relationship between the $k$ and $\omega_0$ is defined in Equation 3.5. When the probe is oscillated at $\omega = \omega_0$ the denominator in Equation 3.4 tends towards infinity, thus dictating $\phi_f(\omega_0)$ is equal to $\pi/2$ rad. By including all tip-sample interactions ($\zeta$), e.g. vdW interactions,

magnetostatic, or electrostatics, the presence of these forces subtly changes the oscillation and subsequently the instrument response. Assuming small displacements ($z$) with respect to the rest position ($z_0$) of the cantilever, the force interactions can be linearly approximated [120]

$$\zeta \approx \sum_i \frac{\partial F_i}{\partial z} \tag{3.6}$$

so Equation 3.3 is modified to

$$F_0 \cos(\omega t) = m z''(t) + \frac{m\omega_0}{Q} z'(t) + \{k - \zeta z(t)\}. \tag{3.7}$$

The modification of the third term in Equation 3.7 describes the effective spring constant ($k_{\text{eff}} = k - \zeta$). Using this, Equation 3.4 can also be adapted to encompass tip-sample interactions as such,

$$\phi(\omega) = \tan^{-1}\left(\frac{m\omega\omega_0}{Q\left(k + \zeta - m\omega^2\right)}\right), \tag{3.8}$$

$$\phi(\omega) = \tan^{-1}\left(\frac{k}{Q\zeta}\right)\Bigg|_{\omega=\omega_0}. \tag{3.9}$$

Finally, the difference between the respective phases of oscillation in the presence and absence of tip-sample interactions can be used to calculate $\Delta\phi(\omega)$ and relate the MFM image to the acting force gradient [106, 108]

$$\Delta\phi(\omega) = \frac{\pi}{2} - \tan^{-1}\left(\frac{k}{Q\zeta}\right)\Bigg|_{\omega=\omega_0} \approx \frac{Q\zeta}{k}. \tag{3.10}$$

Equation 3.10 is particularly useful as a measurement of the probe cantilever's $Q$ and $k$ can be conducted within commercial software prior to the MFM measurement.

### 3.1.3 MFM Probes

#### Commercial Probes

The selection of magnetic probes is an incredibly important part of the MFM measurement. A broad description of a commerical SPM probe was given in Section 3.1.1. An MFM probe is coated with a ferromagnetic material so it becomes sensitive to long-range magnetic forces. Often, a Co-based alloy is used as the magnetic coating on the probe and its thickness defines the magnitude of its moment [121]. Additionally, ultra-high-moment probes may be composed of a stronger Fe-based alloy (e.g. FePt) [122].

The ideal MFM probe is one with high spatial resolution, which does not influence the inherent magnetisation of the sample during imaging and whose own magnetisation is not influenced by the sample. The ideal MFM probe would possess a low stray-magnetic field with a high-coercivity. To engineer this in a batch process is challenging, and often one desirable property is a trade-off for the other. Figure 3.3 (a-d) are scanning electron microscopy (SEM) images of four different MFM probes, demonstrating the different shapes of the probe that can be grown on the end of the cantilever.

Figure 3.3(a) is an example of a probe with a pyramidal architecture. Specifically it depicts the Nanosensor$^{TM}$ PPP-MFMR probe which is formally classified as a standard-moment probe [107]. It has a coating of CoCr alloy of thickness of ~ 40 nm, quoted magnetic coercivity of ~ 30 mT and a remanence magnetisation of $\sim 3 \times 10^5$ A/m. This pyramidal probe architecture is likely the most common among commercial probe manufacturers as many models possess a similar shape (e.g. Bruker$^{TM}$ MESP, and NT MDT MFM01). MFM probes are normally fabricated in two steps: first, reactive-ion etching (RIE) a silicon wafer is used to define the probe shape[123]; subsequently the magnetic coating is sputtered on the probe in a second step.

An alternative architecture is the conical designs in Figure 3.3(b-c), which depicts a Team Nanotec High-Resolution ML1 and NT MDT HA-FM Etalon Series, respectively. In Figure 3.3(b) the probe is composed of a Co-alloy with $t \approx 20$ nm, thus is classified as a low-moment probe. The thinner magnetic coating improves the spatial resolution of the imaging as the apex radius is reduced. The conical design also improves the resolution and reduces asymmetry in images of nanostructures, which is useful for probe modelling [124]. The Etalon probe in Figure 3.3(c) has a "birthday candle" shape in order to increase the resolution and provide less variance in physical properties between probes.

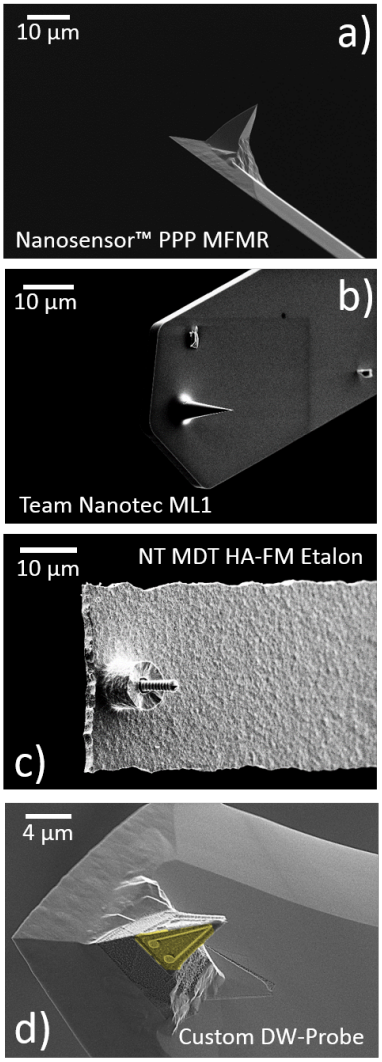


FIGURE 3.3. SEM images of commercial and custom MFM probes. (a) Nanosensors PPP-MFMR; (b) Team Nanotec ML1; (c) NT MDT HA-FM Etalon; (d) custom DW-probe with V-shaped nanostructure on one face of the probe (highlighted in yellow).

**Custom Probes**

With commercially-made probes, the variables to tune the magnetic properties of a probe are limited to architecture and coating thickness in order to reduce fabrication costs. However, custom-made probes may be more versatile or better suited to an application as more variables can be tuned to improve imaging properties. From the literature there are three methods for customising MFM probes for specialised use: fabricated nanostructures on the apex; adapted magnetic coatings; and adhered magnetic structures [106].

Fabricating nanostructures onto the probe's apex allows for engineered magnetic properties not just from the shape anisotropy/structure but also its composite material. It has been shown

that the spatial resolution and signal-to-noise of MFM probes may be improved by depositing a sharp magnetic "spike" onto the probe apex [125, 126]. Equally, the imaging resolution can be improved by sharpening the sputtered magnetic coating on the probe apex by FIB milling.

FIB may also be utilised to mill structures from the sputtered coating, e.g. the V-shaped probe in Figure 3.3(d). The probe depicted is fabricated from a Nanosensor PPP MFMR as a precursor, from which the majority of the magnetic coating was etching away using Ga-ion FIB leaving a V-shaped magnetic nanostructure on just one face of the MFM probe. From the shape anisotropy of the nanostructure, a DW is constrained at the probe apex providing a highly localised point-source for a stray-magnetic field. The design possesses two magnetic states with pinned or curled DW at the nanostructure apex offering an *in situ* tunability of the stray-field for measuring diverse samples [105]. The loss of material also reduces the stray-field without sacrificing resolution and possesses an enhanced sensitivity and coercivity [127]. This is the focus of Chapter 4 for a V-shaped probe of a similar design.

Adapting the magnetic coating of the probe does not require extensive fabrication facilities, just the ability to sputter directly onto a silicon probe. Increased resolution has been demonstrated in partially coating MFM probes [128, 129]; whereas multi-layer partially-coated MFM probes demonstrated tunable magnetic moments by induced ferro-/antiferromagnetic alignment. The latter were fabricated by depositing layers of magnetic material sandwiching a non-magnetic spacer [130, 131]. This offers the ability to control high/low moment magnetic states by switchable ferro- or antiferromagnetic states in the layers to limit the eminent stray-field from the probe's apex.

Finally, adhering materials onto SPM probes allow for localised studies of particular subjects of interest. Adhered magnetic nanostructures on AFM probes have been used to improve the probe magnetic imaging properties, such as high-resolution monopole-like probes using Fe-stuffed carbon nanotubes [132–134]; or evaluation of the sensitivity of spintronic devices to individual magnetic nanoparticles stuck the the probe apex [135, 136].

### 3.1.4 Magnetic probe-sample interactions

As discussed in Section 3.1.1, MFM does not directly quantify stray magnetic fields on the nanoscale for two reasons. First, the MFM signal is a convolution of the probe and sample's magnetic properties, thus quantifying the stray field from the sample is an ill-posed problem. Second, the MFM image is relative to changes in the probe's oscillation parameters (e.g. phase change), rather than a direct measurement of the field. In this section, the relation of the force gradient to the probe and sample's magnetisation in MFM will be derived, followed by the theory and methodology for calibrating a probe's stray magnetic field with a reference thin film with high perpendicular magnetic anisotropy (PMA). This calibration can then be used for quantitative measurement of a measurand.

Accurately describing magnetic interaction forces in MFM can be extremely complex, as the

magnetisation of the tip and sample are not infinitely "rigid". However, for weak magnetostatic interactions, this complexity can be neglected and experimentally the assumption holds true providing adequate probe selection. Assuming negligible electrostatic or vdW interactions, the total magnetic interaction energy, $E_t$, between the MFM probe and magnetic sample can be described by magnetostatic interactions [117, 137]

$$E_t = -\frac{\mu_0}{2}\left[\iiint_{tip} \boldsymbol{M}^{tip}\cdot\boldsymbol{H}^{s}dV \quad + \iiint_{sample} \boldsymbol{M}^{s}\cdot\boldsymbol{H}^{tip}dV\right] = -\mu_0 \iiint_{sample} \boldsymbol{M}^{s}\cdot\boldsymbol{H}^{tip}dV, \tag{3.11}$$

where $\boldsymbol{H}$ and $\boldsymbol{M}$ are the magnetic field and magnetisation, respectively (and superscripts $s$ and $tip$ denote the sample and tip, respectively). Providing the two integrals of Equation 3.11 are equal, it is possible to simplify the expression through the reciprocity relation. When calculating the force acting on the probe, a coordinate system $(x', y', z')$ is required, where the origin $\boldsymbol{t} = t_x, t_y, t_z$ describes the probe's apex position [117, 138–140]

$$E_t(\boldsymbol{t}) = -\mu_0 \iiint_{sample} \boldsymbol{M}^{s}(x', y', z')\cdot\boldsymbol{H}^{tip}[(x', y', z') + \boldsymbol{t}]dV'. \tag{3.12}$$

From Equation 3.12, the energy at each point over a Cartesian volume is related to the convolution of both $\boldsymbol{H}^{tip}$ and $\boldsymbol{M}^{s}$. The energy of interaction may be quantified in terms of magnetic volume charges ($\rho^s = -div\boldsymbol{M}^{s}$) and surface charges ($\sigma^s = \boldsymbol{M}^{s}\cdot\boldsymbol{n}$, where $\boldsymbol{n}$ is the unit vector normal to the surface) by substituting $\boldsymbol{H}^{tip} = -\nabla\phi^{tip}$ (i.e. the scalar potential of the stray field) into equation 3.12 and integrating by parts [5, 137]

$$E_t(\boldsymbol{t}) = -\mu_0 \oint_{sample} \sigma^s(x', y', z')\cdot\phi^{tip}[(x', y', z') + \boldsymbol{t}] \quad dx'dy' + \iiint_{sample} \rho^s(x', y', z')\cdot\phi^{tip}[(x', y', z') + \boldsymbol{t}] \quad dV'. \tag{3.13}$$

In terms of force ($F = -\nabla E_t$), the relation becomes

$$\nabla F(\boldsymbol{t}) = \mu_0 \oint_{sample} \sigma^s(x', y', z')\cdot\nabla\boldsymbol{H}^{tip}[(x', y', z') + \boldsymbol{t}] \quad dx'dy' + \iiint_{sample} \rho^s(x', y', z')\cdot\nabla\boldsymbol{H}^{tip}[(x', y', z') + \boldsymbol{t}] \quad dV'. \tag{3.14}$$

The first and second integrals extend over the sample surface and volume, respectively. In homogeneous magnetic fields, such as the ones used for tip calibration, the second integral is

reduced to zero, leaving the first as an adequate description of how the force gradient scales with the probe and sample's magnetic parameters.

### 3.1.5 Calibrated magnetic force microscopy

#### Why is MFM not quantitative?

[1]So far in this section, it has been demonstrated that the methods of interaction between the probe and the sample are well known, however the relation between the MFM phase contrast and the true magnetic description of the sample remains non-trivial. The interaction between the sample and the tip integrated over the probe-volume results in the MFM image representing a messy convolution of both the probe and the sample's magnetic properties (see Equation 3.14). Therefore, the extraction of magnetic stray-field of the sample is an ill-posed problem as the probe's magnetic properties are unknown *a priori* to measurement [141, 142]. This makes it challenging to accurately quantify the sample's stray-field.

#### Method of TTF approach

##### Stage 1: Data acquisition

From the reciprocity of the probe sample interaction (see Equation 3.11), it is possible to extract the stray-field of the probe from imaging a reference sample with known magnetisation (Figure 3.4 **Step 1**). The reference sample is a film with high PMA, where the magnetisation can vary in $x$ and $y$ but the moment orients normal to the surface plane. The benefit of this is that the sample can be assumed to possess only magnetic surface charges on the top and bottom surfaces equal to $\pm M_s$ so that the volume charges ($\rho$) from Equation 3.14 drops out and simplifies the equation [111, 117].

The sample used for quantitative measurements throughout this thesis was a Co/Pt multilayer sample with the layer architecture [(Co(0.4nm)/Pt(0.9nm)] with 100 repeats (see Section 3.4 for fabrication details). Thin Co layers (0.2-0.6 nm) in a Co/Pt multilayer stack exhibit strong PMA with ferromagnetic coupling through the Pt layers [143]. From the minimisation of exchange, anisotropy and dipolar energy terms the magnetisation of the reference sample in the remanent state forms a labyrinth domain pattern [143, 144]. This reference film has an average domain width of $w$ = 170 nm and domain wall width $w_{\mathrm{dw}} \approx 16$ nm. In the remanent state the power spectrum of the acquired MFM image has a singular prominent frequency equivalent to the domain width. However, the non-periodic domain pattern means the image possesses a wide span of additional spatial frequencies that are useful for the TTF calculation [145].

The magnetic properties of the reference film were quantified by vibrating sample magnetometry (VSM), where the $M_s$ = 554kA/m (±30kA/m) and uniaxial anisotropy ($K_u$ = 0.4 MJ/m$^3$) along

[1]The TTF calculations throughout the present thesis have been performed in collaboration with V.Neu (IFW Dresden, Germany).

the surface normal (see Section 3.4 for details of the fabrication). The Bloch type DW between domains is approximately 16 nm in width, otherwise the magnetisation is assumed to be highly parallel to the surface normal across the whole film. The labyrinth domain pattern develops homogeneously across the whole sample surface, therefore the scan location is not a factor for

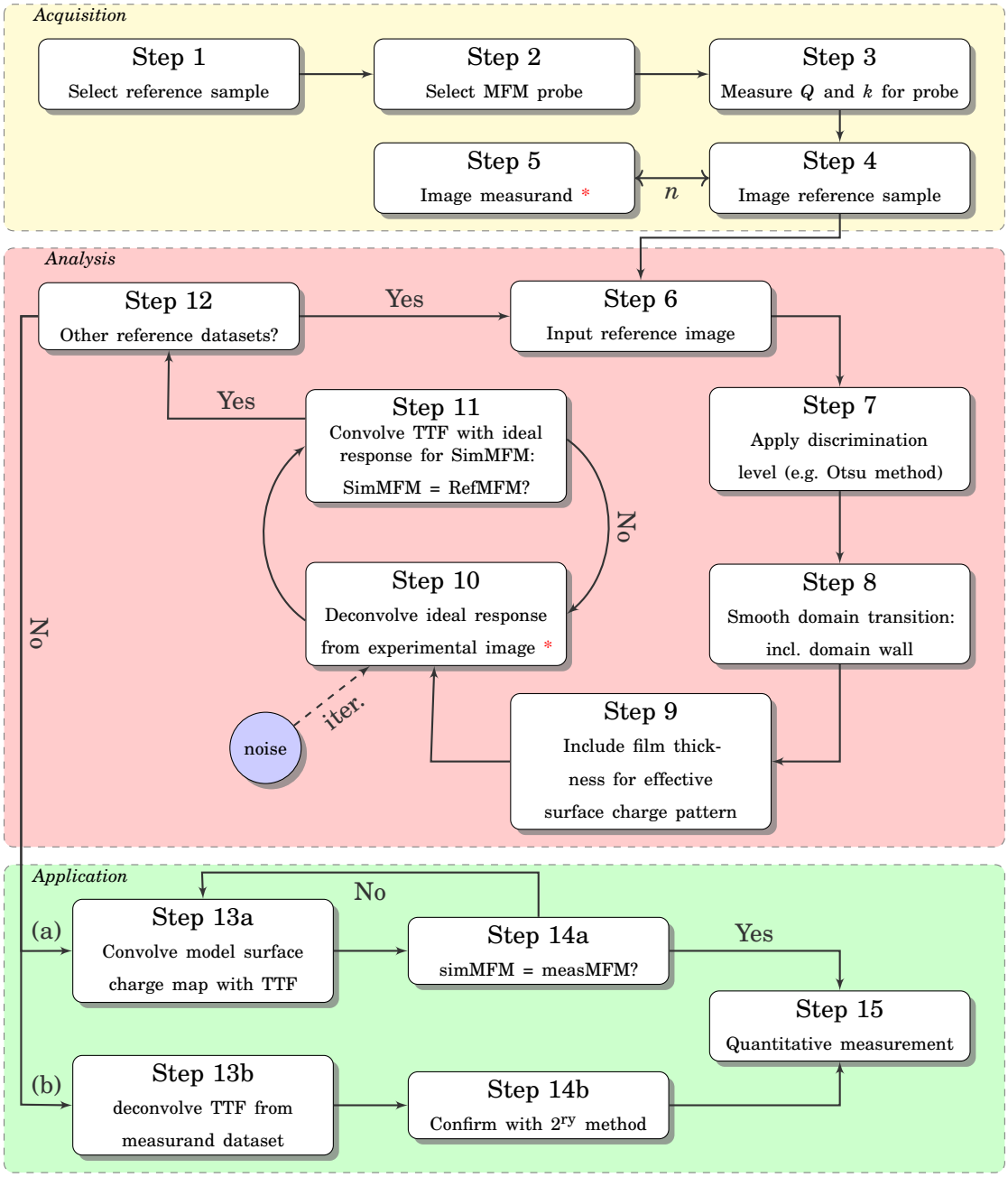


FIGURE 3.4. Flow diagram for the three elements for quantitative magnetic force microscopy measurements: Acquisition of the dataset, the steps for analysis, and the application to a dataset.

qMFM measurements [127, 138].

As discussed in Section 3.1.3, it is imperative that the probe selection is adequate for imaging both the reference and the sample of interest (Figure 3.4 **Step 2**). The assumption for the equations in section 3.1.4 is that the magnetic interaction is hard; i.e. the sample does not influence the probe's magnetisation and *vice versa*. This assumption removes any coercivity/hysteretic effects in the calculation of the force gradient between the sample and the probe [111].

Figure 3.4 **Step 3** is covered extensively in section 3.1.2, as it allows us to relate the MFM contrast to the force gradient in $z$ (Equation 3.10). **Step 4** and **Step 5** are the MFM measurements of the reference sample and the sample of interest, respectively. It is imperative that the measurements are conducted in as similar conditions as possible. This includes the physical parameters of the measurement (e.g. the tip-sample separation). Therefore, parameters should be optimised for the measurement of the measurand, and then applied to the reference sample for quantitative measurement [145]. It is also preferable to image the reference sample at constant intervals of the measurement sequence (e.g. before and after imaging the measurand as a minimum) to assess the change in probe properties over the course of the measurement (e.g. from tip-wear) and thus apply it in the quantitative measurement.

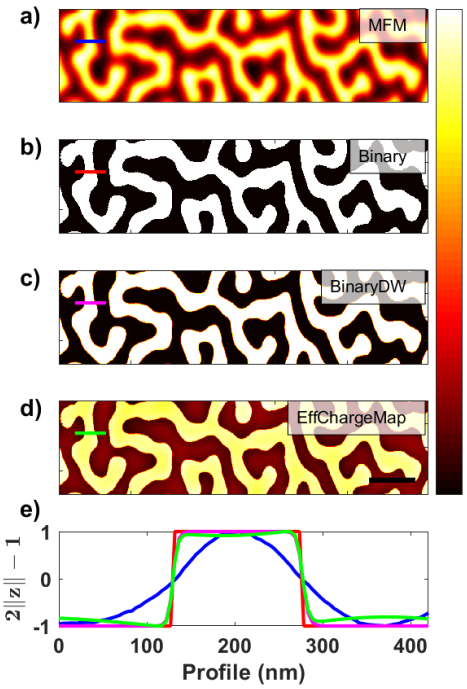


FIGURE 3.5. Plot of MFM (a); thresholded "binary" (b); binary convolved with domain-wall convolution operator (c); and effective surface charge map (d) images. Respective normalised line profiles through a domain (e). Black scale bar in (d) corresponds to 0.625$\mu$m.

### Stage 2: Data Processing and Analysis

After data acquisition, the next stage of the process is the data treatment and analysis. The method for deconvolving the probe's stray magnetic field was originally described by Hug *et al.* [111, 112, 117]. The method used throughout the present work is a slight adaptation as described by the group of Neu *et al.* [127, 138, 140, 145–147]. In 2D imaging, any image (in the absence of parasitic signals, e.g. from artefacts) can be described by Equation 3.15

$$m(\boldsymbol{r}) = s(\boldsymbol{r}) \cdot p(\boldsymbol{r}) + n(\boldsymbol{r}) \tag{3.15}$$

$$\boldsymbol{r} = x, y$$

where $m$ is the measured signal; $s$ is the ideal/actual signal; $p$ is the instrument function (i.e. the point spread function); $n$ represents additive noise introduced into the image; $\boldsymbol{r}$ is the $xy$-coordinate system over the area and the symbol ' $\cdot$ ' is a convolution operator. $p$ acts to blur the signal from $s$ and therefore a vast quantity of literature exists to deblur $m$ in order to extract $s$. $p$ in this case is functional magnetic form of the MFM probe, i.e. its $z$-derivative stray-field [111, 112, 145].

Usually, image processing methods are aimed towards qualitative improvement (i.e. sharpening) of the image rather than extracting quantitative information. Therefore, they estimate $p$ and $n$ until the best representation of the original signal is formed. Instead, qMFM acquires an accurate depiction of $p$ from a known $s$ and $m$ to be deconvolved to the measurand. **Steps 6-9** of Figure 3.4 describe the processes of taking the measured signal of the reference sample and "converting" into $s$ through image processing tools and including known magnetic parameters (Figure 3.5) [111, 112].

As the stray-field of the reference sample is assumed to be only normal to the surface plane, in **Step 7** the reference image (Figure 3.5 a) is thresholded to form a binary image of $\pm 1$'s with sharp transitions between the domains. The method to perform this operation can be as simple as thresholding by the mean of the MFM image, or using an thresholding approach with corrects for local background deviations e.g. the Otsu method [148] (Figure 3.5b).

To satisfy the real magnetic system, a 180° analytical approximation of a DW can be added to smooth the sharp transitions by convolving the binary image with a DW convolution operator (DWCO). In this case, a Bloch DW is introduced with a calculated DW-width, $\delta_{\mathrm{dw}} = \pi\sqrt{A/K_u}$

$$\mathrm{DWCO}(x,y) = \frac{1}{\cosh(\pi\sqrt{x^2+y^2}/\delta_w)}, \tag{3.16}$$

which produces a smooth transitions between the bright/dark contrasts, $\sigma$ (**Step 8**), as seen in figure 3.5 c [140]. A plot of the DWCO is displayed in Figure A.9 in the appendix. The effective surface charge map, $\sigma^s$, is calculated in Fourier space by convolving an exponential film thickness ($t$) factor (**Step 9**) and multiplying the normalised map by the $M_s$ of the material

$$\begin{aligned} \sigma^s(\boldsymbol{k}) &= M_s\sigma(\boldsymbol{k})\cdot(1-e^{-kt}) \\ \boldsymbol{k} &= (k_x,k_y),\ \ k = \sqrt{k_x^2+k_y^2} \end{aligned} \tag{3.17}$$

where the exponential component arises from the magnetic surface charge density at the lower surface of the film [111] (Figure 3.5 d). The effects from the image processing, step-by step, on the original MFM image is shown in line profiles across a two DWs (Figure 3.5 e). This produces the surface charge map (i.e. $s$ in Equation 3.15) that can now be deconvolved from the experimental image to produce the TTF.

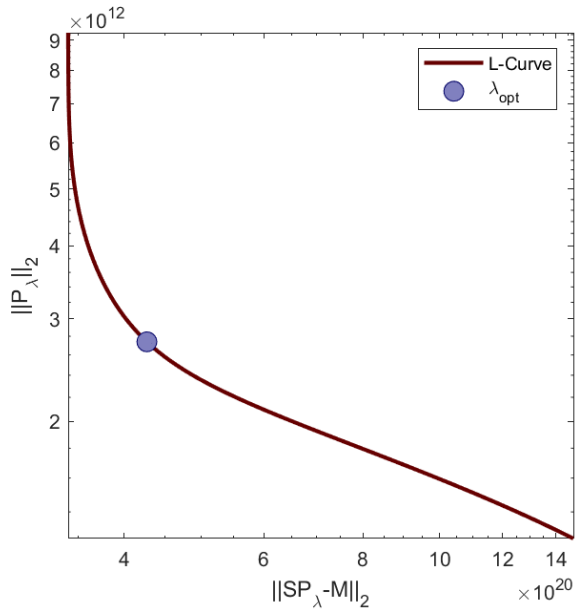


FIGURE 3.6. An example of an L-Curve where optimum $\lambda$ is indicated at the point of maximum curvature, which indicates the optimum trade-off between the two fitting parameters.

In the absence of noise (i.e. $n = 0$ in Equation 3.15) then calculating $p$ would be trivial in the frequency domain by $\hat{P}(\boldsymbol{k}) = \hat{M}(\boldsymbol{k})/\hat{S}(\boldsymbol{k})$, where accented capital letters denote the Fourier transform of the components of Equation 3.15 and $\boldsymbol{k}$ is the coordinate system $\boldsymbol{r}$ in frequency space [145]. However, in the presence of noise, $n$ would dominate at frequencies where $m$ is small, thus a form of filtering is required. There exists a number of ways for regularised deconvolution, the method of choice is the single-parameter pseudo-Wiener deconvolution filter, which assumes the noise is dominated by independent point noise [145]. The *pseudo*-Wiener filter is selected as the spectral density of the point spread function is not known *a priori* thus a suitable regularisation parameter $\lambda$ is used to represent the noise-to-signal ratio of the image

$$\hat{P} = \frac{|M|^2 S^*}{|M|^2|S|^2 + \lambda} M, \tag{3.18}$$

which occurs in Fourier space. The $|.|$ notation represents the magnitude of a complex number and the superscript $*$ denotes the complex conjugate. In **Steps 10-11** $\lambda$ is iterated to a least-squares fitting regime where the Euclidean distance between the simulated MFM image and the experimental image, respectively, is minimised.

Relying solely on this method from Wiener deconvolution does result in a zero-noise simulated MFM image. However, with decreasing $\lambda$, the tip's stray-field loses a reasonable profile expected for an MFM probe [145]. Therefore an "appropriate selection" of the optimum $\lambda$ is required,

from Tikhonov regularisation [149]. The error in the selection of the optimum $\lambda$ is subject to perturbation errors from noise/imaging artefacts and regularisation error from the difference between the regularised and exact problem.

These errors are dampened through regularisation. In practice, the optimum $\lambda$ is realised by the L-curve method, which is a log-log plot of the Euclidean distance of a regularised solution vs. the Euclidean norm of the corresponding residual. It directly compares the fit for the data-set to the size of the regularised solution as a function of $\lambda$ [149, 150]. Figure 3.6 demonstrates a typical L-Curve generated through the fitting process.

The optimum $\lambda$ is identified as the point of maximum curvature $\kappa$, i.e. the corner, of the L-curve (Figure 3.6 purple circle). Left of the identified point the solution is under-regularised, resulting in an unrealistic spatial description of the probe's stray-field, whereas right of the point is over-regularised, resulting in a poor fit of the simulated MFM image compared to the measured

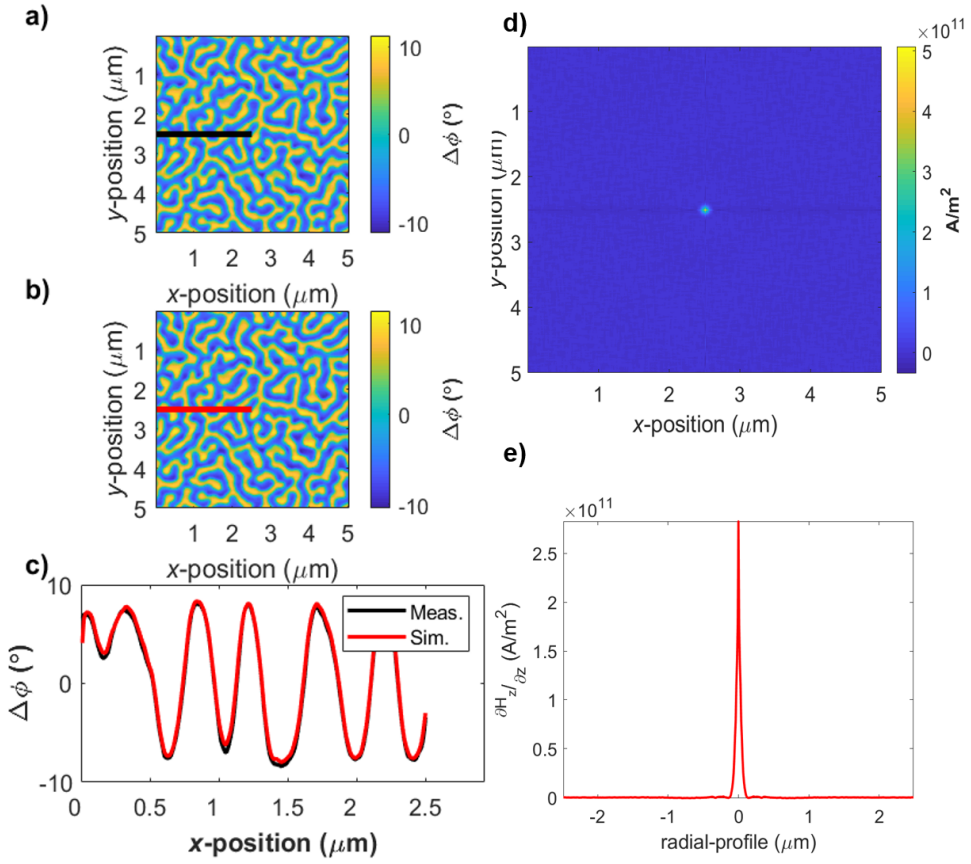


FIGURE 3.7. Experimental (a) and Simulated (b) MFM images of CoPt reference sample in degrees, with comparative line profiles to demonstrate goodness of fit (c, black and red profiles, respectively). (d) RS-TTF extracted from the experimental image (a) and it's respective radially averaged line profile (e).

image. Examples of the effects of over- and under-regularisation are displayed in Figure A.11 in the appendix.

If there are more data-sets of the reference film, then the procedure is repeated (**Steps 6-11**) in order to acquire a measurement series and/or average of the TTF. Or, for quantitative measurement of an unknown sample, we pass to the *Application* section in figure 3.4. Examples of route 13a - 15 are demonstrated in Chapters 4 and 6.

### 3.1.6 Equipment

Two SPM systems were used to acquire MFM measurements throughout the experimental chapters. The first is an NT MDT® NTEGRA Aura microscope (Figure 3.8a), which is highly customisable from its modular design. Of these modes, the *in situ* applied fields was used in order to probe the magnetic reversal of the samples under study (Figure 3.8b). The in-plane electromagnet is capable of ±150 mT field magnitude, however decays with pole-piece separation. The open access to the control panel allows for direct sampling of external signals as a function of the MFM scan or field application, therefore magnetotransport measurements could also be performed between MFM measurements. The second SPM is a Bruker® Dimension Icon microscope, which was used for standard MFM measurements.

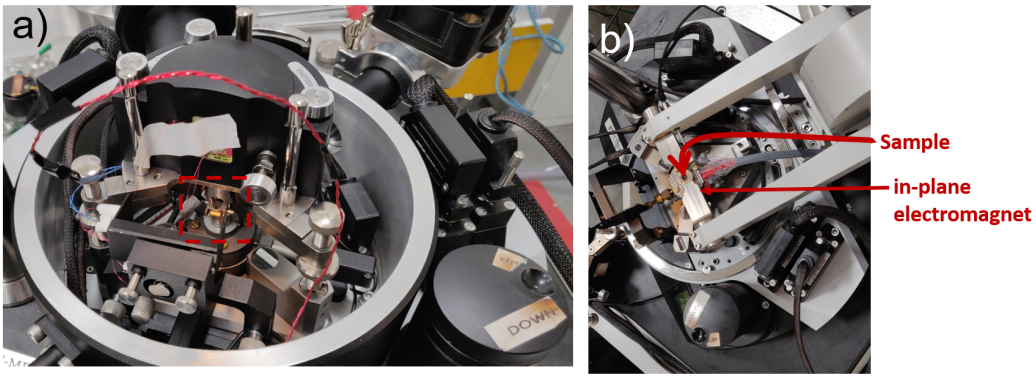


FIGURE 3.8. (a) NT MDT NTEGRA scanning probe microscope with scanning head in place; sample space highlighted by the red box. (b) Sample space without scanning head and with in-plane electromagnets installed.

### 3.1.7 Summary and Outlook

Throughout this section a comprehensive review of MFM was undertaken; from the operating principles of the technique, the physics of the probe-sample interaction, through to the steps for performing specialised qMFM measurements to perform quantitative measurements. MFM has been used frequently to assess the materials under study throughout the thesis. The robustness

of the quantitative measurements have been assessed throughout the experimental chapters as well, including its ability to quantify the stray-field gradient of a patterned MFM probe (Chapter 4) and its subsequent application to quantifying the stray-field from samples under study (i.e. a single nanowire and ASI lattices, Chapters 4 and 6, respectively). For the continued development and uptake of MFM (and qMFM) for application to novel research for future material systems, it is important to continually assess its application and suitability to a variety of experimental conditions and materials. In this way, the inexpensive methodology can continue to be applied to, and developed for, emerging trends on the mesoscale measurements of magnetic materials [106].

## 3.2 Magnetotransport and magnetothermal effects

Magnetotransport is the general term used to describe the measurement of any electrical or thermal effect resulting from a current passing through a conductor or semiconductor in a magnetic field (also known as galvanomagnetic effects). This section outlines the operating principle of the thermally induced magnetotransport effects, which have been performed in both a traditional sense and a more specialised SPM methodology in Chapter 5. The global transport methodology has been described at the end of this section, however the principle of the scanning probe method has been confined to Chapter 5 in order to maintain readability.

### 3.2.1 Anomalous Hall and Nernst effects

In order to explain the Anomalous Nernst effect (ANE) for Chapter 5 the anomalous Hall effect (AHE) should first be described. The AHE is somewhat similar to the ordinary Hall effect as it describes the generation of a transverse voltage in an orthogonal direction to the incident electric field, however the distinct caveat is that the AHE is only present in ferromagnetic materials. Despite the namesake, the mechanism(s) of the AHE is not analogous to the ordinary Hall effect [5, 151]. As a result, a ferromagnetic material has both an ordinary Hall and anomalous Hall components of the electric field ($E_{\mathrm{H}}$ and $E_{\mathrm{ANE}}$, respectively) response to a magnetic field,

$$\rho_{xy} = \frac{E_{\mathrm{H}} + E_{\mathrm{AHE}}}{J_x} = \mu_0 (R_{\mathrm{H}} H_z + R_{\mathrm{s}} M_z), \tag{3.19}$$

where $\rho_{xy}$ is the Hall resistivity, which combines the ordinary and Anomalous Hall coefficients ($R_{\mathrm{H}}$ and $R_{\mathrm{s}}$, respectively) [5, 6]. $R_{\mathrm{H}}$ depends mainly on the density of carriers, however $R_{\mathrm{s}}$ depends on a variety of material specific parameters including the longitudinal resistivity of the material [151]. In addition, the ordinary Hall effect contribution is approximately two orders of magnitude less than the AHE. Measurement of the ordinary and anomalous Hall effects are in principle the same methodology. A current is applied along one direction of the material and the transverse voltage is monitored as a function of a sweeping applied field normal to the surface plane. In a ferromagnetic material with PMA, the magnetisation switches as the critical field is

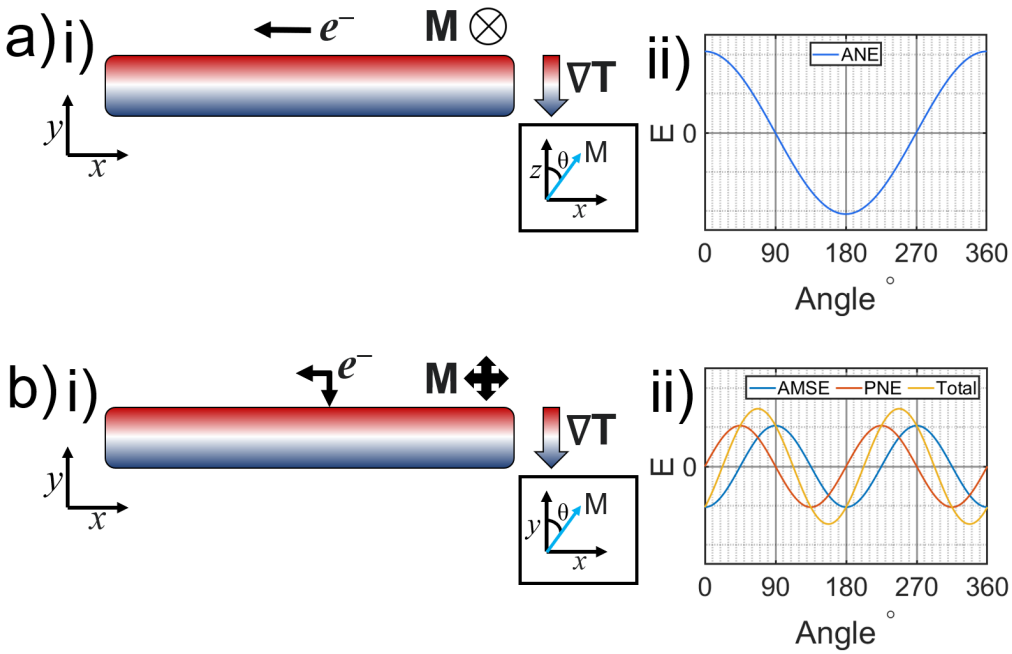


FIGURE 3.9. (a)(i) Schematic of the ANE in a PMA ferromagnetic block, where the electric field acts in the orthogonal direction to the incident thermal gradient $\nabla T$ and magnetisation ($M$); (ii) Plots the ANE response of a single spin at angle, $\theta$, from the $z$-axis. (b) Schematic of the AMSE and PNE in an in-plane ferromagnetic block, where longitudinal and transverse electric fields form from the result of a $\nabla T$ across the material. (ii) Plots of the AMSE, PNE and combined response for a single spin at angle, $\theta$, from the $y$ axis.

reached. This results in a switch of the sign of $E_{\mathrm{AHE}}$. In ferromagnetic materials, the ordinary Hall effect is a parasitic component of the AHE signal, and may be corrected by linear subtraction of the extrapolated gradient above the switching field of the ferromagnetic sample, where the AHE contribution to the signal has saturated (plateaued).

The mechanism of the AHE can be divided into two components: intrinsic and extrinsic to the material. The *intrinsic* component is dominant only in a perfect crystal with no defects, and describes the acquisition of an "anomalous velocity" in charge carriers perpendicular to the incident electric field. This derives from an induced interband coherence in the $d$-states as a consequence of their Berry phase curvature in crystal momentum space [5, 151]. The *extrinsic* components to the AHE are defect-driven scattering events, which may be further divided into two categories. Skew-scattering describes an asymmetric diversion in the mean-free path of the charge carrier from the incident direction due to a spin-orbit coupling. Whereas the side-jump scattering event instead results from a deflection in the electron velocity from the local electric field profiles around the defect [5, 6, 151].

The ANE is analogous to the AHE, but the incident electric field does not originate from an

applied current, instead it arise from thermal diffusion of charge carriers in the presence of a thermal gradient (Figure 3.9a). The ANE is an effect under the label of spin caloritronics, which describes the relation of spins with heat current. It has been a lucrative area of research in recent times for its potential application towards "green" thermoelectric technologies within the energy harvesting sector [152–154]. The resulting electric field ($E_{\mathrm{ANE}}$) is described by Equation 3.20,

$$E_{\mathrm{ANE}} = Q_{\mathrm{s}}(\mu_0 \frac{M_z}{M_s} \times \nabla T_{\perp}), \tag{3.20}$$

where $Q_s$ is the anomalous Nernst coefficient. The schematic of the ANE and its mathematically defined thermoelectric response as a function of angle is displayed in Figure 3.9a(i-ii).The signal is maximum when the spin aligns along the $z$-axis.

To study ANE by magnetotransport, a heater wire (e.g. Pt) is fabricated parallel to the PMA NW to provide the thermal gradient (see Figure 5.1 in Chapter 5). The resulting hysteresis loop is acquired by monitoring the resulting longitudinal resistance of the ferromagnetic NW in a sweeping applied field, akin to the Hall effect measurements. Examples and further details have been provided in Chapter 5

### 3.2.2 Anisotropic magnetoresistance and anisotropic magneto-Seebeck effects

Lithographically patterned samples must exhibit PMA in order to be characterised by the effects described in Section 3.2.1 with the defined coordinate system. Therefore, to characterise samples with IMA, it is best to use the Planar Hall effect (PHE) and/or anisotropic magnetoresistance (AMR). PHE and AMR are interlinked effects that describe the change in the transverse and longitudinal resistance to the incident current in a magnetic field, respectively.

Neither effects are the result of charge carrier deflection mechanisms, therefore differ from the AHE. This is evidenced as the signs of both the PHE and AMR do not reverse with a 180° change in the magnetisation vector [5, 155]. Instead the mechanism within ferromagnets is described through the co-existence of $s$- and $d$-bands near the Fermi surface and strong spin-orbit coupling. Both effects are highly sensitive to the angle between the incident current and applied field, as variations in the field vector results in a change in scattering rates between $s$- and $d$-bands. [156–158]. Equation 3.21 describe the electric fields formed by the AMR and PHE effects as a function of the angle between the current-direction and the magnetisation direction [159, 160].

$$\begin{aligned} E_{\parallel} &= \rho_{\parallel} J_x \cos\phi \\ E_{\perp} &= \rho_{\perp} J_x \sin\phi \end{aligned} \tag{3.21}$$

where $\rho_{\parallel}$ and $\rho_{\perp}$ are the longitudinal and transverse resistivity of the material. Projecting the the equations in Equation 3.21 into $x$- and $y$-coordinates and simplifying using the trigonometric

identities results in the common description of the AMR and PHE

$$E_x = \left(\frac{\rho_\parallel + \rho_\perp}{2} + \frac{\rho_\parallel - \rho_\perp}{2}\cos(2\phi)\right) J_x \tag{3.22}$$
$$E_y = \left(\frac{\rho_\parallel - \rho_\perp}{2}\sin(2\phi)\right) J_x.$$

Just like the ANE is the thermoelectric equivalent of the AHE, thermoelectric equivalents to the PHE and AMR effects are observed in ferromagnetic materials by replacing the incident current density with a thermal gradient. These effects are normally named the Planar Nernst effect (PNE) and anisotropic magneto-Seebeck effects (AMSE), respectively [159–162] (Figure 3.9b). Thus the Equation 3.23 can be modified to describe the relationship with respect to thermal effects,

$$E_x = \left(\frac{S_\parallel + S_\perp}{2} + \frac{S_\parallel - S_\perp}{2}\cos(2\phi)\right) \nabla T_x \tag{3.23}$$
$$E_y = \left(\frac{S_\parallel - S_\perp}{2}\sin(2\phi)\right) \nabla T_x.$$

where $S_\parallel$ and $S_\perp$ are the Seebeck coefficients of the material in the longitudinal and transverse directions [160]. A plot of their respective responses for a rotating spin in the $xy$-plane is presented in Figure 3.9b(ii). Here it is worth highlighting that the contribution from these effects will be negligible in the magnetotransport measurements in Chapter 5, but this chapter also probes the magnetothermal effects on the local scale where these contributions do have a non-negligible contribution. For readability/consistency the important considerations have been consigned to Chapter 5.

### 3.2.3 Magnetotransport methodology

Devices with electrical contacts were fabricated by the methods described in Section 3.4 onto silicon chips. These were electrically contacted to a non-magnetic sample holder with a wire bonder (K&S 4526 wedge bonder) and mounted into the magnetotransport system onto a stage holder. The constant features in the set-up is the source of applied field, which is a GMW 5403 electromagnet driven by an external bidirectional power-supply system (Figure 3.10a); and a BNC breakout box to connect electrical sources and meters directly to the device. The software used to conduct the measurements is a purpose-built LabVIEW program that controls the sources and meters as well as the magnetic field.

Two sets of stage and sample holders are used: the first is a TO8-Header and rotation stage combination that places the sample such that the field from the electromagnet is normal to sample surface (Figure 3.10b). The sample can be rotated ±90° along its $x$-axis with a small motor. The second stage is a simple platform to which a PCB sample holder can be fixed directly such that the field is applied along the sample surface. This stage holder can be rotated on the $z$-axis manually to set the field angle, where the angle is then measured by custom-build MATLAB

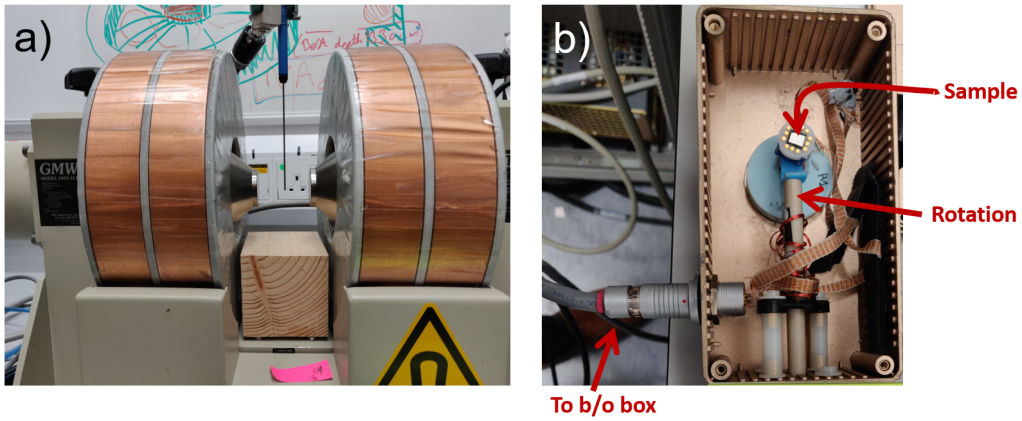


FIGURE 3.10. (a) GMW 5403 Electromagnet used for magnetotransport measurements. (b) TO8 header sample holder, which rotates along the $x$-axis, and connects electrically through indicated cable to breakout (b/o) box.

software. The former was used for the magnetotransport measurements in Chapter 5, whereas the latter was used for measuring the field angles in Chapter 6.

Through the break-out box, a multitude of sources and meters can be connected to the sample for magnetotransport measurements. In DC operation the setup consisted of a current/voltage source (e.g. Keithley 2400) and the relative voltage is monitored by a nano-voltmeter (e.g. Keysight 34420a). Where necessary, the specifics of the experimental set-up will be provided within specific chapters.

## 3.3 Lorentz transmission electron microscopy and Electron Holography

### 3.3.1 Lorentz transmission electron microscopy

[2]Another microscopy technique for spatially probing the nanoscale magnetic properties of materials is Lorentz transmission electron microscopy (LTEM), which directly measures the Lorentz force experienced by the electron in the magnetic field of the sample. It offers high spatial resolution images (~ 10 nm) of the intrinsic magnetic configuration within structures and films rather than the extrinsic components that are probed by MFM [163].

In LTEM, a coherent electron beam passes through an electron-transparent sample and substrate. When passing through a magnetic material, the electron is deflected according to the Lorentz force induced by a magnetic induction normal to the beam path. The emergent beam

[2]LTEM/EH measurements were performed with Mia Anderson, Aurelien Masseboeuf, Christophe Gatel and Etienne Snoeck (CEMES, France) as funded by the European Union's Horizon 2020 research and innovation programme under grant agreement No 823717 – ESTEEM3".

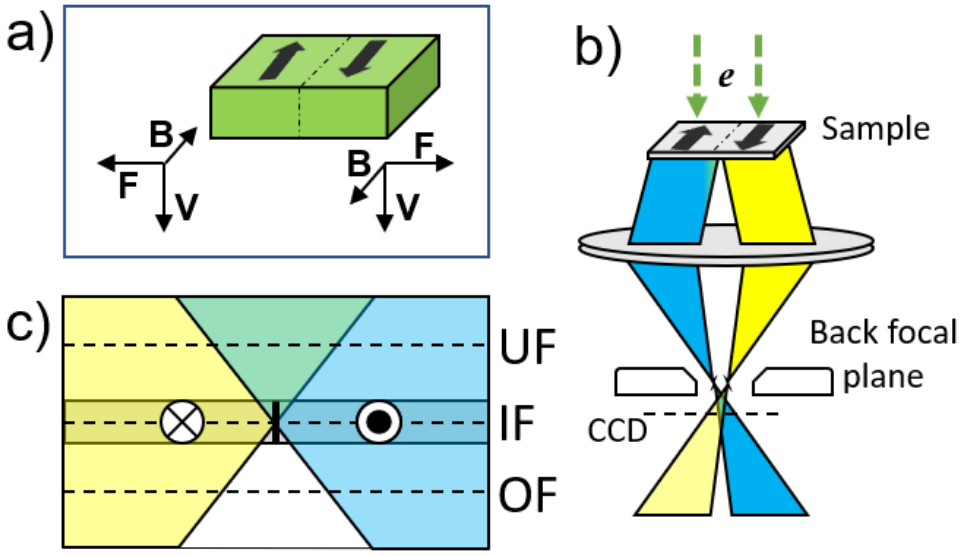


FIGURE 3.11. (a) Coordinate description of the Lorentz force experienced by incident electrons passing through an in-plane magnetised material along the surface-normal.(b) Schematic of Lorentz-transmission electron microscope in Fresnel mode. (c) Schematic of the effect of changing the focal plane to be in-focus (IF), and Under- or over-focused (UF and OF, respectively).

passes through a Lorentz lens to form diffraction patterns of the sample which are projected onto a charge-coupled device (CCD) camera [163, 164].

These interactions can be expressed as a change of phase in an electron ($e$) wave ($\varphi$) as a result of an interaction with an electrostatic vector potential ($V(x,y,z)$) of magnetic vector potential parallel to the electron trajectory ($A_z(x,y,z)$) according to the Aharonov-Bohm effect [165–167]

$$\varphi(x,y) = \int C_E V(x,y,z)dz - \frac{e}{\hbar}\int A_z(x,y,z)dz = \varphi_E(x,y) + \varphi_M(x,y) \tag{3.24}$$

where $C_E$ is an interaction constant proportional to the acceleration voltate of the $e$-beam, and $\hbar$ is the reduced Planck constant. The resultant phase shift is a consequence of both a phase shift from electrostatic and magnetic potential ($\varphi_E$ and $\varphi_M$, respectively). For the sake of this thesis, the $\varphi_E$ contribution is a parasitic effect much in the same effect as electrostatic contributions between the probe and the sample can contaminate MFM contrast. This parasitic contribution was handled in different ways for Chapters 7 and 8. In the former, the LTEM images were conducted closest to the edge of the membrane window, as charging effects from the $e$-beam are amplified near the centre of the TEM window. In the latter chapter, a thin layer of carbon was deposited on the sample to dissipate this effect and allow for specific imaging of the regions of interest.

LTEM measurements were operated in Fresnel-mode, which forms an image of the magnetic contrast by defocusing the Lorentz lens such that the image plane is above or below the sample plane (Figure 3.11(b)). The magnetic contrast is not seen when the image plane is in focus because of a suppressed phase contrast, but defocusing away from the sample plane improves the sensitivity to the magnetic component, at the expense of some spatial resolution. (Figure 3.11(c)) [164, 168, 169]. Variances in magnetisation, e.g. DWs, are easily distinguishable in the reconstructed image as the light and dark contrast, which is a result of convergence or divergence of the emergent electron wave. The effect of changing the focus plane of the image is demonstrated in Figure 3.11(c), where contrast is represented by a convergence (light) or divergence (dark) of the emergent electrons either side of a DW.

The microscope used was a Hitachi HF-3300 (I2TEM-Toulouse) TEM operated at an acceleration voltage of 300 kV. The microscope produces electrons from a cold-field emission gun, which passes through the sample where the inherent deflection occurs. In order to apply field *in situ*, the objective lens was turned off and a Lorentz lens was used for imaging. Between the Lorentz-lens and the back-focal plane, a spherical aberration corrector is placed to increase the spatial resolution of the acquired image at the CCD.

The source of the applied field for *in situ* magnetisation of the magnetic nanostructures is the objective lens, which applies a field normal to the imaging plane. Therefore a double-tilt sample stage was used to enable rotation of the sample in $xy$- and $xz$-directions. In the $xz$-direction the maximum amount of tilt possible was $\pm 60^{\circ}$, meaning there is always a $z$-component to the field application. See Figure A.13 in the appendix for a schematic.

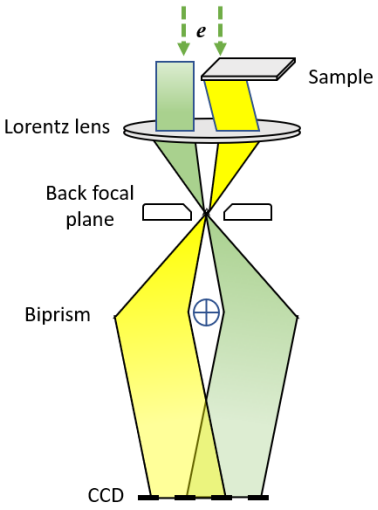


FIGURE 3.12. Schematic representation of off-axis electron holography.

### 3.3.2 Off-axis Electron Holography

Off-axis electron holography (EH) is an interferometric technique that is also carried out in the TEM. It is a highly sensitive technique that measures the intrinsic magnetic flux within a sample as well as the escaping flux surrounding it. The technique images the interference from mixing the object electron wave, which has passed through the sample, with the reference incident wave as part of a Möllenstedt biprism setup [170]. The resulting interference fringes, i.e. the hologram, are controlled locally in contrast and position by modulating the amplitude and phase of the reference wave [164]. In order to obtain the optimum contrast, the incident electron beam must be highly coherent. The resulting image contains information on the phase shift of the incident electron beam induced by both electrostatic and magnetic fields as was described in the LTEM section (Equation 3.24) [170].

## 3.4 Fabrication of magnetic samples

A variety of different samples have been used throughout the present thesis, including those with in-plane and perpendicular anisotropy and on different substrates for compatibility with the techniques presented. This section will briefly go through the fabrication of the relevant samples. Due to very limited access to clean-room/fabrication facilities during the course of the Ph.D., the samples have been prepared by a collection of collaborators. All collaborators are named within each subsection, but I would like to personally extend my thanks to all that have prepared samples for the contents of the present thesis.

### Permalloy nanostructures on $Si/SiO_2$

[3]The permalloy (Py) nanostructures used throughout the thesis are fabricated using a lift-off process. A sputter-deposited permalloy (Py) film on a $Si/SiO_2$ (300 nm) substrate was glued to a silicon wafer that had a conduction layer of gold. The Py thickness throughout this work is 25 nm with a 2 nm platinum capping layer to prevent the oxidation (Figure 3.13a).

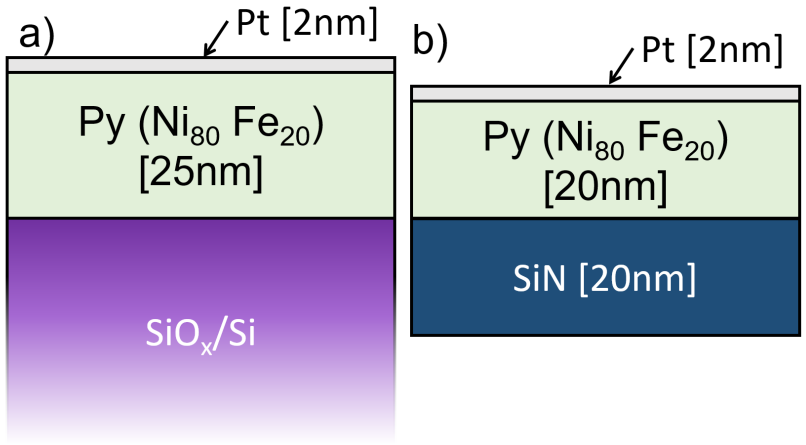


FIGURE 3.13. Stack composition of Permalloy samples on (a) $SiO_x$/Si; and (b) SiN substrates.

Polymethyl methacrylate (PMMA) resist was spin-coated on the Py film and the desired pattern was graved onto the resist using e-beam lithography. The film was developed using a conventional developer for PMMA. The film was inserted into an evaporation chamber where 50 nm of Al was evaporated at a rate of 2 A/s. Afterwards the film was submerged in acetone for more than 12 hours to remove the unwanted resist.

In the etching process, the Py film was etched at the parts where no Al was present by Ar-sputter etching. To remove the Al, a NaOH-based developer was used. After these steps only the desired Py structures could be observed on the substrate surface.

[3]Py structures on $Si/SiO_x$ were grown and patterned by Alex Fernandez-Scarioni (PTB, Germany).

### Permalloy nanostructures on SiN membranes

[4]Patterned Py structures used in the LTEM/EH experiments in Chapters 7 and 8 were fabricated on $Si_3N_4$ membranes ($t$ = 20 nm) (Figure 3.13b). Membranes were spin-coated with ZEP520A:anisole (1:1) at 3 krpm and baked at 180°C for 3 minutes. The ASI arrays were then patterned by $e$-beam lithography using a base dose of 343 $\mu$C/cm$^2$. The pattern was subsequently developed for 70 s in N50 solution. $Ni_{80}Fe_{20}$ ($t$ = 20 nm) was evaporated into the pattern (rate 2 A/s) along with a Pt capping layer ($t$ = 2 nm, rate 1 A/s) to prevent oxidation. Finally, lift-off was performed in SVC-14 solution at 70°C.

### Cobalt-Platinum multilayer reference film

[5]The reference sample for qMFM featured throughout the thesis is a magnetron-sputtered $[Co(0.4nm)/Pt(0.9nm)]_N$ multilayer onto a Si-$SiO_2$ substrate where $N$ = 100 (Figure 3.14). The $M_s$ = 554 kA/m and the interface anisotropy of the Co/Pt interfaces provides a PMA of $K$ = 0.52 MJ/m$^3$, which competes with the shape anisotropy of the thin film.

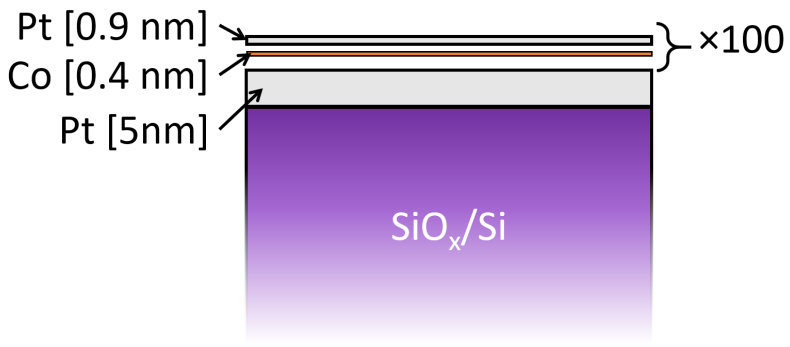


FIGURE 3.14. Stack composition of Co/Pt multilayer reference film on $SiO_x$/Si substrate.

Thus the magnetisation forms a multi-domain state at remanence, forming the well-known labyrinth pattern with neighbouring up and down domains. The average domain width is 170 nm. However, due to a domain wall width of $w_{dw} \approx 16$ nm and the non-regularity of the domain arrangement the sample contains lateral features from about 16 nm up to micron length-scales. This span of spatial frequencies means the method may be applied to a large range of samples whose feature sizes are encompassed by the spatial frequencies of the calculated TTF.

[4]Py structures on SiN membranes were grown and patterned by Mark Rosamond (University of Leeds, United Kingdom).

[5]Co/Pt multilayers were provided by Volker Neu (IFW Dresden, Germany).

### CoFeB nanowires

[6] The PMA wire comprised of Ta(4nm)/Pt(3nm)/$Co_{60}Fe_{20}B_{20}$(0.6nm)/Pt(3nm) sputtered onto a Si/$SiO_2$ substrate (Figure 3.15). Devices were fabricated via a lift-off process using electron-beam lithography to pattern a layer of 50 nm thick PMMA. In cases where transport measurements were conducted on devices, additional non-magnetic wires (Ta(5nm)/Pt(95nm)) were subsequently deposited to provide connections to the CoFeB wire and a heater.

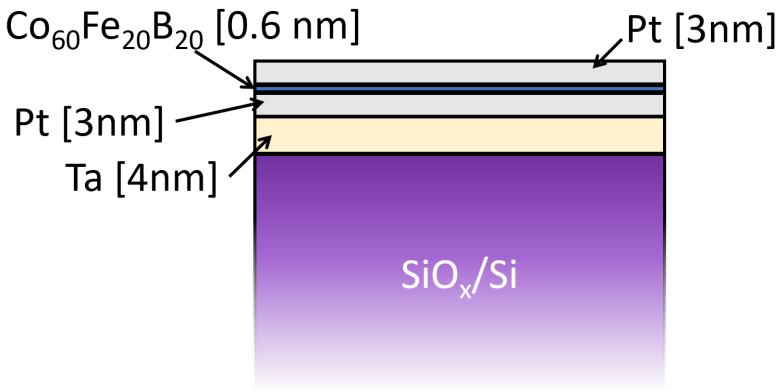


FIGURE 3.15. Stack composition of CoFeB film on $SiO_x$/Si substrate.

## 3.5 Micromagnetic modelling

To accurately model the magnetic configurations of patterned ferromagnetic elements, such as NWs and ASI, a dynamic model is considered where the system under study changes only when it is no longer at an energy minimum. Most micromagnetic models aim to solve the Landau–Lifshitz–Gilbert (LLG), Equation 3.25, which describes the precession of magnetisation around an effective field, $H_{eff}$, (i.e. sum of exchange, magnetostatic, anisotropy and Zeeman fields) [171, 172]

$$\frac{\partial \mathrm{M}}{\partial t} = \frac{\gamma}{1+\alpha^2}\mathrm{M} \times \left[\mathrm{H}_{\mathrm{eff}} + \frac{\alpha}{M_s}(\mathrm{M} \times \mathrm{H}_{\mathrm{eff}})\right]. \tag{3.25}$$

Here, M is the point-wise magnetisation, and $\gamma$ and $\alpha$ are the absolute value of the gyromagnetic ratio and the damping constant, respectively. The damping term speeds up the time taken for the model to converge to allow the magnetisation to align along the direction of the effective field. In the absence of damping ($\alpha = 0$) the time dependence of the magnetisation can be simplified to [172, 173]

[6] Films were grown by Paolo Freitas (INL, Portugal); and patterned by Alex Fernandez-Scarioni (PTB, Germany).

$$\frac{\partial \mathrm{M}}{\partial t} = \gamma [\mathrm{M} \times \mathrm{H}_{\mathrm{eff}}], \tag{3.26}$$

where the system converges upon the local energy minimum when $\mathrm{M}(t) \times \mathrm{H}_{\mathrm{eff}}(t) = 0$

### 3.5.1 GPU-parallised magnetic solver

[7]Micromagnetic modeling of the L-shaped Py nanowire in Chapter 4 and ASI structures in Chapter 6 was performed by means of a GPU-parallelised numerical code able to efficiently solve the LLG equation (Equation 3.25) in large patterned magnetic films [171, 174],

The code implemented a geometric time-integration scheme based on Cayley transform for the magnetisation update [175] and a fast multipole-based approximation for the evaluation of the magnetostatic field. This was separated into a short-range term, which described the interactions between close NIs via Green integration, and a long-range term, which takes into account the contributions from far NIs via a multipole expansion approximation [176]. The exchange field was calculated with a finite difference method able to handle non-structured meshes and thus suitable for the discretisation of NIs with curved boundaries, without introducing fictitious shape anisotropy effects [177]. The damping coefficient was set at 0.1 in order to accelerate the reaching of equilibrium states, according to the analysis reported in Ref. [175].

### 3.5.2 Object-oriented micromagnetic framework (OOMMF)

The object-oriented micromagnetic framework (OOMMF) was developed by Donahue and Porter [178] as an open-source micromagnetic software package, which was used for modelling of individual islands in Chapter 6, and ASI lattices in Chapter 8. OOMMF is a finite difference method solver that calculates the total energy of regularly distributed discretised cells over the object domain by considering the exchange, magnetostatic, anisotropy and Zeeman energies on objects with predetermined magnetisation. The magnetisation within each cell is updated by either a time evolver, which tracks the LLG dynamics directly; or a conjugate gradient (CG) energy evolver, which calculates the local energy minima directly [172, 179]. The energy-evolver is ideal for computationally larger structures, such as ASI lattices, as it allows the problem to reach convergence far quicker than the time-evolvers with the same end result.

## 3.6 Summary

This chapter has described the experimental techniques and the relevant physics required for interpreting the methods used throughout the remaining chapters in the present thesis.

The chapter starts with a detailed introduction to MFM measurements, which includes the use of advanced techniques such as custom probes and quantitative MFM. As the primary

[7]GPU-based micromagnetic modelling in chapters 4 and 6 was performed by Alessandra Manzin (INRIM, Italy)

technique used to investigate the magnetic characteristics of the nanowires and ASI structures throughout the proceeding chapters it is important to understand the process, advantages and pitfalls of the technique.

Magnetotransport measurements were then presented and framed in the context of thermoelectric effects. In addition to the transport measurements performed in the thesis, this section also provides much needed context for Chapter 5, which locally probes the thermoelectric effects of the ANE, AMSE and PNE in a PMA nanowire with a trapped DW.

Subsequently LTEM and EH is discussed from its prominent use throughout Chapters 7 and 8 to compliment scanning probe measurements on ASI lattices. It is ideal for this task from its sensitivity to the in-plane components of the magnetisation.

Following this was an outline of the vast number of samples that have been fabricated for use throughout the contents of this thesis is presented, including those with in-plane and perpendicular magnetic anisotropy and permalloy nanostructures on different substrates.

This chapter concluded on the discussion of micromagnetic modelling that was utilised throughout the majority of the thesis as both inputs to the qMFM methodology and interpretation of switching mechanisms within ASI lattices.

CHAPTER 4

# QUANTITATIVE MFM OF L-SHAPED NANODEVICE WITH A CUSTOM PROBE

## 4.1 Introduction

Before performing any MFM measurement, an MFM probe is selected with properties tailored to the properties of the measurand. This is because a probe with a strong magnetic stray field, i.e. a standard- or high-moment probe (SMP or HMP, respectively), may perturb a sample's magnetic state through magnetic switching. Reciprocally, a low moment probe (LMP) typically possesses high magnetic susceptibility, which can switch whilst scanning samples with highly coercive stray-field. Both of these events result in artefacts in the measurement, resulting in unreliable data or perturbing the sample state into a new magnetic configuration. This balance for probe selection limits applicability of MFM for imaging heterogeneous samples of high and low moment.

To reduce probe manufacturing costs, most commercial MFM probes consist of a silicon AFM probe which has been coated with a magnetic compound of nominal thickness (10's nm). Therefore, commercial probes are either high-moment with low magnetic susceptibility; or low-moment with high magnetic susceptibility. Therefore, there is a market for probes that have high magnetic sensitivity, high spatial resolution, and are low-moment with low magnetic susceptibility [106, 127]. This has emanated in the research of custom magnetic scanning probes that have been engineered to possess tuned properties as described in Section 3.1.3) [105, 106, 127, 130, 131].

The probe featured in the present work possesses a lithographically defined V-shaped magnetic nanostructure on one face of the probe. This probe design was considered to possess both low magnetic moment and low magnetic susceptibility by reducing the magnetic volume on the probe and using shape anisotropy to localise the stray-field to the apex [127]. One component of

this probe design is the switchability of the arms in the V-shaped nanostructure to pin either a head-to-head or head-to-tail DW at the apex. This allows for interchangeable high- and low stray-field at the probe's apex to measure a wider span of material systems without needing to remove the probe from the measurement set-up. This was demonstrated in a recent work within our research group (Ref. [105]).

The work presented in this chapter investigates only the head-to head DW case to demonstrate the engineered properties of the custom MFM probe. This includes an evaluation of the probe's sensitivity, magnetic susceptibility and coercivity compared to two commercial MFM probes. This is investigated by a qMFM methodology that ascertained the characteristic stray-field profile for the V-shaped probe. The applicability for imaging heterogeneous samples with greatly variant magnetic properties is discussed throughout, including where the design may be improved for future application.

## 4.2 Probe design and fabrication

A commercial SMP (Nanosensor PPP MFMR), with coating thickness ~ 30 nm was used as a precursor from which the majority of the ferromagnetic CoCr alloy coating has been etched away using Ga-ion FIB, leaving a V-shaped magnetic nanostructure on just one face of the MFM probe Figure 4.1a[1]. The nanostructure was composed of two arms of length 7.78 $\mu$m and width 400 nm, in a V-shape with a $\sim 40^\circ$ angle between the two arms.

Shape anisotropy governs the magnetic state of the nanostructure as the magnetisation is constrained along the arms. As a result only four stable magnetic configurations is possible: two where the magnetisation "bends" around the corner (i.e. head-to-tail domains) forming a low-moment state (Figure 4.2a-b); and two states where the domains meet tail-to-tail (or head-to-head), resulting in a higher moment at the apex (Figure 4.2) [105, 127, 135, 180]. For the purposes of this chapter, only the head-to-head / tail-to-tail case is considered where the probe demonstrates highly localised stray field at its apex from the presence of a pinned transverse DW. To produce the DW in this probe it must be magnetised transverse to the apex. From the design, it was predicted that the stray-field of the probe would be reduced through customising the design without decreasing its spatial resolution.

To assess the DWP suitability, it was quantitatively tested by imaging two samples of greatly different magnetic strengths against commercial standard- and low-moment probes. The first sample is a sputtered $[\mathrm{Co(0.4nm)/Pt(0.9nm)}]_N$, multilayer where $N = 100$ (see Section 3.4 in the Methods). The interface anisotropy of the CoPt interfaces provides a perpendicular magnetic anisotropy (PMA) of $K = 0.52$ MJ/m$^3$ which competes with the shape anisotropy of the thin film. As a result, the magnetisation collapses into a multi-domain state at remanence, forming a well known labyrinth pattern with neighbouring domains normal to the surface. The average domain

[1]The FIB lithography step was performed by Dr. David Cox (University of Surrey, UK).

width was 170 nm, but due to a domain wall width of $w_{dw} \approx 16$ nm and the non-regularity of the domain arrangement, the sample contains lateral features from about 16 nm up to the scan size

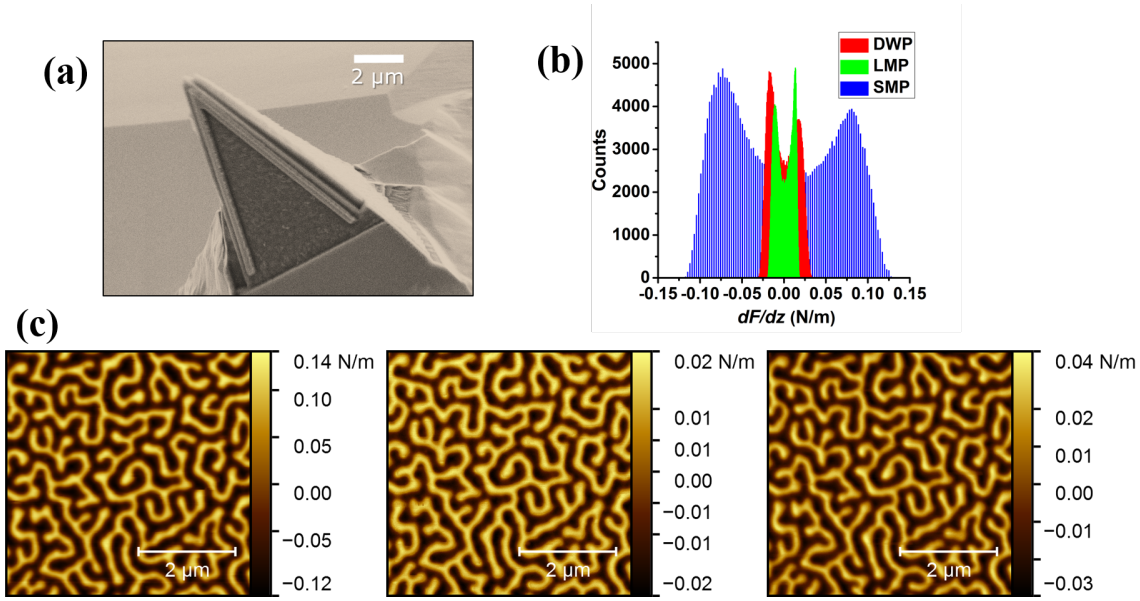


FIGURE 4.1. (a) SEM image of a domain wall probe (DWP) fabricated from a Nanosensor MFMR probe. (b) Full-area histogram of three MFM images. (c) MFM images from the same area of Co/Pt film with SMP (left), LMP (centre) and DWP (right). ©2017 IEEE. Reprinted, with permission, from Puttock *et al.* [127]

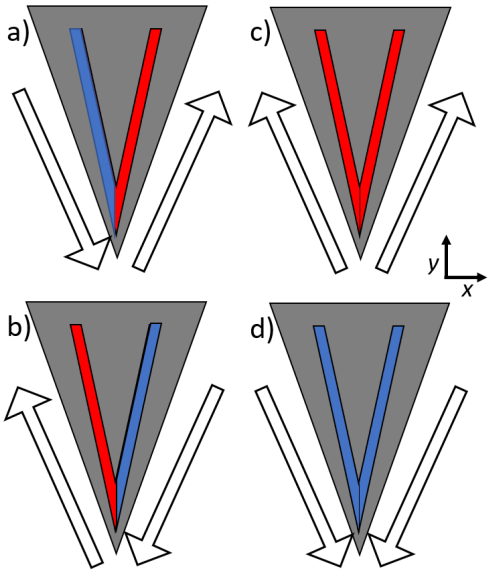


FIGURE 4.2. Possible magnetic domain configurations for the domain wall probe: (a) head-to-tail; (b) tail-to-head; (c) tail-to-tail; (d) head-to-head.

of 5 $\mu$m.

Figure 4.1b represents the force gradient range between the three probes and the reference sample from the MFM images in Figure 4.1c. The benefit of representing this data in force-gradient units is to normalise the influence of the varying physical properties of the probe, such as the spring constant, $k$, and $Q$-factor, $Q$. Equation 3.10 from Section 3.1.2 was used to calculate the force gradient image from the raw MFM phase-difference. The images of the same region of the CoPt reference sample are visually similar in definition and resolution, and the histogram demonstrates the likeness between the sensing ability for DWP and LMP. The SMP has a coating thickness double that of the LMP. Thus, it is not surprising that the interaction force between the SMP and the sample is far greater than the other MFM probes. The LMP range is therefore reduced when compared to the SMP, demonstrating the LMP's smaller stray field.

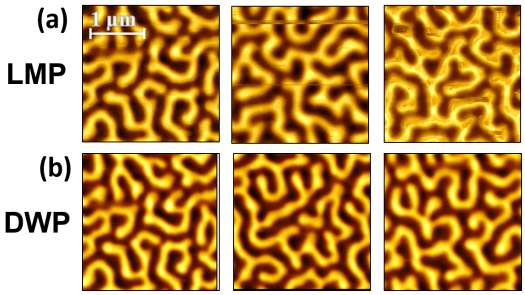


FIGURE 4.3. (a) Imaging artefacts induced by magnetic "switching" of the probe common when imaging a sample with high PMA with an LMP under different scanning parameters; e.g. horizontal streaks and dark-spots in the centre and right-hand images, respectively. (b) DWP demonstrated none of the same imaging artefacts throughout the study under different scan parameters. ©2017 IEEE. Reprinted, with permission, from Puttock *et al.* [127].

Despite the much lower volume of magnetic coating on the DWP compared to both commercial probes, the quality of the image is comparable to the LMP. The similarity in their force profiles suggest that the DWP in head-to-head domain formation behaves comparably to the LMP, rather than the SMP from which it was fabricated. A comparison of the histograms for the LMP and DWP in Figure 4.1(b) indicate a slightly greater sensitivity in the tip-sample force interaction between the DWP and the Co/Pt sample.

LMPs are known to switch magnetic orientation when imaging magnetic samples with strong stray-fields such as the Co/Pt film. This can lead to artefacts and distorted images where the contrast inverts as the moment of the probe switches (Figure 4.3). Due to a distribution of the magnetic susceptibility across manufactured probes, even in the same batch, there is an element of luck as to whether a commercial LMP will be able to image a difficult sample without switching artefacts. Usually, several probes and scanning parameters are tested before finding the ideal probe. The probe typically switches in the first pass where the probe comes into closest contact with the sample. Therefore adjusting the tip-sample separation (i.e. lift-height) in the second-pass does not adequately mitigate this artefact.

However, sometimes reducing the VdW force in the first pass can improve the imaging quality.

For instance all three MFM measurements in Figure 4.3a were performed by the same LMP but with different scanning parameters: the left hand image is as seen in Figure 4.1c with "manually optimised" scanning parameters where a very low set-point in the first pass was used to reduce switching. The central and right-hand images in Figure 4.3a were obtained at lift-heights 75 and 25 nm, respectively, with semi-automated parameters as set by the SPM auto-engage settings. This setting engages on a higher set-point in the first pass, therefore pushes the probe harder into the sample surface. It is also true that with high contact force the probe can physically change (e.g. become blunt or fragment), which can also increase the probes susceptibility.

The DWP was scanned in the same conditions and demonstrated none of these imaging artefacts (Figure 4.3b). It is apparent that a combination of introducing a shape anisotropy in the DWP and the increased thickness of the magnetic nanostructure results in a decreased susceptibility when measuring hard magnetic materials like the CoPt reference sample. This may also be aided by a vertical offset in the nanostructure apex and tip-of the probe, shielding it from physical damage and increasing the separation between the magnetic sensing area and the sample surface. This additional separation between the sample and the sensing area of the probe reduces the magnetic tip-sample interaction, as well as physical deterioration of the nanostructure. The combination of these properties reduces the probe susceptibility and improves its use for measurements of heterogeneous magnetic samples.

## 4.3 Quantifying stray-field from L-Shaped nanowire

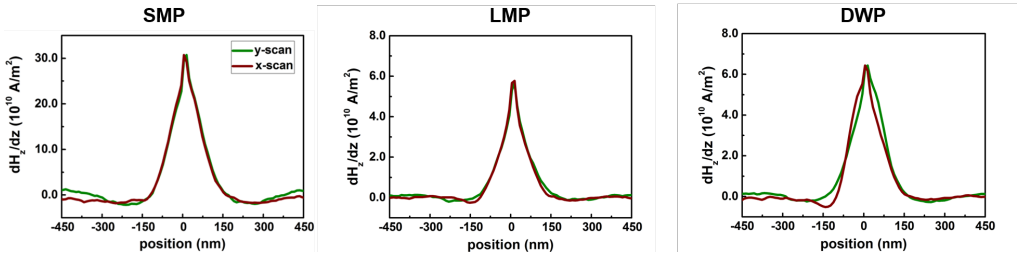


FIGURE 4.4. Cross-sectional plots of the real space TTFs for standard moment (left), low moment (middle) and domain wall (right) probes, respectively, in $x$- and $y$-directions (burgundy and green, respectively). ©2017 IEEE. Reprinted, with permission, from Puttock *et al.* [127]

To further compare the three probes under study, the probes were calibrated from the RS-TTF method (Section 3.1.4) and compared in Figure 4.4[2]. Here, cross-sectional line profiles through the mid-points of the reconstructed TTFs are displayed. The LMP and DWP, as expected, have a reduced stray-field when compared with the SMP; amassing to roughly a five-fold reduction. However, the similarity in magnitude between LMP and DWP strongly correlates with the

[2]The TTF calculation was performed with V. Neu (IFW Dresden)

previous observation that the DWP behaves as an LMP. The commercial probes both possess very symmetrical TTFs, but the asymmetry observed in the DWP RS-TTF is attributed to the presence of the V-shaped nanostructure on a single pyramidal face. The fact that the asymmetry appears in the RS-TTF means that this would not impact the ability to perform further quantitative measurements as it is possible to deconvolve the influence of the asymmetry from the micrograph.

As the TTF profile samples the magnetic charges on the sample surface during MFM measurement, the sharpness of the TTF peak is a qualitative measure of the probe's lateral resolution. The RS-TTFs shows the custom probe has similar resolution to the commercial probes; and the LMP appears to possess the sharpest peak among the three probes under-study.

The TTF was applied to simulate the MFM response *in silico* of a test sample with different magnetic characteristics to the reference sample, and compare it with the real experimental results. The chosen test structure was an L-shaped Py nanostructure of film thickness $t_f$ = 25 nm and arm-width $w$ = 100 nm. Like the macro-spins in ASI the nanodevice has in-plane magnetic anisotropy, however the strong contrast in MFM micrographs results from an increased stray-field emanating from the pinned DW at the L-shaped corner. The test sample also has well-defined magnetic parameters as described in Refs.[171, 174]. Although there are four stable magnetic states for this nanostructure (just like the DWP in Figure 4.2), the focus was on one with tail-to-tail DW generating a highly localised field at the L-shaped corner.

The spatial magnetic distribution (Figure 4.5(a)) was calculated with a parallelised micromagnetic solver [171, 181] (see Section 3.5.1 in Methods). The volume density of effective magnetic charge $\rho = -\nabla M$ was subsequently computed. Due to the small film thickness the surface charge density was approximated as $\sigma^* = t_f \cdot \rho$. The surface charge map in Figure 4.5b is then convolved with the previously obtained RS-TTFs of the three probes to produce a simulated MFM image, which is quantitatively compared with experimental micrographs.

Both LMP and DWP exhibit the expected profile in the local region of the notch, which is indicative of the DW. Both the peak height and width compare remarkably well with the predicted equivalents (Figure 4.5(e) left and right panels, respectively). This is unlike the MFM micrograph produced by imaging with the SMP, which appears to have switched the magnetisation of the nanostructure into a head-to-tail domain configuration. This is clear from the bright and dark contrast either side of the corner in the image in Figure 4.5(d, left). This type of probe-sample interaction is not considered in the micromagnetic modelling. In the DWP image in Figure 4.5(d, right), the DW appears to be physically "squeezed" to the outer boundary of the L-shape corner. This anomaly may arise from: #1 a probe asymmetry larger than derived from the reference measurement #2 the probe's stray field interferes with the remanent domain state of the Py nanostructure. From the shape of the DW-profile in the DWP MFM image, it is more likely to be the latter.

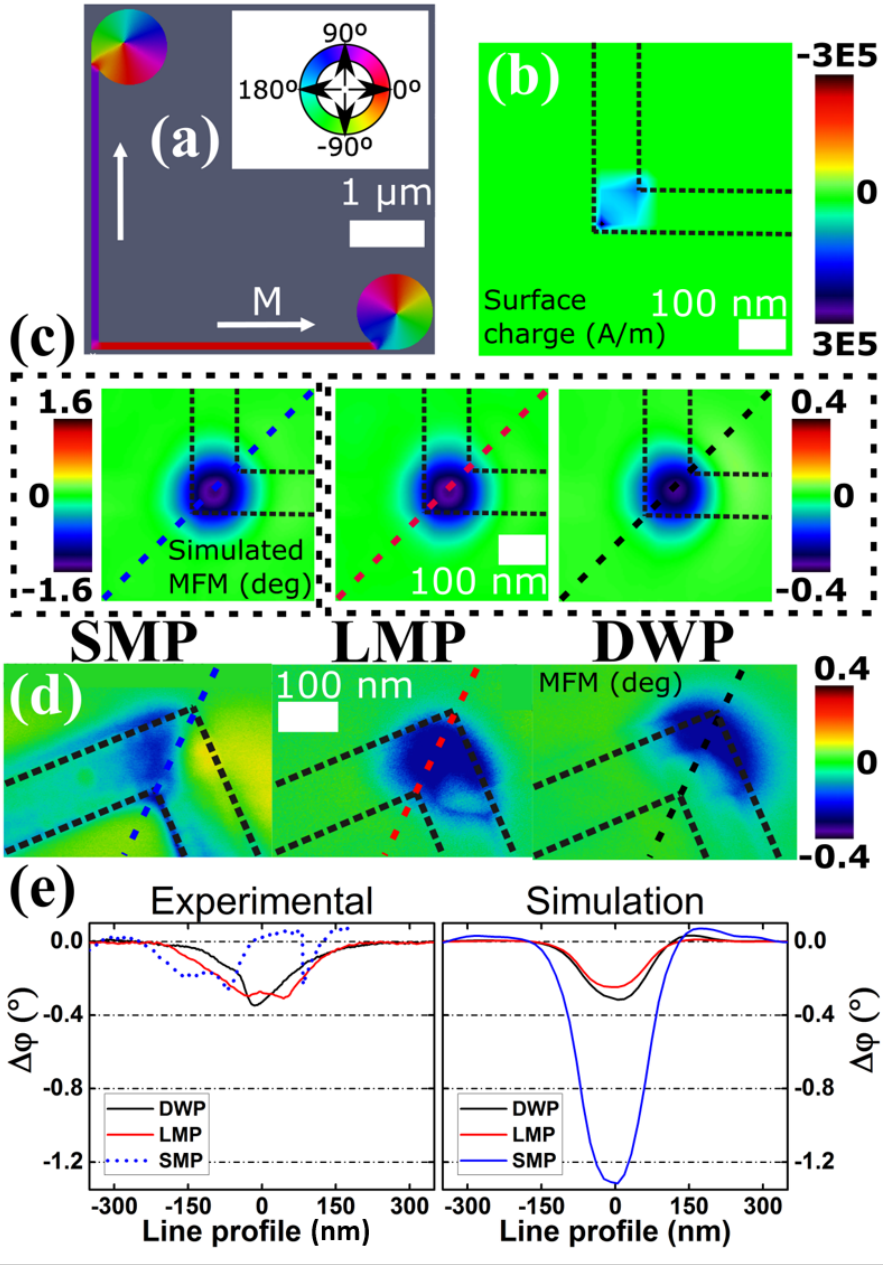


FIGURE 4.5. (a) Modelled magnetisation configuration for Py L-shape nanostructure after field was applied at 45°. (b) Effective sample surface charge map with large negative field at the L-shape's apex. (c) Simulated MFM images alongside (d) experimental results. (e) Experimental (left) and simulated (right) line profiles for all probes from the dashed lines in (c) and (d). ©2017 IEEE. Reprinted, with permission, from Puttock *et al.* [127]

## 4.4 Summary and Conclusion

Within this work, the custom DWP was assessed in its applicability in measuring heterogeneous samples through the qMFM procedure against commercially available MFM probes. The DWP in the head-to-head DW configuration performs similarly to the commercial probes, with comparable moment and sensitivity to the LMP and a lower coercivity. Calibration of the three probes to quantify their stray-fields confirmed the similarity in sensitivity and lateral resolution between the DWP and the commercial equivalents. The asymmetry in the RS-TTF for the DWP demonstrated the qMFM technique is highly sensitive to the probe asymmetry, which in turn means that this asymmetry does not impact the ability to perform further quantitative measurements.

The DWP in head-to-head configuration was shown to be capable of measuring the pinned-DW in the L-shaped nanodevice without changing its magnetic state before and after the measurement. However, there was a small degree of unfavourable probe-sample interaction during the measurement. This means the presented iteration of the design was still too coercive. This could be corrected by changing the the material parameters or the physical dimensions of the V-shaped nanostructure, for example by increasing the separation between the V-shaped nanostructure and the probes apex. Additionally, the lower-moment configuration of the DWP probe with a head-to-tail DW as shown in Ref. [105] may also have reduce the parasitic tip-sample interaction at the expense of some magnetic sensitivity.

CHAPTER 5

# MAGNETOTHERMAL IMAGING OF MAGNETIC NANOWIRES

## 5.1 Introduction

The previous chapter focused on the magnetic imaging of an in-plane magnetised nanostructure by SPM, where magnetostatic interactions between the MFM probes and magnetic samples have been shown to induce imaging artefacts. While this was shown that it can be mitigated in the Py L-shaped nanowire, this chapter focuses on a different type of sample, a high magnetic susceptibility nanowire that was lithographically prepared from a material with PMA. As a result of its high magnetic susceptibility it cannot be effectively imaged by MFM as most MFM probes are too coercive. Thus a new technique is introduced that investigates the magnetic configuration of the nanowire through locally induced spin caloritronic effects.

Spin caloritronics describes the interplay between spintronic effects and thermal transport phenomena. It has emerged as an intensely researched area both for the fundamental physical understanding but also the genuine technological potential towards future applications. The main disciplines where these efforts are targeted include "green" thermoelectric technologies for energy harvesting [152–154] and biotechnology [136, 182, 183], where particular emphasis is paid to the figure of merit of energy conversion [184]. In light of this research, significant efforts have focused on the application spin caloritronic phenomena, such as: spin-Seebeck [185, 186]; spin-Peltier[187, 188] and the spin Nernst effects [189]. This is in addition to thermal analogues of the Hall effects, which include the Righi-Leduc [152, 190], Ettingshausen [191], and Nernst effects [192–194]. Recently, locally induced thermoelectric phenomena has been used to understand domain configurations in materials using laser-induced heating [159, 194–196]. The hotspot from the Joule-heated probe is shown to be more confined, resulting in far greater spatial resolution than these laser-based imaging techniques.

The geometry of the NW allows for the controllable pinning of a 180° Néel DW, which in turn lends itself to the study of the ANE and other spin caloritronic effects through the localised generation of thermal gradients across the material. A careful consideration of the thermoelectric effects that may be present is analytically discussed, showing high resolution and sensitivity to the pinned DW in the notch region.

## 5.2 Thermoelectric and magnetic characterisation of PMA nanowire

As demonstrated in several of the chapters related to MFM imaging, many artefacts are induced by using the stray-field of one magnetic body to image the stray-field of another, such as in MFM. This is particularly troublesome for imaging soft magnetic materials that may switch when the probe comes into close-proximity of the sample.

The device under study here is a NW composed of an ultrathin Pt/$Co_{60}Fe_{20}B_{20}$/Pt trilayer to establish high PMA (see Section 3.4). The NW was defined by $e$-beam lithography with width $w = 800$ nm with a notch width $w_N \approx 700$ nm located in the device centre. Figure 5.1a-b shows a confocal and atomic force micrograph of the device under study, respectively, where the main features of the design are labelled. An electrically isolated Pt heater is deposited parallel to the magnetic NW, which is employed to characterise the global thermoelectric response of the device through the ANE. The NW was fabricated with a bulbous end and a sharp end to break the lateral symmetry of the device and promote DW-propagation along one direction. This allows for

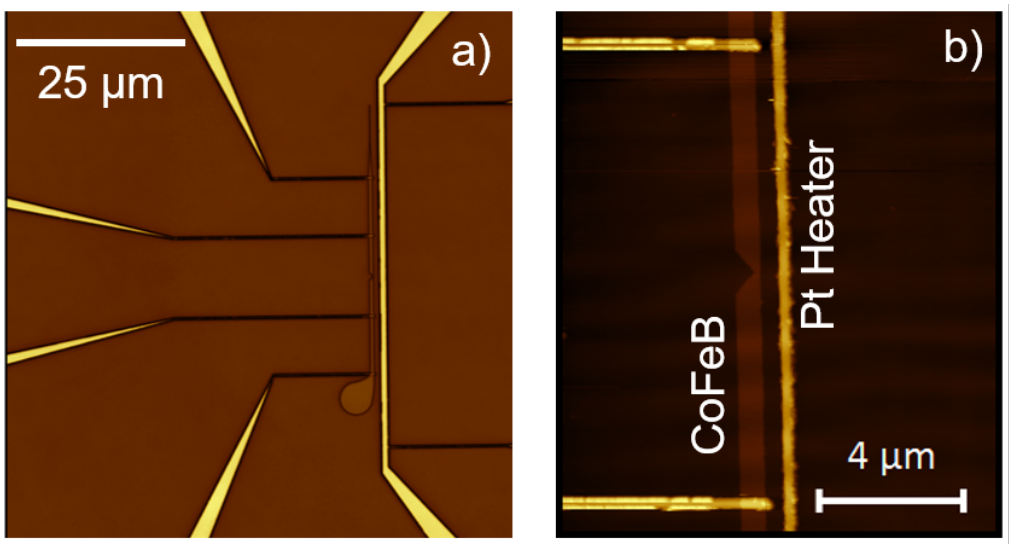


FIGURE 5.1. (a) Confocal micrograph of the device topology with electrical contacts. (b) Atomic force micrograph of ANE device, where CoFeB and Pt heater wires are labelled.

controllable nucleation of DWs during the magnetic reversal.

The magnetisation of the NW was first characterised by ANE-magnetotransport measurements.The longitudinal voltage of the NW was monitored as a function of a sweeping magnetic field applied normal to the sample surface. To generate the thermal gradient required for ANE measurements, the parallel Pt heater provides a Joule-heated thermal current across the CoFeB wire. Figure 5.2a displays the mean hysteresis loops (20-repeats) of the NW when the field is applied exactly normal to the sample surface for different heater currents ($I_{\text{heater}}$ = 0.5-5.0 mA).

The coercive field for this device is approximately $\mu_0 H_c \sim \pm 17$ mT along the surface normal, which is relatively small. It is also apparent that there is little-to-no DW pinning, as the DW cleanly passes through the notched area of the NW. Figure 5.2b plots the average magnitude of the saturated region vs. the heater current, which displays an expected quadratic relationship as $V_{\text{ANE}} \propto \nabla T \propto P_{\text{heater}}$, thus $V_{ANE} \propto I^2_{\text{heater}}$. Figure 5.2c plots a hysteresis loop where the field was applied 19° away from the surface normal. This field offset resulted in a significant reduction of the coercive field and promoted DW-pinning as evidenced by the short plateaus around $\mu_0 H_\perp \sim \pm 10$ mT. For means of reference the mean hysteresis loop (20-repeats) is plotted where the field angle is applied along the surface normal direction.

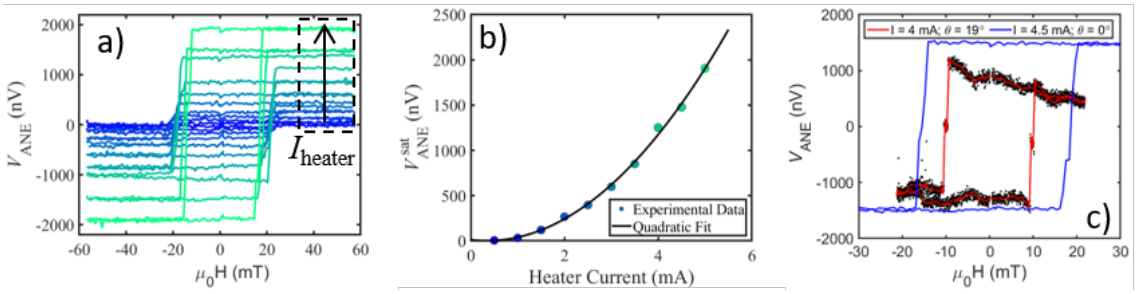


FIGURE 5.2. (a) ANE hysteresis loops of CoFeB NW under increasing current applied to the heater ($I_{\text{heater}}$ = 0.5-5.0 mA); field has been applied along the surface normal of the device. (b) Plot of the positive saturated ANE voltage (indicated by dashed box in (a)) as a function of $I_{\text{heater}}$ showing quadratic dependence. (c) ANE hysteresis loop of CoFeB wire when field is applied along and ~ 19° away from the surface normal (blue and red, respectively); $I_{\text{heater}}$ = 4.5 mA, and 4.0 mT, respectively.

Commercial MFM low moment probes have a wide-span of coercivity of ~10-50 mT at the probe apex [197, 198]. Therefore, it is clear that it is both difficult to nucleate the DW at the notched area and, if successful, to image the pinned DW by MFM due to the NWs weak coercivity. Therefore it is not trivial to probe the local magnetic properties of weakly-coercive materials without the use of centralised facilities or other highly specialised equipment. From herein a new method to locally map the thermoelectric response of the NW with and without a pinned Néel DW is demonstrated with high spatial resolution.

## 5.3 Scanning Thermoelectric Microscopy

A schematic representation of the scanning thermoelectric microscopy (SThEM) technique is presented in Figure 5.3a where the key components are highlighted. A local heat current is induced in the NW by adapting a scanning thermal microscopy (SThM) [199–201] method. Joule heating of a Si based cantilever, Figure 5.3a, [199] is used to heat the magnetic sample locally. By raster scanning the heated probe over the magnetic structure the local thermoelectric response induced in the NW is sampled as a function of tip-position, thus mapping the integrated thermoelectric response of the NW in two-dimensions. Recently, this SPM-based method has been used for locally probing the thermoelectric coefficients in Graphene [202, 203], and very recently the spin Seebeck effect in Pt/YIG stack [204]. However, SThEM is still a novel method for locally probing electrically contacted systems that is clearly gaining traction as a tool to probe material systems.

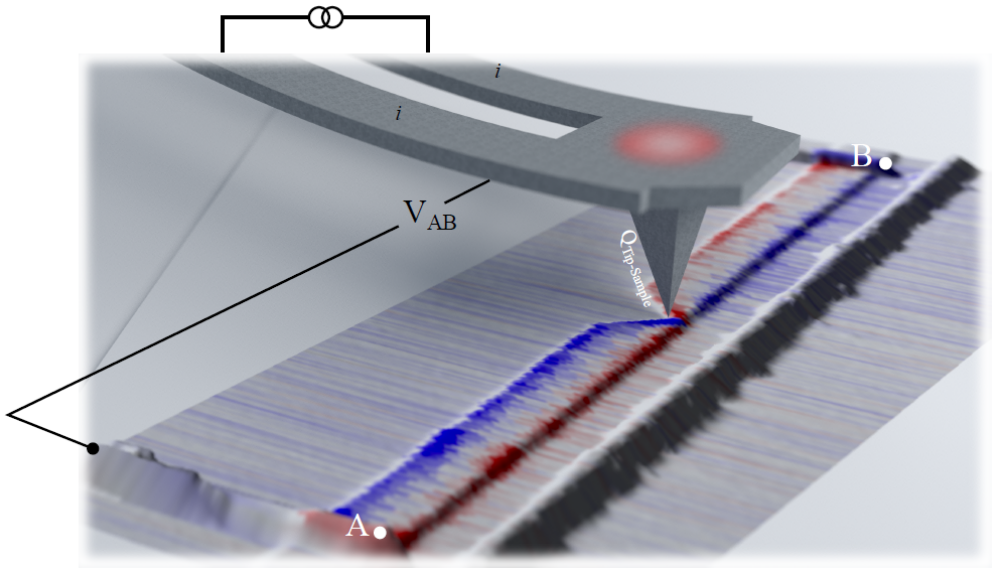


FIGURE 5.3. [1]Schematic representation of SThEM where the heated AFM probe is used to apply the local heat current and thermal gradient whilst the voltage is monitored along $y$; the integrated response is mapped pixel-wise.

The spatial resolution of SThM techniques (and thus the effective heat-spot size) in ambient conditions typically ranges between 50 nm - 100 nm, but it is notoriously difficult to ascertain quantitatively [205, 206]. This is because the tip-temperature is never truly known because of parasitic heat transfer between the tip and sample, including: radiative, or conduction through air and water-meniscus. This is made even more complex when scanning heterogeneous samples with different thermal conductivities that may anisotropically spread from the localised heat-source. As the extraction of quantitative values are not the focus of this study, the localised heat-source

is assumed to be a 2D-Gaussian for the analysis in Section 5.4, as shown in Figure A.12 in the Appendix.

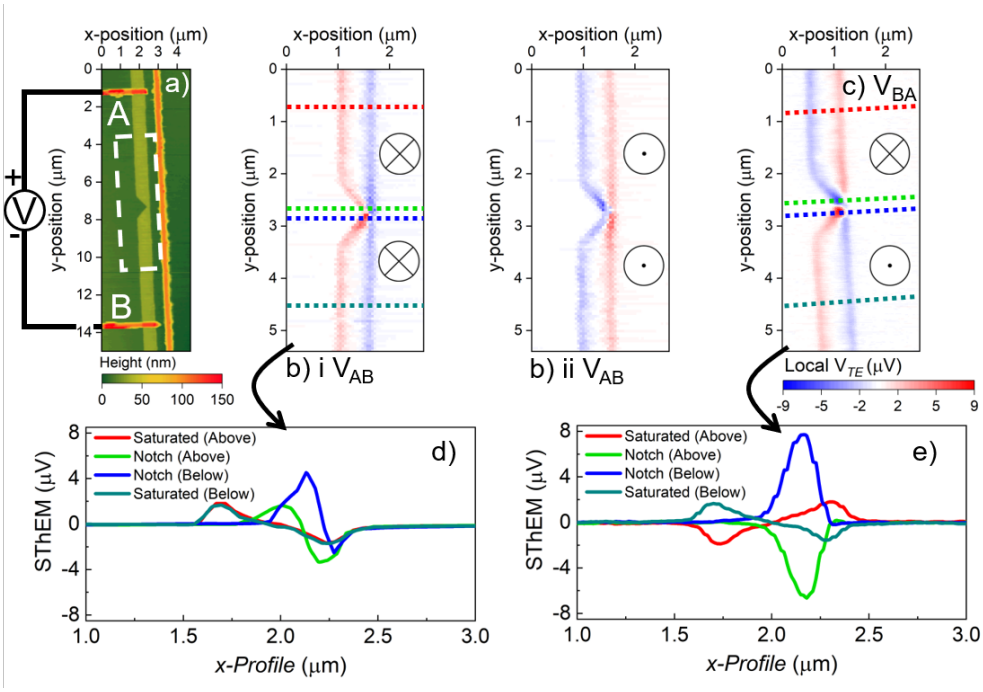


FIGURE 5.4. (a) atomic force micrograph of the NW showing the notched region and the electrical measurement contact points denoted A and B. (b)i-ii SThEM micrographs for two magnetisation states $m_z = \pm 1$ of the device, respectively. The asymmetry in the thermal gradient $\nabla T_x$ as the heated probe approaches the notch region results in an increase in the thermoelectric response in the notched region. (c) SThEM micrograph for the pinned DW where an inverted local thermoelectric response is shown either side of the notch ($m_z = \pm 1$). (d) Line profiles across the data in the saturated state, b(i), for the saturated region away from the notch and at the local signal-maxima in the notch-region. (e) line profiles taken in equivalent regions through the signal maxima/minima in (c).

The results from the local SThEM study of the magnetic NW are depicted in Figure 5.4, where the response from the device at magnetic saturation and with DW pinned at the notch is discussed. Figure 5.4a displays an atomic force micrograph of the device structure and details the electrical contact arrangement for measurement points, A and B, used to record the local thermoelectric response. Figure 5.4b(i-ii) shows SThEM micrographs of the CoFeB nanowire at remanence for the saturated magnetic state of the device in both positive and negative $z$-axis. Along each side of the device a voltage maximum or minimum is represented by the red and blue regions, respectively. The signal reverses sign under the application of reversed magnetic field confirming that the effect is magnetic in origin. By considering the results from the magnetothermal transport data,

[1]Figure prepared by C. Barton (NPL, UK.)

Figure 5.2, and the modelling in the following section (Section 5.4) the signal above and below the notch is solely due to the ANE. The square magnetisation reversal behaviour of the nanowire indicates that $m_z \approx \pm 1$ thus by moving the heated probe across the nanowire width a thermal gradient is generated along the short-axis $\nabla T_x$, resulting a transverse electric field $E_y$ (voltage) along $y$.

As the probe traverses the nanowire, the signal inverts, which can be understood from the integrated response of $\nabla T_x$ across the nanowire. In the opposite saturation the thermoelectric signal also inverts either side of the nanowires centre position (Figure 5.4b(ii)). The SThEM image for the case where a DW is pinned in the notch region is displayed in Figure 5.4c. Here, the presence of the DW gives rise to a reversal in the signal of the thermoelectric response dependent on the localised magnetisation direction. This is again consistent within the picture of the ANE where the longitudinal electric field $E_y$ results from a non-zero $z$-component of the magnetisation $m_z \neq 0$.

Cross-sectional profiles of the notched region in the saturated state are presented in Figure 5.4(d), where the profiles are taken at the position of maximum signal in the notch-region and away from it. The line profiles show a slight increase in the maximum signal in the notched region compared to the profile away from the notch. This may be attributed to a small contribution to the thermoelectric voltage by the anisotropic magneto-Seebeck effect (AMSE) because the geometric symmetry is broken when the probe passes either side of the notch, giving rise to a non-zero $\nabla T_y$. This effect is investigated further in Section 5.4.

The signal direction and magnitude seen in Figure 5.4b(i-ii) matches that seen when the DW is present away from the notch in Figure 5.4c (noting the opposite topology of the electrical measurement between Figure 5.4b and c). However, what is apparent is that at the notch an additional thermoelectric response is shown, which is greater than that shown in the saturated state. This is demonstrated in the cross-sectional profiles taken in the notched region at saturation in Figure 5.4d and with DW pinned in Figure 5.4e. The increased thermoelectric response arises from additional contributions due to non-zero components of the magnetisation in-plane from the presence of the Néel domain wall pinned in the notch. It is anticipated that this signal amplification at the notch area is due to the in-plane components of the local magnetisation contributions from the AMSE and/or the transverse equivalent planar Nernst effect. These effects are defined in Section 3.2.

## 5.4 Analytical model of thermoelectric response

In this section, a 2D analytical model for the thermoelectric effects induced in the CoFeB wire from the heated scanning probe is built[2]. The derivation is adapted from references [159, 160]. A thermomagnetic matrix can be constructed comprised of the transverse and longitudinal Seebeck

[2]With thanks to C. Barton (NPL, UK), and E. Saugar Gotor and O. Chubykalo-Fesenko (CSIC, Madrid), for assistance with the model derivation.

coefficients for the material ($S_\perp$ and $S_\parallel$, respectively) and the Nernst coefficient, $S_N$. Equation 5.1 describes a magnetisation parallel to the $z$-axis

$$\nabla V_T = \begin{pmatrix} S_\perp & -S_N & 0 \\ S_N & S_\perp & 0 \\ 0 & 0 & S_\parallel \end{pmatrix} \nabla T. \tag{5.1}$$

For a magnetisation in the $yz$-plane, i.e. is the case for a Néel domain wall, the tensor should be rotated on the $x$-axis according to the angular deviation from the $z$-axis, $\theta$,

$$\nabla V_T = \begin{pmatrix} 1 & 0 & 0 \\ 0 & \cos(\theta) & -\sin(\theta) \\ 0 & \sin(\theta) & \cos(\theta) \end{pmatrix} \begin{pmatrix} S_\perp & -S_N & 0 \\ S_N & S_\perp & 0 \\ 0 & 0 & S_\parallel \end{pmatrix} \begin{pmatrix} 1 & 0 & 0 \\ 0 & \cos(\theta) & \sin(\theta) \\ 0 & -\sin(\theta) & \cos(\theta) \end{pmatrix} \nabla T \tag{5.2}$$

$$= \begin{pmatrix} S_\perp & -S_N & 0 \\ S_N\cos(\theta) & S_\perp\cos(\theta) & S_\parallel\sin(\theta) \\ S_n\sin(\theta) & S_\perp\sin(\theta) & S_\parallel\cos(\theta) \end{pmatrix} \begin{pmatrix} 1 & 0 & 0 \\ 0 & \cos(\theta) & \sin(\theta) \\ 0 & -\sin(\theta) & \cos(\theta) \end{pmatrix} \nabla T \tag{5.3}$$

$$= \begin{pmatrix} S_\perp & -S_N\cos(\theta) & -S_N\sin(\theta) \\ S_N\cos(\theta) & S_\perp\cos^2(\theta)+S_\parallel\sin^2(\theta) & S_\perp\sin(\theta)\cos(\theta)-S_\parallel\sin(\theta)\cos(\theta) \\ S_N\sin(\theta) & S_\perp\sin(\theta)\cos(\theta)-S_\parallel\sin(\theta)\cos(\theta) & S_\parallel\cos^2(\theta)+S_\perp\sin^2(\theta) \end{pmatrix} \nabla T \tag{5.4}$$

For the coordinate system of the experiment, only the electric potential along $y$, $\nabla V_y$, is necessary to measure the electric potential along the wire,

$$E_{\text{tot}} = \nabla V_y = \overbrace{-S_N\cos(\theta)\nabla T_x}^{\text{ANE}} - \overbrace{[S_\perp\cos^2(\theta)+S_\parallel\sin^2(\theta)]\nabla T_y}^{\text{AMSE}} - \overbrace{[S_\perp\sin(\theta)\cos(\theta)-S_\parallel\sin(\theta)\cos(\theta)]\nabla T_z}^{\text{PNE}}. \tag{5.5}$$

Here, the three terms relate to the ANE, AMSE and PNE, respectively. As the CoFeB NW is ultra-thin, it is assumed that $\nabla T_z$ is negligible and the PNE term drops out of Equation 5.5. For simplicity, the magnetisation of the wire has been defined by analytical equations, thus fixing the spins in the wire to be purely along the $yz$-axis and changeable DW size. The thermal profile was modelled by as a Gaussian profile with $T_{\max} = 425$ K to resemble the temperature of the tip apex and ambient temperature of 300 K with peak width (FWHM = 112 nm) (see Figure A.12 in the Appendix).

In order to unambiguously identify the contributions to the SThEM micrographs presented in section 5.3, the electric potentials ($E_{\text{tot}}$) of a geometrically defined straight and notched wire with and without DW are calculated in the remainder of the present section. Values for the Nernst coefficient, $S_N = -370$ $\mu$V/K, and Seebeck coefficients, $S_\perp = -184$ nV/K & $S_\parallel = -186$ nV/K, were acquired from literature that study similar systems [194, 196, 207].

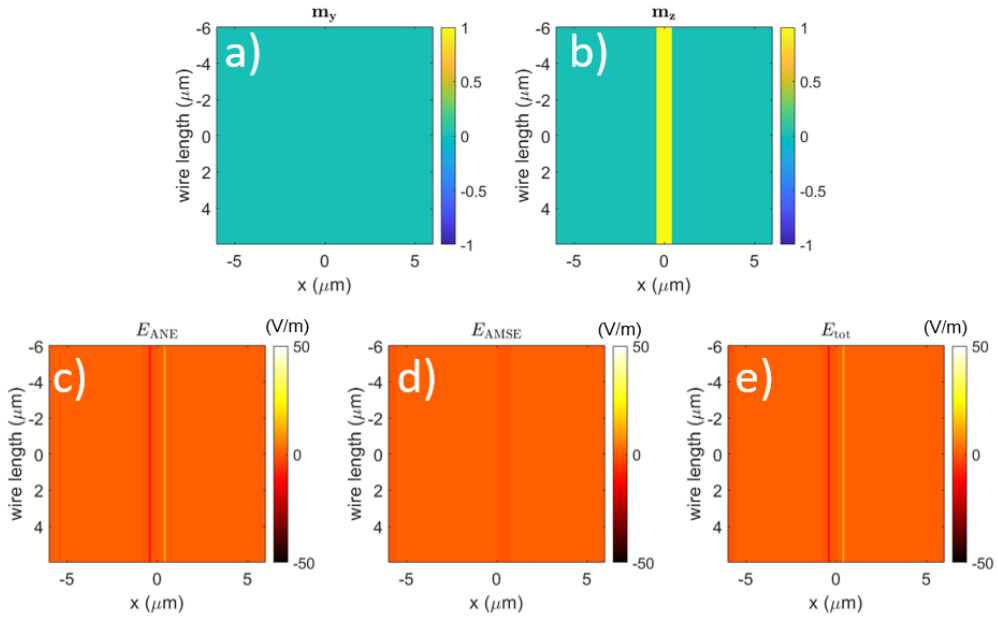


FIGURE 5.5. Maps of the $m_y$ and $m_z$ components of a saturated straight NW with PMA ((a) and (b), respectively). Calculated maps of the induced electric potential (in arbitrary units) from the ANE (c), AMSE (d), and combined (e) effects when excited by a circularly symmetric thermal gradient.

### 5.4.1 Modelling of straight wire

To assess the models without inclusion of TE signals from geometric effects, Figure 5.5 presents the calculated thermoelectric response from a straight wire saturated along $+z$ to represent a single-domain nanowire with PMA. Figure 5.5 a-b are magnetisation vector maps of the magnetic state, which is used as the magnetic input for the thermoelectric analysis Figure 5.5c-e. These magnetisation maps and the others in the remainder of the chapter have been generated from analytical expressions (i.e. as arrays of $\pm 1$'s and 0's in the dimensions of the wire, rather than an output of micromagnetic modelling. Here only the ANE contributes to the total electric potential in the absence of an in-plane component to the magnetisation, where long-edges of the wire in Figure 5.5(e) possesses inverted contrast that is not disrupted along the length of the wire. In addition, from the geometric symmetry in the $x$-plane at each tip-location, and the circularly symmetric thermal gradient no additional contributions to the signal are seen.

The saturated case can be compared with the case in Figure 5.6, where a Néel DW has been analytically described with placement in the centre of the straight wire (with $w_{\mathrm{dw}} = 100$ nm) as a coherent rotation along the $y$-axis between two domains of opposite sign (Figure 5.6a-b). Here the $E_{\mathrm{ANE}}$ map shows a similar response away from the DW location to the saturated case in Figure

5.5, but above and below the DW location the contrast inverts along the length of the wire as the magnetisation rotates across the wall. This signal inversion is replicated in the experimental micrographs away from the notch in the SThEM micrographs presented in Figure 5.4c.

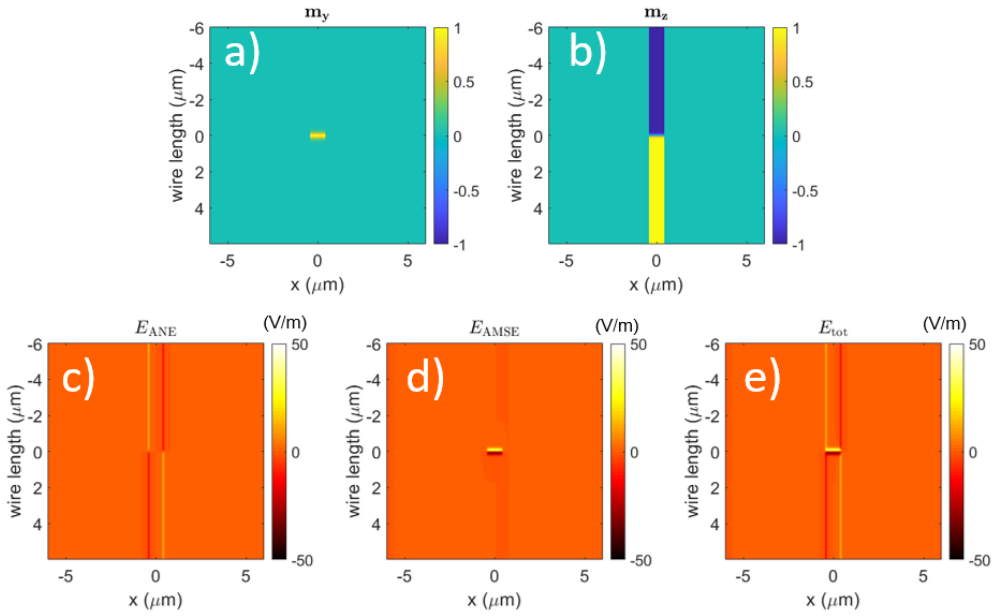


FIGURE 5.6. Maps of the $m_y$ and $m_z$ components of a straight NW with PMA and a Néel DW $w_{dw} = 100$ nm artificially placed in the centre of the wire ((a) and (b), respectively). Calculated maps of the induced electric potential from the ANE (c), AMSE (d), and combined (e) effects when excited by a circularly symmetric thermal gradient.

There is also a new contribution from the $E_{AMSE}$ in the DW region that was not present for the saturated case. Here, the signal maxima/minima occur at $\theta = 45°$ from the $z-$axis. This is because the AMSE has a $\cos(2\theta)$ dependence, which can be derived from Equation 5.5 using the trigonometric transformations

In the absence of any geometric contributions to the modelled straight wire, it is apparent that the Néel DW gives a strong contrast at the artificially pinned DW location that is similar to the contrast seen in the experimental SThEM micrographs in Figure 5.4c. The two cases for a straight wire can now be directly compared with a model that includes a notch comparable to the one under study in Section 5.3.

### 5.4.2 Modelling of wire with notch

Figure 5.7 displays the results of the modelling for a saturated wire in the $+z$ direction with a notch in the wire centre, where (a-b) displays the $m_y$ and $m_z$ components, respectively. Figure 5.7c-

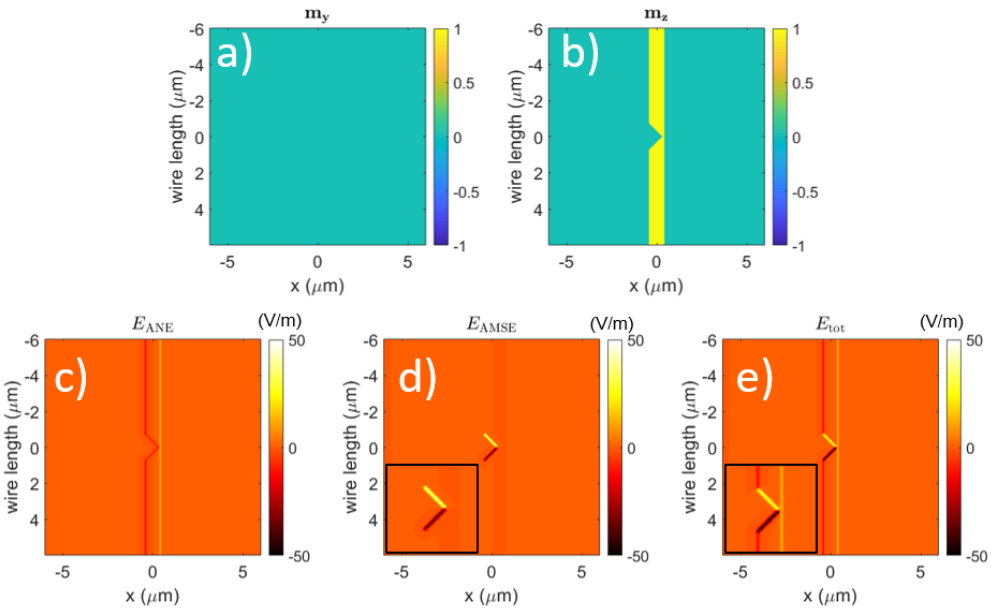


FIGURE 5.7. Maps of the $m_y$ and $m_z$ components of a saturated notched NW with PMA ((a) and (b), respectively). Calculated maps of the induced electric potential from the ANE (c), AMSE (d), and combined (e) effects when excited by a circularly symmetric thermal gradient; *inset* (d-e) zoomed area of the notched area.

e presents the calculated electric potentials from the ANE, AMSE, and combined contributions, respectively.

Comparison of the contrast in Figure 5.7c-e to the saturated straight wire in Figure 5.5c-e shows that the ANE contribution is replicated. However, there is now a new thermoelectric contribution from the AMSE (Figure 5.7d) on the non-continuous edge. This results from the geometric asymmetry of the notch with respect to the thermal gradient, resulting in the sharp increase of signal in the notched region in the total signal (Figure 5.7e). This qualitatively complements the experimental results for the saturated CoFeB wire in Figure 5.4b and d, which also displayed an enhancement of signal in the notch and an asymmetry either side of the notch centre.

The signal contribution from the geometric asymmetry appears considerably larger in the model compared the the experimental micrographs. There are many possible reasons as to why this geometric contribution may be over-exaggerated in the model: the model does not account for any thermal asymmetry in the probe's temperature profile; nor does it account for any topography induced artefacts that changes the probe-sample contact when stepping onto the wire; finally it assumes the thermal profile does not change as the probe passes over the wire, which would occur from the large differences in the thermal conductivities of the metallic stack and $SiO_2$ substrate.

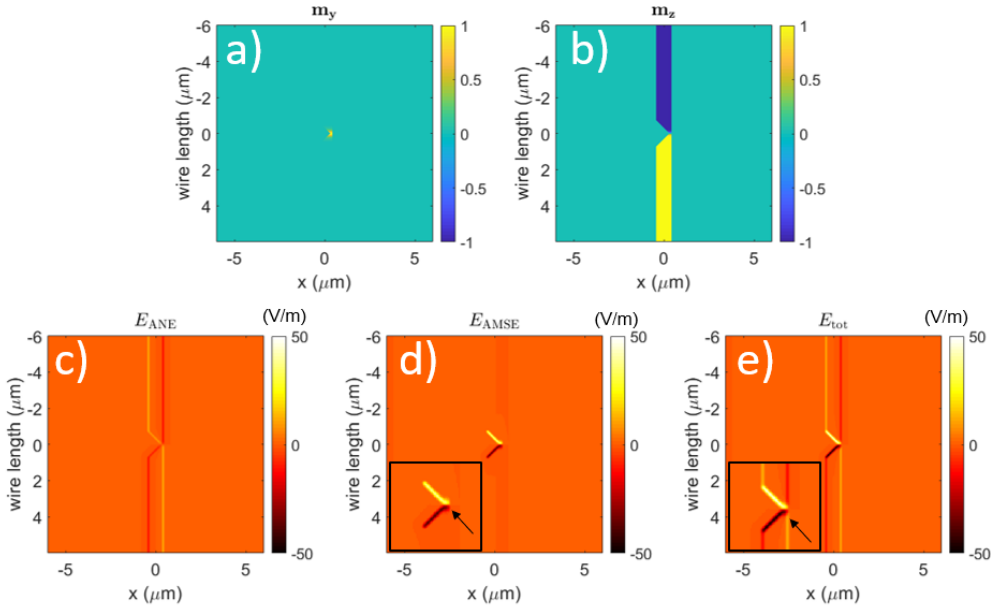


FIGURE 5.8. Maps of the $m_y$ and $m_z$ components of a notched NW with PMA and a Néel DW ($w_{dw}$ = 100 nm) ((a) and (b), respectively). Calculated maps of the induced electric potential from the ANE (c), AMSE (d), and combined (e) effects when excited by a circularly symmetric thermal gradient; *inset* (d-e) zoomed area of the notched area, with the domain wall contribution indicated by the black arrow.

Figure 5.8 plots the results of modelling the nanowire with a Néel DW ($w_{dw}$ = 100 nm) pinned at the notch site, where Figures 5.8(a-b) present the $y$- and $z$-magnetisation components, respectively. The thermoelectric potential plots in Figures 5.8(c-e) culminate the collective results from the previous Figures 5.5-5.7. The total electric field presented in Figure 5.8e possesses an inversion of signal away from the notch from the ANE in the saturated regions of the wire. In the notch region there is an additional AMSE contribution to the signal, compared to the saturated case, from the coherent rotation of spins in the DW in addition to the geometric effect of the nonsymmetric notch area. As with the saturated wire in Figure 5.7, the geometric artefact is considerably enhanced resulting in a masking of the magnetic signal that is more clear in the straight wire (Figure 5.6). In the inset images in Figure 5.8d-e, the DW contribution is visible to the right of the geometric artefact, and is qualitatively comparable to the experimental images.

To represent the electric potentials as simulated SThEM maps, Equation 5.5 is integrated over the distance, $d$, between the contacts ($V_{tot} = -E_{tot}d$). The simulated voltage maps for the straight and notched wires are presented in Figure 5.9a-b(i), where the distance between the contacts was $d = 12\mu$m. These can be directly compared with the SThEM micrograph in Figure 5.9c(i). It is apparent that the calculated voltages for the simulated wires are several orders

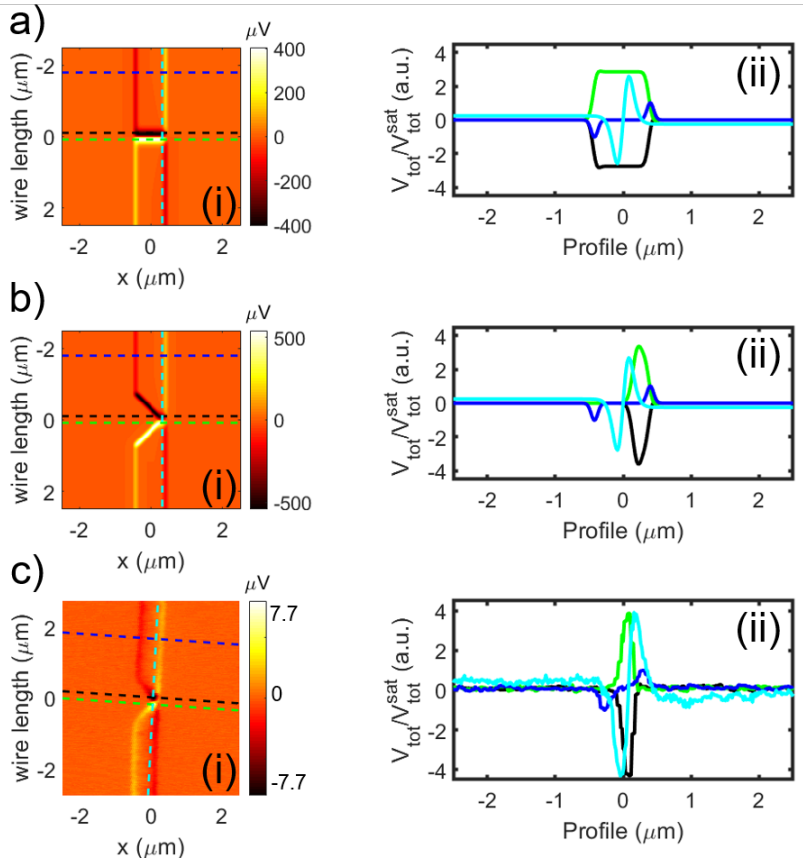


FIGURE 5.9. Modelled SThEM voltage maps (i) and corresponding line profiles normalised by ANE contribution (ii) for the straight (a) and notched (b) nanowire with analytically described Néel domain wall at the wire centre with parameters provided from literature. (c) Experimental SThEM micrograph (i) and corresponding line profiles (ii) normalised by ANE contribution.

of magnitude larger ($\sim 200\times$). It would be possible to effectively force the model to represent more similar values to the experimental results by tuning the various input parameters, such as the Seebeck/Nernst coefficients and the thermal gradient. However, this quickly becomes a complex multi-parameter fit. As no physical modelling of the magnetic or thermal inputs has been performed this could result in the loss of physical meaning.

Figures 5.9a-c(ii) present line-profiles through the corresponding thermoelectric wire responses in c(i) normalised by the ANE contribution away from the notch $\left(V_{\mathrm{tot}}/V_{\mathrm{tot}}^{\mathrm{sat}}\right)$. The royal-blue profiles represent the ANE contrast away from the notch, thus the peak and trough have been normalised to $\pm 1$ across all three plots. The shape of this profile is very consistent across the modelled and experimental datasets, showing good agreement. Black and green profiles pass through the signal minima and maxima above and below the notch, respectively. These profiles for the straight wire in Figure 5.9a are perfectly antisymmetric with $V_{\mathrm{tot}}/V_{\mathrm{tot}}^{\mathrm{sat}} = \pm 2.8$ in

the middle of the wire. The edges have a combination of ANE and AMSE signals in the straight wire, resulting in an additional ±0.05 signal amplitude at the wire edges.

The black and green profiles through the modelled wire with notch (Figure 5.9b(ii)) show a greater enhancement of the signal with the additional geometric effect. Here the peak minima/maxima is larger, equalling $V_{tot}/V_{tot}^{sat} = \pm 3.9$, respectively. By comparison, the cyan-profile in Figures 5.9a-b(ii) that samples the thermoelectric voltage longitudinally at the edge away from the notch (to exclude the geometric effect in 5.9b(ii)) are equal $V_{tot}/V_{tot}^{sat} = \pm 2.8$, showing that the amplitude increase in b(ii) is only from the geometric artefact. This shows that although the inclusion of the notch in the modelling shows the parasitic component of the geometric artefact well, it does not provide any additional information for the DW response.

The equivalent experimental profiles are displayed in Figure 5.9c(ii). Here, the longitudinal (cyan) and transverse (black and green) profiles pass through the same lobe minima/maxima in the SThEM image, thus possessing the same minima/maxima. These are $V_{tot}/V_{tot}^{sat} = -4.3/+3.9$ for the lobe minima and maxima, respectively. This asymmetry about the peak magnitudes in the experimental data suggests that the thermal distribution from the probe is asymmetric, which has not been captured in the modelling. Although the values and signal contributions have not perfectly aligned the modelling has been able to provide "ball-park" similarities to the experimental results

## 5.5 Summary and Conclusion

In this chapter, a new SPM method for locally probing the spin textures of a ferromagnetic nanowire has been performed and has demonstrated good spatial resolution and magnetic sensitivity. SThEM has been shown to be less perturbing than MFM for the material system under study as it did not result in perturbation of the NW magnetic state. Through modelling the possible thermoelectric signals for a Néel DW, the technique has been shown to be sensitive to the coherent rotation of spins in the ultra-thin ferromagnetic wire with PMA. Compared to other thermoelectric imaging techniques in literature, i.e. those using a laser for the generation of a thermal current [196], the spatial imaging resolution of SThEM is far greater as the point-heat source is more localised. This method may be used for local investigation of several other spin textures in electrically connected devices.

To assess the robustness of the technique, further measurements should be performed on new material systems. This includes more accurate modelling of the magneto-thermal effects that may occur when using a heated probe to measure magnetic response to measure the invasiveness of the technique; the more complicated thermoelectric signals that may arise from novel material systems; and possibly the extraction of the magnetothermal coefficients. For example, one problem that has been challenging in the field of SThM is exactly how to calibrate the heated probe as it too is a complicated inverse problem as the temperature and thermal distribution on different

surfaces is not known *a priori* [206].

Perhaps, magnetic reference materials with well-defined properties could be used to calibrate the thermal gradients of thermal probes. Equally, the technique may provide the ability to investigate systems that have been traditionally difficult to investigate by MFM using thermoelectric measurements [106]. The results in this chapter show that the technique is sensitive to both in- and out-of-plane magnetisation through combinations of the ANE and AMSE/PNE. Qualitatively, the SThEM method introduced throughout this chapter has proved fruitful for the measurement of the as described nanodevice, and can be used as an additional tool for understanding spin phenomena in nanodevices with SPM-level resolution.

CHAPTER 6

# MFM CHARACTERISATION OF MULTIMODAL ARTIFICIAL SPIN ICE

## 6.1 Introduction

As outlined in Chapter 2, switchable 2D nanomagnetic networks, such as ASI, have attracted attention as engineered reconfigurable metamaterials that exhibit collective dynamics. This is from geometric frustration and dipolar coupling between the constituent mesoscopic "macro-spins". ASI have applications as programmable magnonic metamaterials, logic devices and probabilistic computing. Random-walk style chains of correlated excitations typically form throughout the magnetic reversal process of traditional ASI designs, e.g. the Kagomé [208] and square lattices [37], which act as potential low-energy pathways for the aforementioned applications.

A highly active research topic is utilising novel architectures to tailor the magnetisation dynamics and compare competing interactions within truly degenerate states. This has been recently epitomised by investigating coupled nanomagnets in ASI lattices (see Figure 2.7d in Chapter 2 for schematic), which exhibit both ferro-/antiferromagnetic coupling and ground-state degeneracy (e.g. Toroidal [78] and Quadrupolar [79] ASI designs). The commonality between research in ASI is studying the reconfigurable degenerate states and their collective dynamics under external stimuli. Increasing the degrees of freedom at each frustration site has significant interest for both the fundamental understanding of ASI systems and their use in applications where selective reconfigurability is a necessity, such a logical computation.

In this chapter, a novel ASI design (the quasi-hexagonal (QH) lattice) is introduced and its behaviours are analysed by advanced MFM-techniques/analysis. The QH-ASI design demonstrates a modal magnetic behaviour within an Ising regime at remanence under low-field sequences. Under one field protocol the intrinsic geometry of the lattice generates nanoscale 1D channels of low energy pathways in a background of high-energy vertices.

The formation of chiral magnetic textures (Landau states) is investigated in the coupled nanoelements that are aligned perpendicular to the applied incident field in the QH lattice. The energies of the Landau states are investigated by MFM and micromagnetic modelling. Using the method outlined for the Py L-shaped nanostructure in Chapter 4, qMFM analysis is used to correlate the micromagnetic modelling with the experimental data to test its validity. Finally the deterministic formation of Landau states, and their intrinsic chirality, are investigated.

## 6.2 Ising behaviour of QH-ASI Lattice

Figure 6.1 introduces the novel ASI lattice design. The lattice is a hybrid of both the classical honeycomb and square ASI designs as it possesses a quasi-hexagonal (QH) unit cell, and maintains four-interacting NIs at each vertex (Figure 6.1(a)). The lattice has parallel NIs between the unit cells introducing ferro-/antiferromagnetic interactions into the usual frustration-based macro-spin interaction. Three vertex shapes are present in the lattice, X- and Y-shapes in a one-to-two stoichiometric ratio (Figure 6.1(b)), with one Y rotated 180° (herein referred to as reversed-Y (rY)).

From this distribution of vertex shapes, modal magnetic configurations are produced dependent on the applied field vector. In statistics, modality describes multi-frequency populations in ASI systems. The modal magnetic states are exhibited in Figures 6.1(c-d) by MFM images at remanence after $B$ is applied along the $y$- and $x$-axis, respectively. From the oblong aspect ratio of the unit cell, there is globally one easy axis and one hard axis (i.e. along the $y$- and $x$-axes, respectively). Micromagnetic modelling of the shape anisotropy for the QH-lattice is represented in Figure 6.1e, showing the remanent magnetisation ($M_R$) after saturation along a particular field angle ($\beta$) from the $x$-axis. When magnetised along the easy axis, the moments at all the vertices conform to the uniform ice rule allowed Type II ($T_2$) configuration, as visualised in the MFM image in Figure 6.1(c). This state is defined as unimodal (UM) as it possesses a single distribution of energy states.

When the QH lattice is magnetised along its in-plane hard-axis the diagonal NIs magnetically align along the field-direction (Figure 6.1(d), and the magnetic state is conserved upon release of the field. The magnetisation in the NIs orthogonal to the applied field resist switching because of their shape anisotropy and orientation relative to the field vector. This results in a bimodal (BM) state where the X-shaped vertices are in the $T_2$ magnetic state and the Y/rY-shaped vertices are in the higher energy Type III ($T_3$) state. The resulting magnetic landscape is thus confined into dispersed rows of alike energies, producing low-energy pathways in the X-vertices across the globally higher energy lattice.

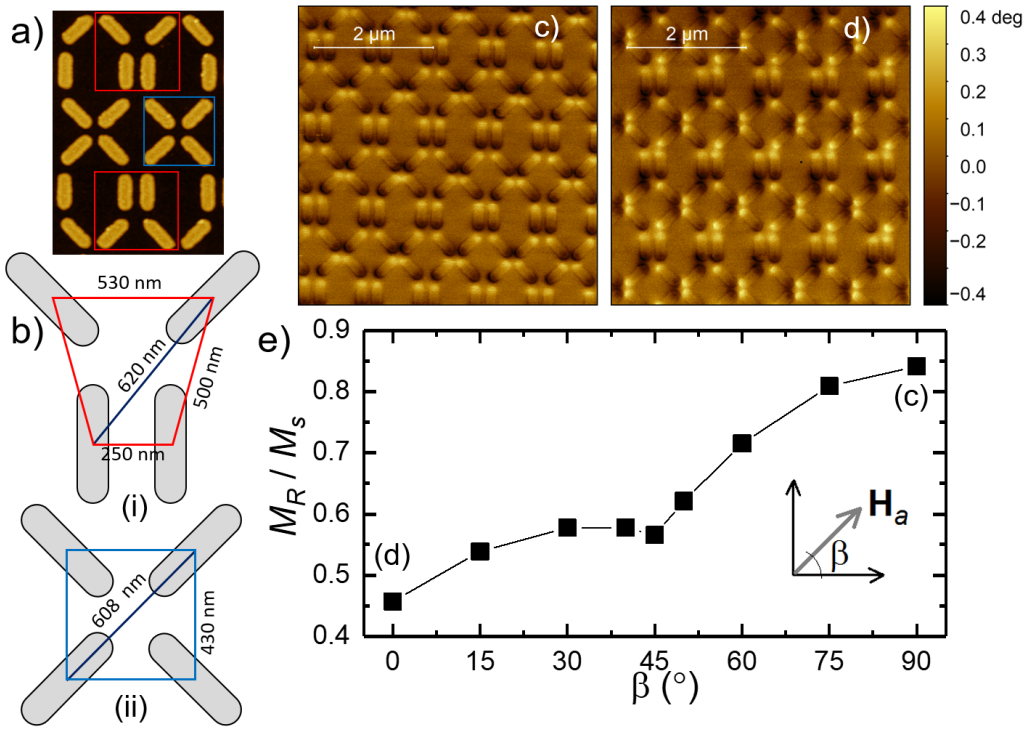


FIGURE 6.1. (a) AFM Image of four unit cells of the QH-ASI lattice, where boxes indicate X and Y/rY junctions (blue and red, respectively). (b) Schematic of the dimensions of Y (i) and X (ii) junctions. MFM images at remanence of QH-ASI lattice in unimodal (c) and bimodal (d) magnetic configurations, respectively. Calculated remanence magnetisation (normalised to the magnetic saturation), as a function of the angle $\beta$ of the applied field with respect to the $x$-axis (see inset); $\beta$ required for MFM images (c-d) are specified.

## 6.3 Evaluating the energy landscape

The evolution of the magnetic states within the lattice was assessed as a function of field magnitude applied along the lattice in-plane hard-axis (Figure 6.2a). MFM images of QH ASI were taken at remanence at defined field steps within the range $B$ = 25-224 mT to assess the transitions between modal landscapes. Initially the lattice magnetisation is set in the UM configuration. The MFM images at each field-step are displayed in Figure A.3a in the Appendix. The reproducibility of the states formed is addressed in Section 6.5. Figure 6.2a plots the population frequency of the energy types across the MFM images as a function of the field, where the plot is divided into three segments to highlight the different modal states. The left and central segments represent the stable field regions where the UM and BM states are formed, respectively. The switch between these modal states at $B = 35-50$ mT was not instantaneous, instead it progressed via a two-step mechanism displayed in Figure A.3c in the Appendix.

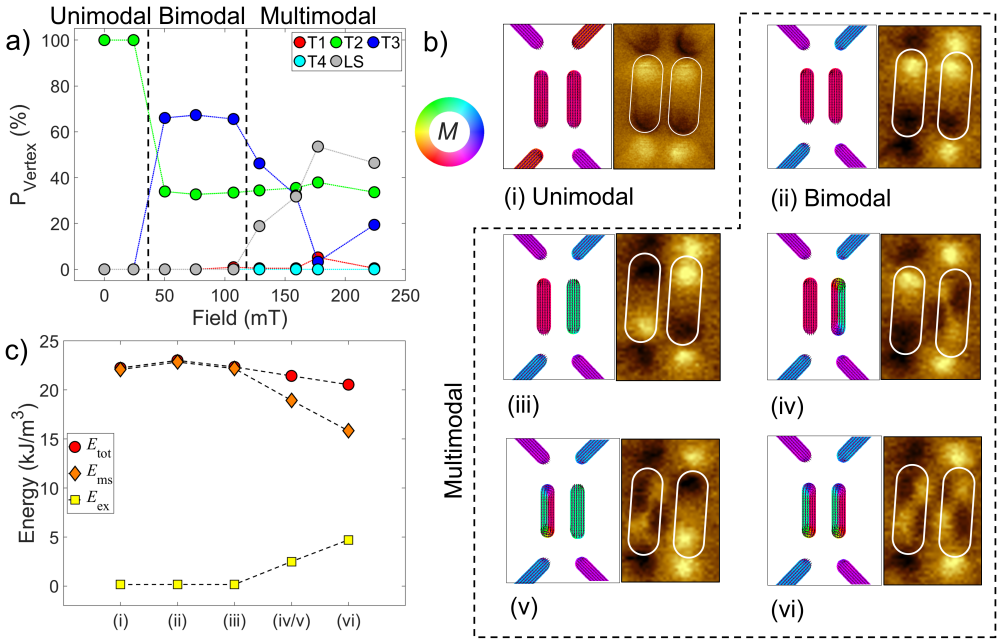


FIGURE 6.2. a) Vertex population of QH-ASI as a function of field applied along the in-plane hard-axis of the lattice after an initial unimodal state (lines are included as guides for the eye). b) Modeled magnetisation configurations (the colour-wheel represents the angle between the magnetisation vector in the xy-plane and the $x$-axis) and experimental MFM images at remanence (left and right, respectively) of Y/rY vertices in unimodal (i), bimodal (ii) and the five states observed under the multimodal regime (ii-vi). c) Magnetostatic and exchange energy terms (and their summed total) calculated at remanence for the six states displayed in (b). ©2020 Wiley VCH. Reprinted, with permission, from Puttock *et al.* [209].

Considering the same applied-field protocol, the evolution in the magnetic configuration of the QH-lattice was studied by micromagnetic modelling[1], which is reported in Figure 6.3a. The remanent magnetisation maps are provided in Figure A.4 in the Appendix. Here, the remanent BM state appears after applying $B \approx 75$ mT field along the $x$-axis direction, closely matching the experimental values. The modelling confirmed that the remanence states at the beginning of the sequence are strongly influenced by the initial UM configuration, thus the lattice exhibits hysteretic properties where the magnetic distribution is frozen into the starting configuration.

Above a critical field, $B_c \approx 125$ mT, the plot in Figure 6.2a shows a far more chaotic distribution of energy configurations in the third segment. This results from a loss of magnetic periodicity across the lattice as some NI "macro-spins" break down into Landau states (LSs). This forms a multimodal (MM) configuration, where more than two vertex energy types occur across the lattice. Figure 6.2b presents MFM images and modelled magnetisation maps at remanence of the

[1]GPU-based modelling has been performed by A. Manzin (INRIM, Italy).

Y/rY junctions: the UM (i), BM (ii), and MM states (ii-vi). In the MFM images the single domain NIs have uniform magnetisation with confined stray-field emanating from the vertices, whereas LSs present as a chequerboard pattern in the MFM images. LSs are not uniformly distributed across the lattice, creating a spatially aperiodic magnetic pattern. From the initial BM Ising state the parallel magnetised NIs can form one of four possible new configurations. Two configurations result from a single NI change: antiparallel Ising pair (iii), and single LS (iv); and two result from both NIs switching: one Ising flip plus one LS (v), and double LS (vi).

In the micromagnetic modelling of the ASI lattice (Figure 6.3a) the MM configuration is formed at $B \approx 275$ mT (6.3a(iii)), where LSs of mixed chirality form uniformly across the lattice (i.e. only state vi). Here, both the field at which the LSs form and the multiplicity of states differ from the experimental dataset. These deviations between the experimental and the modelled values can be mitigated by reducing the inter-island separation in the model to half of the nominal distance (Figure 6.3b). Magnetisation maps and schematics of these structures are provided in Figure A.5 in the Appendix.

The greater dipole-dipole coupling between neighbouring NIs results in an additional step in the energy progression where the full multitude of states shown in Figure 6.2b are observed (3b(iii)). This reduced distance may still resemble the experimental system well, as scattering events in the lithography process would result in an effecting broadening of the nanostructures, reducing the inter-island distance from the original design used as the input to the model [210]. At a higher field ($B \approx 300$ mT), all of the Ising states in the couple NIs are pushed out of the lattice (Figure 6.3b(iv)), which is comparable with the 1.0× separation factor in Figure 6.3a(iii). A further discussion of the lattice at high fields is addressed in the following section.

To understand the complex balance of energies for each configuration in Figure 6.2b, the magnetostatic, exchange and total energies ($E_{ms}$, $E_{ex}$ and $E_{tot}$, respectively) were extracted from micromagnetic simulations for the original lattice separation, where each configuration is uniformly distributed across the QH-lattice (Figure 6.2c).A saturation magnetisation of 860 kA/m and an exchange constant of 13 pJ/m were used for Py in the simulations of the lattices. Contributions from thermal noise were assumed to be negligible. For further details of the modelling, please see Section 3.5.1 in Methods.

The three Ising configurations (i-iii) are dominated by $E_{ms}$ as NIs are in a single domain configuration. $E_{tot}$ for states (i-iii) are 22.25, 23.02, 22.35 kJm$^{-3}$, respectively. A sharp increase in $E_{ex}$ is seen upon formation of LSs, however the resulting demagnetisation reduces $E_{tot}$ to 21.44 kJm$^{-3}$ (states iv-v) and 20.55 kJm$^{-3}$ (state vi). The reduction in $E_{ms}$ upon formation of LSs implies a reduced frustration at the vertex-junctions as the LS flux-closure occurs within the NI. As a result, the degree of correlation across the lattice is likely diminished, allowing for the loss of long-range order in MFM images and the calculated magnetisation maps.

To further support these conclusions, modelling of a single NI away from any inter-island interactions was performed (Figure 6.4). The NI in a LS configuration results in two-fold greater

energy than the single-domain case. These calculations were performed using OOMMF (see

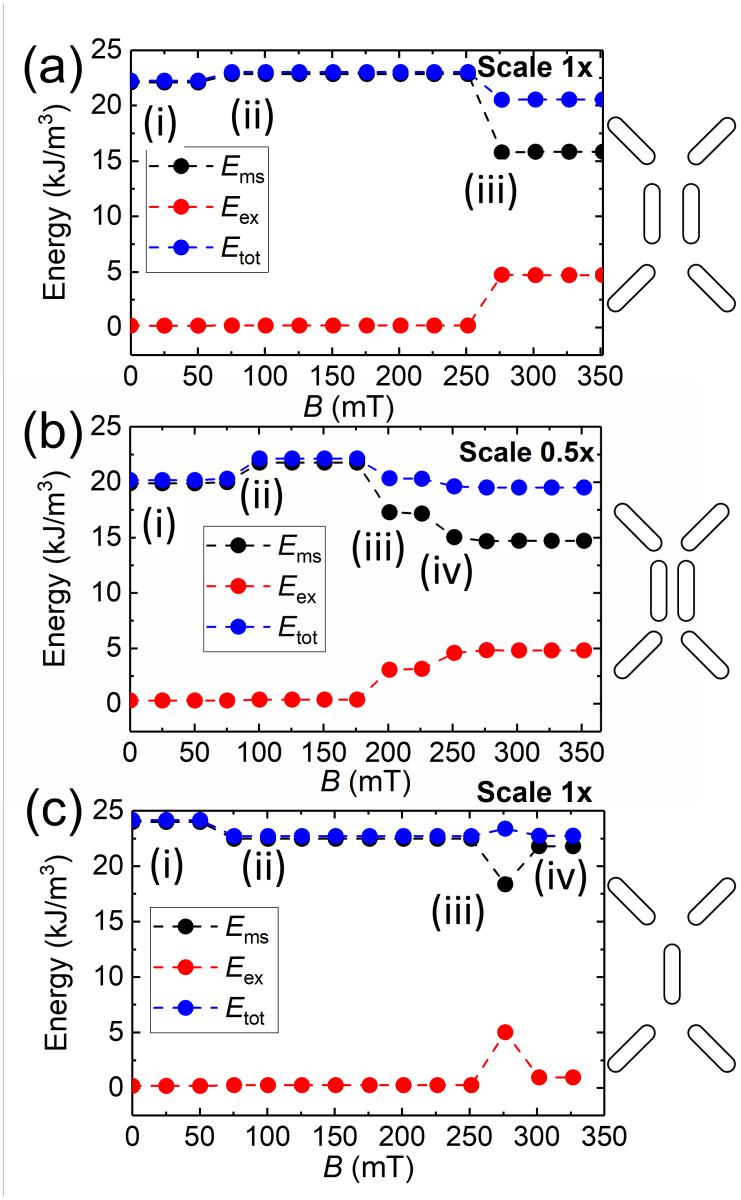


FIGURE 6.3. Magnetostatic (black), exchange (red) and combined (blue) energy terms calculated at remanence for each field step after gradually reaching the field set-point and then subsequently releasing the field for the QH-ASI lattice with inter-island separation factor 1.0× (a) and 0.5× (b) the nominal value. (c) displays the predicted energy configuration of the QH-ASI lattice where the parallel islands are replaced by an individual element (with a separation factor of 1.0×). Labelling marks the evolution in the magnetic configuration for the three lattices, which are displayed in Figure A.4-A.6 in the Appendix. ©2020 Wiley VCH. Reprinted, with permission, from Puttock *et al.* [209].

section 3.5.2) with the same material parameters and dimensions as before with the exception of changing the thickness to $t = 24$ nm. As OOMMF operates using FFT methods for its calculations, changing the thickness to be a multiple of 2 helped to accelerate the simulations. In addition, the damping parameter, $\alpha$, was set to 0.5 , which is nominally higher than the previous modelling due to computational constraints. The nanoelement was discretised into voxels (3D pixels) of size $2 \times 2 \times 2$ nm$^3$ for the time-evolved simulations.

Figure 6.4(a) and (b) show the initial and relaxed magnetisation configurations for two instances where the magnetisation is highly deviated from a typical single domain nanoelement. The initial configuration is full saturation along the in-plane hard-axis of the nanoelement. Upon

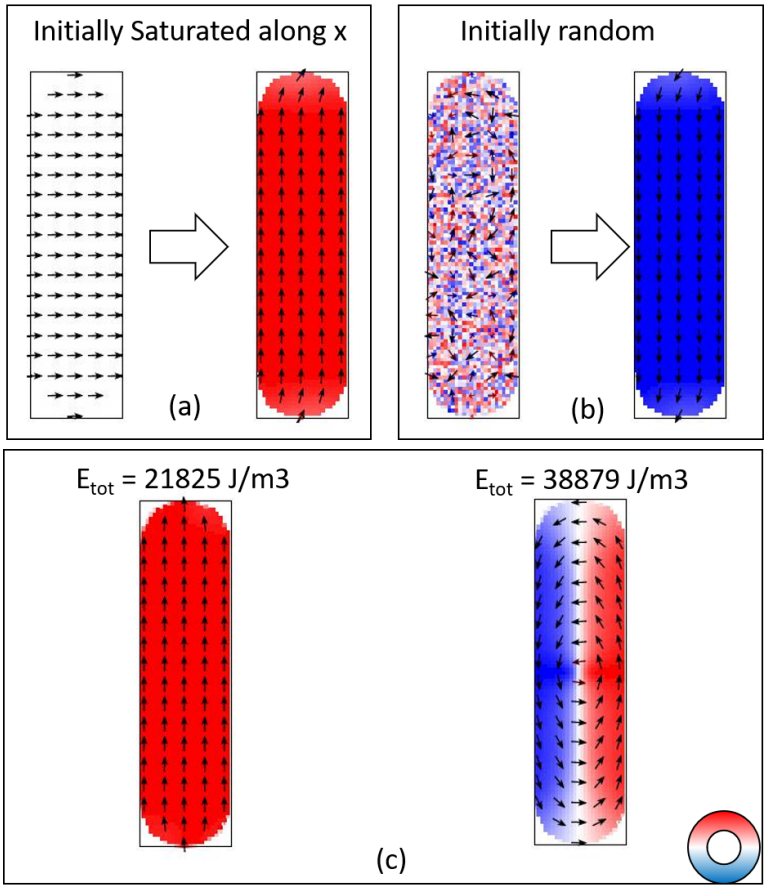


FIGURE 6.4. a) Initial and final (converged) magnetisation maps for a stadium-geometry nanoelement when initially saturated along the in-plane hard axis. (b) Initial and final (converged) magnetisation maps for a stadium-geometry nanoelement when initially the magnetization is randomized. (c) Converged magnetisation maps when the initial magnetization of the nanoelement was single- and multi-domain (left and right, respectively), alongside their respective total energies. The colour-wheel represents the $m_y$ component of the magnetisation. ©2020 Wiley VCH. Reprinted, with permission, from Puttock *et al.* [209].

relaxation of the field, the model converged into a single-domain nanoelement with magnetisation aligned along its easy axis. The same result (albeit inverted) occurred when the initial configuration was randomised. This is a demonstration that LS formation is unfavourably when a single NI is saturated along its in-plane hard-axis or thermalised.

Figure 6.4(c) shows the final converged configuration after forcing the magnetisation of the nanoelement to be single-domain (left) and multi-domain (right). Here the relative total energy densities are displayed alongside the converged magnetisation maps. The energy difference is almost two-fold between the multi and single-domain state, showing that its formation is not energetically favourable. From these values, we can calculate the energy cost of LS formation as $38879 - 21825$ J/m$^3$ = 17054 J/m$^3$. Therefore, a relative reduction in total energy upon formation of LSs in a lattice demonstrates that it is an energetically stabilised state due to the surrounding magnetic landscape and inter-island coupling.

In order to highlight the unique magnetic properties of the QH-lattice, we compared the simulations with a modeled example of the QH-design without the coupled NIs (Figure 6.3c). Magnetisation maps and schematics are provided in Figure A.6 in the Appendix. Under the same field-history we see that hosting LSs pushes the lattice into a higher total energy (Figure 6.3c(iii)), deviating from the cases with parallel NIs as displayed in Figure 6.3(a-b). At the next field increment, LSs are pushed-out and the NIs return to an Ising ground state ( Figure 6.3c(iv)). This signals that the presence of the parallel nanomagnets in the QH-ASI lattice causes a deviation from the expected mean-field theory for LS generation within this field protocol, resulting in the MM configuration.

The formation of LSs in ASI lattices provides greater degrees of freedom compared to traditional Ising configurations resulting in a loss of magnetic periodicity. In a lattice without coupled parallel NIs, LS formation is meta-stable resulting from partially saturated spins along the in-plane hard-axis of the NI. In the presence of coupled NI's in this lattice, the LSs are instead stabilised by the surrounding magnetic interactions, resulting in the favourable summed energy contributions upon their formation. This favourable LS formation and violation of the 16-vertex model may apply to other ASI lattices consisting of coupled parallel NIs such as the quadrupolar or trident ASI [77–79].

## 6.4 Direct Correlation of Experiments and Modelling by qMFM

When measuring the stray-field of a nanostructure it can be difficult to directly correlate the $z$-stray-field contrast as detected by MFM and a micromagnetic model because of the many reasons discussed in Section 3.1.4. Tip-sample interactions and point-spreading within the acquired image are the most prominent. To link the modelling performed in Section 6.3 and experimental results throughout this chapter, the stray magnetic field emanating from the QH-ASI structure is quantified by qMFM measurements. These were performed with calibrated probes and analysed

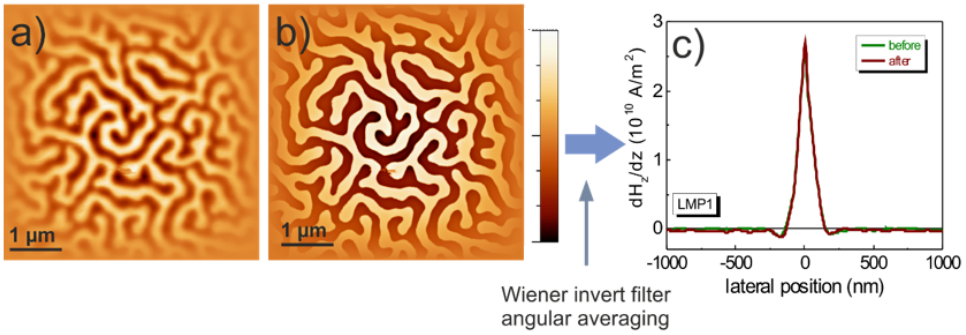


FIGURE 6.5. Welch-windowed $5 \times 5\mu$m MFM image (a) and calculated surface charge map (b) of $[Co/Pt]_{100}$ reference sample by a low-moment MFM probe. (c) Line profile of the real-space tip-transfer function for the low-moment probe before and after qMFM measurement on ASI.

as described in Section 3.1.4 and Refs. [127, 138, 145]. The procedure for the proceeding analysis is set-out in Figure 6.5[2].

Figures 6.5a-b present the MFM phase contrast of the $[Co/Pt]_{100}$ reference multilayer and the computed surface charge pattern obtained using a calculated domain wall width $w_{dw} = 16$ nm and film thickness $t = 130$ nm. An assumption of the TTF method is that the MFM measurement extends to infinity and have idealised periodicity across the image. As a consequence, data acquired at the edges of the scan size are problematic as the sensing area of the probe extends beyond the scan area boundary. In addition, a contamination of the Fourier component due to discontinuous image edges can result in a cross-shaped artefact in the RS-TTF [145]. To reduce the influences from these parasitic effects at the image boundaries, Welch-windowing [211] was applied to Figure 6.5a-b to smoothly ramp the boundaries to zero so the periodicity across the image is conserved when the Wiener deconvolution is performed. Line profiles along the probe cantilever length of the RS-TTFs are plotted before and after measurement of the ASI (Figure 6.5c). The probe's imaging properties have not changed throughout the experiment as the probe calibration before and after the experiment was largely identical. This indicates that the probe has not undergone any physical deformations throughout the experiment which would impede the assessment of the qMFM results.

Figure 6.6a presents three MFM images of the QH-ASI in the UM, BM and MM states (i-iii, respectively). A simulated MFM contrast was calculated from the micromagnetic model to compare the calculated output with the experimental measurements (Figure 6.6b). The surface charges were calculated by the methodology outlined in Section 4.3 for a single ASI unit cell and periodically extending laterally to the dimensions of the scan area.

As the TTF is regularised over a grid equivalent to the MFM image resolution, the irregu-

[2]The TTF calculation was performed with V. Neu (IFW Dresden)

larised simulated surface charge map from the micromagnetic modelling must also be transformed onto the same mesh-shape to perform the calculation. However, it is not trivial to perform this mesh transformation at the sample surface as regularising complex structures such as the LS introduces localised inaccuracies at the interface of the mesh-cells [177]. To perform the necessary transformation, the map was projected $z = 7.5$ nm away from the top surface onto the regularised grid of dimensions equal to the experimental MFM image. This removes the sharp transitions between the regularised mesh-cells. Subsequently, the surface charge map was convolved with the averaged RS-TTF from Figure 6.5, resulting in a calculated MFM contrast (Figure 6.6b) that shows the typical blurring of the surface charges due to the volume character of the probe at a tip-sample separation.

By projecting the surface charge map away from the top-surface we introduce a synthetic tip-sample separation on top of the lift-height. In order to account for this transformation, the experimental MFM image was also projected $z = 7.5$ nm away. While the surface charges are concentrated at the island ends and are influenced by the NI curvature and surrounded environment, the calculated MFM contrast resembles isotropic poles with a diameter of 140 nm (full-width half-maximum). Selected line profiles through experimental and calculated data show very good qualitative agreement (Figure 6.6c), and has good quantitative agreement for the UM state. Here, simulated and experimental values match when a correction factor of $\times 1.3$ is applied to the simulated data.

To corroborate this finding, qMFM measurements have been performed with two additional probes (Figure A.7 in the Appendix). Despite their largely different quantitative characteristics and resulting MFM signal, calculated MFM profiles matches the experimental data well when the corresponding TTFs are employed. In these experiments, samples were not fully UM as some isolated magnetic defects remained. Line profiles through the $T_2$ states also provided good agreement between simulations and experimental results within 10% deviation.

Quantitative evaluation of the experimental and simulated MFM images for the BM state (Figure 6.6b (ii)) is comparatively inferior. A larger correction factor of $\times 1.45$ is required to match the experimental MFM image with the simulated values. In addition, an underestimation of the attractive regime is measured because the measured MFM contrast at the two negative poles is both stronger and laterally more confined. Contrary to this, along a profile through two neighbouring positive poles in Figure 6.7 shows the corresponding double peak is neither increased substantially nor narrowed.

This finding is attributed to an unfavourable magnetic interaction between the probe and the sample because the former experiences a strong net stray field when positioned above the $T_3$ energy vertex. When the probe experiences a repulsive force, the MFM contrast is less affected. However, in the attractive regime contrast enhancement in MFM measurements is often observed due to a focusing of the probe's magnetisation configuration in the sample's stray field or vice versa. This focusing effect is even an advantage in MFM measurements with superparamagnetic

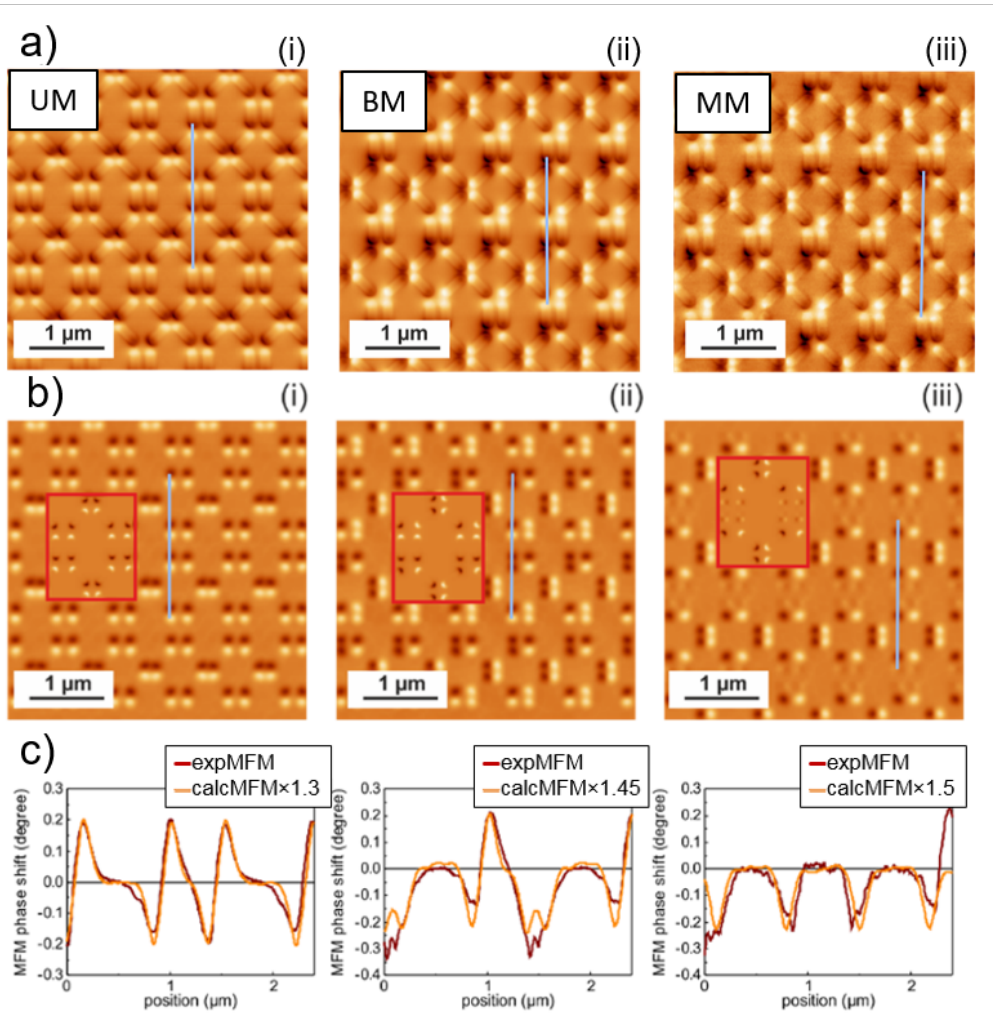


FIGURE 6.6. (a) MFM images of QH-ASI in unimodal, bimodal and MM (with single instance of non-Ising state). (b) Calculated MFM images for (i) unimodal, (ii) bimodal and (iii) non-Ising remanent states obtained by forward convolution of the simulated surface charge patterns (inset) with the TTF (Figure 6.5c). c) (i-iii) line profiles across the simulated MFM images compared to the experimentally measured results. The former are scaled to quantitatively match the experimental profiles in the contrast (scaling factors are shown in the legend).

probes [212].

Comparing the results from the two Ising (UM and BM) magnetic configurations, it is apparent that the Y/rY vertex junctions have a higher coercivity when in the higher energy $T_3$ state. This net stray-field of alike poles in close proximity has the undesired effect on the probe's imaging property, described above, resulting in a further deviation between the calculated and experimental MFM images.

The qualitative comparison of the MFM image of the non-Ising state (Figure 6.6a (iii)) is

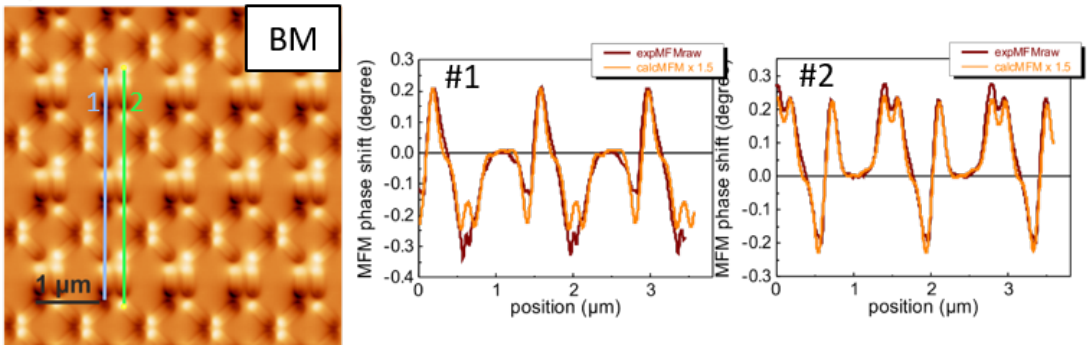


FIGURE 6.7. MFM measurement of the sample in the BM state with line profiles through two neighbouring rows of magnetic poles.

convincingly estimated by the calculated MFM data (Figure 6.6b(iii)). However, a quantitative comparison of the profile is only possible in the close ($\approx 2\mu$m) proximity of the experimentally measured LS. Experimental and modelled profiles coincide both in peak height and shape when a correction factor of $\times 1.5$ is applied (Figure 6.6c (iii)). A small anisotropy in the profile of the LS in the experimental image may indicate a slight tip-sample interaction where the chiral configuration is perturbed by the probe's stray-field. However, it may also stem from a non-idealised domain configuration. The domain configuration in multiple LSs is assessed in greater detail in the next chapter.

## 6.5 Landau state characterisation

So far in this chapter, LSs have been shown to favourably form at a sufficient field vector and is stabilised by the presence of the parallel NIs incorporated into the lattice. This has proved to be irregular from the shape anisotropy of the constituent components of the lattice and the dipolar coupling between islands should prevent these states from forming. This section investigates the formation of LS and their characteristics within the QH lattice. In particular, an assessment of the role of the field vector and the stochasticity of formation will be performed.

In Figure 6.8 the distribution in chirality where the flux-closing configuration rotates clockwise (CW) or counterclockwise (CCW) is assessed. Figure 6.8a depicts MFM images of the square- (left) and QH-lattice (right) at remanence after applying field $B = 177$ mT at an angle, $\beta = -1.1°$, from both lattice $x$-axes. The square ASI has a far greater asymmetry in LS chirality (72%) than the QH-lattice (53%) and higher proportion of LSs formed (80% and 60% in square and QH-lattice, respectively). Figure 6.8b plots the number of LSs ($N_L$) across MFM images of the QH-lattice, normalised by the number of coupled NIs arranged perpendicular to the in-plane field ($N_T$), as a function of $\beta$ across a range of field magnitudes (177-600 mT). The trend follows a Gaussian profile irrespective of the field magnitude, which shows that LS formation is highly dependent on $\beta$. From the fit the maximum population frequency of LSs in this lattice is calculated as 67%

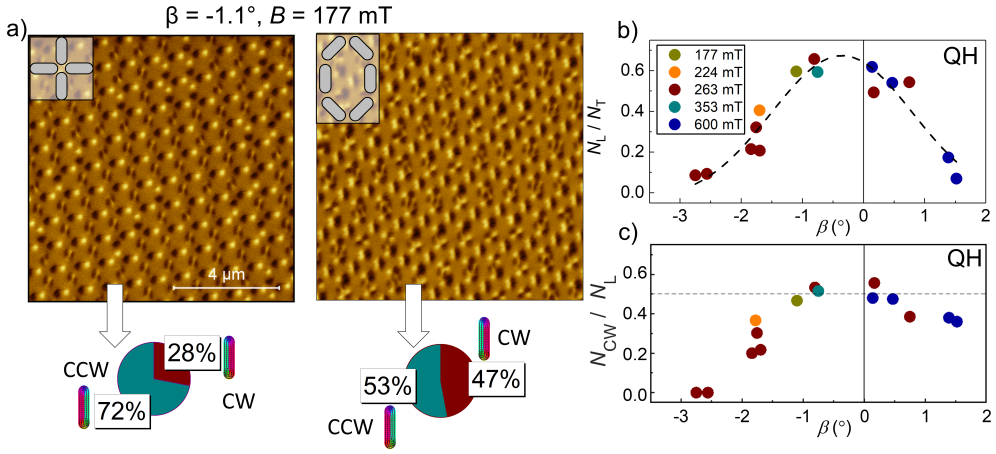


FIGURE 6.8. (a) MFM images of square (left) and QH-ASI (right) lattices at remanence after application of $B = 177$ mT at angle $\beta = -1.1°$ from the $x$-axis; unit cells are shown in the inset of the respective MFM images. Chirality pie-charts depict the distribution of counterclockwise (CCW, teal) and clockwise (CW, burgundy) in the respective MFM images. (b) Landau proportion in coupled nanomagnets in the QH-lattice as a function of applied field angle ($\beta$) at specified field magnitudes above the critical field. (c) Ratio of CW LSs to total number of LSs as a function of $\beta$. ©2020 Wiley VCH. Reprinted, with permission, from Puttock *et al.* [209].

in the coupled NIs. A slight $x$-offset in the peak in Figure 6.8b likely originates from systematic error in the angle measurement. A full saturation of LS across the lattice from in-plane field does not seem to be possible due to the dipolar interactions in surrounding magnetic environment. This results in the disordered, non-periodic environment of Ising and Landau state coexistence.

Figure 6.8c plots the angular dependence of the ratio of chiral states for the same dataset as displayed in Figure 6.8b. Near parity in CW/CCW LSs is demonstrated within ±1° range of the in-plane hard-axis direction. Outside of this range the chirality of LSs is tunable with $\beta$. We also observe a bias towards CCW Landau formation as the field angle deviates from the in-plane hard-axis direction, where the sign of $\beta$ does not affect the chirality bias. We predict this bias is a result of the surrounding magnetic environment upon relaxation of the field.

The experimentally observed frequency/chirality of LSs was compared to the modelled QH lattices in Figures 6.3 and A.4-A.6 in the Appendix. At the maximum field magnitude $B = 350$ mT ($\beta = 0$) a 100% proportion of calculated LSs in the NIs perpendicular to the incident field for the two QH-ASI with parallel NIs is seen. This does not match the experimental results but the chaotic distribution in chirality is matched between the experiment and modelling.

The state depicted at remanence after a field application of $B = 200$ mT for the reduced inter-island distance in Figure 6.3b(iii) and A.5(iii) more closely resembles the final magnetic states observed in the experiments. However, this modelled state is not formed at higher saturation fields such as those depicted in Figure 6.8(b-c). The QH-lattice without coupled-nanomagnets

(Figure 6.3c and A.6) possessed only one chirality of LSs when the saturation field was $B = 275$ mT, which more closely resembles the square lattice's experimental response in Figure 6.8a.

This confirms that the chaotic magnetic configuration is a unique property of the QH-lattice when $\beta = 0$ from the presence of the coupled nanomagnets perpendicular to the applied field-direction. The ability to tune both LS population and chirality across a $\sim 6^\circ$ window results in a degree of control in both formation and magnetic configuration of the lattice, which in turn has far greater use in, e.g., logic applications, than a truly stochastic effect.

To understand any further potential randomness or intrinsic bias in our system, the distribution and chirality of non-Ising states in the NIs under a repeated field protocol is assessed. Figure 6.9 (a-b) depicts the observed states at remanence and their relative population frequencies as a function of $\beta$ ($B = 600$ mT) in MFM images. When $\beta > 3.5^\circ$, only parallel Ising states are observed (state A) in NIs perpendicular to the perturbation field. The other states (B-H) become more prevalent at smaller field angles. Some datasets with energetically equivalent states, e.g. CW/CW and CCW/CCW states, have been combined for simplicity. This plot demonstrates a true break in uniformity across the Y/rY vertices from the formation of multiple iterations of Ising/non-Ising pairs when $\beta \approx 0^\circ$.

To assess and quantify the stochasticity in the MM configurations, identical regions of interest (ROIs) were analysed by MFM after repeated field application along the lattice in-plane hard-axis. Prior to each field iteration on display, the magnetic configuration of the lattice was reset to the UM configuration. MFM images were converted into numerical arrays where NIs with Ising magnetization were assigned to 0, and CW/CCW LSs to $1/-1$, respectively (see an example for a row of parallel NIs in Figure 6.9c, top). The Hamming distance ($\chi_H$) is a metric to compare differences between two strings of equal size, and it was used to quantify the normalised number of differences in the magnetic configuration between each measurement [41,42]. The $\chi_H$-value is equal to the sum of differences across the image normalised by the number of elements. Thus, $\chi_H = 0$ when the magnetic configuration between MFM images $i$ and $j$ is identical, and $\chi_H = 1$ when the images are completely dissimilar. This quantifies the stochasticity per NI between each MFM image after application of a field with angle $\beta$ for both Ising-LS formation from an Ising configuration, and changes in chirality.

The $\chi_H$-values obtained in designated ROIs in the array were compared to a dataset where the scan location was taken at random. The non-periodicity of the QH lattice in the MM configuration ensured that the sampled states were dissimilar for each measurement and provided a benchmark value (BMV) for stochastic formation and chirality of LSs. MFM images of the areas #1 and #2 (taken in the corner and central regions of the lattice, respectively) were analysed separately to determine a possible effect of symmetry breaking due to absence of neighbouring elements. The two ROIs and the control measurement were imaged at remanence after application of a field $B = 265$ mT where the field angle was in the range $-1.8^\circ < \beta < 0.7^\circ$. Figure 6.8c (bottom) plots $\chi_H$ against the angular difference of the field vectors between each MFM image. The grey region is

the mean BMV and expanded uncertainty ($2\sigma$) from the control dataset, $\hat{\chi}_H = 0.602 \pm 0.160$. The graph shows that the magnetic configuration in the lattice is generated deterministically as $\chi_H$ is minimal when the field angles between images are near-identical (i.e. $\beta_i - \beta_j \approx 0$). Thus, the individual NIs response is reproducible under identical field-protocols in both the transformation of Ising configuration to LSs, and the LS chirality.

In addition, there is a negligible difference in response when comparing areas #1 and #2, signaling the absence of a symmetry breaking effect. Circular data-points in Figure 6.9c specify MFM images where $\beta$ was closest to the in-plane hard-axis alignment, $-1.1° < \beta < 0.2°$, which is distinctly below the BMV region and provides a linear response as the field angle difference increases. The greatest variability between datasets occurs when $\beta_i - \beta_j \approx 1°$, which is correlated

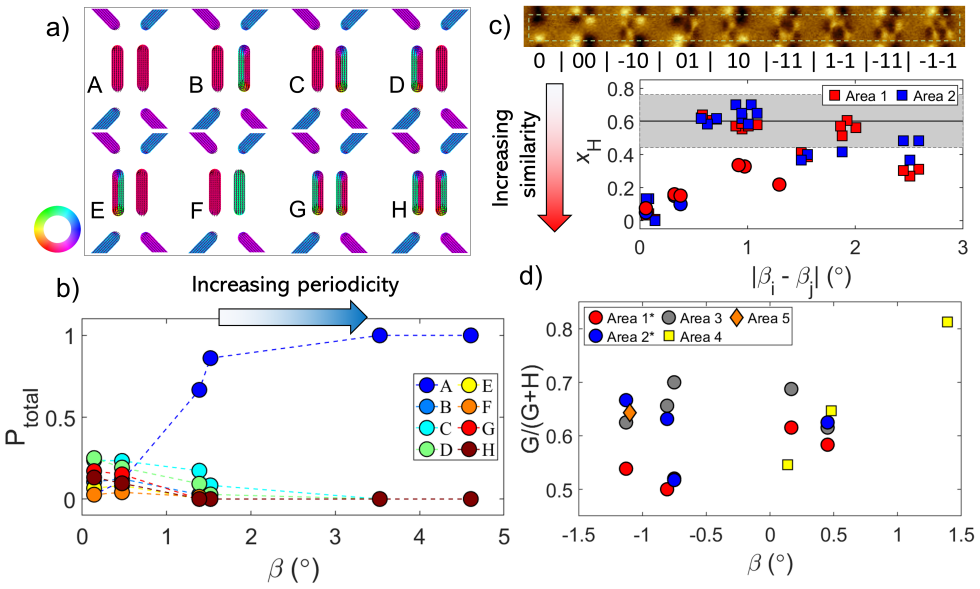


FIGURE 6.9. (a)Modelled magnetisation configuration of the paired states observed in experimental conditions. b) Population of states in (a) as a function of field angle at $B = 600$ mT. c) (top) Schematic of one line of lattice in multimodal state imaged by MFM, at remanence, after exposure to field $B = 265$ mT along the in-plane hard axis and the assigned numerical integers; (bottom) plot of Hamming distance between MFM images, $i$ and $j$, as a function of absolute difference in the applied field angle, circles are a subset of data where $\beta$ is closely aligned with the lattice in-plane hard axis ($-1.1° < \beta < 0.2°$); greyed area indicates mean and expanded uncertainty from the control dataset. d) Ratio of matching chirality in parallel NIs (state G in (a)) to total number of double-Landau states (G + H in (a)); asterisk indicates areas 1 and 2 from (c); areas-3–5 are randomized-area datasets taken at remanence after application of field with amplitude: $B = 265$ mT, $B = 600$ mT, and $B = 177$ mT, respectively. ©2020 Wiley VCH. Reprinted, with permission, from Puttock *et al.* [209]

to the steepest regions of the bell-curve in Figure 6.8b. For a field angle difference greater than $\sim 1.5°$, the Hamming value declines with increasing $\beta_i - \beta_j$, as the lattice is dominated by Ising states.

Highlighting just double LSs, the selectivity of states G and H in Figure 6.9a is demonstrated in Figure 6.9d when $\beta = \pm 1.5°$. Areas #1-2 are the areas described in Figure 6.9c; whereas Area #3 is the control dataset with randomised scan location; Areas #4-5 are additional datasets in randomized locations obtained at remanence after application of field with amplitude equal to 600 mT and 177 mT, respectively. The population frequency of G-states is independent from $\beta$ within the bounds $-1.2° < \beta < 1°$; instead, the population frequency of G-states has far greater variability (between 0.5 to 0.7) compared to the highly reproducible responses shown in Figure 6.8b-c. This dissimilarity likely stems from the favorable formation of double LSs in the coupled nanomagnets, as it is the lowest energy configuration.

To conclude the results from Figures 6.8 and 6.9, the LS state formation and chirality is highly deterministic and dependent on the applied field angle. The complex aperiodic magnetic configuration of the MM state and relative stability of the LSs in the QH lattice is a result of the magnetic environment and the lattice design, specifically in the coupled parallel NIs. In addition, the approximate parity of CW/CCW states is likely a result of balancing the energy of the extended full lattice in a highly correlated system. However, the field angle appears to have little effect on the handedness of the double chiral states in the coupled nanomagnets; contradicting the data from Figures 6.8b-c. This could be the result of the far reduced $E_{ms}$ upon formation of the double LSs, which in turn reduces the frustration at the vertex junction, and thus the influence of the nearest neighbours for a greater dispersion of chiral states.

## 6.6 Summary and Conclusion

MFM-based techniques have been used to demonstrate a violation of the 16-vertex model in ASI lattices where Ising states break down into LSs in response to a perturbation field. In the novel QH lattice the perturbation field breaks the magnetic periodicity as a coexistence of Ising and Landau states (of mixed chirality) is realised. The typically correlated system loses its long-range order as the frustration at the vertex junctions is impacted. A combination of experimental and micromagnetic modelling analysis demonstrated the LSs form in many ASI lattices. However, it is only energetically favourable in a lattice comprised of coupled NIs aligned perpendicular to the perturbation field. This has significance for other ASI/frustrated designs that are composed of ferro-/antiferromagnetically coupled elements.

A direct comparison between the micromagnetic modelling and the experimental dataset was performed through qMFM. Quantitative evaluation of the $z$-derivative of the stray-field of the QH-lattice in the three modal states were performed. The analysis showed that quantifying these values was possible, but only with relatively large correction factors due to the high susceptibility

of the Py nanostructures unfavourably interacting with the MFM probe.

It has been shown that variations in the perturbation field angle can be used to tune the ratio of both Landau-to-Ising states, and the LS chirality. These properties are shown to be deterministic and highly repeatable when the field vector is conserved. LS formation not only disrupts the otherwise highly correlated energy landscape of several frustrated ASI lattices, but controllable formation results in additional degrees of freedom for application in frustration-based logic devices.

The open question at the end of this chapter is *why* LSs favourably form despite influences from nearest-neighbour NIs and shape anisotropy, and how does the lattice deterministically compensate the presence of these states. The following chapter will aim to answer these questions by studying the same QH-ASI structures by LTEM and EH, which is sensitive to in-plane components of the sample magnetisation and extrinsic flux between the constituent NIs.

CHAPTER 7

# MAPPING THE PLANAR INTERACTIONS OF THE QUASI-HEXAGONAL ARTIFICIAL SPIN ICE LATTICE

## 7.1 Introduction

In the previous chapter, the magnetic state of the QH-ASI lattice was studied and characterised under specific field protocols by MFM and micromagnetic modelling. Although it is possible to infer the way that the islands stabilise and interact by these methods, specialised methods that can directly observe the planar coupling and domain configuration are required to truly understand the system. This chapter investigates the remanent characteristics of the NIs in the QH-ASI lattice in the different modal configurations. Quantifying the strength of interactions between the islands and flux-pathways throughout the complicated lattice provides additional insight into why the LSs form and how they are magnetostatically compensated.

The breakdown of single-domain NIs into LSs has a significant effect on the frustration of the total system as it weakens the dipolar coupling across the vertex junction and between parallel NIs. The collective properties of the lattice diminish in the MM configuration. Here, the $xy$-component of the stray-field and magnetisation (or magnetic induction) will be assessed across the junctions using Fresnel-mode LTEM and EH. These measurements were possible due to access to equipment and resources through the European Union's Horizon 2020 research and innovation programme, ESTEEM3 (823717)[1].

These two techniques provide a better understanding of the fine magnetic structure of the Ising and non-Ising states, and how the constituent components of the lattice interact. Through post-processing of the gradient in the EH images, a relative quantification of the strength of the

[1] M. Anderson, A. Masseboeuf, and E. Snoeck operated the TEM for data acquired in this chapter (CEMES/CNRS, France).

in-plane magnetic interactions is achieved. With the combination LTEM and EH, the stabilisation of the QH lattice in its modal configurations and inherent frustration can be better understood to complement the results presented in Chapter 6.

## 7.2 Unimodal configuration

Quantifying the stray-magnetic fields by MFM provides a good understanding of the magnetic charges at the poles of the NIs. However, the MFM technique is only sensitive to the stray-field derivative in the $z$-axis. From the MFM contrast of ASI we can infer the in-plane magnetisation of the Ising configurations from the sign of the isotropic poles either end of the NI. The MFM response of the LS does not provide many insights into the intrinsic flux-closure or domain configuration within the nanostructure. In addition, MFM is insensitive to the escaping in-plane flux closure between the NIs. LTEM and EH (introduced in Subsection 3.3.1) is ideally equipped to visualise these in-plane magnetic distributions with nanoscale resolution.

EH provides visualisations of the distribution of intrinsic magnetic induction within the material and any escaping demagnetisation field between structures, which provides key information about how the NIs stabilise and interact with each other at the nanoscale. To describe the relevant interactions between NIs, the terminology of vertex moments ($\mu$) and charges ($q$) will be used, as established in subsection 2.2.2. Figure A.1 in the Appendix provides a schematic of the relevant dimensions of the X and Y junction shapes.

The *in situ* field applied during the LTEM measurement is fixed normal to the imaging plane. Therefore, a double-tilt rotation stage was used for control of the applied field vector with respect to the sample plane. The stage possesses a maximum rotation angle of $\pm 60^{\circ}$, which means that in-plane field applied always has a $z$-component with respect to the sample plane. This is unlike the field protocol presented in Chapter 6. From the shape anisotropy of the Py structures it was assumed that the $\mu_0 H_z$ component to the applied field was not enough to significantly influence the final remanent state throughout the measurement sequence. In-plane hysteresis loops of a Kagomé unit cell with NI dimensions equal to those used in this study were modelled in OOMMF with and without the OOP applied field component [178]. The results (Figure A.17 in the appendix) indicated that the switching mechanism does not change with the inclusion of an OOP field, but a reduction in the switching field is observed. All images presented throughout this chapter have been taken at remanence (i.e. under no applied field) after the application of the quasi-static applied field "pulse".

Prior to imaging the QH-ASI lattice in Figure 7.1, the sample was magnetised along the $y$-direction (towards the bottom of the page) by aligning the sample such that the applied field is aligned along the $yz$-direction. An under-focused (UF) LTEM image of the QH-ASI lattice at remanence after application of the field is depicted in Figure 7.1(a), which provides a map of the NI magnetisation of the lattice to compare with EH. The lattice corner was sampled

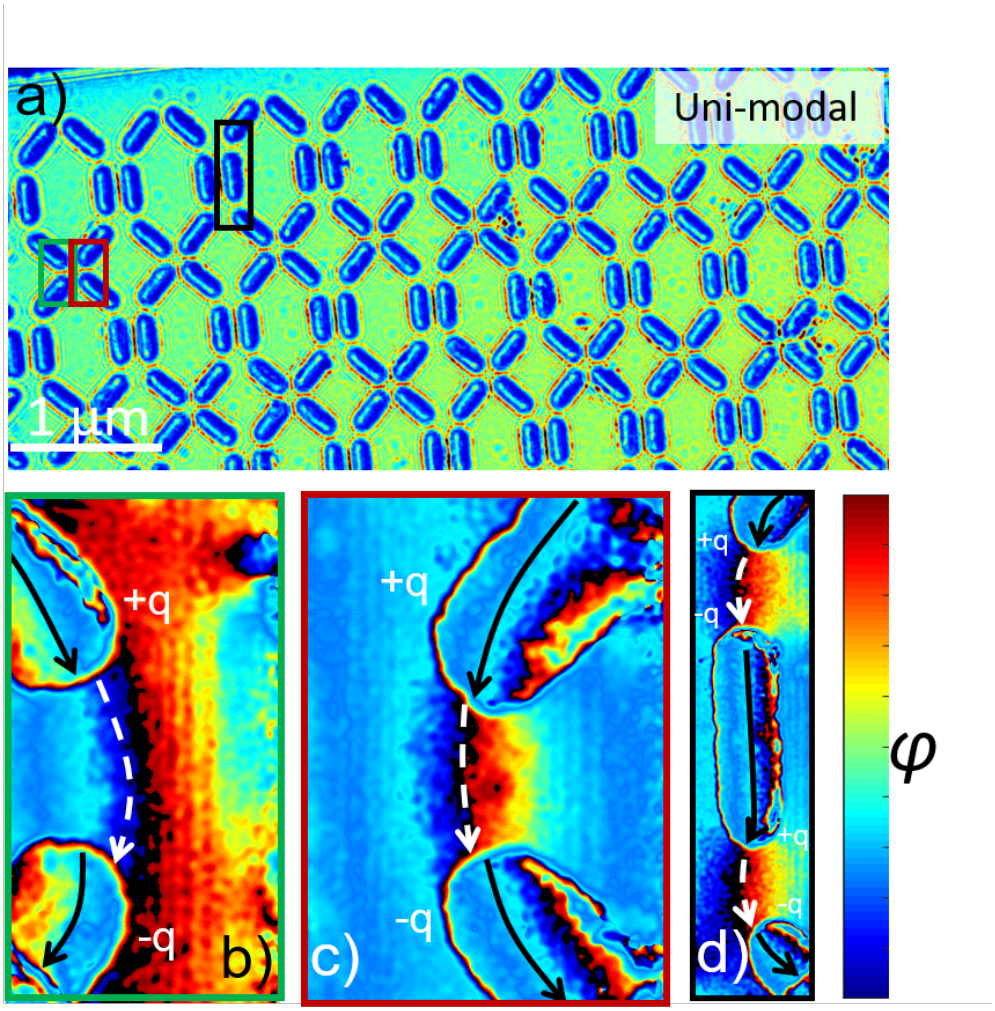


FIGURE 7.1. (a) Under-focused Lorentz TEM image of QH-ASI lattice; where vertices depicted by electron holographs (b-d) are indicated by green, red and black boxes, respectively. Arrows indicate the direction of the intrinsic (black, solid) and extrinsic (white, dashed) magnetic flux and $\pm q$ represents the vertex charge.

instead of the bulk of the lattice in order to minimise parasitic electrostatic contributions to the reconstituted signal. Internal bright-to-dark gradient along the short-axis represents a single domain magnetisation in the NI. Bright contrast on the left of the NI structures indicates that the net magnetisation is pointing down to the bottom of the page.

Figure 7.1(b-d) displays the electron holographs for three regions of interest in the remanent state (after the acquisition of the LTEM image in (a). The NI vertices in (b-d) are marked by coloured boxes on the LTEM image (red, blue and yellow, respectively). As the contrast of the phase images are relative with a rolling colour-scale, the magnetisation vector is ascertained by the gradient of the phase. The flux directions have been indicated by arrows, mapped onto

the highest-contrast trajectory where possible. EH has a limited field-of-view as it requires the overlapping of the incident and reference electron waves. In a periodic array with no disruptions, such as the one under study, this can result in a considerable parasitic shadowing effect where neighbouring NI's can impose on the interference image. The presence of this imaging artefact greatly reduced the field-of-view in this study and is particularly noticeable where NIs appear to abruptly end at the corners of images where neighbouring NI's intersect the imaging area (a visual representation of the shadowing effect is showing in Figure A.14 in the appendix). Where possible, parasitic anomalies have been cropped for the ease of representing the relevant data.

The holographs in Figure 7.1 demonstrate the expected single-domain configuration within the NIs, with $\mu$ aligned along the $y$-axis of the lattice. The $C/S$-shaped bending of the magnetisation at the ends of the NIs is apparent in the images due to the inter-island coupling between poles of opposite charge [94]. The solid-black arrows highlight this by mapping the contrast lines of the internal induction. The colour contrast outside of the NI topography represents the in-plane escaping stray-field from the NIs, where a strong interaction occurs between the two closest NIs of opposite vertex magnitude (b-c) (dashed, white arrows). Figure 7.1(d) is a holograph of half of the Y/rY junction, also showing the strongest interactions occur between nearest-neighbour NIs. This is consistent with a micromagnetic model of the stray-field of an X-shaped junction provided in Figure 2.10 in Chapter 2.

Figure 7.2(a-c) presents the Figures 7.1(b-d) as flux images, respectively. They were constructed by applying a cosine function on the magnetic phase-shift image. These images reveal

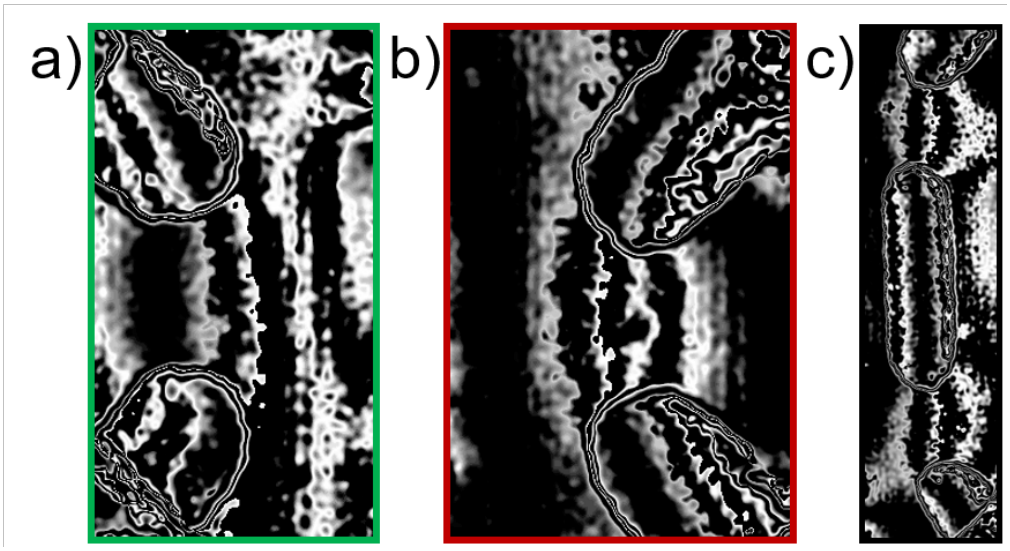


FIGURE 7.2. Magnetic flux images in the UM state reconstructed from figures 7.1b-d (a-c, respectively) with amplification factor ×15. Direction of flux-lines indicates stray-field coupling direction and the quantity of lines is representative of the field-strength coupling.

the flux-pathway both between magnetic islands (i.e. flux closure routes) as well as the internal flux of the nanostructures. It is common to amplify the phase image by a multiplication factor in order to increase the number of flux-lines and consequently improve the representation of the data. The flux-images throughout this section use the same amplification factor of $\times 15$, which means the number of flux lines per unit area are a qualitative measure of the flux-strength, and can be compared between images. In Figure 7.2 the curling of the magnetisation at the NI apexes is clearer and flux line densities between images are comparable. The extrinsic flux is minimised resulting in the high internal flux density as shown in Figure 7.2a-c.

## 7.3 Bimodal configuration

Prior to obtaining the LTEM/EH images displayed in Figure 7.3, $\mu_0 H_T = 122$ mT was applied at 20° from the surface plane along the $xz$-axis ($\mu_0 H_\parallel = 42$ mT, $\mu_0 H_\perp = 114.6$ mT) to generate the BM state. Figure 7.3 represents the magnetic phase contrast of the same region of the lattice, as displayed in the previous section, under zero-field. The colour-coded regions in the LTEM image of Figure 7.3a are visualised in the respectively holographs (b-g). Holographs in Figure 7.3 have also been spatially represented in Figure A.15 in the Appendix. Comparing the LTEM images of Figures 7.1(a) and 7.3(a), it is clear that the magnetisation has switched to form the same BM state as described throughout Chapter 6.

All holographs in Figure 7.3 show that the extrinsic stray-field has a clear $x$-component pointing towards the right-hand side of the image due to the reconfigured vertex charges. There is also a historic $y$-component towards the bottom of the image in the coupled NIs from the initial magnetic configuration as outlined in the Section 7.2.

Figure 7.3(b) depicts an X-shaped junction that shows the internal magnetisation of the interacting NIs as single-domain; matching the other experimental data-sets throughout Chapter 6. The external flux profile in this image travels across this particular junction, resulting in a high energy metastable state as the strongest contrast runs from the top-left NI to the bottom right. *A priori*, the ground-state flux-closure would be expected to resemble that seen in Figure 7.3(c) and follows $\mu$ between nearest neighbours. As a result of this metastable flux-closure, the NIs (bottom left and top right) appear to be shielded from interacting at the junction resulting in strong internal phase contrast at the NI vertices. The corresponding flux-image in Figure 7.4(a) shows that the uncompensated NIs (top-right and bottom-left) have considerable curling of the magnetisation at the NI vertices, highly deviated from a macro-spin Ising assumption.

Figures 7.3(d-g) present the phase images focused on the Y/rY vertex interactions, which also display both $x$- and $y$-components to the magnetisation vector at remanence. Figure 7.3(c) shows very clearly the net component of the escaping flux follows the same meta-stable trajectory and the flux closure in Figure7.3(b), i.e. across the junction rather than between nearest neighbours. The net moment of the Y junction (top) in the $T_3$ energy state skews to the bottom right of the

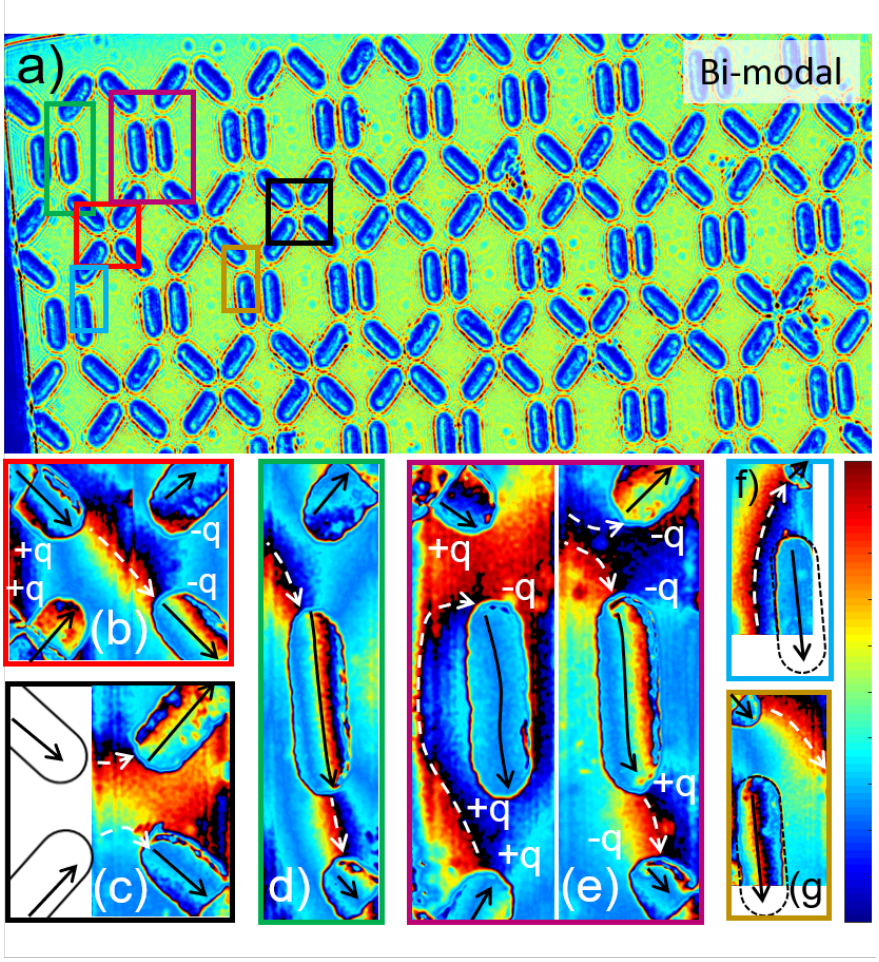


FIGURE 7.3. (a) LTEM image of the QH-ASI lattice in BM configuration; where vertices depicted by electron holographs (b-f) are indicated by red, black, blue, green and magenta boxes, respectively. Arrows indicate the direction of the intrinsic (black, solid) and escaping (white, dashed) magnetic flux. Images (b,c and e) comprise of spliced images to provide a better understanding of total flux at junctions, however direct comparison of colour between images is not precise.

image, breaking the vertex symmetry. Equally this is reciprocated in the rY (bottom) junction where the net charge at the $T_3$ vertex is inverted ($Q = -2q$). This net $\mu$ direction in the Y/rY junctions may influence the adjacent X-shaped junction behaviour in Figure 7.3(b), providing an explanation for the flux-lines are no longer passing between nearest neighbours.

Figure 7.3(e-f) gives two examples of interesting high-energy flux-closure that opposes the direction of the net magnetisation in the Y-shaped vertices. Here, the flux follows a trajectory directed towards the top-right of the respective images. For example, the flux escaping from the bottom left-side of Figure 7.3(e) bends around the $y$-oriented NI to terminate at the top-apex, rather than between the nearest vertex of opposite charge. The related flux image in Figure 7.4(d)

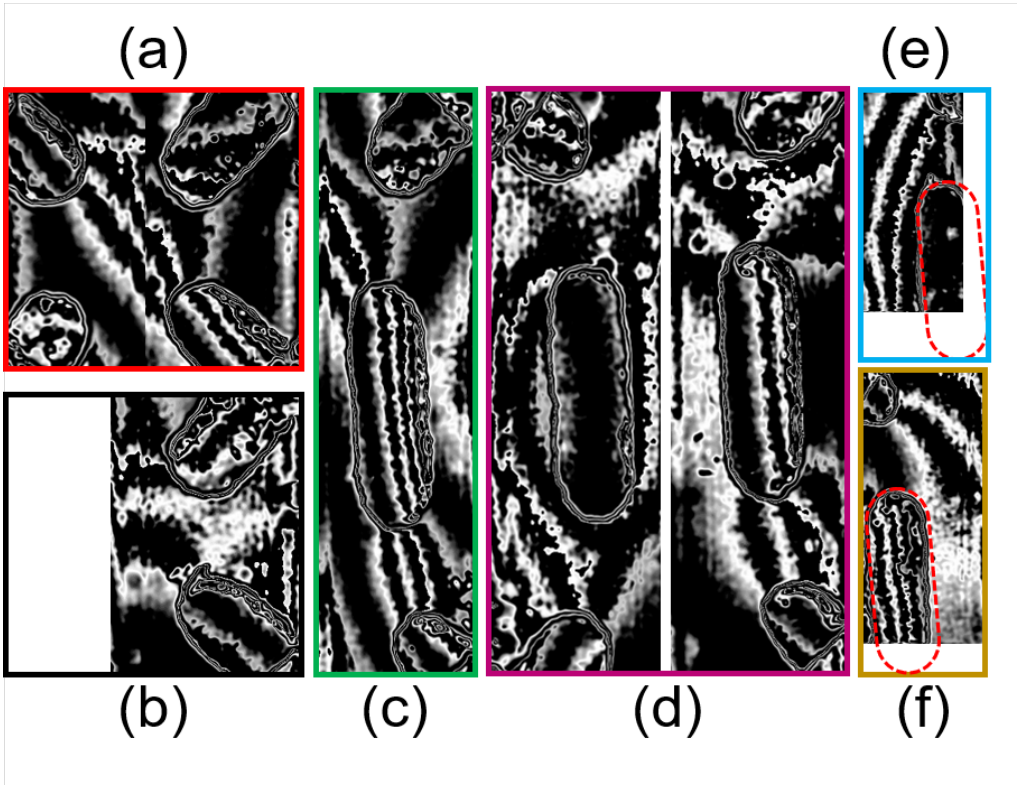


FIGURE 7.4. Magnetic flux images of the BM state reconstructed from figures 7.3b-g (a-f, respectively) with amplification factor ×15.

shows a far reduced internal flux in the left-sided $y$-oriented NI compared to the others. This effect is also apparent n the right-sided $y$-orientated NI in Figure 7.4e. This reduced internal flux is likely the result of the curl of the flux around the outside of structure (e.g. on the left of Figure 7.4(d)). This is unlike the island on its right, where the flux clearly passes through the inside of the NI.

## 7.4 Multimodal configuration

Figure 7.5 presents the UF-LTEM image (a) and respective electron holographs (b-h) of the Y/rY vertices in the MM configuration. The field pulse applied here was $\mu_0 H_T = 366$ mT 20° from the surface plane along the $xz$-axis ($\mu_0 H_\parallel = 125$ mT, $\mu_0 H_\perp = 344$ mT).

It is clear from the internal contrast of the EH images that the magnetisation in some of the structures is no longer Ising-like by the strong contrast in the NI centre. This strong contrast represents the formation of a DW inside the NI. This is also seen in the LTEM image in Figure 7.5(a) where the bright contrast of some islands is concentrated in the centre of the nanostructure. A clearer depiction of the different response of Ising and non Ising states in LTEM image is

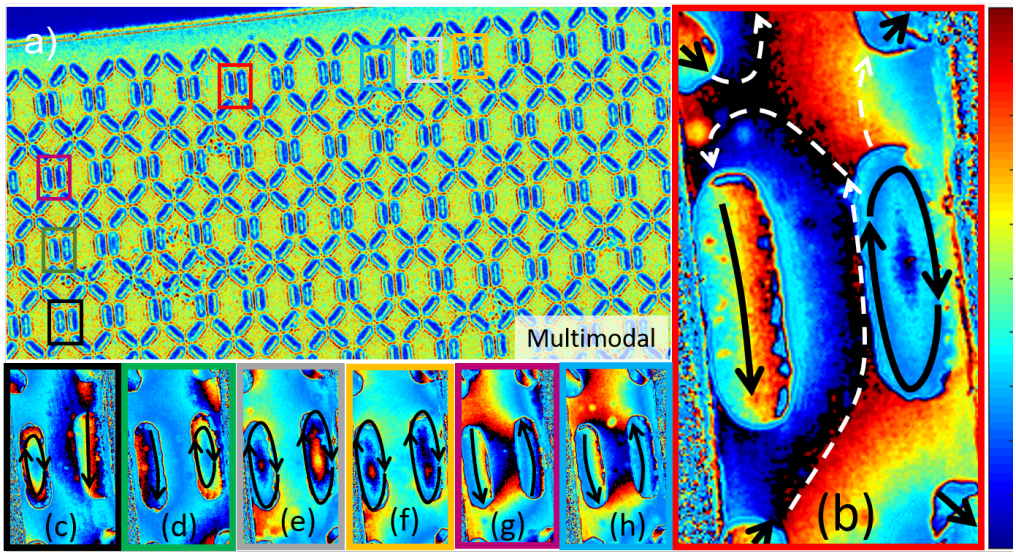


FIGURE 7.5. (a) LTEM image of the QH-ASI lattice in MM configuration. Electron holographs of the Y/rY vertex junctions of the QH-lattice in the MM state, where some NI's have broken down into non-Ising states. (b-d) represent the junctions where one NI has broken down into a non-Ising state, whereas the other parallel NI remains single-domain; (e-f) present double non-Ising states; and (g-h) presents the junction with antiparallel Ising NIs.

shown in Figure A.16 in the Appendix.

Figure 7.5(b) displays the Y/rY vertex junctions where the right-hand NI has broken down into the non-Ising state, creating an Ising/non-Ising pair. It is clear from the contrast that there is a cyclic component to the magnetisation inside of the NI around a central position, highlighted by the black arrows. This is even clearer in the corresponding flux image (Figure 7.6(a)).

There is a highly complex and strong coupling between neighbouring NIs in the holograph in Figure 7.5(b), particularly at the non-Ising NI apexes where the magnetisation has the greatest degree of divergence. As noted in the previous section, the flux does not pass through the NI in the LS, resulting in a reduction in signal magnitude compared to the double non-Ising states in Figure 7.5(e-f). Line-profiles through different NIs show this as a reduced gradient in Figure 7.7). This flux characteristic is also seen to a lesser extent in Figure 7.5(c-d) and in the corresponding flux images in Figure 7.6(b-c). These images also depict Ising/non-Ising pairs in the parallel NIs.

The holographs for the double non-Ising states (Figures 7.5(e-f)), and respective flux images (Figures 7.6(d-e)), indicate considerably less interaction between NIs and strong internal contrast. The flux is almost completely internalised in the parallel NI's with minimal coupling between neighbouring islands. This suggests that there is an effective quench in the frustration at the vertices and NIs across the junction are no longer coupled when the parallel NIs are in the magnetic state. The antiparallel Ising states in Figure 7.5(g-h) instead possess strong inter-island

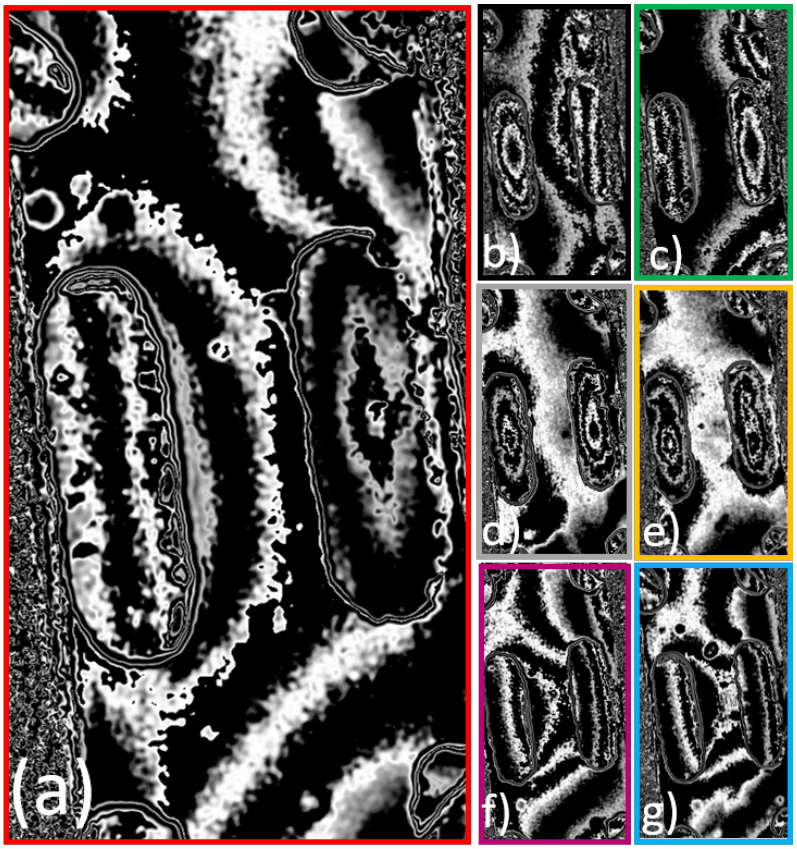


FIGURE 7.6. Magnetic flux images in MM configuration reconstructed from figures 7.5b-h (a-g, respectively) with amplification factor ×15.

coupling between themselves with a some interaction between neighbouring NIs in the junction. What is surprising is the similarity of the external flux profiles for the Ising/non-Ising pairs in (b-d) and the antiparallel pairs in (g-h), providing some understanding as to why it is favourable to form a plethora of magnetic states.

## 7.5 Summary and Conclusion

This chapter directly probed the $xy$-component of the magnetic induction of NIs in the lattice by LTEM and EH, to further complement the results presented in Chapter 6. Expected flux pathways were observed for the QH-ASI lattice in the UM state, where the flux closure follows the magnetisation and extrinsic flux is closed between nearest neighbours in the lattice. However, the BM and MM states are far more complex as a number of different flux-closing pathways are seen to exist across the lattice.

The historic effects of the initial saturation in the $\pm y$-direction results in the promotion

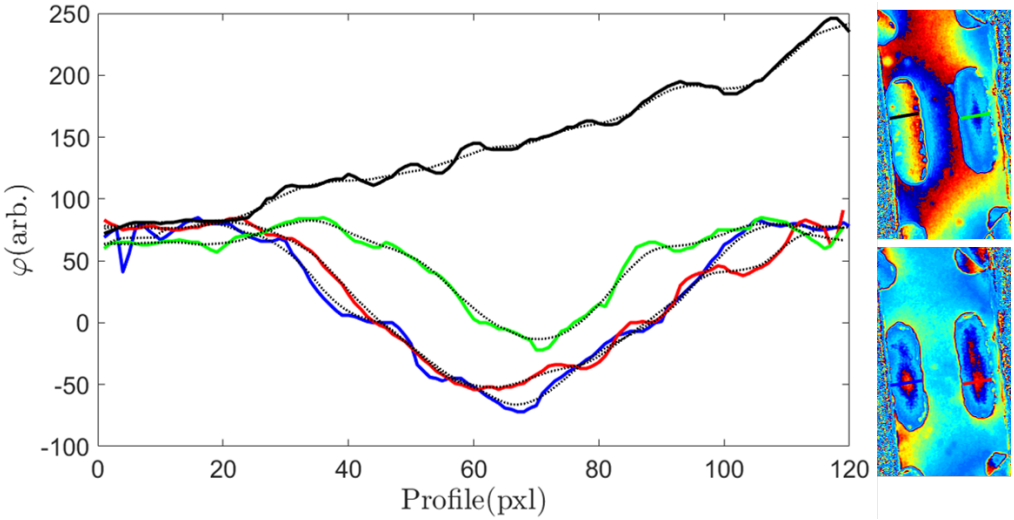


FIGURE 7.7. Line profiles through the electron holographs depicted in Figure 7.5b and f. Dashed lines represent five-point moving averages.

of local minima at remanence where the external flux closure pathways do not pass between obvious nearest-neighbour vertices. Seemingly at random, NIs do not internalise the flux-pathway resulting in a dispersion of both internal and external flux across the lattice. This mix of flux-closure states opposes the apparent periodicity of the lattice magnetisation in the BM state as described in Chapter 6. This dispersion may explain the non-uniform LS distribution in the MM configuration.

In the MM configuration, both the internal domain structure and the way the LSs are stabilised through interaction with surrounding NIs in the lattice are now better understood through EH. The internal flux of the chiral states show the magnetisation curls around a shape of the NI geometry, rather than break-down into clearly defined multi-domain states. The formation of LSs and their chirality is a result of the local energy minimisation and a compensation of the surrounding environment, which explains the loss of periodicity in the lattice described in the previous chapter. The degree of flux-internalisation in LSs is also inhomogeneous across the lattice, as with some of the Ising NIs in the BM state.

CHAPTER 8

# DEFECT DYNAMICS WITHIN ARTIFICIAL SPIN ICE SYSTEMS

## 8.1 Introduction

In the QH-ASI structure it is evident that the strong inter-island coupling between NIs results in behavioural changes in the lattice from the magnetostatic interaction. Upon breaking the periodicity of the lattice through formation of non-Ising defects the collective behaviour of the lattice changes from a geometrically frustrated lattice into a far more complex configuration.

Defects in systems are a frequent consequence of a world governed by thermodynamics. For example, crystals are particularly prone to point defects (e.g. vacancies and interstitial defects), line defects (e.g. topological edge dislocations) and plane defects (e.g. grain boundaries) [213–215]. Defects can also refer to particulates or material seeds that act as nuclei during the nucleation step of crystallisation. The presence of defects often have significant effects on the material properties of a crystal, which sometimes results in a refinement of desired structural or physical properties (e.g. ice growth [216]).

One example is the influence of defects on a otherwise pristine "real" 3D spin ice as they can impact, single-monopole detection; the observation of monopole currents; and therefore the design of potential spin ice devices [217, 218]. For example, "stuffed" spin ice refers to the substitution of non-magnetic $M^{4+}$ ions for magnetic rare-earth ions $R^{3+}$ into a pristine lattice, where oxide ions are lost to conserve the charge [217, 219, 220]. Revell *et al.* [221] demonstrated that stuffing the lattice resulted in the inclusion of slow dynamics that are more typically associated with disordered systems. These were explained through Monte Carlo simulations as the result of the attraction of existing monopoles to the defect site and an increase in the number of monopoles created adjacent to it. Similarly, Aldus *et al.* [220] noted that stuffing spin ice resulted in a loss of

the long-range ice rule correlation, but remain ice-like of shorter length-scales.

As discussed in Chapter 2, ASI can be used to experimentally model crystallographic phenomena by lithographically defining defects [50]. Drisko *et al.* [222] for example investigated structural dislocations in square ASI. When thermalised, a chain of higher-energy states propagate from the defect location disrupting the antiferromagnetic $T_1$ ground-state ordering. Interestingly, the chain from the defect always terminated either at the site of another topological defect or at the edge of the array, separating the lattice into domains of low-energy states with a higher energy wall between them. This behaviour when defects are imposed onto a continuous lattice had been predicted in theory, showing a convergence between experiment and simulation [223, 224]. This branch of research poses an interesting question around the role of defects in controlling the collective dynamics of the ASI lattice; DW propagation pathways; and how defect-driven systems apply to ASI technologies.

In this chapter, a hybrid lattice is proposed that combines the Kagomé lattice with an artificial magnetic defect fabricated into the lattice centre. The magnetic defect maintains the structural topology of the lattice, resulting in a triangular defect with honeycomb-shaped edges. Its large magnetic volume and many lattice interfaces make it an interesting system to study how a magnetic clustered defect may influence the local magnetic response upon excitation with applied field.

Here, both connected and disconnected lattices are investigated. The complex interplay between the defect and the connected Kagomé lattice is understood by MFM under increasing applied field. The shape anisotropy of the MFM probe means its own magnetisation is unperturbed by the Zeeman field below a threshold, but the technique may only be used in the low-field regime. Therefore, the results of the MFM study are complemented with micromagnetic modelling and LTEM[1] of an equivalent disconnected lattice to understand defect driven magnetisation dynamics in the Kagomé lattice.

## 8.2 Defect-ASI design

A schematic of the defect in a connected Kagomé lattice is displayed in Figure 8.1. The lattice and defect are fabricated from Py with thickness $t$ = 20 nm. The defect is triangular with honeycomb-shaped edges to avoid topological disruption to the lattice structure [222]. In the connected lattice, the defect is 4.22$\mu$m in length and 2.48$\mu$m in width about its centre. The defect is surrounded by the Kagomé ASI lattice, which extends to $\sim 50 \times 50\mu$m total lattice area. Each nanowire is 1.35$\mu$m$\times$0.1$\mu$m in length and width, respectively. The dimensions of the nanowires in the disconnected lattice are reduced to 0.38$\mu$m$\times$0.1$\mu$m, thus the defect is also reduced in size proportionally to 2.95$\mu$m$\times$1.73$\mu$m. For comparison, vacant defects were also fabricated where the

[1]Measurements made possible through access to equipment and resources through ESTEEM3, measurements performed by C. Gatel (CEMES France).

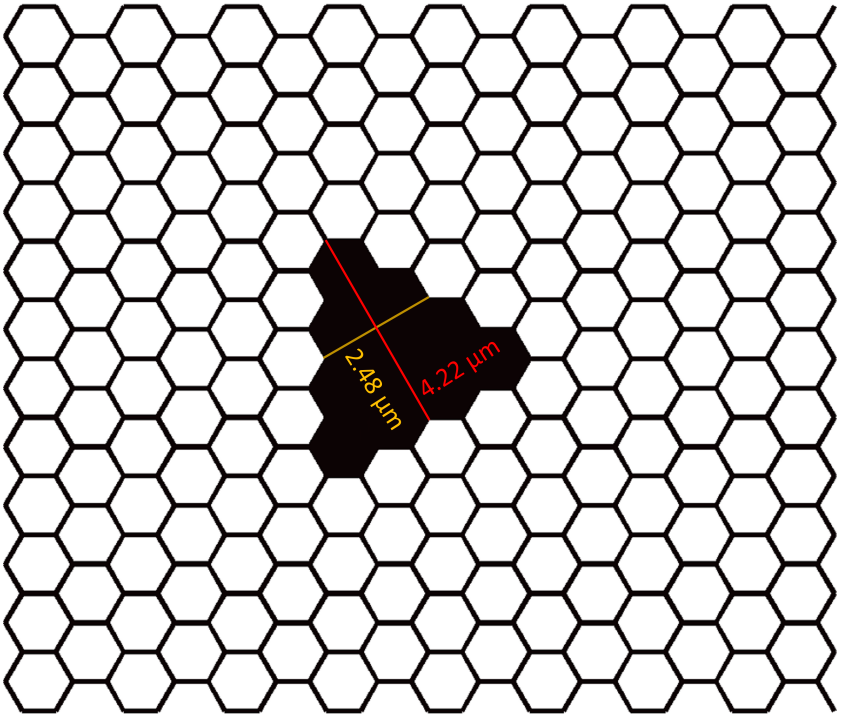


FIGURE 8.1. Schematic of defect-ASI with length and width of the defect indicated in red and yellow, respectively; nanowires are 1.35$\mu$m×0.1$\mu$m in length and width, respectively.

vertices inside the defect area have been removed, but have not been filled with ferromagnetic material.

Connected structures were fabricated on Si/$SiO_x$ by methods described in Section 3.4. A small lithographic "zig-zag" defect was present on the defect on Si/$SiO_x$ substrate (see AFM image in Figure 8.2b). However, it does not effect the interfacial coupling between the defect and the lattice. Disconnected structures were fabricated on thin SiN TEM membranes ($t$ = 20 nm) for LTEM measurements, fabrication of these samples is also described in Section 3.4. The structural artefact was not present in the disconnected array.

The solid defect is also composed of Py, which is a soft magnetic material and has very little magnetic anisotropy compared to the nanowires and NIs in the connected and disconnected lattices. Thus, the susceptibility of the defect is much weaker than the surrounding lattice and saturates at far lower field magnitude. Therefore, the defect can act as a DW nucleation pad that can inject DWs into the surrounding lattice through several defect-lattice interfaces (i.e. the corners of the honeycomb edges) [225, 226].

In a pristine connected Kagomé lattice, the switching cascades will usually begin at the lattice edges, forming the emergent monopole, and propagate through the structure before terminating at another edge or annihilating with another monopole of inverse charge. As a result of the high

exchange coupling between the vertices in the connected Py lattice, and the unfavourable energy cost of hosting a monopole on any vertex, it proves difficult to map the DW propagation events within the field-of-view of many imaging techniques. Thus a direct comparison with disconnected structures, which have a far reduced exchange energy at the vertices, is required to aid in the interpretation of the results. A discussion of the credibility of this is outlined in Section 2.2.3.

## 8.3 Domain wall injection into connected defect-ASI lattice

Figure 8.2a presents the ($15 \times 15\mu$m) MFM micrographs under a field application measurement sequence of the connected defect-ASI. Digitally sharpened MFM images of the interface between the left-most apex of the defect and surrounding nanowires are inset in each respective micrograph. The respective topography is displayed in the AFM micrograph in Figure 8.2b, which shows a zig-zag shaped fabrication deformity on the right-side. The zig-zag deformity can act as a pinning site under the field reversal and affect the domain configuration. As a result, it could reduce the strength of interaction between the triangular defect and the ASI lattice along this interface.

To obtain the initial state Figure 8.2a(i), the lattice was saturated with a field applied along the $x$-axis (along the one of three possible easy-axes of the lattice/defect system) such that all the spins are net-aligned towards the right of the image. Light contrast indicates a negative vertex charge (i.e. $-q$), and the inverse for the dark contrast (i.e. $+q$). This alternating pattern where each vertex charge is shielded by nearest neighbours of inverse charge is a low energy configuration of the lattice. The magnetisation remain aligned along the easy axis of the nanowires from the shape anisotropy with a net alignment along the initial field direction. From the much larger size of the defect and reduced shape anisotropy the magnetisation forms a "leaf-like" multi-domain structure.

The following sequence of images (Figure 8.2a(ii-vi)) are micrographs at the stated fields applied in the direction opposite from the initial saturation direction. Figure 8.2a(ii) shows no change to the magnetic contrast in the lattice at $\mu_0 H = 3$ mT, whereas the defect has reconfigured to a new multi-domain state where the domains most aligned with the field direction have grown. The zig-zag deformity appears to have impacted on the domain contrast on the right-side, where DWs are pinned between the fabrication defect apices and the apices at the edge of the structure.

Under increasing field ($\mu_0 H = 7$ mT, Figure 8.2a(iii)), a DW was injected into the ASI vertex neighbouring the defect on the left-side (blue circle #1). This has formed an emergent monopole in the connected vertex ($\Delta Q = +2q$) that is stabilised by the almost saturated defect. The increased contrast in the image and the line profile in Figure 8.2c reveals this is the ice-rule forbidden $+3q$ state where three head-to-head vertices are pinned at the vertex.

Under increasing field increments, Figure 8.2a(iv-v), the emergent monopole remains pinned at the same location, whilst the defect is now saturated along the direction of the applied

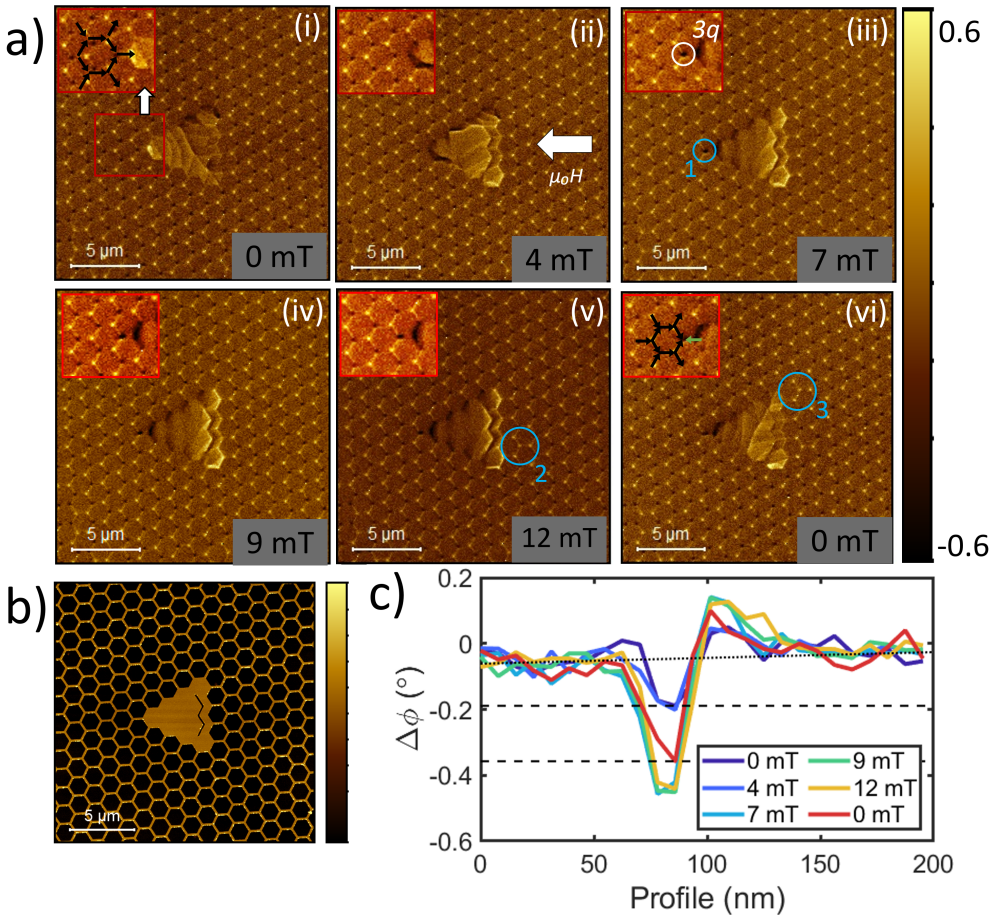


FIGURE 8.2. (a) *in situ* MFM micrographs of the defect ASI lattice at set field magnitudes applied in the direction to the left of the page; blue circles indicate switching events; inset: enhanced MFM images of the defect/ASI interface in highlighted red box. (b) AFM micrograph of Defect-ASI lattice corresponding to MFM images. (c) 200 nm 3-pixel averaged line profiles through the vertex of interest at each field application for a(i-vi); dashed lines indicate MFM contrast minima at $\mu_0 H = 0$ mT before and after field was applied.

field, although some domain contrast remains at the site of the zig-zag deformity. At $\mu_0 H = 12$ mT (Figure 8.2a(v)), further DW injection forms an emergent monopole of the inverse charge ($\Delta Q = -2q$) at the interface of the right-side of the defect and the lattice (blue circle, #2). The rest of the lattice remains unperturbed.

The final MFM micrograph in Figure 8.2a(vi) displays the lattice once again at remanence under zero-field. The reduction of Zeeman energy results in the return of a leaf-like domain pattern in the defect. It is rotated 60° to align along the previous field direction. One additional switching event is highlighted on the right-side of the defect (blue circle #3), which has resulted from the reconfiguration of the defect magnetisation. All three monopole defects (#1-3) are

conserved in the lattice at remanence. The formation of emergent monopoles #2-3 on the right-side of the defect shows that the zig-zag deformity has not significantly impeded the nucleation-sites on this side.

Line profiles were drawn through the high-energy vertex #1 at each field increment (Figure 8.2c), which show the $+3q$ energy state has been conserved after the field is released. A small reduction in contrast at $\mu_0 H = 12mT$ and $\mu_0 H = 0mT$ has arisen from the reduction of Zeeman energy on the vertex. A comparison of the line-profiles before and after the measurement sequence (purple and red, respectively) shows an approximate $\times 2$ signal contrast enhancement. Although a significant increase in signal, this is less than the expected $\times 3$ signal enhancement for a vertex changing from $+q$ to $+3q$ [55]. This reduction in contrast may be from an undesired probe-sample interaction resulting in an underestimation of the signal contrast when the probe is over the high-contrast vertex (e.g. as was seen in Chapter 6.

The micrographs in Figure 8.2 show that the defect acts as a monopole nucleation site at reduced applied field compared to the rest of the Kagomé lattice. This is a result of DW injection on the left and right sides faces of the defect. It is interesting that this emergent monopole is bound to the defect interface rather than forming a free moving monopole-antimonopole pair as is common in ASI [31, 55]. Low-energy formation and propagation of a magnetic charge through a complex lattice, with positional control, is lucrative in spintronic applications [31, 47, 227].

The high energy vertex ($+3q$) is also seemingly fixed at the vertex adjacent to the defect. As stated in Section 2.2.3, it is energetically inexpensive to move the monopoles throughout the lattice as the vertices that are incorporated into the string pathway are energetically equivalent to the surrounding lattice (providing the ice-rule is predominantly conserved). Due to this, further spin flips result in non-determinate Dirac string lengths and pathways between a monopole-antimonopole pair [25]. It is therefore assumed that there is considerable pinning that prevents propagation of the $3q$ and termination at the lattice edge. This pinning could be overcome by adapting the Kagomé vertex shape [228].

The results from *in situ* MFM were further compared to micromagnetic modelling (OOMMF) of the defect-ASI lattice. The measurement sequence was expanded to include a higher field regime where defect independent magnetic reversal in the lattice is also observed. The constituent dimensions have been conserved in the model but the array size was reduced to $16.76\mu$m $\times 14.46\mu$m, i.e. as displayed in Figure 8.1. The zig-zag deformity in the nanostructure has been omitted from the modelling for the sake of simplicity.

The magnetic parameters of Py were used for the micromagnetic modelling were $M_s = 800 \times 10^3$ A/m and $J_{ex} = 13 \times 10^{-12}$ J/m, and the mesh was comprised of $4 \times 4$ nm cells so to properly resolve the features of the nanowires and below the exchange length $l_{ex} \approx \sqrt{2A/(\mu_0 M_s^2)} \approx 5.7$ nm [229].

Figure 8.3a-g displays the magnetisation maps of the modelled Defect-ASI lattice throughout half of a hysteresis loop where colour is representative of the magnetisation direction with respect

to the $x$-axis as shown in the colour-wheel. The modelled $m_x$ and $m_y$ components are plotted as a function of the full field sweep in Figure A.8 in the Appendix, which shows the defect-ASI lattice exhibits field reversal symmetry. The initial state of the defect-ASI lattice is from a point of saturation along the $x$-axis in the direction to the left of the image with an applied field $\mu_0 H_x = 200$ mT).

The results of the modelling are displayed in Figure 8.3. At $\mu_0 H_x = -5$ mT, the energy contribution from the Zeeman field is minimal and the the defect magnetisation collapses into a multi-domain state while the magnetisation in the remainder of the lattice is unperturbed (Figure 8.3a). Application of higher field, $\mu_0 H_x = -15$ mT, disrupts the defect magnetisation to be mostly saturated along the field direction. This is shown in Figure 8.3b.

Figure 8.3c-d demonstrates the first set of nanowires switching under applied field $\mu_0 H_x = -19$

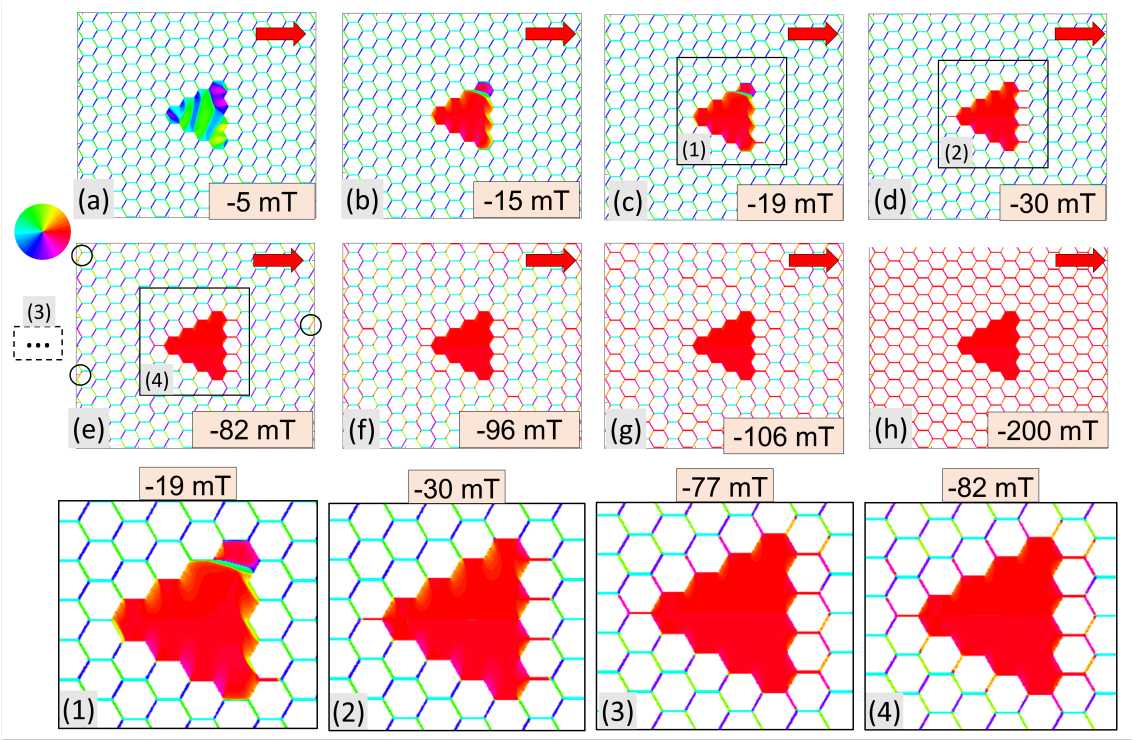


FIGURE 8.3. Magnetisation maps of the defect-ASI along half of a hysteresis loop where the field is swept along the $x$-axis, the magnitude and field direction is shown in each image. The initial state is saturated in the positive direction ($\mu_0 H = 200$ mT); the field is subsequently swept through zero-field and applied in the opposite direction (a-g) until saturated along the opposite direction to the initial state (h). Circles on (e) show the first defect-independent magnetisation-reversal starting at the edges. Boxes 1-4 are zoomed-in magnetisation maps of the defect and immediately surrounding lattice as the defect-driven reversal takes place ($\mu_0 H = -19$, $-30$, $-77$ and $-82$ mT, respectively).

and $\mu_0 H_x = -30$ mT, respectively, at the defect-lattice interface. This modelled dataset nicely complements the MFM observations from Figure 8.2 where the DWs between the defect and the nanowires are injected into the surrounding lattice and pinned at the nearest-neighbour vertices. A magnification of the magnetisation maps at the defect-site under the applied fields stated are shown in boxes #1-2.

Between $\mu_0 H_x = -30$ and $\mu_0 H_x = -82$ mT the defect-adjacent islands continue to switch expanding the length of the strings 2-3 vertices away from the defect (Figure 8.3, box #3). The nanowires north of the defect that are not oriented along the field direction switch, whilst the macro-spins to the south of the defect are fixed in the original saturation direction.

At $\mu_0 H_x = -82$ mT (Figure 8.3e, and box #4) the first nanowires away from the defect switch at the discontinuous edges of the lattice (black circles). This is the typical process initiating the start of the magnetic reversal event in an ASI lattice from the reduced geometric frustration at the lattice edges. Above this field, a typical avalanche of cascading switching events occurs throughout the lattice (Figures 8.3f-g) to the point of full saturation in the inverse direction to the initial state, depicted in Figure 8.3h.

The modelling has expanded upon the MFM dataset to show that there is a large field window where the DWs injected into the lattice at the defect site are able to exist and propagate. These monopole defects do not appear to freely propagate far away from the defect until the critical switching field of the lattice is reached. This bears some resemblance to the observation in stuffed spin ice discussed in the introduction of this chapter, which also noted an increase in the number of monopoles created next to the defect in Monte Carlo simulations [221].

The micromagnetic modelling in Figure 8.3 also reveals an asymmetry of switching in the wires adjacent to the defect that are not orientated parallel to the applied field (Figure 8.3, boxes 3 and 4), when it would be expected that this would be simultaneous (when controlling for field angle misalignment). Those adjacent wires that do not switch (south of the defect) instead switch at the same fields as the remainder of the lattice, i.e. inconsequential of the defect. This observation will be explored further in the following section.

Once the defect-independent magnetic reversal mechanism starts in the ASI lattice, it becomes difficult to track the path of the defect-bound monopoles, particularly by MFM. This is because of the sheer number of reversal events occurring throughout the MFM image, in addition to complications with annihilation events where two strings combine and the near random pathways the field reversal mechanism can undertake. It is also far easier for the DW to propagate through a connected lattice from the high coupling between arms across the vertices. Thus, the remainder of the chapter will investigate the same lattice design formed of disconnected nanoelements. The reduced coupling from increasing the vertex spacing in the lattice results in a slower propagation, which in turn will enable the tracking of defect-driven effective monopole propagation by imaging techniques.

## 8.4 Magnetic reversal in disconnected Defect-ASI lattice by LTEM

### 8.4.1 Visual representation of magnetic reversal mechanism for defect-ASI

LTEM was used to provide stepwise mapping of the defect-driven propagation events in the disconnected lattice on transparent TEM membranes. This method was preferred to an MFM study is threefold: (1) the sample rate of LTEM is far greater than MFM, with an additional higher sensitivity to deviations in the in-plane magnetisation of the nanostructures under study; (2) MFM is less reliable at higher applied fields as the magnetisation of the probe can be perturbed. Although, it would be possible to apply a field and image at remanence (as was performed in Chapter 6) the domain formation in the defect upon relaxing the field could result in additional switching events as was seen between Figures 8.2a(v-vi); (3) and the LTEM method used in this section includes a very accurate $xy$-drift correction system that is of high importance for the differential analysis method described from herein.

The LTEM instrumental set-up is described in Section 3.3.1 in the Methods. A double-tilt sample stage was used to enable rotation of the sample away from the $z$-plane to provide the in-plane component to the applied field relative to the sample. For reference, the schematic in Figure A.13 in the Appendix details the coordinate system of the field application. However, the methodology differs from those performed in Chapter 7 as the images were rapidly acquired as a function of tilt away from the $z$-plane under a constant field. This gives the effect of gradually increasing the in-plane component of the field, thus the magnetisation of the lattice is imaged as a function of in-plane field (step-size $\mu_0 H_\parallel \sim 1$ mT).

The LTEM method does come with its own complications: #1 Larger in-plane fields are a consequence of tilting away from the imaging plane, which can obscure the magnetic contrast in the image; #2 the field component perpendicular to the sample plane ($\mu_0 H_\perp$) is present. Both of these limitations are overcome by using a large incident field $\mu_0 H_{\text{tot}} = 488$ mT, which allows relatively minimal tilt from the imaging plane for the $\mu_0 H_\parallel$ component and a near constant $\mu_0 H_\perp$ component acting on the sample. The data presented in this section are all within $\pm 2°$ from the image plane, which places the OOP component within the bounds of $487.7 \leq \mu_0 H_\perp \leq 488$ mT. OOMMF modelling with and without a large $z$-component to the applied field (Figure A.17 in the Appendix) revealed a small reduction in the switching field of the NIs in the Kagomé lattice. However, it was not large enough to saturate the NIs OOP and no change in the switching mechanism was seen. For simplicity, the following results will be discussed in terms of the in-plane applied field ($\mu_0 H_\parallel$).

A key for interpreting the differential LTEM images is shown in Figure 8.4. For each dataset, the lattice starts saturated in the opposite direction of the field-sweep. In the measurement sequence the field is swept up to $\mu_0 H_\parallel \approx \pm 50$ mT. The following figures summarise the most interesting switching events by shading the NIs in a colour indicative of their switching field in

the measurement sequence. This shading is limited to seven field values for readability. Solid shading of the NI indicates a magnetisation reversal in that island.

Figure 8.4a demonstrates the propagation of a monopole that was injected into the lattice at the defect site. The white circle represents the negatively charged effective monopole according to the key provided in Figure 8.4d. It propagates from the defect-lattice interface through the lattice along the colour-gradient depicted above it. Under the same field vector a monopole with positive charge (black) propagates in the opposite direction.

This defect dependent propagation is separated from the nucleation and propagation of a defect independent monopole/antimonopole pair, which is exhibited as white/black squares in Figure 8.4b. These progress along the colour-gradient in both directions dependent on the charge

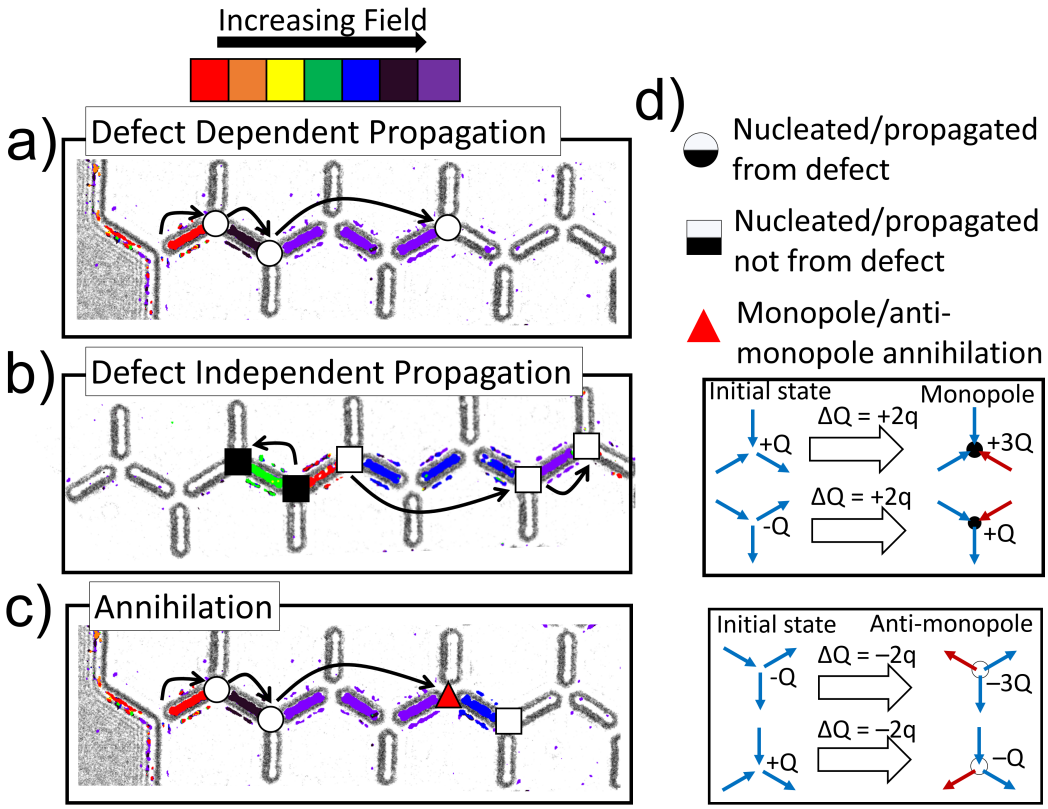


FIGURE 8.4. Key for reading differential LTEM images, where coloured islands are indicative of the individual switching fields of the nanoislands. (a-c) displays the three propagation events seen for the monopole excitations in the system (defect dependent and independent propagation; and monopole/antimonopole annihilation, respectively) along the arrow directions according to the key in (d). The colour represents net positive (black) or negative (white) charge at each vertex under field reversal; and shape differentiates between defect or lattice-based nucleation (circle and square, respectively).

of the monopole and field vector. This shows that the coloured NIs between the effective monopoles in (b), and between the defect and monopole in (a), represent Dirac strings. These are described in Section 2.2.3. Finally, annihilation occurs when two oppositely charged monopoles from separate strings converge on the same vertex. This results in a joining of the two independent strings together (Figure 8.4c). Annihilation events are indicated by a red triangle.

Using this key to interpret the results, Figure 8.5 presents the LTEM images of the disconnected DASI lattice with a solid (a-b) and vacant (c-d) defect in the array centre. The vacant defect is a control measurement used to distinguish between propagation events from magnetic coupling and those from introducing a discontinuous edge. Here, the zig-zag deformity is not present and we can therefore ascertain its impact by direct comparison. The field angle in these images is applied at $37.2^\circ \pm 1.5^\circ$ away from the horizontal line of the image (or the [1 1] direction as indicated by the straight black arrow and the schematic below the micrographs). This field direction is equivalent to the easy-axis direction from the previous section as the field is parallel to ~ 1/3 of the NI easy-axes.

This differential analysis shows both the total magnetic reversal of each NI in the image, and some of the non-Ising deviations at the NI ends, where the spins near the NI-ends cant away from the easy-axis due to the inherent frustration and increasing Zeeman energy. This effect is best seen in the NIs on the left-side of the defect in Figure 8.5a, where orange/yellow flecks appear on the NI ends closest to the defect. To keep the micrographs readable, only the starting and finishing locations of the defect-dependent propagation are indicated by markers that are summarised below the figure.

There are a few striking observations. *First* is the quantity of monopoles that form at the defect-lattice interface at reduced switching fields. This nicely correlates with the MFM and modelling results in a connected lattice shown in Figures 8.2-8.3, respectively. This shows that the defect is still acting as an injection site even in a disconnected lattice. The switching magnetisation in surrounding NIs occur due to the high-stray-field of the defect when saturated and the strong defect-island coupling. The LTEM analysis of the vacant defect in Figure 8.5c-d shows that the switches at the defect site are not a result of discontinuity of the lattice. Comparing, for example, Figures 8.5a and c; no switching events are observed below $\mu_0 H_\parallel = -12.9$ mT in the analysis of the vacant defect lattice and a far larger proportion of NIs switch homogeneously at $\mu_0 H_\parallel = -17.2$ mT compared to Figure 8.5a.

The *second* observation is the clear separation of monopoles by their charges on either side of the defect. Typically when monopoles form they are bound to their anti-monopole pair elsewhere in the lattice through a Dirac string [24, 25]. This is clearly seen in the defect-independent propagation events and in Figure 8.5c-d. Instead the defect-driven monopoles in Figure 8.5a-b are bound to the defect, through the Dirac string. The defect is compensating the charge of the individual separated monopoles of either charge. Thus, it is assumed that the antimonopoles of these defect-bound monopoles are contained within the defect itself. This observation has

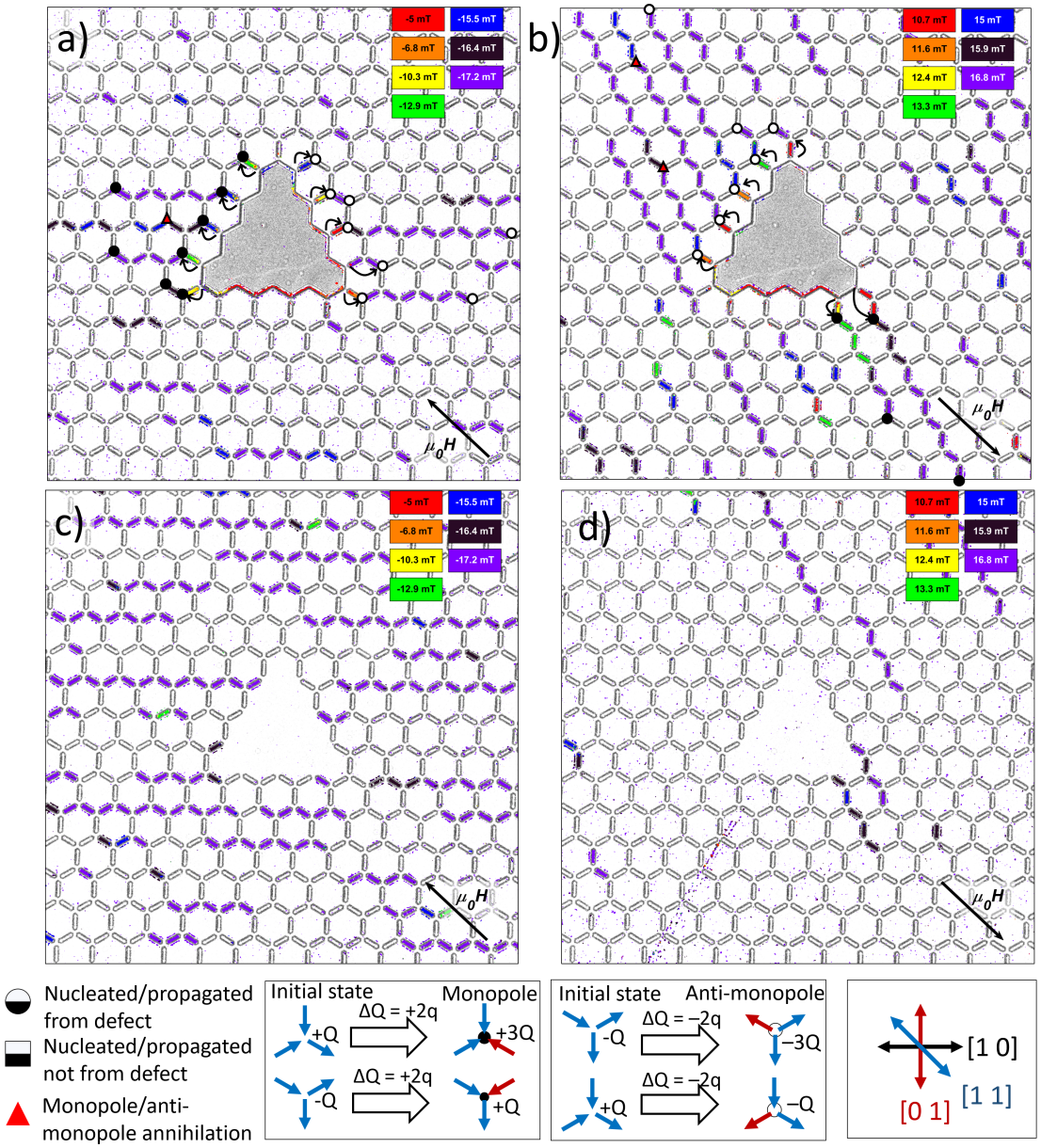


FIGURE 8.5. Differential Lorentz TEM analysis of a disconnected Kagomé lattice with a solid (a-b) and vacant (c-d) defect in the array centre under field reversal applied along the [1 1] lattice direction. Coloured nanoislands indicate the in-plane switching field required to reverse their moment. Coloured circles indicate starting and finishing emergent monopole vertex locations as a function of applied field according to the table (bottom).

interesting applications in functional devices where switching or cascade effects need to be generated locally/deterministically with lower energy of formation (e.g. hardware neural networks

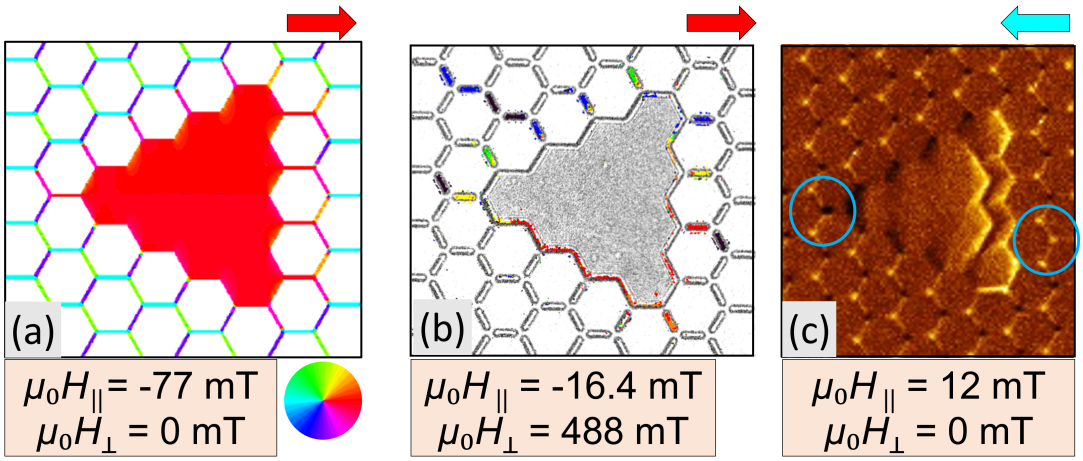


FIGURE 8.6. Zoomed-in snapshots of the defect and surrounding lattice within the OOMMF, LTEM and MFM datasets (a-c, respectively); where the LTEM micrograph has been rotated 30° to normalise the lattice orientation. The in-plane ($\mu_0 H_{\parallel}$) and out-of-plane ($\mu_0 H_{\perp}$) applied fields are stated in the boxes below the respective images, and the $\mu_0 H_{\parallel}$ direction is indicated by the arrow top-right of the image.

and reconfigurable magnonic crystals), or modelling the behaviour of rare-earth ion defects in 3D spin ice.

The *third* observation is the difference in propagation direction between Figures 8.5a-b and c-d. In Figure 8.5a and c the propagation events depicted are along the [1 0] direction of the lattice, whereas (b) and (d) follow the [1 1] direction. As it is repeated in both solid and vacant defect cases, this asymmetric behaviour is independent of the defect-type. It is also improbable that the lattice is stuck in a minor-loop as lattice is fully saturated during the measurement, as can be seen in the full statistical analysis of the reversal mechanism in the following section. This asymmetric response may be explained by a combination of the offset field angle relative to the easy axis and the chirality of the DW during switching. This has been discussed previously for connected Kagomé lattices in Ref. [230] and could plausibly be translated into an asymmetry of dipolar coupling between the NIs in a disconnected lattice.

Figure 8.6 is a comparative snapshot of the modelling, LTEM, and MFM data (a-c, respectively), showing good agreement between respective methods. Regardless of the propagation direction, the LTEM analysis and the micromagnetic modelling of the connected lattice in the previous section agree on the preferential switching of NIs along one edge of the lattice, whereas those on the other side of the defect are unperturbed at the applied fields shown. The modelling correctly captured this asymmetric effect and suggests a favourable coupling between the lattice-defect interface as a function of the field. As the *in situ* MFM dataset does not go to high fields the same asymmetric effect was not replicated. The relative fewer switches on the right-side of

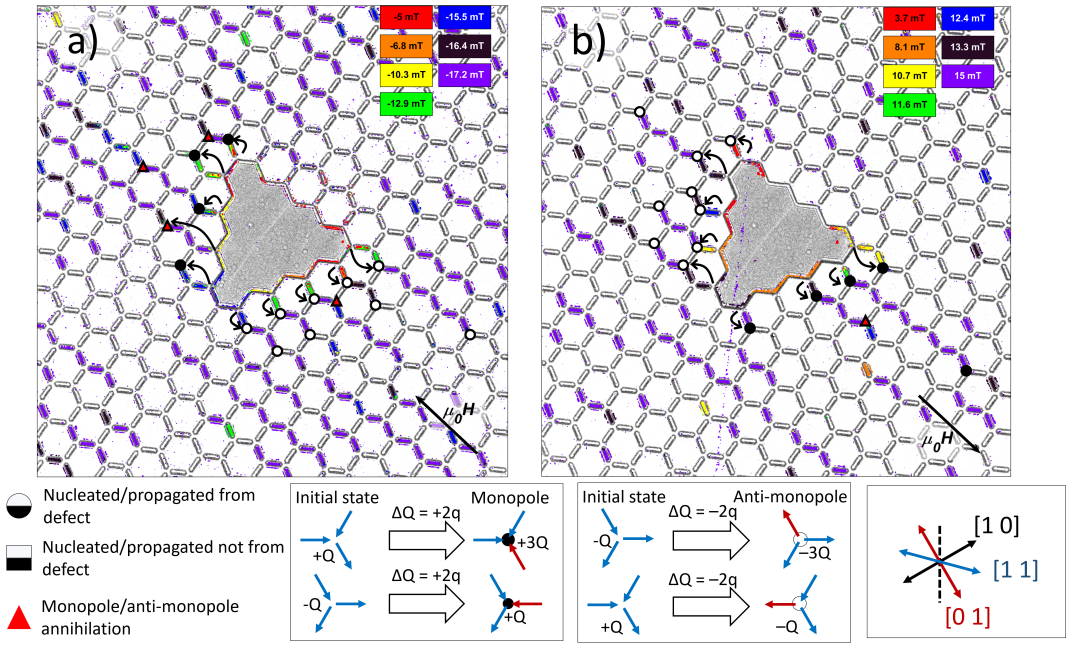


FIGURE 8.7. Differential Lorentz TEM analysis of a disconnected Kagomé lattice with a solid (a-b) defect in the array centre under field reversal applied along the [0 1] lattice direction. Coloured nanoislands indicate the in-plane field required to magnetically switch them. Coloured geometric shapes indicate emergent monopole vertex locations as a function of applied field according to the table to the right of the images and arrows indicate the propagation direction.

the defect in the MFM image could also be due to the present of the zig-zag deformity. However, the switching in the wires and islands left and right of the defect along the field applied direction is seen across all three methods.

Most of these observations translate across to the case where $\mu_0 H_{\parallel}$ is applied along the zig-zag axis of the lattice (i.e. along the [0 1] direction perpendicular to 1/3 of the NIs in the Kagomé lattice, see schematic under micrographs in Figure 8.7). Figure 8.7 presents the LTEM micrographs with differential analysis on the lattice when rotated 30° in the $xy$-plane from the position in Figure 8.5. Here the cascade events propagate along the applied field direction, where NIs aligned along the direction of the field preferentially switch.

It is apparent that defect-independent monopoles form more readily in this field orientation. This is evidenced by an increase of NI switching events at lower fields that the previous dataset away from the defect. However, a greater amount of events are still concentrated at the defect site.

Other observations detailed in Figure 8.5 are also seen in Figure 8.7, where the primary result is the low-field formation of monopoles bound to the defect-lattice interface. The equivalent differential LTEM micrographs of the lattice with a vacant defect are included in Figure A.18 in

the Appendix, which showed no preferential switching at the vacant-defect site.

Figures 8.5-8.7 provide the visual representation of the emergent monopole injection into the lattice. However, the full reversal mechanism cannot be shown in this way as it would make an already complex plot completely unreadable. Instead the switching fields of each NI in the image can be plotted as a function of the distance from the defect centre to show the full influence of the defect on the lattice components.

### 8.4.2 Statistical analysis of switching events in defect-ASI

To perform this summarising analysis, image segmentation is required to identify each NI, their orientation, and their distance from the defect. For this, the components of the lattice were segregated based on intensity and size to form a mask for each NI. This was performed using image segmentation tools available in MATLAB®, by a morphological reconstruction method

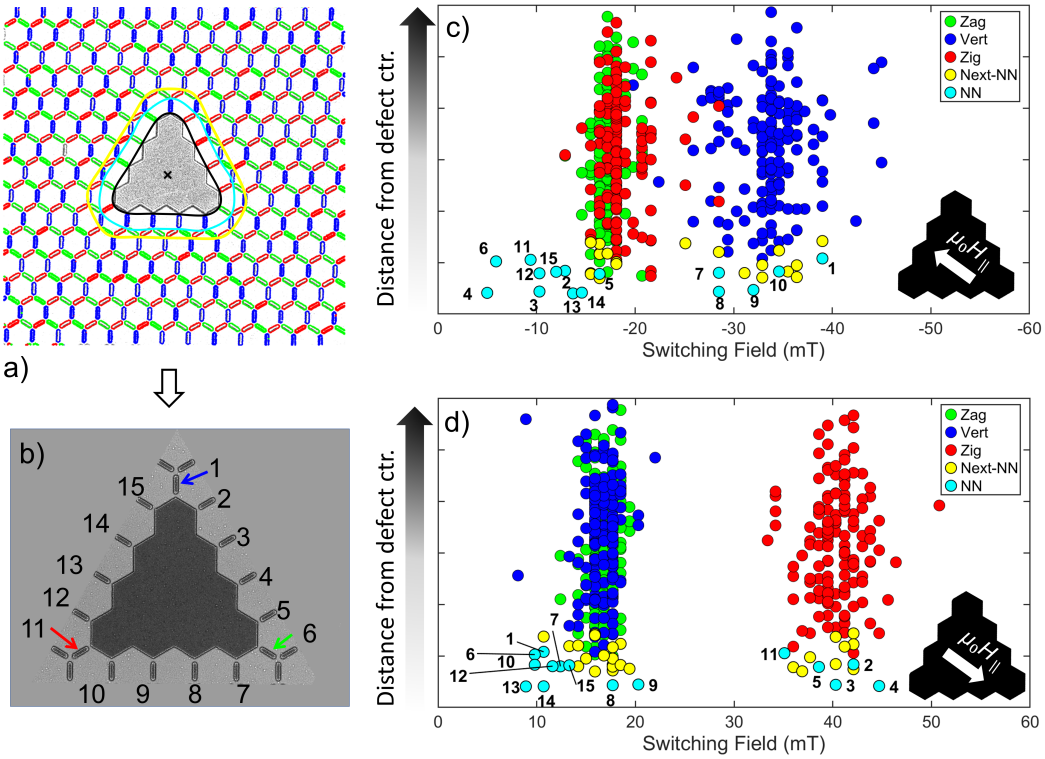


FIGURE 8.8. (a) LTEM image segmentation key, with “Zig”, “Zag” and “Vert” islands outlined in red, green and blue, respectively; nearest and next nearest-neighbours (NN and NNN) are enclosed in the cyan and yellow boundaries, respectively, and the defect centre indicated by black cross. (b) TEM image of defect region where NN islands are labelled from #1-15 clockwise. (c-d) Grouped scatter-plots of each NI’s switching field and their respective distance from the defect centre under field-sweep applied along the [1 1] and [1 -1] directions, respectively.

[231, 232]. The defect region was excluded from the final segmentation as were NIs that are not fully encompassed in the image bounds. Figure 8.8a shows the outlines of each mask, which have been separated into three categories: NI's aligned along the vertical direction of the image are labelled "*Vert*" highlighted in blue; whereas the diagonal elements are labelled as "*Zig*" and "*Zag*" (red and green, respectively).

The centre of the defect was calculated as the centre-of-mass without the other elements of the array and is represented as the black-cross in the image. The cyan and yellow outlines represent the regions that include nearest- and next nearest-neighbours, NN and NNN islands respectively, i.e. NIs that are directly adjacent to the defect and NIs that are two vertices away from the defect, respectively. A close-up of the defect and NN elements is displayed in Figure 8.8b, and the NNs are labelled (#1-15) clockwise from the North-most NI. Arrow colours indicate the NI classification as described in for Figure 8.8a.

**Easy-axis field alignment**

Figures 8.8c and d are grouped scatter plots of the switching field for each NI against their distance from the defect centre for the datasets displayed in Figure 8.5a-b, respectively. Due to the magnetic reversal propagation travels along the [1 0] direction of the lattice in Figure 8.5a, the majority of "Zig" and "Zag" islands (red and green respectively) switch before the majority of "Vert" islands in Figure 8.8c. Between $\mu_0 H_{\parallel} \approx -20 - -30$ mT there is a small crossover in the distributions of switching fields for the "Zig" and "Vert" islands. This is not seen for the dataset in Figure 8.8d where the propagation events occur along the [1 1] direction. Here, a large window between the zag-vert transitions and the zig-switching events is clearly seen. This asymmetric behaviour with field-sweep direction is indicative of the unique angle described in the previous subsection that results in the more favourable skipping between the NI rows.

The NN and NNN data-points have been separately coloured (cyan and yellow, respectively) from the NIs in the surrounding lattice in Figure 8.8c-d. The "Zig" and "Zag" NN islands (#2-6, and #11-15) in Figure 8.8c are clustered together close to the origin due to their close proximity to the defect and their alignment to the Zeeman field. This results in the data-point clustering at significantly reduced switching fields than seen for the remainder of the lattice, unambiguously demonstrating the influence of the defect on the NN islands. This contrasts the distribution of switching fields of the vertical NN islands (#1, #7-10) which possess a similar distribution to the other vertical islands in the lattice. This better shows that the NN islands along one face of the defect do not possess a reduced switching field despite their close proximity to the defect. Therefore, there is a demonstrable asymmetry coupling between the three defect faces.

The NN behaviours described in Figure 8.8c are replicated in the reverse field-sweep direction in (d), despite the change in the propagation direction. Vert (#1,#7-10) and Zag (#6,#12-15) are mostly clustered near the origin of the plot, whereas the Zig NN islands (#2-5,#11) are similarly distributed to the Zig NIs away from the defect. This exactly replicates the micromagnetic

modelling of the connected lattice in Section 8.3. In this field orientation there is seemingly no change in the switching fields of the NNN islands (yellow) in Figures 8.8c-d as their switching field distribution largely follows the distribution of the NIs in the surrounding lattice.

The NN switching field clustering seen in Figure 8.8 shows that the switching fields are adequately reduced along two faces of the defect, and matches the lattice population along the third face. Figure 8.9a-b statistically summarises the distribution of switching fields present in Figure 8.8c-d as box-plots, which serve as a useful tool for comparing units and sub-units within vast datasets [233, 234].

As shown in the legend in Figure 8.9c the boxes represent the inter-quartile range (IQR) (i.e. between the $25^{\text{th}}$ (Q1) and $75^{\text{th}}$ (Q3) quartiles to encompass 50% of the dataset) and the median is displayed as the red horizontal line in the boxes. The placement of the median inside of the IQR box is a proxy-measurement for the skewness of the distribution of data-points. Its placement in the centre indicates a normal distribution whereas its placement nearer one of the IQR bounds implies a skewness in the distribution. The bars (or whiskers) are $\pm 1.5\times$ the IQR on top of the Q1 and Q3 percentiles such that they span 99.3% (or $\pm 2.7\sigma$) of the dataset. Data-points outside of these bounds, i.e. outliers, are represented as black circles. Finally, the mean switching fields for the respective classifications are represented as the coloured dotted vertical lines.

The data presented in Figure 8.9 again segregates the islands by their orientation to the

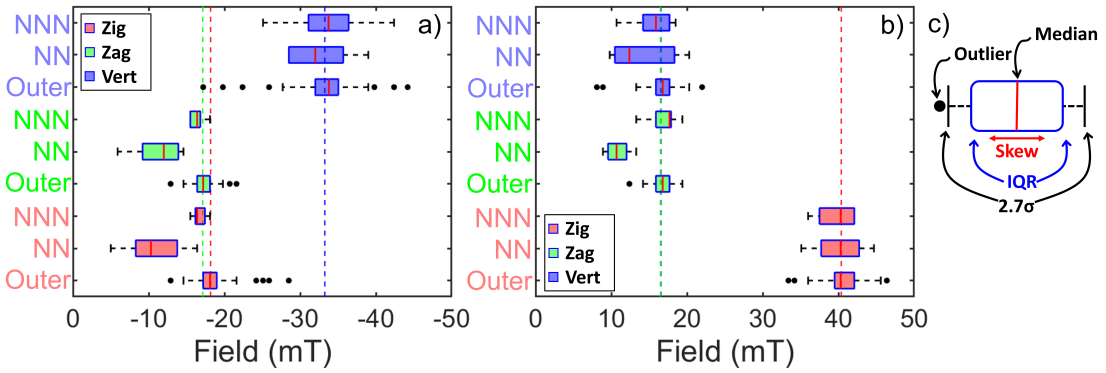


FIGURE 8.9. (a-b) Box-plots representing the summarised data from Figure 8.8c-d for Zig, Zag, and Vert island classifications (red, green and blue, respectively. (c) Legend describing the box-plots: boxes represent the interquartile range (IQR) of the dataset; vertical red-line represents the median; whiskers represent the lower- and upper-quartiles (spanning 99.3% of the data-series); and dots are outliers. Within each coloured subset in (a-b) the box-plots represent the distribution of island switching fields excluding the NN and NNN islands, i.e. the 'outer'-islands (bottom); and the switching field distributions for the NN and and NNN islands (middle and top, respectively). Dashed lines in (a-b) represent the mean of the total Zig, Zag and Vert island switching-field distributions (red, green and blue, respectively).

$x$-axis of the lattice, Zig, Zag and Vert (red, green and blue, respectively). Within each coloured subset three classifications of the data are shown. From bottom-to-top, the box-plot subsets are: the full dataset excluding NN and NNN contributions; and the separate NN and NNN contributions, respectively.

It is clear for the Zig and Zag island classifications that the NN islands are greatly dissimilar from the other datasets. The NNN distributions for Zig and Zag islands are more similar to the surrounding lattice than the NN islands. In the Vert islands, all four box-plots are similar as they are normally distributed about the median switching field ($\mu_0 H_{\parallel} \approx 34$ mT). The Vert NN island distribution is slightly down-shifted in switching field. However, this is likely a product of the much smaller sample size.

Figure 8.9b summarises the data displayed in Figure 8.8d. It draws the same conclusions as the analysis for Figure 8.9a asides from the change in propagation direction resulting in the positive and negative shift in switching field among the Zig and Vert island distributions, respectively. The NN Zag dataset is clearly dissimilar to the NNN and surrounding lattice. In the Vert island distributions the IQR is quite large for the NN island distribution because islands #8-9 switched at a higher field than the other NN islands.

The box-plots indicate that when the field is applied along the easy-direction of the lattice, the defect directly influences the NN but has little-to-no effect on the switching field of the NNN islands and beyond. This indicates that the emergent monopoles are injected into the neighbouring vertices to the defect and are fixed until the Zeeman energy is above a pinning threshold to induce the monopole propagation events, which is equivalent to the energy of defect independent monopole formation. This is unlike the modelling of the connected lattice, which showed a few propagation events from the defect prior to the remainder of the lattice switching; this is likely a consequence of comparing disconnected and connected lattices, where propagation through the lattice is more difficult in the former.

### Hard-axis field alignment

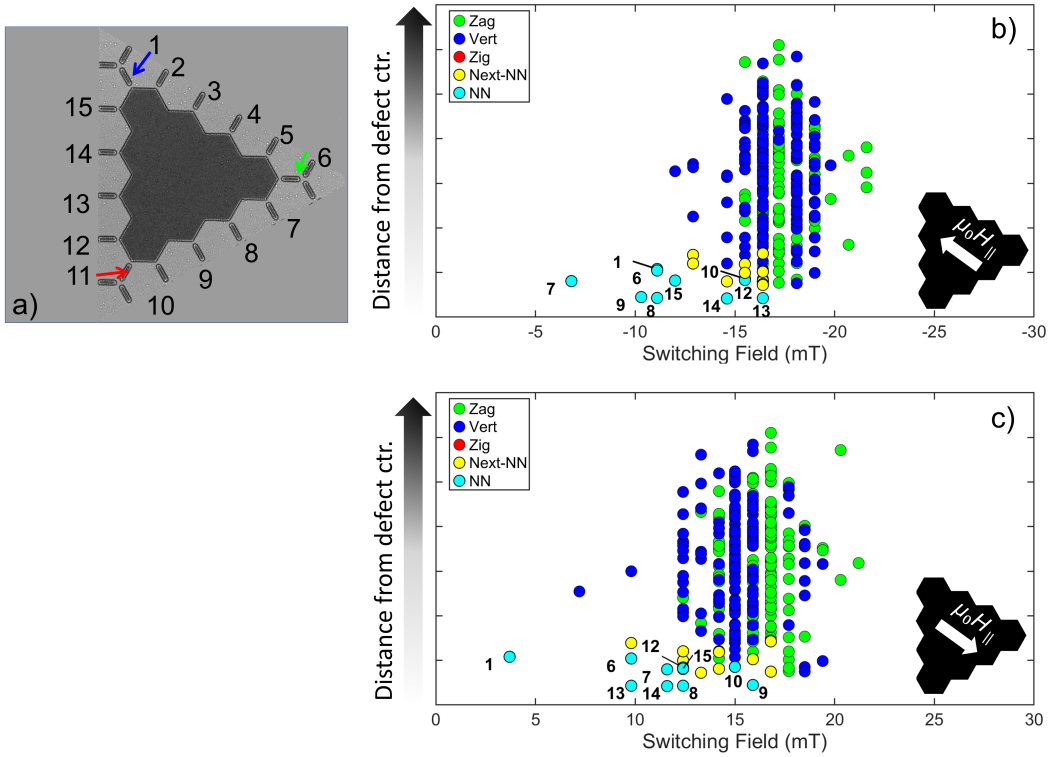


FIGURE 8.10. (a) TEM image of defect region where NN islands are labelled from #1-15 clockwise. (b-c) Grouped scatter-plots from data presented in Figure 8.7a-b, respectively, of each NI's switching field and their respective distance from the defect centre under field-sweep applied along the [0 1] and [0 -1] directions, respectively.

The same analysis has also been performed on the datasets where the field is applied along the lattice hard-axis (i.e. those displayed in Figure 8.7). The nomenclature and colour-classification are preserved upon rotating the lattice 30° (Figure 8.10a) to enable direct comparison with the previous datasets. The grouped scatter plots are shown in Figure 8.10b-c for the islands depicted in Figure 8.10d-e, respectively. Here, the "Zig" islands do not switch during the entire field-sweep as the critical field required is not reached during data acquisition. Hence, they are excluded from the following analyses. Between the acquisition of datasets, the Zig islands switch when saturated in maximum field applied along the [0 1] axis, so the datasets on display do not represent a minor loop.

The Zag and Vert islands away from the defect (green and blue, respectively) in Figure 8.10b-c behave in much the same way as described in the easy-axis dataset. The NN islands (cyan) are also clustered away from the main distribution of islands, correlating a reduction of the switching

field to the island proximity to the defect. The notable difference between the two datasets is the distribution of the NNN islands (yellow), which appear to be clustered towards a lower switching field compared to the remainder of the lattice as well.

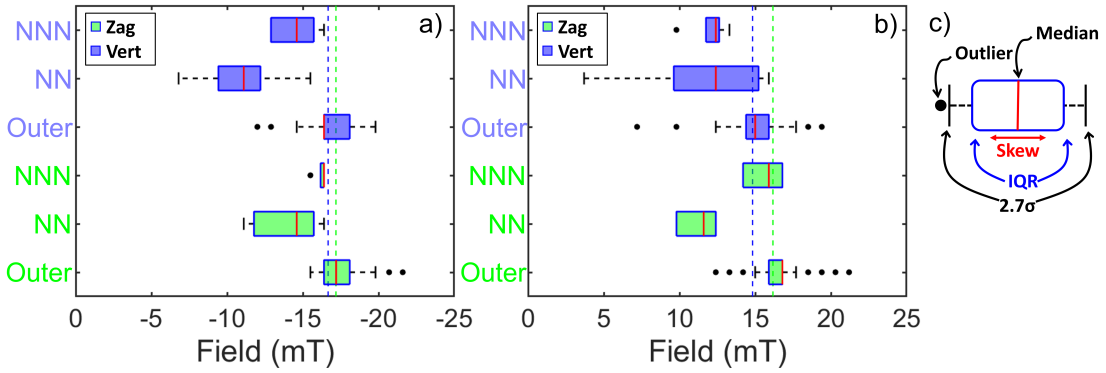


FIGURE 8.11. (a-b) Box-plots representing the summarised data from Figure 8.10b-c for Zag and Vert island classifications (green and blue, respectively. Boxes represent the interquartile range of the dataset; horizontal red-line represents the median; whiskers represent the lower- and upper-quartiles (spanning 99.3% of the data-series); and dots are outliers. Within each coloured subset, the box-plots represent (from left-to-right): full data-range in the classification; the data-range excluding the NN and NNN data-sets; and the NN and NNN datasets, respectively.

To quantify this, boxplots of the data represented in Figures 8.10b-c are summarised in Figure 8.11a-b, respectively. As described for the box-plots for Figure 8.9: the full dataset excluding NN and NNN contributions, i.e. the outer-islands; and the separate NN and NNN contributions, respectively, are presented from bottom to top within each coloured subset.

First, the outer-islands for both Zag and Vert classifications in Figure 8.11a-b possess similar switching fields and ranges regardless of polarity of the applied field. Similar to the previous dataset, the distribution of the NN island switching fields is considerably reduced compared to the outer-island population. However, more interestingly the Vert NNN island distributions are also considerably reduced compared to the mean and median switching fields of the greater population. This suggests the propagation of the emergent monopoles formed at the NN vertices propagate more easily in this lattice orientation.

## 8.5 Summary and Conclusion

This chapter has combined the use of *in situ* MFM, differential LTEM and micromagnetic modelling to study the role of a magnetic defect as a source of propagation events in connected and disconnected Kagomé ASI lattices. The *in situ* MFM and micromagnetic modelling of connected lattices showed that the defect is a DW nucleation pad that asymmetrically injects DWs at

reduced field compared to the surrounding lattice. In addition, it is shown that the defect stabilises energetically unfavourable $3q$ charge states close to the defect site.

Micromagnetic modelling of the field reversal mechanism showed the defect-dependent monopoles only propagate 2-3 vertices away from the defect below the field required to induce defect-independent switching. This clustering of magnetic monopoles at the site of a magnetic defect matches literature descriptions of similar effects in stuffed spin ice well. The pinning energy at the connected vertices prevents the free propagation through the lattice at fields below the defect-independent switching field.

Complementary studies of the field reversal mechanism of an equivalent disconnected lattice by LTEM both mapped the pathway of the emergent monopoles upon application of higher fields, and provided statistical analysis of the switching fields of the islands as a function of distance from the defect. The strong extrinsic flux of the saturated defect, and the effects from island-defect coupling, induces the formation of monopole defects adjacent to the defect site. The results of the disconnected lattice resembled the DW injection mechanism seen in the connected lattices despite the inter-component separation at the vertex locations.

Comparing the switching fields of the constituent islands of the defect-ASI along two axial directions showed that defect-dependent propagation events were slightly easier when the field was aligned along the hard-axis, which was evident from a larger proportion of NNN switches below the mean and median switching field of alike NIs in the surrounding lattice.

The results of the LTEM analysis of the disconnected lattice were compared to the results of the micromagnetic modelling of the connected lattice to ascertain similarities. Those found included: (1) The formation of monopoles in the vertices near the magnetic defect; (2) the defect-dependent propagation extending to 2-3 vertices away from the defect below the defect-independent lattice switching field; (3) the preferential switching of the NN islands on just two of three edges of the defect. The differential LTEM analysis qualitatively demonstrated that these effects are not the result of the introduction of lattice discontinuity, as a vacant defect did not yield the same reduction of the switching field.

Lithographically defining magnetic defects in ASI has some interesting implications to both traditional spin ice and ASI-based technologies. The two-dimensional model presented here has a good resemblance to stuffed spin ice, including the local generation of effective monopoles at the defect site; and the highly localised influence of the defect [220, 221]. Modifications to the lattice/defect design or dimensions (e.g. thermally-activated ASI) and/or methods for excitation (e.g. current pulses) may allow easier control of the defect-bound monopole without inducing defect-independent switching. To possess the ability to manipulate the magnetic cascade behaviours in an extended array is particularly palatable for logic devices, probabilistic computing, and signal propagation.

CHAPTER 9

# SUMMARY, CONCLUSIONS AND FUTURE OUTLOOK

Advances in spintronics are a result of improvements in device design, fabrication and methods to probe their physical properties. As such, they remain highly relevant for the developing key industry sectors including novel computation and sensing. In the present thesis, advanced SPM techniques were used to investigate local spin textures within spintronic systems. Domain walls pinned in high-susceptibility nanowires were visualised through customised SPM instrumentation, including MFM measurements with a custom probe and a novel spin caloritronic technique. Both techniques showed great promise for measuring diverse and otherwise challenging samples. Contemporary image processing methods and magnetic imaging techniques were used to assess novel energy states within ASI lattices. The behaviour of the spontaneous formation of Landau states in the QH-ASI lattice was quantified and evaluated by a combination of MFM/qMFM, micromagnetic modelling and EH; whereas effective monopole dynamics in a Kagomé lattice with a magnetic defect were mapped and characterised by *in situ* MFM, modelling, and LTEM.

## Summary and Conclusions

The thesis begun with a review of the primary themes that run throughout. **Chapter 1** outlined the most relevant principles of micromagnetics, paying attention to the interplay of energy contributions and domain theory. This was proceeded by a literature review of artificial spin ice in **Chapter 2**, which encompasses a rich field of frustration-based phenomena that was relevant for many of the experimental chapters. **Chapter 3** introduced the theory and methodology of several of the techniques used to explore the physical systems presented, including: an in-depth review of MFM and advanced MFM techniques; the framework of spin caloritronic phenomena; LTEM/EH; sample fabrication; and micromagnetic modelling.

Chapters 4 and 5 investigated customised/specialised SPM methods for the analysis of domain structures in ferromagnetic nanowires. **Chapter 4** compared a custom patterned MFM probe against commercial equivalents in its ability to measure samples with high and low coercivity. It was recently shown that head-to-head and head-to-tail domain configurations allow for imaging both hard and soft magnetic structures, respectively, with the same probe [105]. This switchable property removes the need to change probes when alternating between samples of different magnetic field strength and demonstrates the impressive versatility of the design. Results showed that from shape anisotropy the probe in the "high-moment" configuration possessed lower magnetic susceptibility than commercial low-moment probes and was comparable in both resolution and durability to the commercial equivalents. QMFM possessed sensitivity to the asymmetric stray-field characteristics of the probe, which meant it was compatible with the calibration procedure. The stray-field of the DWP did not irreversibly change the magnetisation of a DW pinned in a highly susceptible L-shaped test nanostructure, but did perturb it from the resting state. However, this could be overcome by an improvement in the design (e.g. increasing the separation between the V-shape and Si probe apex).

**Chapter 5** demonstrated a novel SThEM method for imaging the magnetisation of a PMA nanowire with very high susceptibility, such that it could not be imaged by conventional MFM techniques. This method used a Joule-heated probe to induce spin caloritronic effects in the nanowire and map the magnetisation of the wire directly as a function of its thermoelectric output. The numerous thermoelectric contributions to the signal were ascertained from an analytical model. The SThEM method was a surprisingly elegant and a methodologically promising solution for probing spin textures in electrically connected magnetic materials, and could be applied to several other material systems.

The remaining chapters focused on the investigation of novel ASI systems by MFM/qMFM, complimented with micromagnetic modelling and LTEM/EH. **Chapter 6** introduced the QH-ASI lattice and investigated the generation of Landau state defects, where it was established that they are energetically favoured in this lattice from the inclusion of parallel nanoislands in the periodic lattice array. However, the results showed that instead of a total breakdown in the magnetisation of these participating elements, LSs were randomly distributed across the lattice with a predicted maximum of $\sim 67\%$ of the population when the field was aligned along the optimum direction. Using parallel islands in ASI arrays has been extensively used in recent literature to include additional effects induced by ferro-/antiferromagnetic coupling, thus it is important to establish how their Ising-like properties may deviate from the lattices without parallel elements.

The formation of LSs was shown to be highly deterministic, when all field protocols were taken into account, and highly dependent on small variations in the incident field angle. The applied field magnitude was found not to be a factor for their formation once a threshold magnitude was passed. QMFM was used to directly correlate the micromagnetic models in this study that describe the energetics of the system with the experimental MFM micrographs. This showed

good qualitative agreement across the three statistically defined states in the QH-ASI lattice but revealed that the strong stray-field emanating from the $T_3$ vertices resulted in unfavourable probe-sample interactions that affected the quantification. To interpret the described behaviours of the QH-ASI when it hosted LSs, and to better understand the domain configuration of the LSs at remanence, a study of the three modal states were investigated by electron holography in **Chapter 7**. These measurements of the intrinsic and extrinsic magnetic flux pathways revealed that the coupling between the NIs was rather complex in the bi- and multi-modal configurations. Nearest-neighbour interactions were not always the preferred energy minimisation route, which may explain why the chiral magnetic states are aperiodically distributed.

The final experimental chapter (**Chapter 8**) investigated the interplay of effects in a defect-ASI system where a solid defect site was artificially incorporated into the lattice. Through a combination of *in situ* MFM, micromagnetic modelling and big data analysis of rapid acquisition LTEM measurements, the defect was shown to inject emergent monopoles into both connected and disconnected lattices at applied fields well below the switching field of the lattice. As such, effective monopoles were bound to the defect-site and were not able to freely propagate past more than a few vertices until the threshold field of the lattice switched. The results from coupling the defect and ASI systems together may be interesting for many of the touted ASI fields of interest including phase-transitions, magnetricity and probabilistic computing.

## Future Work and Outlook

To conclude the thesis, the remainder of this chapter will discuss the potential avenues to expand the works discussed throughout, as well as their broader application in the respective fields.

**Customising MFM probes** to either improve the methodology of MFM or to extract a greater amount of information from an MFM image will certainly continue due to the continuous development in this field (see section 3.1.3). If these probes were to be commercialised the challenge is in the fabrication process. It has been shown in the thesis that FIB-milling can be used to remove the magnetic coating leaving the desired structure, but to perform this on a mass-scale would not be sustainable. However, It would be possible to adapt the fabrication method to grow the structures on the probe directly, such as has been achieved for scanning thermal microscopy probes (e.g. Figure 3 in Ref. [235]). In addition, the design of the V-shaped probe could be altered to mitigate tip-sample interactions (e.g. angle of the arms or distance of the nanostructure from the tip apex). With consumer demand and perhaps a few more iterations to optimise the design, there would be no reason why this design could not be marketable.

The **scanning thermoelectric microscopy** method demonstrated in Chapter 5 on the PMA nanowire was shown to be a particularly useful method to probe thermoelectric effects in nanoscale wires with high magnetic susceptibility. The study demonstrated here shows that locally inducing thermoelectric effects on the nanoscale, alongside recent studies both within

magnetism [196, 204, 236–239] and outside it [202, 203, 240], is a topic that has growing interest within the nanoscience community. To develop the technique further it will be important to use the tool to study many different material systems with wide variety of properties to understand the full power and/or limitations of the technique compared to more conventional microscopy methods. In addition, the role of magneto-thermal effects, such as thermally-induced DW depinning or nucleation/termination events, should be investigated.. If these magnetothermal effects can be demonstrated with the heated probe, it would generate great interest in manipulating nanoscale spin-textures for e.g. heat-assisted magnetic recording and programmable logic technologies.

Since the methodology of **quantitative MFM** was first proposed by Hug *et al.* [111, 112], it has been surprising that it has remained a niche tool even within the MFM community. This is mostly because the implementation is complex and requires significant development and time. Macroscopic magnetic field measurements are traceable to nuclear magnetic resonance quantum standards, however this calibration standard only relate to measurements of fields that are constant and homogeneous over macroscopic volumes and/or surface areas. This is not amicable for industries which are currently accelerating the fastest within magnetism e.g. magnetic sensors or information technology. These instead require traceable measurements of magnetic fields on the nanometre scale [106]. One hurdle that had to be overcome was the widespread access to a toolkit that can perform these calculations. This has been addressed by the inclusion of qMFM modules in the *Gwyddion* SPM data-analysis software [145, 241], which is open-source and freely available to use. Some of the works discussed throughout this thesis (mainly Chapters 4 and 6) have been useful application notes in this achievement and will assist the research and industrial communities in implementing the technique in a more widespread capacity.

The **quasi-hexagonal artificial spin ice** lattice that were studied in Chapter 6 and 7 demonstrated unusual magnetic responses with respect to external stimuli (namely applied field). The realisation that the favourable formation of Landau states results from the inclusion of coupled-NIs into the lattice has particular relevance for future designs and, inherently, applications of ASI lattices. In particular, examples from literature have shown more frequent use of coupled or throupled lattice designs to induce ferro- and antiferromagnetic coupling between "macro-spins" where this non-Ising behaviour should be justly considered [78, 79]. It was demonstrated in the thesis that the non-uniform, multi-chiral, yet deterministic formation of the Landau states across the array resulted from unexpected plethora of local coupling between islands at the vertices. What was not addressed was whether these local coupling effects could be controllably induced, which would be interesting for programmable logic application e.g. non-Boolean computing [242]. On the other-hand, control of the stochasticity of the Landau state formation would have exciting applications in probabilistic computing, e.g. non-volatile random-number generation, which might be possible in different lattice designs or systems.

The investigation of **defects in ASI lattices** is one that is relatively under-represented in

ASI literature, considering that defects locally adapt the thermodynamics of otherwise continuous lattices. One reason for this could be a case of practicality and implementation in functional devices. However, this could be overcome through improved engineering to accommodate “moving” defects, such as has been demonstrated with localised MFM writing [40, 243], or clever device design [32]. The ability to tune and probe the magnetic states through defect integration shall always remain attractive within the ASI community. There are a number of different avenues to build on the results presented in Chapter 8. One example includes a study the effect of defects in a thermally-activated ASI system, where the influence of the defect would be more prominent [222, 224]. Alternatively, using different excitation sources on the defect-ASI lattice (e.g. current-pulses or thermal excitation), or a study of the magneto-transport response with and without the defect would allow for assessing the plausibility of integration into functional frustration devices. Finally, it would be exciting to tune the defect and lattice parameters further through changes in the defect or lattice dimensions/geometry, or utilise multi-step lithography to include multi-material systems.

APPENDIX A

# Appendix

This appendix contains several additional figures and supporting information for works related to the thesis. The appendix is sorted by topic for ease of readability. In each caption is a reference back to the relevant sections and/or chapters.

## A.1 Artificial spin ice

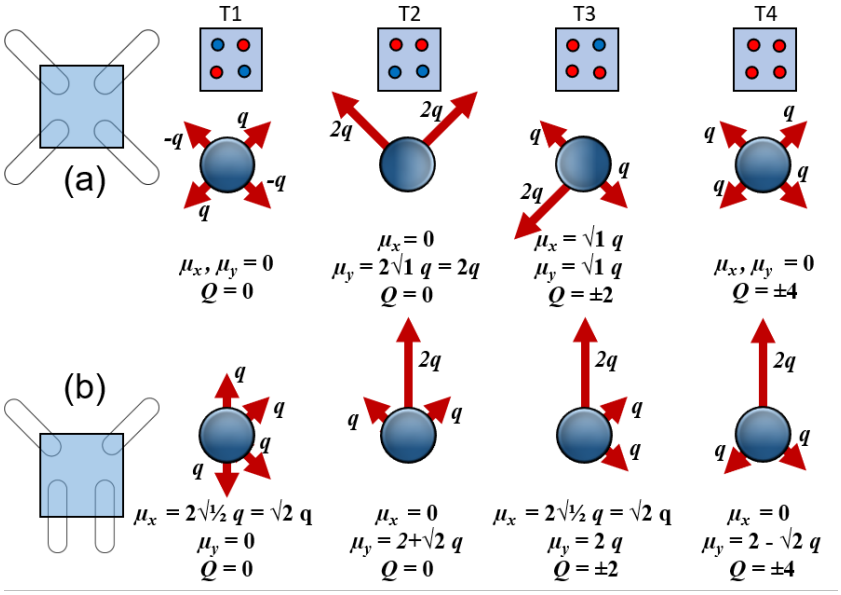


FIGURE A.1. Schematic demonstrating the magnetic moments ($\mu$) and charges $q$ for four-apex X- and Y-junctions, (a) and (b), respectively. Related chapters: 2; 7

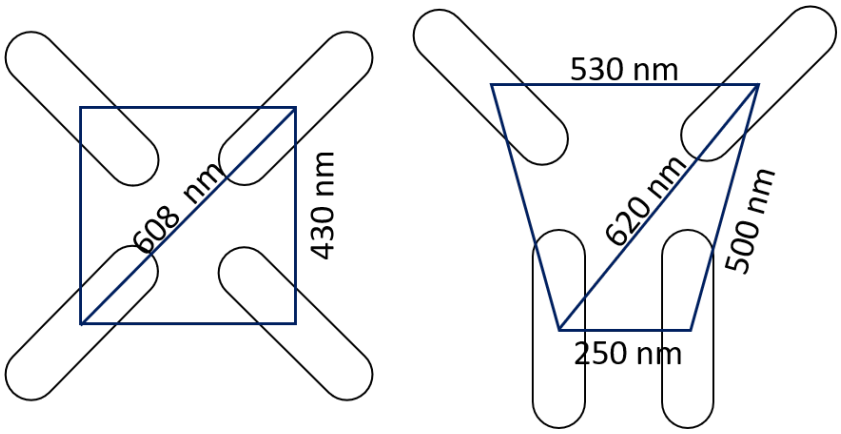


FIGURE A.2. Dimensions of the X and Y vertex junctions in the QH-ASI design. Related chapters: 6; 7.

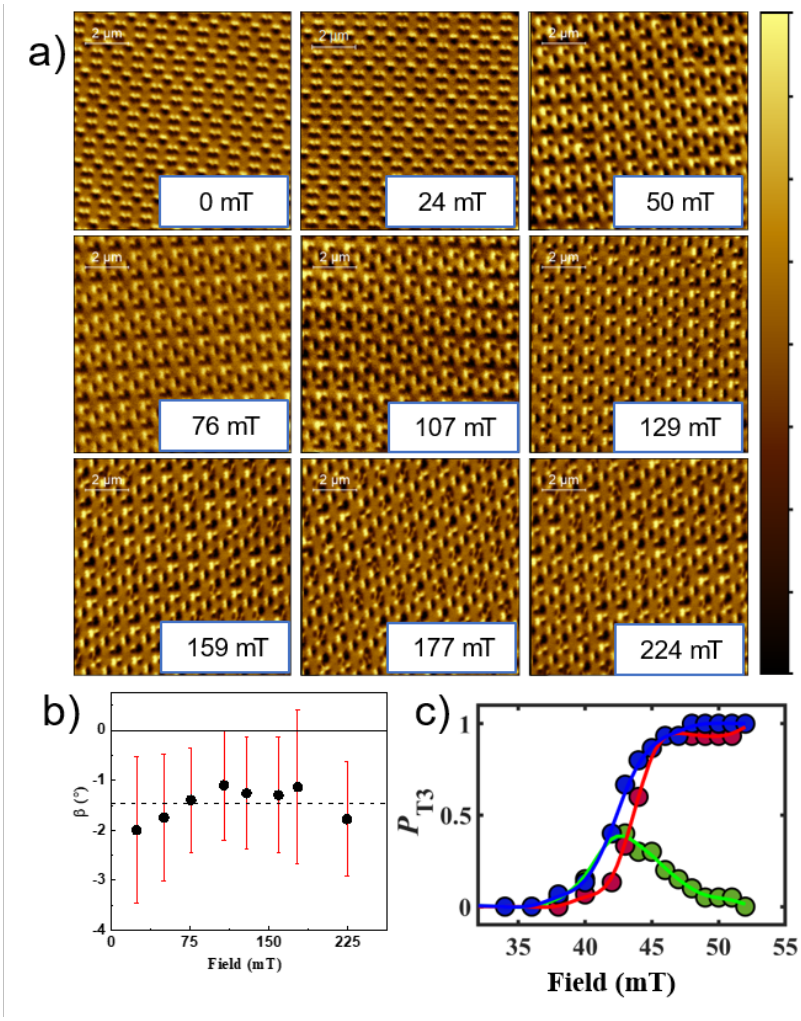


FIGURE A.3. (a) $10 \times 10 \mu m^2$ MFM images taken at remanence at the center of the QH-lattice post application of specified field along the hard-axis of the lattice; switching from unimodal, to bimodal and finally to a multimodal state. (b) The field angle ($\beta$) and uncertainty ($2\sigma$) for each field magnitude applied to the sample. (c) Population frequency of $T_3$ energy states across X (green), Y (red) and rY (blue) vertices within the field-range 35-50 mT, demonstrating a two-step transition between uni- and bimodal states. Related chapter: 6.

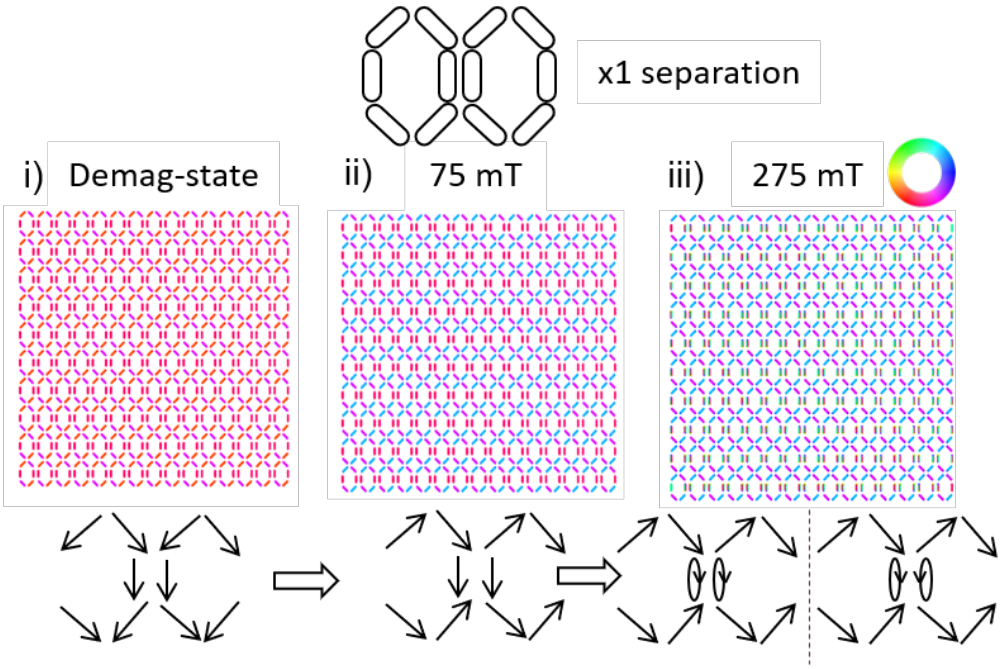


FIGURE A.4. Remanence magnetization configurations calculated for the QH-ASI lattice with nominal separation following the field sequence described in chapter 6. (i) initial state after demagnetisation process along $y$-axis and the application of an $x$-orientated field magntidue: (ii) 75 mT and (iii) 275 mT, which corresponds to the uni-, bi- and multimodal states, respectively. The colour wheel represents the angle that the magnetisation vector forms with the $x$-axis. Related chapter: 6.

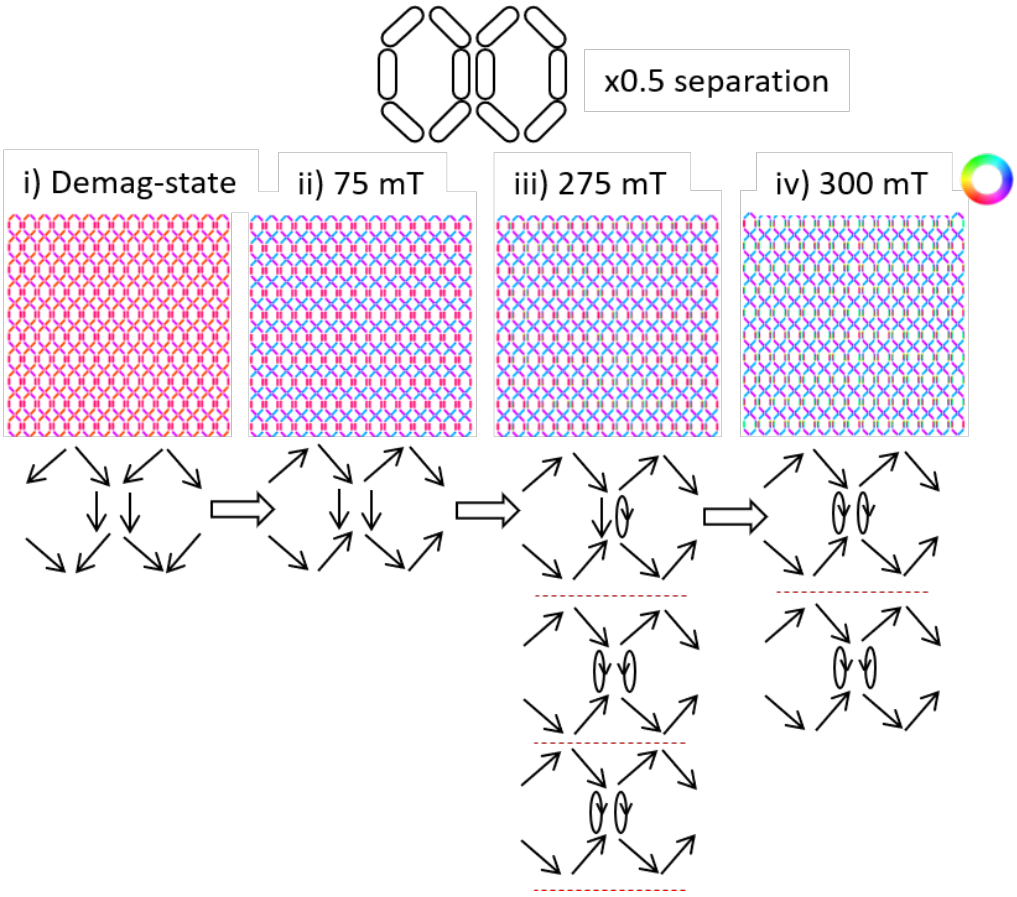


FIGURE A.5. Remanence magnetisation configurations for the QH-ASI lattice, at half inter-island separation, calculated following the field sequence described in chapter 6. (i) initial state after demagnetisation process along $y$-axis and the application of an $x$-orientated field magntiude: (ii) 100 mT, (iii) 200 mT (iv) 300 mT, which corresponds to the uni-, bi- and multimodal states, respectively. The colour wheel represents the angle that the magnetisation vector forms with the $x$-axis. Related chapter: 6.

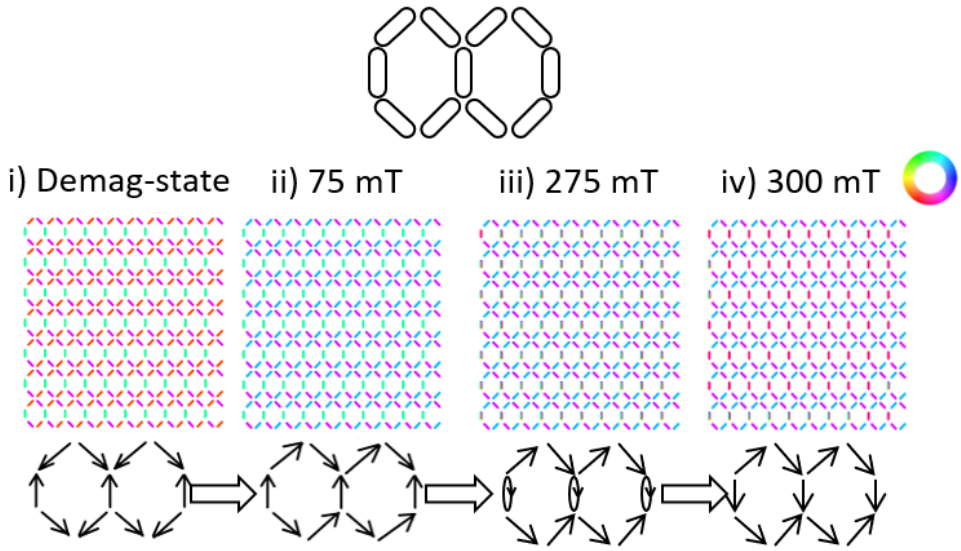


FIGURE A.6. Remanence magnetisation configurations calculated along the field sequence described in chapter 6 on a lattice without coupled parallel islands. (i) Initial state after the demagnetisation process along $y$-axis, and the application of an $x$-orientated field of (ii) 75 mT, (iii) 275 mT and (iv) 301 mT. The colour wheel represents the angle that the magnetisation vector forms with the $x$-axis. Schematics of the NI magnetisation are included for reference. Related chapter: 6.

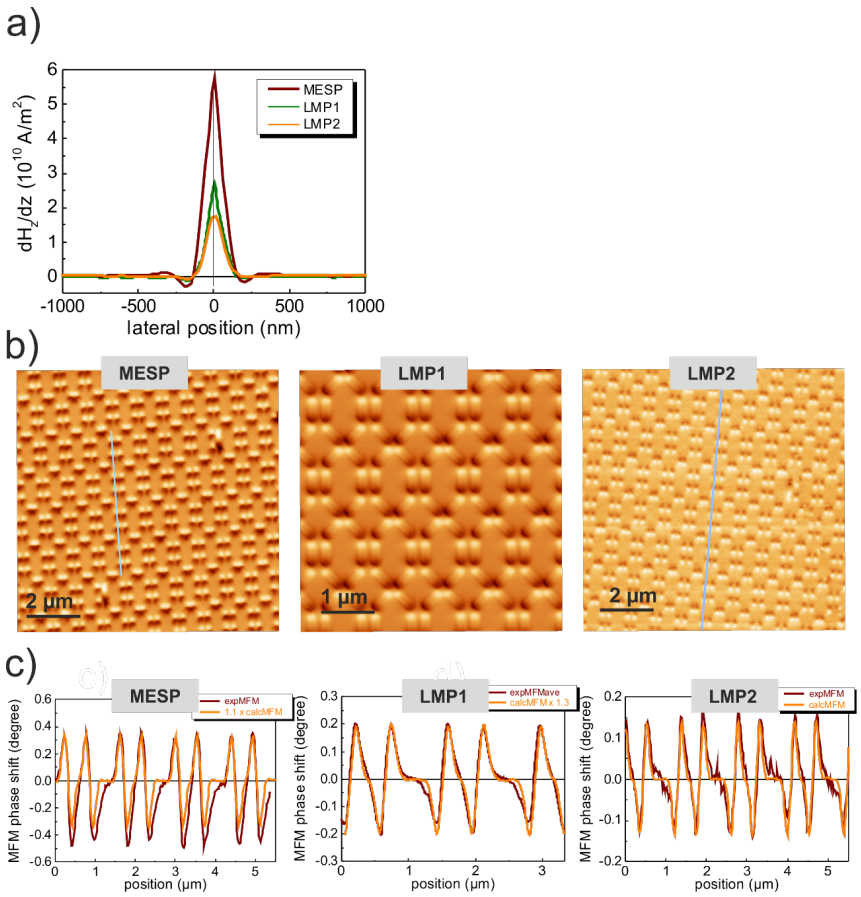


FIGURE A.7. a) One dimensional cut through the Real-space tip transfer function (RS-TTF) along the direction of the cantilever length for three different MFM probes, i.e. a standard moment probe (Bruker MESP, brown), the low moment probe LMP1 displayed in Fig. 6.6c (green) and another low moment MFM probe by NT-MDT (LMP2, orange). The TTFs were derived by deconvolution of MFM measurements with the effective surface charge pattern by means of a Wiener invert filter. For noise reduction, data are averaged in angular segments around the peak maximum with a sliding average of 30°. b) MFM measurements of the UM state with the three probe characterized in a) displaying largely different phase shift contrast. c) Line profiles comparing experimental and calculated MFM signals. The former data are projected 7.5 nm away from the sample surface, the latter are calculated by convolving the effective surface charge pattern (obtained in an elevated height of 7.5 nm) of the ASI with the respective TTF. Related chapter: 6.

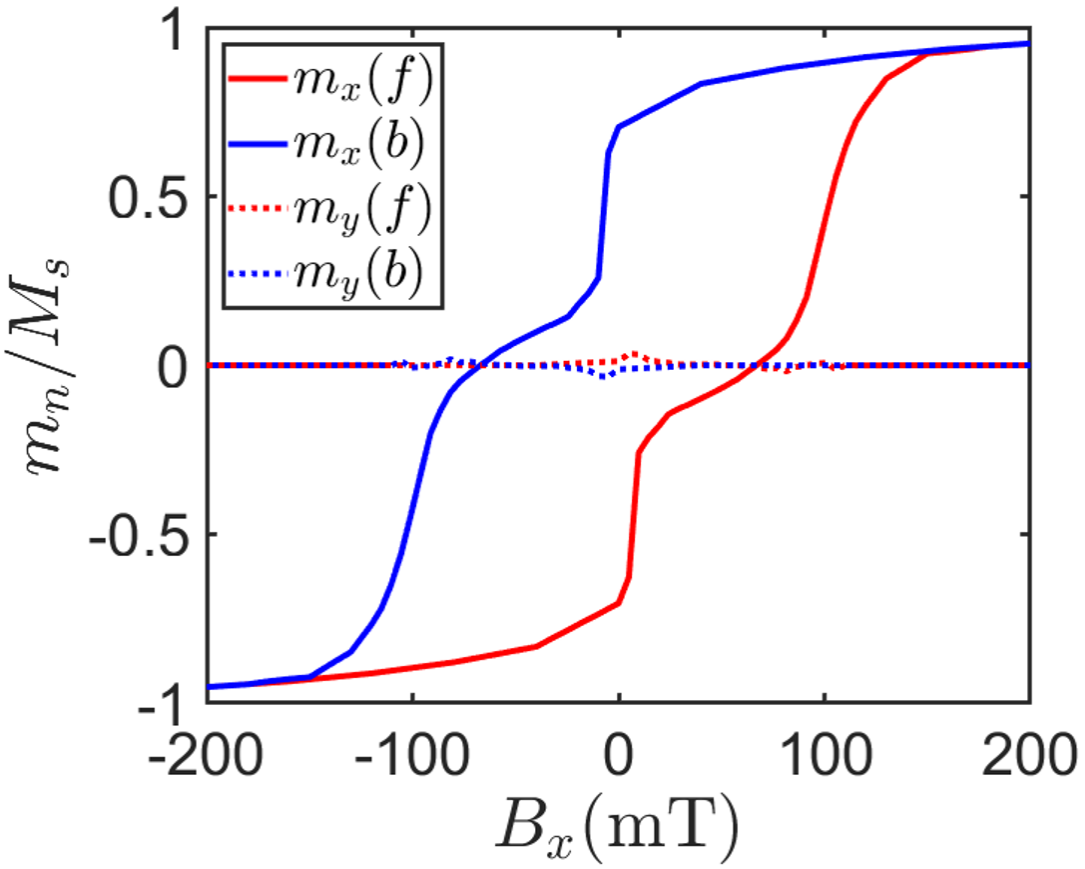


FIGURE A.8. Forward (red) and backward (blue) field-reversal curves for the defect-ASI lattice modelled. Solid and dashed lines depicy the $x$ and $y$-components of the magnetisation, respectively. Related chapters: 8

## A.2 qMFM

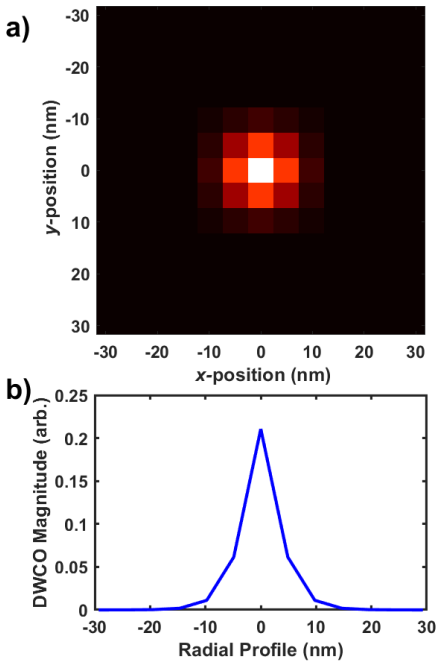


FIGURE A.9. Example of the Domain wall convolution operator (a), and its radially averaged profile (b). Related chapter: 3

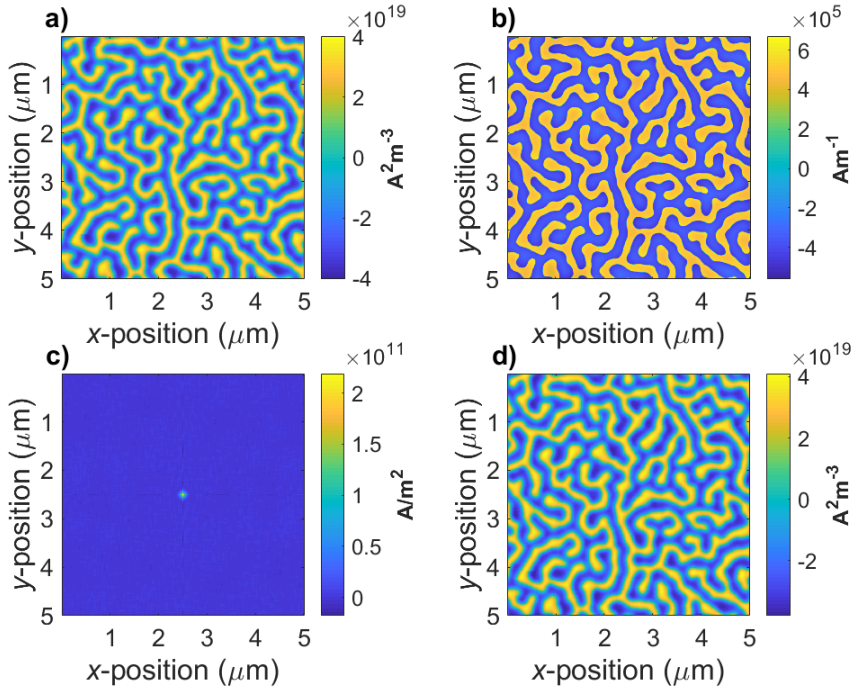


FIGURE A.10. (a) 5$\mu$m×5$\mu$m measured MFM image of CoPt reference sample converted into magnetic force gradient units. (b) Surface charge pattern as calculated from (a). (c) RS-TTF extracted from the deconvolution of (b) from (a) with optimum $\lambda$. (d) Reconstituted MFM image in magnetic force gradient units from convolving (c) and (d). Related chapter: 3.

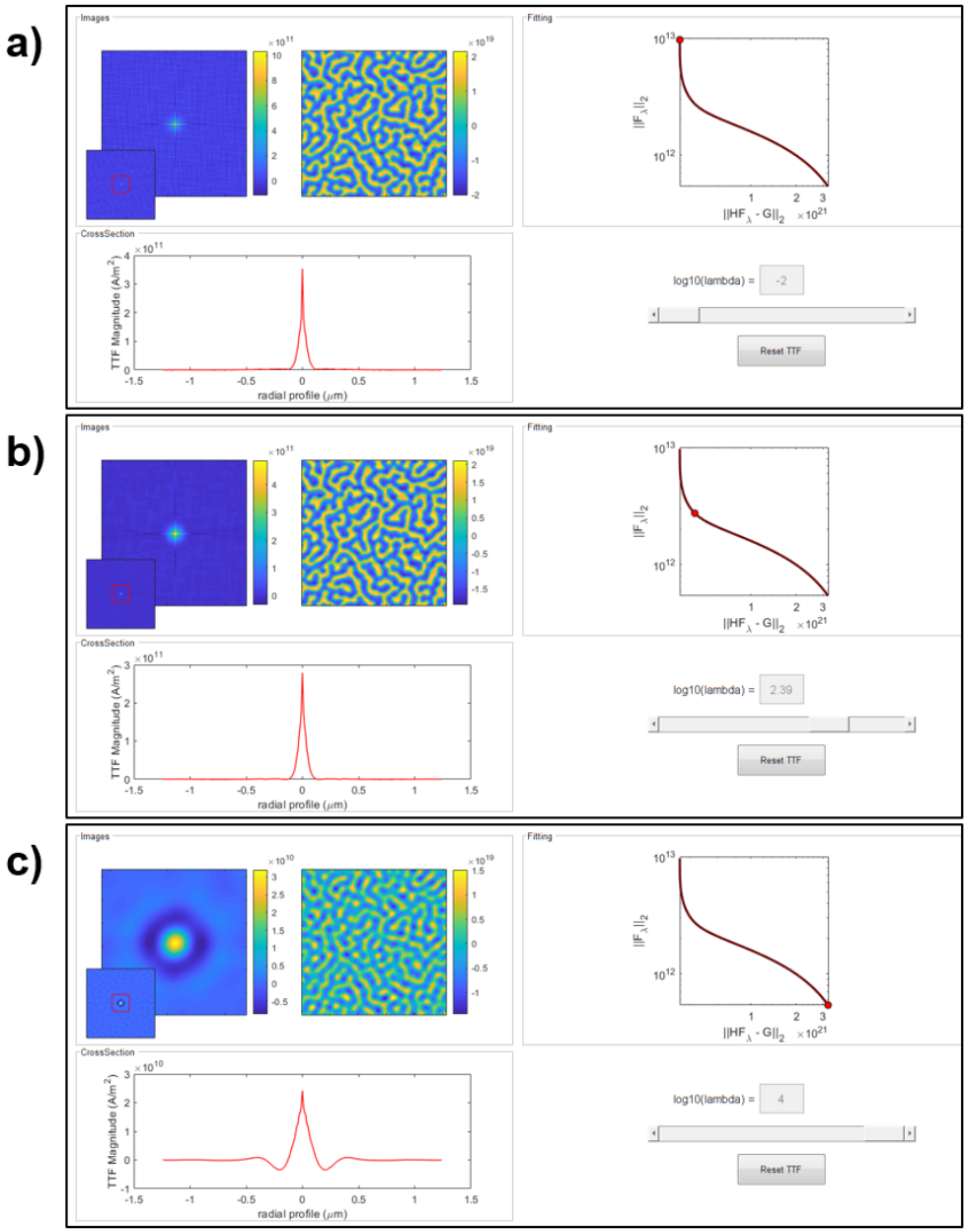


FIGURE A.11. The effect of regularisation parameter ($\lambda$) selection on the TTF and simulated MFM image of the reference sample. Demonstrated is the effect of underdamping (a), adequately damping (b) and overdamping (c) errors in the RS-TTF deconvolution step. Related chapter: 3

## A.3 Local ANE

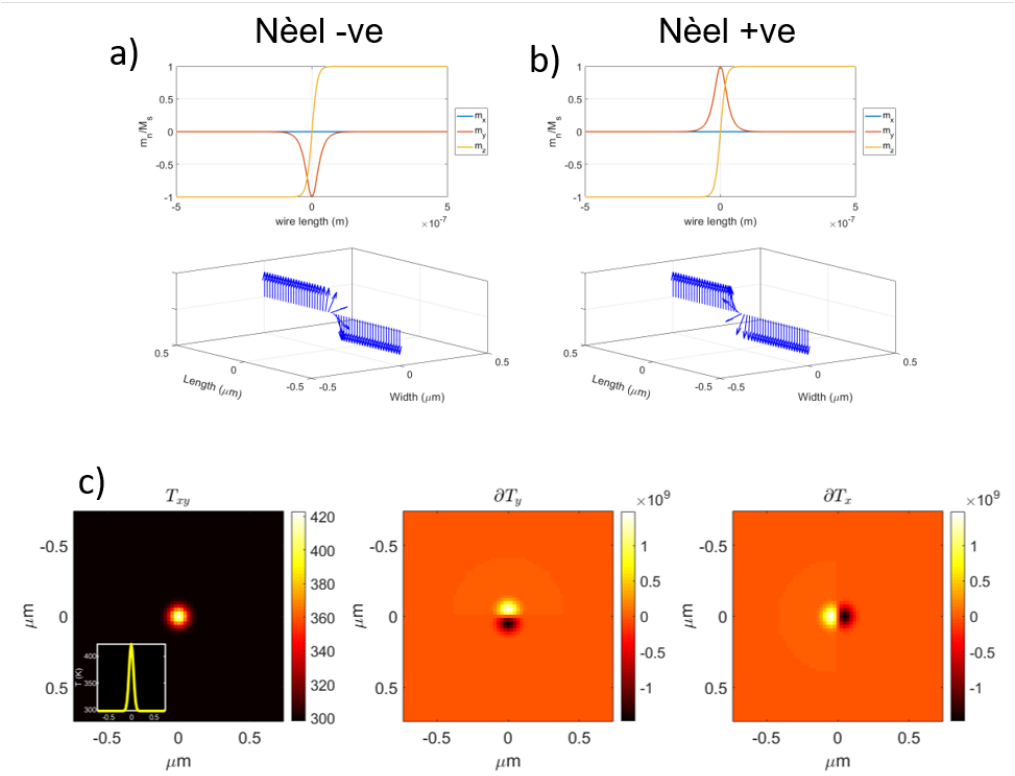


FIGURE A.12. 2D (top) and 3d (bottom) line profile plots of wire with Néel DW in negative (a) and positive (b) direction. (c) Modelled thermal distribution and respective thermal gradients parallel and perpendicular to the modelled wire length. Related chapter 5

## A.4 Electron holography/LTEM

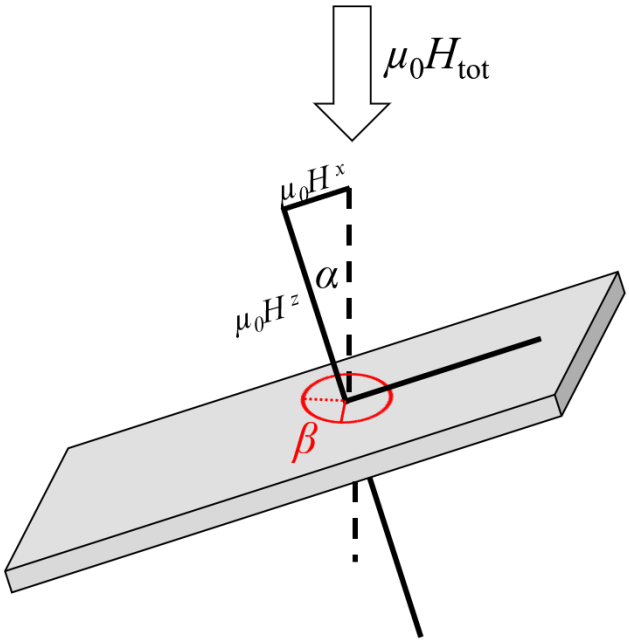


FIGURE A.13. Schematic of field application within TEM using a double-tilt rotation stage. Related chapter: 7.

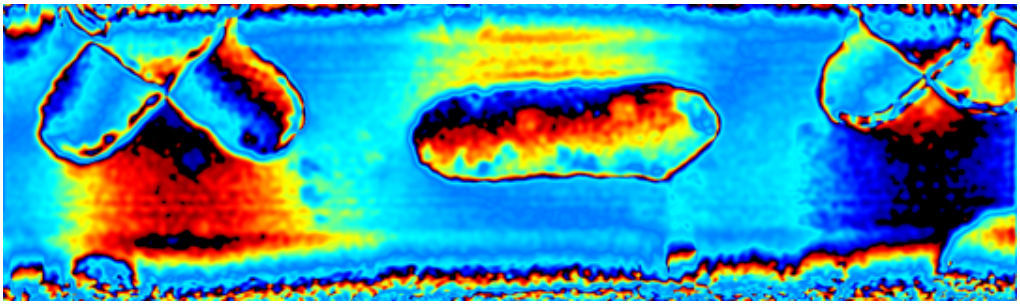

FIGURE A.14. Example of the shadowing effect in electron holography, where the neighbouring NIs impose on the holograph from the tight field-of-view. Related chapter: 7.

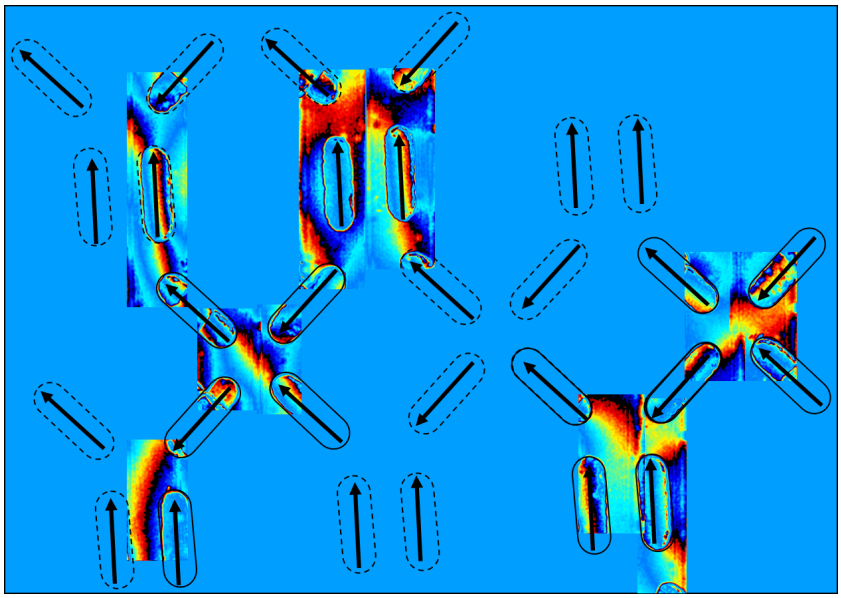

FIGURE A.15. EH of QH-ASI spatially mapped onto the lattice region. Where possible, images have been spliced together to form a full image of a junction, however colour-scheme does not always match due to variances in the intensity within images. Related chapter: 7.

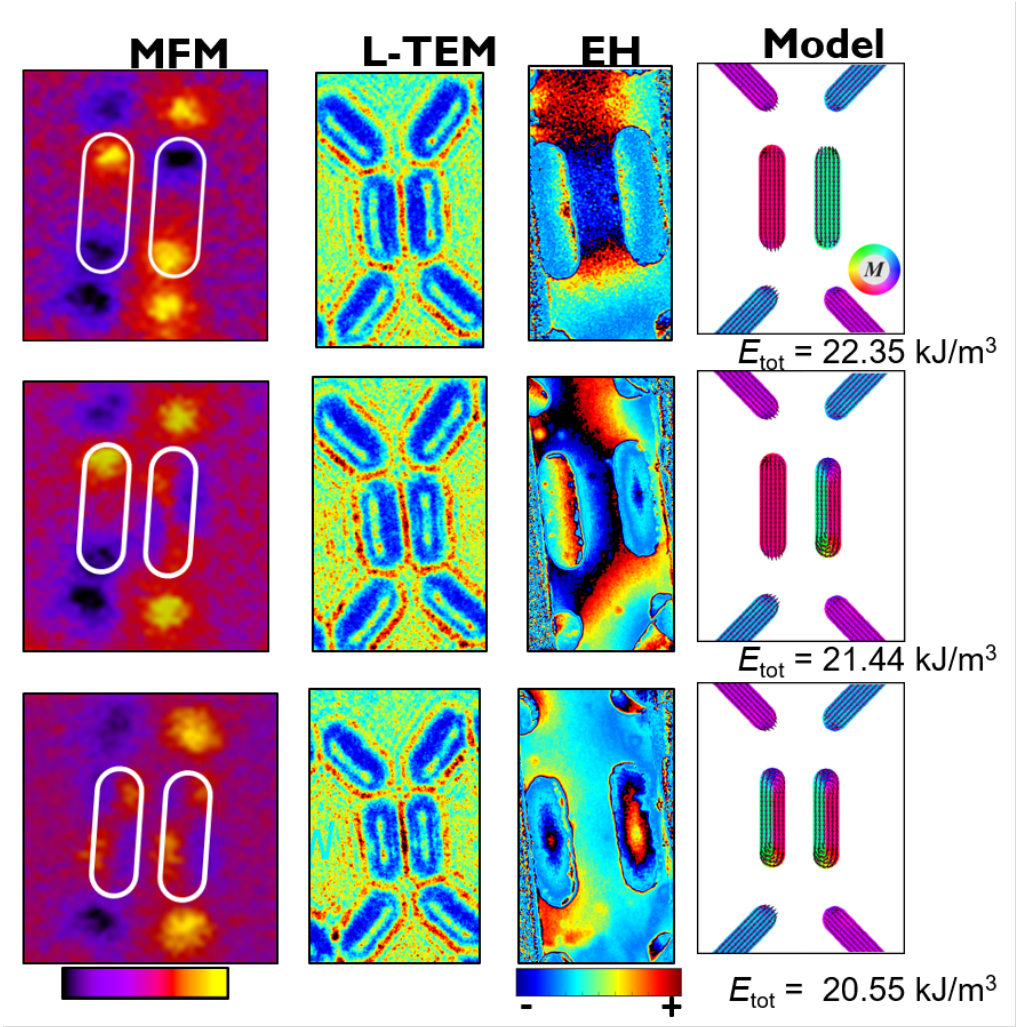


FIGURE A.16. Table comparing simulated magnetisation maps to experimental results from MFM; Lorentz-TEM; and electron holography. Related chapters: 6; 7.

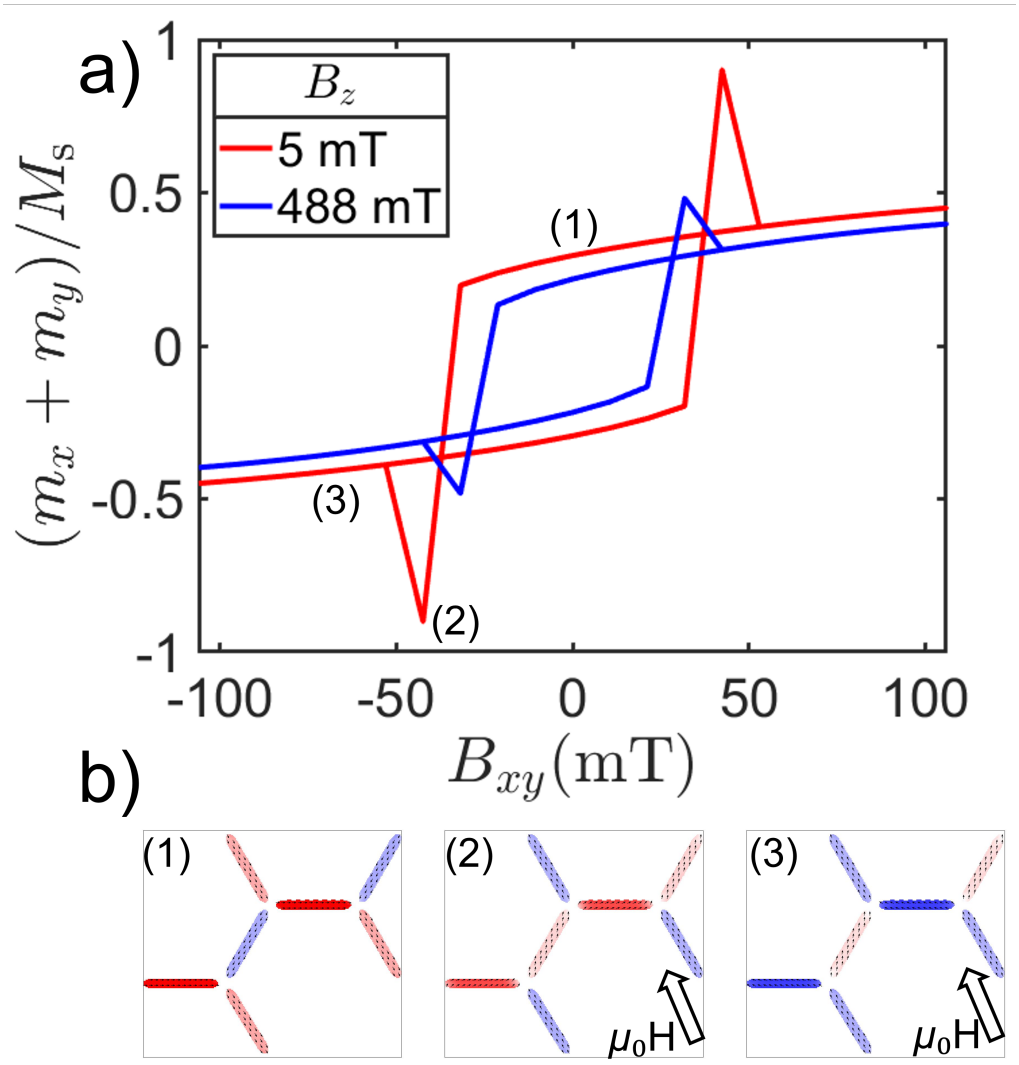


FIGURE A.17. (a) Modelled hysteresis loop demonstrating the effect of out-of-plane field on magnetic reversal of a Kagomé lattice unit cell with field angle $\theta = 67°$ from the horizontal plane. Related chapters: 7; 8

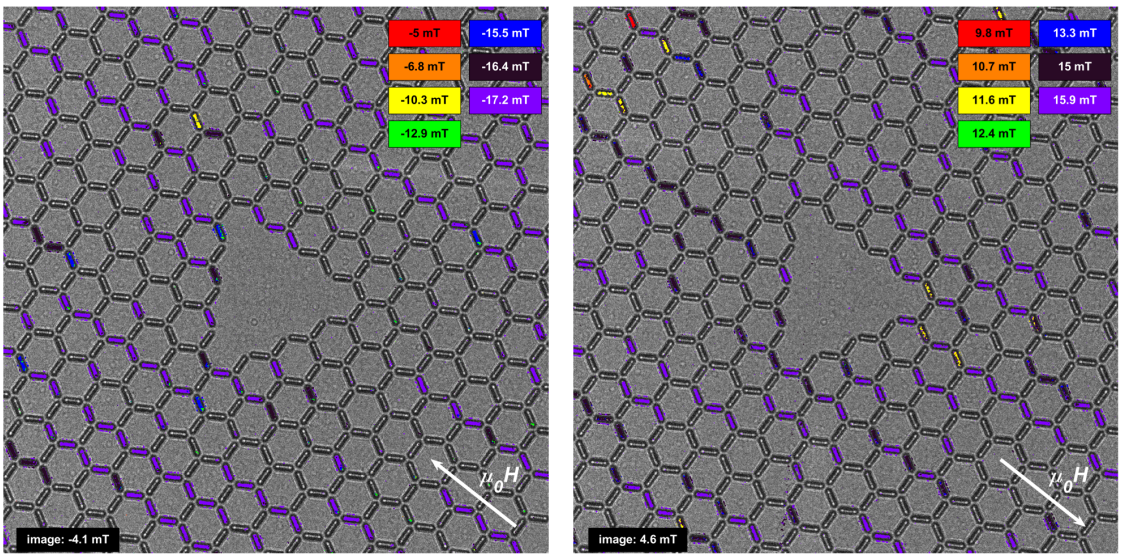


FIGURE A.18. Differential LTEM images of the vacant-defect ASI lattice, image displayed is the reference image and the coloured islands indicate the applied field necessary to result in a field reversal. Related chapters: 8

# BIBLIOGRAPHY


[1] M. Getzlaff, *Fundamentals of Magnetism*.
New York: Springer Berlin Heidelberg, 2008.

[2] N. Spaldin, *Magnetic Materials*.
New York: Cambridge University Press, second ed., 2011.

[3] M. S. Dresselhaus, "SOLID STATE PHYSICS III Magnetic Properties of Solids," 2011.

[4] V. Chaudhary and R. V. Ramanujan, "Magnetocaloric Properties of Fe-Ni-Cr Nanoparticles for Active Cooling," *Scientific Reports*, vol. 6, p. 35156, dec 2016.

[5] R. O'Handley, *Modern magnetic materials : principles and application*.
New York: Wiley and Sons Inc., 2000.

[6] J. M. D. Coey, *Magnetism and magnetic materials*.
New York: Cambridge University Press, 2009.

[7] U. B. Arnalds, J. Chico, H. Stopfel, V. Kapaklis, O. Bärenbold, M. A. Verschuuren, U. Wolff, V. Neu, A. Bergman, and B. Hjörvarsson, "A new look on the two-dimensional Ising model: Thermal artificial spins," *New Journal of Physics*, vol. 18, no. 2, 2016.

[8] R. B. Goldfarb, "The Permeability of Vacuum and the Revised International System of Units," *IEEE Magnetics Letters*, vol. 8, no. 2017, pp. 1–3, 2017.

[9] A. S. Arrott, "Visualization and Interpretation of Magnetic Configurations Using Magnetic Charge," *IEEE Magnetics Letters*, vol. 7, pp. 1–5, 2016.

[10] J. Salach, R. Szewczyk, A. Bieńkowski, and P. Frydrych, "Methodology of testing the magnetoelastic characteristics of ring-shaped cores under uniform compressive and tensile stresses," *Journal of Electrical Engineering*, vol. 61, no. 7 SUPPL, pp. 93–95, 2013.

[11] E. Klokholm and J. A. Aboaf, "The saturation magnetostriction of permalloy films," *Journal of Applied Physics*, vol. 52, no. 3, pp. 2474–2476, 1981.

[12] J. Staunton, P. Strange, B. L. Gyorffy, M. Matsumoto, J. Poulter, H. Ebert, and N. P. Archibald, "Theory of Magnetocrystalline Anisotropy," in *The Effects of Relativity in Atoms, Molecules, and the Solid State* (S. Wilson, ed.), pp. 295–317, New York: Plenum Press, 1991.

[13] B. D. Cullity and C. D. Graham, *Introduction to magnetic materials*. Hoboken, NJ, USA: WILEY-VCH Verlag, second ed., 2009.

[14] E. C. Stoner and E. P. Wohlfarth, "A Mechanism of Magnetic Hysteresis in Heterogeneous Alloys," *Philosophical Transactions of the Royal Society A: Mathematical, Physical and Engineering Sciences*, vol. 240, pp. 599–642, may 1948.

[15] L. Neel, "Magnetism and Local Molecular Field," *Nobel Lecture Series*, 1970.

[16] F. Bloch, "Zur Theorie des Austauschproblems und der Remanenzerscheinung der Ferromagnetika," *Zeitschrift für Physik*, vol. 74, no. 5-6, pp. 295–335, 1932.

[17] A. DeSimone, H. Knüpfer, and F. Otto, "2-d stability of the Néel wall," *Calculus of Variations and Partial Differential Equations*, vol. 27, pp. 233–253, oct 2006.

[18] M. J. P. Gingras, "Spin Ice," in *Frustrated Spin Systems*, pp. 383–474, WORLD SCIENTIFIC, mar 2009.

[19] J. D. Bernal and R. H. Fowler, "A theory of water and ionic solution, with particular reference to hydrogen and hydroxyl ions," *The Journal of Chemical Physics*, vol. 1, no. 8, pp. 515–548, 1933.

[20] L. Pauling, "The Structure and Entropy of Ice and of Other Crystals with Some Randomness of Atomic Arrangement," *Journal of the American Chemical Society*, vol. 57, no. 12, pp. 2680–2684, 1935.

[21] S. T. Bramwell, "Spin Ice State in Frustrated Magnetic Pyrochlore Materials," *Science*, vol. 294, pp. 1495–1501, nov 2001.

[22] J. S. Gardner, M. J. Gingras, and J. E. Greedan, "Magnetic pyrochlore oxides," *Reviews of Modern Physics*, vol. 82, no. 1, pp. 53–107, 2010.

[23] A. P. Ramirez, A. Hayashi, R. J. Cava, R. Siddharthan, and B. S. Shastry, "Zero-point entropy in 'spin ice'," *Nature*, vol. 399, pp. 333–335, may 1999.

[24] C. Castelnovo, R. Moessner, and S. L. Sondhi, "Magnetic monopoles in spin ice," *Nature*, vol. 451, pp. 42–45, jan 2008.

[25] S. T. Bramwell, S. R. Giblin, S. Calder, R. Aldus, D. Prabhakaran, and T. Fennell, "Measurement of the charge and current of magnetic monopoles in spin ice," *Nature*, vol. 461, pp. 956–959, oct 2009.

[26] P. A. M. Dirac, "Quantised Singularities in the Electromagnetic Field," *Proceedings of the Royal Society A: Mathematical, Physical and Engineering Sciences*, vol. 133, pp. 60–72, sep 1931.

[27] L. D. C. Jaubert and P. C. W. Holdsworth, "Signature of magnetic monopole and Dirac string dynamics in spin ice," *Nature Physics*, vol. 5, pp. 258–261, apr 2009.

[28] D. J. P. Morris, D. A. Tennant, S. A. Grigera, B. Klemke, C. Castelnovo, R. Moessner, C. Czternasty, M. Meissner, K. C. Rule, J.-U. Hoffmann, K. Kiefer, S. Gerischer, D. Slobinsky, and R. S. Perry, "Dirac strings and magnetic monopoles in the spin ice Dy2Ti2O7," *Science*, vol. 326, no. 411, pp. 411–414, 2009.

[29] S. R. Giblin, S. T. Bramwell, P. C. Holdsworth, D. Prabhakaran, and I. Terry, "Creation and measurement of long-lived magnetic monopole currents in spin ice," *Nature Physics*, vol. 7, no. 3, pp. 252–258, 2011.

[30] E. Y. Vedmedenko, "Dynamics of Bound Monopoles in Artificial Spin Ice: How to Store Energy in Dirac Strings," *Physical Review Letters*, vol. 116, p. 077202, feb 2016.

[31] S. H. Skjærvø, C. H. Marrows, R. L. Stamps, and L. J. Heyderman, "Advances in artificial spin ice," *Nature Reviews Physics*, vol. 2, pp. 13–28, jan 2020.

[32] H. Arava, P. M. Derlet, J. Vijayakumar, J. Cui, N. S. Bingham, A. Kleibert, and L. J. Heyderman, "Computational logic with square rings of nanomagnets," *Nanotechnology*, vol. 29, no. 26, 2018.

[33] M. Krawczyk and D. Grundler, "Review and prospects of magnonic crystals and devices with reprogrammable band structure," *Journal of Physics Condensed Matter*, vol. 26, no. 12, 2014.

[34] S. Gliga, E. Iacocca, and O. G. Heinonen, "Dynamics of reconfigurable artificial spin ice: Toward magnonic functional materials," *APL Materials*, vol. 8, p. 040911, apr 2020.

[35] A. Libál, C. Reichhardt, and C. J. Reichhardt, "Realizing colloidal artificial ice on arrays of optical traps," *Physical Review Letters*, vol. 97, no. 22, pp. 1–4, 2006.

[36] A. Ortiz-Ambriz and P. Tierno, "Engineering of frustration in colloidal artificial ices realized on microfeatured grooved lattices," *Nature Communications*, vol. 7, pp. 1–7, 2016.

[37] R. F. Wang, C. Nisoli, R. S. Freitas, J. Li, W. McConville, B. J. Cooley, M. S. Lund, N. Samarth, C. Leighton, V. H. Crespi, and P. Schiffer, "Artificial 'spin ice' in a geometrically frustrated lattice of nanoscale ferromagnetic islands," *Nature*, vol. 439, pp. 303–306, jan 2006.

[38] J. P. Morgan, A. Stein, S. Langridge, and C. H. Marrows, "Thermal ground-state ordering and elementary excitations in artificial magnetic square ice," *Nature Physics*, vol. 7, no. 1, pp. 75–79, 2011.

[39] Y. Wang, S. Kang, A. Khan, G. Ruttner, S. Y. Leigh, M. Murray, S. Abeytunge, G. Peterson, M. Rajadhyaksha, S. Dintzis, S. Javid, and J. T. Liu, "Quantitative molecular phenotyping with topically applied SERS nanoparticles for intraoperative guidance of breast cancer lumpectomy," *Scientific Reports*, vol. 6, no. February, pp. 1–12, 2016.

[40] J. C. Gartside, D. M. Arroo, D. M. Burn, V. L. Bemmer, A. Moskalenko, L. F. Cohen, and W. R. Branford, "Realization of ground state in artificial kagome spin ice via topological defect-driven magnetic writing," *Nature Nanotechnology*, vol. 13, pp. 53–58, jan 2018.

[41] Y. Li, G. W. Paterson, G. M. Macauley, F. S. Nascimento, C. Ferguson, S. A. Morley, M. C. Rosamond, E. H. Linfield, D. A. MacLaren, R. Macêdo, C. H. Marrows, S. McVitie, and R. L. Stamps, "Superferromagnetism and Domain-Wall Topologies in Artificial "Pinwheel" Spin Ice," *ACS Nano*, vol. 13, pp. 2213–2222, jan 2019.

[42] E. Mengotti, L. J. Heyderman, A. F. Rodríguez, F. Nolting, R. V. Hügli, and H. B. Braun, "Real-space observation of emergent magnetic monopoles and associated Dirac strings in artificial kagome spin ice," *Nature Physics*, vol. 7, no. 1, pp. 68–74, 2011.

[43] E. Iacocca, S. Gliga, R. L. Stamps, and O. Heinonen, "Reconfigurable wave band structure of an artificial square ice," *Physical Review B*, vol. 93, no. 13, 2016.

[44] M. B. Jungfleisch, J. Sklenar, J. Ding, J. Park, J. E. Pearson, V. Novosad, P. Schiffer, and A. Hoffmann, "High-Frequency Dynamics Modulated by Collective Magnetization Reversal in Artificial Spin Ice," *Physical Review Applied*, vol. 8, no. 6, pp. 1–7, 2017.

[45] A. Ghosh, F. Ma, J. Lourembam, X. Jin, R. Maddu, Q. J. Yap, and S. Ter Lim, "Emergent Dynamics of Artificial Spin-Ice Lattice Based on an Ultrathin Ferromagnet," *Nano Letters*, 2019.

[46] T. Dion, D. M. Arroo, K. Yamanoi, T. Kimura, J. C. Gartside, L. F. Cohen, H. Kurebayashi, and W. R. Branford, "Tunable magnetization dynamics in artificial spin ice via shape anisotropy modification," *Physical Review B*, vol. 100, no. 5, pp. 1–11, 2019.

[47] S. Lendinez and M. B. Jungfleisch, "Magnetization dynamics in artificial spin ice," *Journal of Physics: Condensed Matter*, vol. 32, no. 1, p. 013001, 2020.

[48] Y. Strengers, *Smart Energy Technologies in Everyday Life*.
London: Palgrave Macmillan UK, 2013.

[49] N. R. Council, *Meeting the Energy Needs of Future Warriors*.
Washington, D.C.: National Academies Press, aug 2004.

[50] C. Nisoli, R. Moessner, and P. Schiffer, "Colloquium: Artificial spin ice: Designing and imaging magnetic frustration," *Reviews of Modern Physics*, vol. 85, no. 4, pp. 1473–1490, 2013.

[51] J. G. Ku, X. Y. Liu, H. H. Chen, R. D. Deng, and Q. X. Yan, "Interaction between two magnetic dipoles in a uniform magnetic field," *AIP Advances*, vol. 6, p. 025004, feb 2016.

[52] G. Möller and R. Moessner, "Artificial Square Ice and Related Dipolar Nanoarrays," *Physical Review Letters*, vol. 96, p. 237202, jun 2006.

[53] Y. Perrin, B. Canals, and N. Rougemaille, "Extensive degeneracy, Coulomb phase and magnetic monopoles in artificial square ice," *Nature*, vol. 540, pp. 410–413, dec 2016.

[54] Y. Qi, T. Brintlinger, and J. Cumings, "Direct observation of the ice rule in an artificial kagome spin ice," *Physical Review B*, vol. 77, p. 094418, mar 2008.

[55] S. Ladak, D. E. Read, G. K. Perkins, L. F. Cohen, and W. R. Branford, "Direct observation of magnetic monopole defects in an artificial spin-ice system," *Nature Physics*, vol. 6, pp. 359–363, may 2010.

[56] W. R. Branford, S. Ladak, D. E. Read, K. Zeissler, and L. F. Cohen, "Emerging Chirality in Artificial Spin Ice," *Science*, vol. 335, pp. 1597–1600, mar 2012.

[57] B. L. Le, J. Park, J. Sklenar, G. W. Chern, C. Nisoli, J. D. Watts, M. Manno, D. W. Rench, N. Samarth, C. Leighton, and P. Schiffer, "Understanding magnetotransport signatures in networks of connected permalloy nanowires," *Physical Review B*, vol. 95, no. 6, pp. 1–5, 2017.

[58] S. Olivari, *Magnetotransport measurements of NiFe Artificial Spin Ice lattices*.
PhD thesis, Cardiff University, 2016.

[59] B. L. Le, *Magnetotransport of connected artificial spin ice*.
PhD thesis, University of Illinois, 2016.

[60] C. Nisoli, "Topology by Design in Magnetic Nano-materials: Artificial Spin Ice," in *The Role of Topology in Materials* (S. Gupta and A. Saxena, eds.), pp. 85–112, Springer, Cham., 1 ed., 2018.

[61] H. Arava, N. Leo, D. Schildknecht, J. Cui, J. Vijayakumar, P. M. Derlet, A. Kleibert, and L. J. Heyderman, "Engineering Relaxation Pathways in Building Blocks of Artificial Spin Ice for Computation," *Physical Review Applied*, vol. 11, p. 054086, may 2019.

[62] V. S. Bhat, J. Sklenar, B. Farmer, J. Woods, J. T. Hastings, S. J. Lee, J. B. Ketterson, and L. E. De Long, "Controlled magnetic reversal in permalloy films patterned into artificial quasicrystals," *Physical Review Letters*, vol. 111, no. 7, pp. 1–5, 2013.

[63] V. Brajuskovic, A. Addi, C. Phatak, and A. K. Petford-Long, "Observation of transient states during magnetization reversal in a quasicrystal artificial spin ice," *Physical Review B*, vol. 98, no. 9, pp. 1–9, 2018.

[64] D. Shi, Z. Budrikis, A. Stein, S. A. Morley, P. D. Olmsted, G. Burnell, and C. H. Marrows, "Frustration and thermalization in an artificial magnetic quasicrystal," *Nature Physics*, vol. 14, no. 3, pp. 309–314, 2018.

[65] F. Barrows, V. Brajuskovic, A. K. Petford-Long, and C. Phatak, "Emergent magnetic ordering and topological frustration in quasicrystal artificial spin ices," *Physical Review B*, vol. 99, p. 094424, mar 2019.

[66] C. L. Henley, "The "Coulomb Phase" in Frustrated Systems," *Annual Review of Condensed Matter Physics*, vol. 1, pp. 179–210, aug 2010.

[67] M. J. Morrison, T. R. Nelson, and C. Nisoli, "Unhappy vertices in artificial spin ice: New degeneracies from vertex frustration," *New Journal of Physics*, vol. 15, 2013.

[68] G.-W. Chern, M. J. Morrison, and C. Nisoli, "Degeneracy and Criticality from Emergent Frustration in Artificial Spin Ice," *Physical Review Letters*, vol. 111, p. 177201, oct 2013.

[69] I. Gilbert, G.-W. Chern, S. Zhang, L. O'Brien, B. Fore, C. Nisoli, and P. Schiffer, "Emergent ice rule and magnetic charge screening from vertex frustration in artificial spin ice," *Nature Physics*, vol. 10, pp. 670–675, sep 2014.

[70] Y. Lao, F. Caravelli, M. Sheikh, J. Sklenar, D. Gardeazabal, J. D. Watts, A. M. Albrecht, A. Scholl, K. Dahmen, C. Nisoli, and P. Schiffer, "Classical topological order in the kinetics of artificial spin ice," *Nature Physics*, vol. 14, pp. 723–727, jul 2018.

[71] H. Stopfel, E. Östman, I.-A. Chioar, D. Greving, U. B. Arnalds, T. P. A. Hase, A. Stein, B. Hjörvarsson, and V. Kapaklis, "Magnetic order and energy-scale hierarchy in artificial spin-ice structures," *Physical Review B*, vol. 98, p. 014435, jul 2018.

[72] S. Gliga, G. Hrkac, C. Donnelly, J. Büchi, A. Kleibert, J. Cui, A. Farhan, E. Kirk, R. V. Chopdekar, Y. Masaki, N. S. Bingham, A. Scholl, R. L. Stamps, and L. J. Heyderman,

"Emergent dynamic chirality in a thermally driven artificial spin ratchet," *Nature Materials*, vol. 16, no. 11, pp. 1106–1112, 2017.

[73] R. Macêdo, G. M. Macauley, F. S. Nascimento, and R. L. Stamps, "Apparent ferromagnetism in the pinwheel artificial spin ice," *Physical Review B*, vol. 98, p. 014437, jul 2018.

[74] M. Wyss, S. Gliga, D. Vasyukov, L. Ceccarelli, G. Romagnoli, J. Cui, A. Kleibert, R. L. Stamps, and M. Poggio, "Stray-Field Imaging of a Chiral Artificial Spin Ice during Magnetization Reversal," *ACS Nano*, vol. 13, pp. 13910–13916, dec 2019.

[75] G. M. Macauley, G. W. Paterson, Y. Li, R. Macêdo, S. McVitie, and R. L. Stamps, "Ice-rule made manifold: phase transitions, topological defects and manifold restoration in two-dimensional artificial spin systems," *arXiv preprint arXiv:1908.08903*, pp. 1–18, aug 2019.

[76] X. Zhou, G.-L. Chua, N. Singh, and A. O. Adeyeye, " Large Area Artificial Spin Ice and Anti-Spin Ice Ni 80 Fe 20 Structures: Static and Dynamic Behavior ," *Advanced Functional Materials*, vol. 26, no. 9, pp. 1437–1444, 2016.

[77] A. Farhan, C. F. Petersen, S. Dhuey, L. Anghinolfi, Q. H. Qin, M. Saccone, S. Velten, C. Wuth, S. Gliga, P. Mellado, M. J. Alava, A. Scholl, and S. van Dijken, "Nanoscale control of competing interactions and geometrical frustration in a dipolar trident lattice," *Nature Communications*, vol. 8, p. 995, dec 2017.

[78] J. Lehmann, C. Donnelly, P. M. Derlet, L. J. Heyderman, and M. Fiebig, "Poling of an artificial magneto-toroidal crystal," *Nature Nanotechnology*, vol. 14, no. 2, pp. 141–144, 2019.

[79] J. Sklenar, Y. Lao, A. Albrecht, J. D. Watts, C. Nisoli, G.-W. Chern, and P. Schiffer, "Field-induced phase coexistence in an artificial spin ice," *Nature Physics*, vol. 15, pp. 191–195, feb 2019.

[80] F. Y. Wu, "The Potts model," *Reviews of Modern Physics*, vol. 54, pp. 235–268, jan 1982.

[81] E. Östman, H. Stopfel, I. A. Chioar, U. B. Arnalds, A. Stein, V. Kapaklis, and B. Hjörvarsson, "Interaction modifiers in artificial spin ices," *Nature Physics*, vol. 14, no. 4, pp. 375–379, 2018.

[82] J. S. Song, "Theory of Magnetic Monopoles and Electric-Magnetic Duality: A Prelude to S -Duality," *J. Undergrad. Sci*, vol. 3, no. Summer, pp. 47–55, 1996.

[83] K. M. Ellis, "Magnetic Monopoles: Quantization and Quasiparticles," 2013.

[84] J. P. Morgan, A. Stein, S. Langridge, and C. H. Marrows, "Magnetic reversal of an artificial square ice: Dipolar correlation and charge ordering," *New Journal of Physics*, vol. 13, 2011.

[85] S. D. Pollard, V. Volkov, and Y. Zhu, "Propagation of magnetic charge monopoles and Dirac flux strings in an artificial spin-ice lattice," *Physical Review B - Condensed Matter and Materials Physics*, vol. 85, no. 18, pp. 1–5, 2012.

[86] A. Farhan, P. M. Derlet, L. Anghinolfi, A. Kleibert, and L. J. Heyderman, "Magnetic charge and moment dynamics in artificial kagome spin ice," *Physical Review B*, vol. 96, p. 064409, aug 2017.

[87] Y. Shen, O. Petrova, P. Mellado, S. Daunheimer, J. Cumings, and O. Tchernyshyov, "Dynamics of artificial spin ice: a continuous honeycomb network," *New Journal of Physics*, vol. 14, p. 035022, mar 2012.

[88] P. Mellado, O. Petrova, Y. Shen, and O. Tchernyshyov, "Dynamics of Magnetic Charges in Artificial Spin Ice," *Physical Review Letters*, vol. 105, p. 187206, oct 2010.

[89] K. Zeissler, S. K. Walton, S. Ladak, D. E. Read, T. Tyliszczak, L. F. Cohen, and W. R. Branford, "The non-random walk of chiral magnetic charge carriers in artificial spin ice," *Scientific Reports*, vol. 3, pp. 1–7, 2013.

[90] D. M. Burn, M. Chadha, S. K. Walton, and W. R. Branford, "Dynamic interaction between domain walls and nanowire vertices," *Physical Review B - Condensed Matter and Materials Physics*, vol. 90, no. 14, pp. 1–6, 2014.

[91] S. K. Walton, K. Zeissler, D. M. Burn, S. Ladak, D. E. Read, T. Tyliszczak, L. F. Cohen, and W. R. Branford, "Limitations in artificial spin ice path selectivity: The challenges beyond topological control," *New Journal of Physics*, vol. 17, 2015.

[92] T. J. Broomhall and T. J. Hayward, "Suppression of Stochastic Domain Wall Pinning Through Control of Gilbert Damping," *Scientific Reports*, vol. 7, p. 17100, dec 2017.

[93] N. Rougemaille, F. Montaigne, B. Canals, M. Hehn, H. Riahi, D. Lacour, and J.-C. Toussaint, "Chiral nature of magnetic monopoles in artificial spin ice," *New Journal of Physics*, vol. 15, p. 035026, mar 2013.

[94] S. Gliga, A. Kákay, L. J. Heyderman, R. Hertel, and O. G. Heinonen, "Broken vertex symmetry and finite zero-point entropy in the artificial square ice ground state," *Physical Review B*, vol. 92, p. 060413, aug 2015.

[95] A. Tikhonov and V. Arsenin, *Solutions of Ill-Posed Problems*.
New York: Winston, 1977.

[96] Y. Martin and H. K. Wickramasinghe, “Magnetic imaging by "force microscopy" with 1000 Å resolution,” *Applied Physics Letters*, vol. 50, no. 20, pp. 1455–1457, 1987.

[97] J. J. Sáenz, N. García, P. Grütter, E. Meyer, H. Heinzelmann, R. Wiesendanger, L. Rosenthaler, H. R. Hidber, and H. Güntherodt, “Observation of magnetic forces by the atomic force microscope,” *Journal of Applied Physics*, vol. 62, pp. 4293–4295, nov 1987.

[98] H. J. Hug, “A low temperature ultrahigh vaccum scanning force microscope,” *Review of Scientific Instruments*, vol. 70, no. 9, pp. 3625–3640, 1999.

[99] D. Peterka, A. Enders, G. Haas, and K. Kern, “Combined Kerr microscope and magnetic force microscope for variable temperature ultrahigh vacuum investigations,” *Review of Scientific Instruments*, vol. 74, no. 5, pp. 2744–2748, 2003.

[100] Y. Seo, P. Cadden-Zimansky, and V. Chandrasekhar, “Low-temperature high-resolution magnetic force microscopy using a quartz tuning fork,” *Applied Physics Letters*, vol. 87, no. 10, pp. 10–12, 2005.

[101] U. Celik, O. Karci, Y. Uysalli, H. O. Ozer, and A. Oral, “Radiation pressure excitation of a low temperature atomic force/magnetic force microscope for imaging in 4-300 K temperature range,” *Review of Scientific Instruments*, vol. 88, p. 013705, jan 2017.

[102] M. Serri, M. Mannini, L. Poggini, E. Vélez-Fort, B. Cortigiani, P. Sainctavit, D. Rovai, A. Caneschi, and R. Sessoli, “Low-Temperature Magnetic Force Microscopy on Single Molecule Magnet-Based Microarrays,” *Nano Letters*, vol. 17, no. 3, pp. 1899–1905, 2017.

[103] S. Vock, K. Tschulik, M. Uhlemann, C. Hengst, S. Fähler, L. Schultz, and V. Neu, “Magnetostatic nearest neighbor interactions in a Co48Fe52 nanowire array probed by in-field magnetic force microscopy,” *Journal of Applied Physics*, vol. 118, no. 23, 2015.

[104] A. Haldar and A. O. Adeyeye, “Vortex chirality control in circular disks using dipole-coupled nanomagnets,” *Applied Physics Letters*, vol. 106, no. 3, 2015.

[105] H. Corte-León, L. A. Rodríguez, M. Pancaldi, C. Gatel, D. Cox, E. Snoeck, V. Antonov, P. Vavassori, and O. Kazakova, “Magnetic imaging using geometrically constrained nano-domain walls,” *Nanoscale*, vol. 11, no. 10, pp. 4478–4488, 2019.

[106] O. Kazakova, R. Puttock, C. Barton, H. Corte-León, M. Jaafar, V. Neu, and A. Asenjo, “Frontiers of magnetic force microscopy,” *Journal of Applied Physics*, vol. 125, p. 060901, feb 2019.

[107] “"Point Probe® Plus Magnetic Force Microscopy - Reflex Coating" From Nanosensors.”

[108] R. García and R. Perez, “Dynamic atomic force microscopy methods,” *Surface Science Reports*, vol. 47, pp. 197–301, sep 2002.

[109] M. R. Freeman, "Advances in Magnetic Microscopy," *Science*, vol. 294, pp. 1484–1488, nov 2001.

[110] D. Sander, S. O. Valenzuela, D. Makarov, C. H. Marrows, E. E. Fullerton, P. Fischer, J. McCord, P. Vavassori, S. Mangin, P. Pirro, B. Hillebrands, A. D. Kent, T. Jungwirth, O. Gutfleisch, C. G. Kim, and A. Berger, "The 2017 Magnetism Roadmap," *Journal of Physics D: Applied Physics*, vol. 50, p. 363001, sep 2017.

[111] H. J. Hug, B. Stiefel, P. J. A. van Schendel, A. Moser, R. Hofer, S. Martin, H.-J. Güntherodt, S. Porthun, L. Abelmann, J. C. Lodder, G. Bochi, and R. C. O'Handley, "Quantitative magnetic force microscopy on perpendicularly magnetized samples," *Journal of Applied Physics*, vol. 83, pp. 5609–5620, jun 1998.

[112] P. J. Van Schendel, H. J. Hug, B. Stiefel, S. Martin, and H. J. Güntherodt, "A method for the calibration of magnetic force microscopy tips," *Journal of Applied Physics*, vol. 88, no. 1, pp. 435–445, 2000.

[113] J. Lohau, S. Kirsch, A. Carl, G. Dumpich, and E. F. Wassermann, "Quantitative determination of effective dipole and monopole moments of magnetic force microscopy tips," *Journal of Applied Physics*, vol. 86, no. 6, pp. 3410–3417, 1999.

[114] J. Lohau, S. Kirsch, A. Carl, and E. F. Wassermann, "Quantitative determination of the magnetization and stray field of a single domain Co/Pt dot with magnetic force microscopy," *Applied Physics Letters*, vol. 76, no. 21, pp. 3094–3096, 2000.

[115] D. Sarid, *Scanning Force Microscopy: With Applications to Electric, Magnetic, and Atomic Forces*.
New York: Oxford University Press, 1994.

[116] D. Sarid, *Exploring Scanning Probe Microscopy with MATHEMATICA*.
WILEY-VCH Verlag GmbH and Co, second ed., 2007.

[117] E. Meyer, H. J. Hug, and R. Bennewitz, *Scanning Probe Microscopy*.
Advanced Texts in Physics, Berlin, Heidelberg: Springer Berlin Heidelberg, 2004.

[118] S. N. Magonov, V. Eilings, and M.-H. Whangbo, "Phase imaging and stiffness in tapping-mode atomic force microscopy," *Surface Science*, vol. 375, pp. 385–391, 1997.

[119] M.-h. H. Whangbo, G. Bar, and R. Brandsch, "Description of phase imaging in tapping mode atomic force microscopy by harmonic approximation," *Surface Science*, vol. 411, pp. L794–L801, aug 1998.

[120] E. W. Weisstein, ""Taylor Series." From MathWorld–A Wolfram Web Resource."

[121] M. Jaafar, A. Asenjo, and M. Vázquez, "Calibration of coercive and stray fields of commercial magnetic force microscope probes," *IEEE Transactions on Nanotechnology*, vol. 7, no. 3, pp. 245–250, 2008.

[122] L. Yue and S.-H. Liou, "Magnetic Force Microscopy Studies of Magnetic Features and Nanostructures," in *NanoScience and Technology* (B. Bhushan, ed.), no. January 2011 in NanoScience and Technology, pp. 287–319, Berlin, Heidelberg: Springer Berlin Heidelberg, 2011.

[123] T. Wakayama, T. Kobayashi, N. Iwata, N. Tanifuji, Y. Matsuda, and S. Yamada, "Microfabrication of silicon/ceramic hybrid cantilever for atomic force microscope and sensor applications," *Sensors and Actuators A: Physical*, vol. 126, pp. 159–164, jan 2006.

[124] S. Porthun, L. Abelmann, and C. Lodder, "Magnetic force microscopy of thin film media for high density magnetic recording," *Journal of Magnetism and Magnetic Materials*, vol. 182, pp. 238–273, feb 1998.

[125] M. Rolandi, D. Okawa, S. A. Backer, A. Zettl, and J. M. Fŕchet, "Fabrication of magnetic force microscopy probes via localized electrochemical deposition of cobalt," *Journal of Vacuum Science and Technology B: Microelectronics and Nanometer Structures*, vol. 25, no. 5, 2007.

[126] L. M. Belova, O. Hellwig, E. Dobisz, and E. Dan Dahlberg, "Rapid preparation of electron beam induced deposition Co magnetic force microscopy tips with 10 nm spatial resolution," *Review of Scientific Instruments*, vol. 83, no. 9, 2012.

[127] R. Puttock, H. Corte-Leon, V. Neu, D. Cox, A. Manzin, V. Antonov, P. Vavassori, and O. Kazakova, "V-Shaped Domain Wall Probes for Calibrated Magnetic Force Microscopy," *IEEE Transactions on Magnetics*, vol. 53, pp. 1–5, nov 2017.

[128] M. Precner, J. Fedor, J. Tóbik, J. Šoltýs, and V. Cambel, "High resolution tips for switching magnetization MFM," *Acta Physica Polonica A*, vol. 126, no. 1, pp. 386–387, 2014.

[129] O. Iglesias-Freire, M. Jaafar, E. Berganza, and A. Asenjo, "Customized MFM probes with high lateral resolution," *Beilstein Journal of Nanotechnology*, vol. 7, pp. 1068–1074, jul 2016.

[130] T. Wren, R. Puttock, B. Gribkov, S. Vdovichev, and O. Kazakova, "Switchable bi-stable multilayer magnetic probes for imaging of soft magnetic structures," *Ultramicroscopy*, vol. 179, pp. 41–46, aug 2017.

[131] V. Panchal, H. Corte-León, B. Gribkov, L. A. Rodriguez, E. Snoeck, A. Manzin, E. Simonetto, S. Vock, V. Neu, and O. Kazakova, "Calibration of multi-layered probes with low/high magnetic moments," *Scientific Reports*, vol. 7, no. 1, pp. 1–13, 2017.

[132] F. Wolny, T. Mühl, U. Weissker, A. Leonhardt, U. Wolff, D. Givord, and B. Büchner, "Magnetic force microscopy measurements in external magnetic fields—comparison between coated probes and an iron filled carbon nanotube probe," *Journal of Applied Physics*, vol. 108, p. 013908, jul 2010.

[133] S. Vock, F. Wolny, T. Mühl, R. Kaltofen, L. Schultz, B. Büchner, C. Hassel, J. Lindner, and V. Neu, "Monopolelike probes for quantitative magnetic force microscopy: Calibration and application," *Applied Physics Letters*, vol. 97, no. 25, pp. 10–13, 2010.

[134] Y. Lisunova, J. Heidler, I. Levkivskyi, I. Gaponenko, A. Weber, C. Caillier, L. J. Heyderman, M. Kläui, and P. Paruch, "Optimal ferromagnetically-coated carbon nanotube tips for ultra-high resolution magnetic force microscopy," *Nanotechnology*, vol. 24, p. 105705, mar 2013.

[135] H. Corte-León, B. Gribkov, P. Krzysteczko, F. Marchi, J. F. Motte, H. W. Schumacher, V. Antonov, and O. Kazakova, "Magnetic scanning gate microscopy of a domain wall nanosensor using microparticle probe," *Journal of Magnetism and Magnetic Materials*, vol. 400, pp. 225–229, 2016.

[136] J. Wells, P. Krzysteczko, A. Caprile, B. Gribkov, H. W. Schumacher, J. H. Lee, R. Cowburn, and O. Kazakova, "Magnetic Particle Nanosensing by Nucleation of Domain Walls in Ultra-Thin CoFeB/Pt Devices," *IEEE Transactions on Magnetics*, vol. 52, pp. 1–5, jul 2016.

[137] A. Hubert, W. Rave, and S. Tomlinson, "Imaging Magnetic Charges with Magnetic Force Microscopy," *physica status solidi (b)*, vol. 204, pp. 817–828, dec 1997.

[138] S. Vock, Z. Sasvári, C. Bran, F. Rhein, U. Wolff, N. S. Kiselev, A. N. Bogdanov, L. Schultz, O. Hellwig, and V. Neu, "Quantitative magnetic force microscopy study of the diameter evolution of bubble domains in a (Co/Pd)80 multilayer," *IEEE Transactions on Magnetics*, vol. 47, no. 10, pp. 2352–2355, 2011.

[139] P. J. A. V. Schendel, *Investigation of Magnetization Structures in Ferromagnetic and Superconducting Samples by Magnetic Force Microscopy*.
PhD thesis, University of Basel, 1999.

[140] S. Vock, *Resolving local magnetization structures by quantitative magnetic force microscopy*.
PhD thesis, TU Dresden, 2014.

[141] M. Bertero, P. Boccacci, and F. Maggio, "Regularization methods in image restoration: An application to HST images," *International Journal of Imaging Systems and Technology*, vol. 6, no. 4, pp. 376–386, 1995.

[142] A. Banyasz, E. Matyus, and E. Keszei, "Deconvolution of ultrafast kinetic data with inverse filtering," *Radiation Physics and Chemistry*, vol. 72, no. 2-3, pp. 235–242, 2005.

[143] O. Hellwig, A. Berger, J. B. Kortright, and E. E. Fullerton, "Domain structure and magnetization reversal of antiferromagnetically coupled perpendicular anisotropy films," *Journal of Magnetism and Magnetic Materials*, vol. 319, pp. 13–55, dec 2007.

[144] C. Kittel, "Physical theory of ferromagnetic domains," *Physical Review*, vol. 21, no. 4, p. 745, 1949.

[145] D. Nečas, P. Klapetek, V. Neu, M. Havlíček, R. Puttock, O. Kazakova, X. Hu, and L. Zajíčková, "Determination of tip transfer function for quantitative MFM using frequency domain filtering and least squares method," *Scientific Reports*, vol. 9, p. 3880, dec 2019.

[146] S. Vock, C. Hengst, M. Wolf, K. Tschulik, M. Uhlemann, Z. Sasvári, D. Makarov, O. G. Schmidt, L. Schultz, and V. Neu, "Magnetic vortex observation in FeCo nanowires by quantitative magnetic force microscopy," *Applied Physics Letters*, vol. 105, no. 17, 2014.

[147] V. Neu, S. Vock, T. Sturm, and L. Schultz, "Epitaxial hard magnetic SmCo5 MFM tips-a new approach to advanced magnetic force microscopy imaging," *Nanoscale*, vol. 10, no. 35, pp. 16881–16886, 2018.

[148] N. Otsu, "A Threshold Selection Method from Gray-Level Histograms," *IEEE Transactions on Systems, Man, and Cybernetics*, vol. 9, pp. 62–66, jan 1979.

[149] P. C. Hansen, "The L-curve and its use in the numerical treatment of inverse problems," in *Computational Inverse Problems in Electrocardiology* (P. R. Johnston, ed.), WIT Press, 2001.

[150] X. Hu, G. Dai, S. Sievers, A. F. Scarioni, V. Neu, M. Bieler, and H. W. Schumacher, "Uncertainty Analysis of Stray Field Measurements by Quantitative Magnetic Force Microscopy," *IEEE Transactions on Instrumentation and Measurement*, pp. 1–1, 2020.

[151] N. Nagaosa, J. Sinova, S. Onoda, A. H. MacDonald, and N. P. Ong, "Anomalous Hall effect," *Reviews of Modern Physics*, vol. 82, pp. 1539–1592, may 2010.

[152] G. E. W. Bauer, E. Saitoh, and B. J. van Wees, "Spin caloritronics," *Nature Materials*, vol. 11, pp. 391–399, may 2012.

[153] B. Sothmann, R. Sánchez, and A. N. Jordan, "Thermoelectric energy harvesting with quantum dots," *Nanotechnology*, vol. 26, no. 3, 2015.

[154] H. Yu, S. D. Brechet, and J.-P. Ansermet, "Spin caloritronics, origin and outlook," *Physics Letters A*, vol. 381, pp. 825–837, mar 2017.

[155] Ching-Ray Chang, "A hysteresis model for planar Hall effect in thin films," *IEEE Transactions on Magnetics*, vol. 36, pp. 1214–1217, jul 2000.

[156] I. A. Campbell, A. Fert, and O. Jaoul, "The spontaneous resistivity anisotropy in ni-based alloys," *Journal of Physics C: Solid State Physics*, vol. 3, no. 1S, pp. S95–S101, 1970.

[157] M. Trushin, K. Výborný, P. Moraczewski, A. A. Kovalev, J. Schliemann, and T. Jungwirth, "Anisotropic magnetoresistance of spin-orbit coupled carriers scattered from polarized magnetic impurities," *Physical Review B - Condensed Matter and Materials Physics*, vol. 80, no. 13, pp. 1–15, 2009.

[158] A. A. Taskin, H. F. Legg, F. Yang, S. Sasaki, Y. Kanai, K. Matsumoto, A. Rosch, and Y. Ando, "Planar Hall effect from the surface of topological insulators," *Nature Communications*, vol. 8, p. 1340, dec 2017.

[159] P. Krzysteczko, X. Hu, N. Liebing, S. Sievers, and H. W. Schumacher, "Domain wall magneto-Seebeck effect," *Physical Review B*, vol. 92, p. 140405, oct 2015.

[160] O. Reimer, D. Meier, M. Bovender, L. Helmich, J.-O. Dreessen, J. Krieft, A. S. Shestakov, C. H. Back, J.-M. Schmalhorst, A. Hütten, G. Reiss, and T. Kuschel, "Quantitative separation of the anisotropic magnetothermopower and planar Nernst effect by the rotation of an in-plane thermal gradient," *Scientific Reports*, vol. 7, p. 40586, feb 2017.

[161] S. R. Boona, R. C. Myers, and J. P. Heremans, "Spin caloritronics," *Energy and Environmental Science*, vol. 7, no. 3, p. 885, 2014.

[162] K. I. Uchida, S. Daimon, R. Iguchi, and E. Saitoh, "Observation of anisotropic magneto-Peltier effect in nickel," *Nature*, vol. 558, no. 7708, pp. 95–99, 2018.

[163] A. Petford-Long and J. Chapman, "Lorentz Microscopy," in *Magnetic Microscopy of Nanostructures* (H. Hopster and H. P. Oepen, eds.), ch. 4, pp. 67–86, Springer Berlin Heidelberg, 2005.

[164] R. E. Dunin-Borkowski, T. Kasama, M. Beleggia, and G. Pozzi, "Lorentz Microscopy and Electron Holography of Magnetic Materials," in *Handbook of Nanoscopy*, vol. 1, ch. 7, pp. 221–251, Weinheim, Germany: Wiley-VCH Verlag GmbH and Co. KGaA, may 2012.

[165] Y. Aharonov and D. Bohm, "Significance of Electromagnetic Potentials in the Quantum Theory," *Physical Review*, vol. 115, pp. 485–491, aug 1959.

[166] D. Bohm and B. J. Hiley, "On the Aharonov-Bohm Effect," *Nuovo Cimento*, vol. 52, no. 3, pp. 295–308, 1979.

[167] L. A. Rodríguez, C. Bran, D. Reyes, E. Berganza, M. Vázquez, C. Gatel, E. Snoeck, and A. Asenjo, "Quantitative Nanoscale Magnetic Study of Isolated Diameter-Modulated FeCoCu Nanowires," *ACS Nano*, vol. 10, no. 10, pp. 9669–9678, 2016.

[168] L. Alfredo González Rodríguez, *In situ Lorentz microscopy and electron holography in magnetic nanostructures*.
PhD thesis, Université Toulouse III Paul Sabatier (UT3 Paul Sabatier), 2014.

[169] R. M. Reeve, H.-J. Elmers, F. Büttner, and M. Kläui, "Magnetic Imaging and Microscopy," *arXiv preprint arXiv:1806.07767*, jun 2018.

[170] I. M. Andersen, L. A. Rodríguez, C. Bran, C. Marcelot, S. Joulie, T. Hungria, M. Vazquez, C. Gatel, and E. Snoeck, "Exotic Transverse-Vortex Magnetic Configurations in CoNi Nanowires," *ACS Nano*, vol. 14, no. 2, pp. 1399–1405, 2020.

[171] O. Bottauscio and A. Manzin, "Parallelized micromagnetic solver for the efficient simulation of large patterned magnetic nanostructures," *Journal of Applied Physics*, vol. 115, p. 17D122, may 2014.

[172] S. Sundara Mahalingam, B. V. Manikandan, and S. Arockiaraj, "Review - Micromagnetic Simulation Using OOMMF and Experimental Investigations on Nano Composite Magnets," *Journal of Physics: Conference Series*, vol. 1172, no. 1, 2019.

[173] K. Zeissler, *Magnetic and electrical transport properties of artificial spin ice*.
Doctoral, Imperial College London, 2013.

[174] A. Manzin, V. Nabaei, H. Corte-Leon, O. Kazakova, P. Krzysteczko, H. W. Schumacher, H. Corte-León, O. Kazakova, P. Krzysteczko, and H. W. Schumacher, "Modeling of anisotropic magnetoresistance properties of permalloy nanostructures," *IEEE Transactions on Magnetics*, vol. 50, pp. 10–13, apr 2015.

[175] A. Manzin and O. Bottauscio, "Connections between numerical behavior and physical parameters in the micromagnetic computation of static hysteresis loops," *Journal of Applied Physics*, vol. 108, no. 9, pp. 1–9, 2010.

[176] A. Manzin, V. Nabaei, and O. Kazakova, "Modelling and optimization of submicron Hall sensors for the detection of superparamagnetic beads," *Journal of Applied Physics*, vol. 111, no. 7, 2012.

[177] O. Bottauscio and A. Manzin, "Spatial reconstruction of exchange field interactions with a finite difference scheme based on unstructured meshes," *IEEE Transactions on Magnetics*, vol. 48, no. 11, pp. 3250–3253, 2012.

[178] D. G. Porter and M. J. Donahue, "OOMMF User's Guide, Version 1.0," tech. rep., National Institute of Standards and Technology, Gaithersburg, 1999.

[179] Y. Guerra, R. Peña-Garcia, and E. Padrón-Hernández, "Dipolar magnetic interaction effects in 2D hexagonal array of cobalt hollow-spheres," *Journal of Magnetism and Magnetic Materials*, vol. 451, pp. 269–275, apr 2018.

[180] M. Donolato, M. Gobbi, P. Vavassori, M. Leone, M. Cantoni, V. Metlushko, B. Ilic, M. Zhang, S. X. Wang, and R. Bertacco, "Nanosized corners for trapping and detecting magnetic nanoparticles," *Nanotechnology*, vol. 20, p. 385501, sep 2009.

[181] A. Manzin and O. Bottauscio, "A micromagnetic solver for large-scale patterned media based on non-structured meshing," *IEEE Transactions on Magnetics*, vol. 48, no. 11, pp. 2789–2792, 2012.

[182] S. Bader and S. Parkin, "Spintronics," *Annual Review of Condensed Matter Physics*, vol. 1, pp. 71–88, aug 2010.

[183] C. Vautrin, M. Vyazmensky, S. Engel, S. M. Murtry, M. Hehn, F. Montaigne, D. Lacour, and R. S. Marks, "Biochip based on arrays of switchable magnetic nano-traps," *Sensors and Actuators, B: Chemical*, vol. 251, no. May, pp. 699–705, 2017.

[184] H. S. Kim, W. Liu, G. Chen, C.-W. Chu, and Z. Ren, "Relationship between thermoelectric figure of merit and energy conversion efficiency," *Proceedings of the National Academy of Sciences*, vol. 112, pp. 8205–8210, jul 2015.

[185] K. Uchida, S. Takahashi, K. Harii, J. Ieda, W. Koshibae, K. Ando, S. Maekawa, and E. Saitoh, "Observation of the spin Seebeck effect," *Nature*, vol. 455, no. 7214, pp. 778–781, 2008.

[186] H. Adachi, K. I. Uchida, E. Saitoh, and S. Maekawa, "Theory of the spin Seebeck effect," *Reports on Progress in Physics*, vol. 76, no. 3, 2013.

[187] S. Daimon, R. Iguchi, T. Hioki, E. Saitoh, and K.-i. Uchida, "Thermal imaging of spin Peltier effect," *Nature Communications*, vol. 7, p. 13754, dec 2016.

[188] Y. Ohnuma, M. Matsuo, and S. Maekawa, "Theory of the spin Peltier effect," *Physical Review B*, vol. 96, no. 13, pp. 1–4, 2017.

[189] S. Meyer, Y. T. Chen, S. Wimmer, M. Althammer, T. Wimmer, R. Schlitz, S. Geprags, H. Huebl, D. Kodderitzsch, H. Ebert, G. E. Bauer, R. Gross, and S. T. Goennenwein, "Observation of the spin Nernst effect," *Nature Materials*, vol. 16, no. 10, pp. 97–981, 2017.

[190] Y. Onose, T. Ideue, H. Katsura, Y. Shiomi, N. Nagaosa, and Y. Tokura, "Observation of the Magnon Hall Effect," *Science*, vol. 329, pp. 297–299, jul 2010.

[191] P. W. Bridgman, "The Connections between the Four Transverse Galvanomagnetic and Thermomagnetic Phenomena," *Physical Review*, vol. 24, pp. 644–651, dec 1924.

[192] W. Nernst, "Ueber die electromotorischen Kräfte, welche durch den Magnetismus in von einem Wärmestrome durchflossenen Metallplatten geweckt werden," *Annalen der Physik und Chemie*, vol. 267, no. 8, pp. 760–789, 1887.

[193] D. Meier, D. Reinhardt, M. Schmid, C. H. Back, J. M. Schmalhorst, T. Kuschel, and G. Reiss, "Influence of heat flow directions on Nernst effects in Py/Pt bilayers," *Physical Review B - Condensed Matter and Materials Physics*, vol. 88, no. 18, pp. 1–6, 2013.

[194] P. Krzysteczko, J. Wells, A. Fernández Scarioni, Z. Soban, T. Janda, X. Hu, V. Saidl, R. P. Campion, R. Mansell, J.-H. Lee, R. P. Cowburn, P. Nemec, O. Kazakova, J. Wunderlich, and H. W. Schumacher, "Nanoscale thermoelectrical detection of magnetic domain wall propagation," *Physical Review B*, vol. 95, p. 220410, jun 2017.

[195] M. Cubukcu, D. Venkateshvaran, A. Wittmann, S. J. Wang, R. Di Pietro, S. Auffret, L. Vila, J. Wunderlich, and H. Sirringhaus, "Electrical nucleation and detection of single 360° homochiral Néel domain walls measured using the anomalous Nernst effect," *Applied Physics Letters*, vol. 112, no. 26, 2018.

[196] E. Pfitzner, X. Hu, H. W. Schumacher, A. Hoehl, D. Venkateshvaran, M. Cubukcu, J. W. Liao, S. Auffret, J. Heberle, J. Wunderlich, and B. Kästner, "Near-field magneto-caloritronic nanoscopy on ferromagnetic nanostructures," *AIP Advances*, vol. 8, no. 12, 2018.

[197] H. Corte-León, V. Neu, A. Manzin, C. Barton, Y. Tang, M. Gerken, P. Klapetek, H. W. Schumacher, and O. Kazakova, "Comparison and Validation of Different Magnetic Force Microscopy Calibration Schemes," *Small*, vol. 16, no. 11, pp. 1–14, 2020.

[198] X. Hu, G. Dai, S. Sievers, A. Fernández-Scarioni, H. Corte-León, R. Puttock, C. Barton, O. Kazakova, M. Ulvr, P. Klapetek, M. Havlíček, D. Nečas, Y. Tang, V. Neu, and H. W. Schumacher, "Round robin comparison on quantitative nanometer scale magnetic field measurements by magnetic force microscopy," *Journal of Magnetism and Magnetic Materials*, vol. 511, p. 166947, oct 2020.

[199] S. Gomès, A. Assy, and P.-O. O. Chapuis, "Scanning thermal microscopy: A review," *Physica Status Solidi (A) Applications and Materials Science*, vol. 212, pp. 477–494, mar 2015.

[200] F. Menges, H. Riel, A. Stemmer, and B. Gotsmann, "Nanoscale thermometry by scanning thermal microscopy," *Review of Scientific Instruments*, vol. 87, p. 074902, jul 2016.

[201] Y. Zhang, W. Zhu, F. Hui, M. Lanza, T. Borca-Tasciuc, and M. Muñoz Rojo, "A Review on Principles and Applications of Scanning Thermal Microscopy (SThM)," *Advanced Functional Materials*, vol. 30, p. 1900892, may 2020.

[202] A. Harzheim, J. Spiece, C. Evangeli, E. McCann, V. Falko, Y. Sheng, J. H. Warner, G. A. D. Briggs, J. A. Mol, P. Gehring, and O. V. Kolosov, "Geometrically Enhanced Thermoelectric Effects in Graphene Nanoconstrictions," *Nano Letters*, vol. 18, no. 12, pp. 7719–7725, 2018.

[203] A. Harzheim, C. Evangeli, O. V. Kolosov, and P. Gehring, "Direct mapping of local Seebeck coefficient in 2D material nanostructures via scanning thermal gate microscopy," *2D Materials*, vol. 7, no. 4, p. 041004, 2020.

[204] A. Sola, C. Barton, V. Basso, C. Dubs, M. Pasquale, and O. Kazakova, "Local Spin Seebeck Imaging with a Scanning Thermal Probe," *Physical Review Applied*, vol. 14, p. 034056, sep 2020.

[205] K. Kim, W. Jeong, W. Lee, and P. Reddy, "Ultra-High Vacuum Scanning Thermal Microscopy for Nanometer Resolution Quantitative Thermometry," *ACS Nano*, vol. 6, pp. 4248–4257, may 2012.

[206] E. Guen, P. Klapetek, R. Puttock, B. Hay, A. Allard, T. Maxwell, P.-o. Chapuis, D. Renahy, G. Davee, M. Valtr, J. Martinek, O. Kazakova, and S. Gomès, "SThM-based local thermomechanical analysis: Measurement intercomparison and uncertainty analysis," *International Journal of Thermal Sciences*, vol. 156, p. 106502, oct 2020.

[207] J. Wells, E. Selezneva, P. Krzysteczko, X. Hu, H. W. Schumacher, R. Mansell, R. Cowburn, A. Cuenat, and O. Kazakova, "Combined anomalous Nernst effect and thermography studies of ultrathin CoFeB/Pt nanowires," *AIP Advances*, vol. 7, no. 5, 2017.

[208] M. Tanaka, E. Saitoh, H. Miyajima, T. Yamaoka, and Y. Iye, "Magnetic interactions in a ferromagnetic honeycomb nanoscale network," *Physical Review B - Condensed Matter and Materials Physics*, vol. 73, no. 5, pp. 3–6, 2006.

[209] R. Puttock, A. Manzin, V. Neu, F. Garcia-Sanchez, A. Fernandez Scarioni, H. W. Schumacher, and O. Kazakova, "Modal Frustration and Periodicity Breaking in Artificial Spin Ice," *Small*, vol. 16, p. 2003141, oct 2020.

[210] Z. Luo, T. P. Dao, A. Hrabec, J. Vijayakumar, A. Kleibert, M. Baumgartner, E. Kirk, J. Cui, T. Savchenko, G. Krishnaswamy, L. J. Heyderman, and P. Gambardella, "Chirally coupled nanomagnets," *Science*, vol. 363, no. 6434, pp. 1435–1439, 2019.

[211] P. D. Welch, "The Use of Fast Fourier Transform for the Estimation of Power Spectra: A Method Based on Time Averaging Over Short, Modified Periodograms," *IEEE Transactions on Audio and Electroacoustics*, vol. 15, no. 2, pp. 70–73, 1967.

[212] P. Kumar, Y. Suzuki, Y. Cao, S. Yoshimura, and H. Saito, "High resolution magnetic field energy imaging of the magnetic recording head by A-MFM with Co-GdO x superparamagnetic tip," *Applied Physics Letters*, vol. 111, p. 183105, oct 2017.

[213] T. L. Gilbert, "A phenomenological theory of damping in ferromagnetic materials," *IEEE Transactions on Magnetics*, vol. 40, no. 6, pp. 3443–3449, 2004.

[214] R. Ozerov and A. Vorobyev, *Physics for Chemists*.
Elsevier, first ed., 2007.

[215] Ö. Özdemir, D. J. Dunlop, and T. S. Berquó, "Morin transition in hematite: Size dependence and thermal hysteresis," *Geochemistry, Geophysics, Geosystems*, vol. 9, no. 10, 2008.

[216] J. W. Glen, "Structure and point defects of ice: their effect on the electrical and mechanical properties," *Science Progress (1933-)*, vol. 57, no. 225, pp. 1–21, 1969.

[217] G. C. Lau, R. S. Freitas, B. G. Ueland, B. D. Muegge, E. L. Duncan, P. Schiffer, and R. J. Cava, "Zero-point entropy in stuffed spin-ice," *Nature Physics*, vol. 2, pp. 249–253, apr 2006.

[218] G. Sala, M. J. Gutmann, D. Prabhakaran, D. Pomaranski, C. Mitchelitis, J. B. Kycia, D. G. Porter, C. Castelnovo, and J. P. Goff, "Vacancy defects and monopole dynamics in oxygen-deficient pyrochlores," *Nature Materials*, vol. 13, pp. 488–493, may 2014.

[219] H. D. Zhou, C. R. Wiebe, Y. J. Jo, L. Balicas, Y. Qiu, J. R. D. Copley, G. Ehlers, P. Fouquet, and J. S. Gardner, "The origin of persistent spin dynamics and residual entropy in the stuffed spin ice Ho 2.3 Ti 1.7 O 7-d," *Journal of Physics: Condensed Matter*, vol. 19, p. 342201, aug 2007.

[220] R. J. Aldus, T. Fennell, P. P. Deen, E. Ressouche, G. C. Lau, R. J. Cava, and S. T. Bramwell, "Ice rule correlations in stuffed spin ice," *New Journal of Physics*, vol. 15, p. 013022, jan 2013.

[221] H. M. Revell, L. R. Yaraskavitch, J. D. Mason, K. A. Ross, H. M. L. Noad, H. A. Dabkowska, B. D. Gaulin, P. Henelius, and J. B. Kycia, "Evidence of impurity and boundary effects on magnetic monopole dynamics in spin ice," *Nature Physics*, vol. 9, pp. 34–37, jan 2013.

[222] J. Drisko, T. Marsh, and J. Cumings, "Topological frustration of artificial spin ice," *Nature Communications*, vol. 8, p. 14009, apr 2017.

[223] R. C. Silva, R. J. C. Lopes, L. A. S. Mól, W. A. Moura-Melo, G. M. Wysin, and A. R. Pereira, "Nambu monopoles interacting with lattice defects in a two-dimensional artificial square spin ice," *Physical Review B*, vol. 87, p. 014414, jan 2013.

[224] D. Thonig and J. Henk, "Pinning of thermal excitations at defects in artificial dipolar arrays: A theoretical investigation," *Journal of Magnetism and Magnetic Materials*, vol. 386, pp. 117–124, jul 2015.

[225] M. T. Bryan, P. W. Fry, T. Schrefl, M. R. J. Gibbs, D. A. Allwood, M.-Y. Im, and P. Fischer, "Transverse Field-Induced Nucleation Pad Switching Modes During Domain Wall Injection," *IEEE Transactions on Magnetics*, vol. 46, pp. 963–967, apr 2010.

[226] T. J. Hayward and K. A. Omari, "Beyond the quasi-particle: stochastic domain wall dynamics in soft ferromagnetic nanowires," *Journal of Physics D: Applied Physics*, vol. 50, p. 084006, mar 2017.

[227] B. Dieny, I. L. Prejbeanu, K. Garello, P. Gambardella, P. Freitas, R. Lehndorff, W. Raberg, U. Ebels, S. O. Demokritov, J. Akerman, A. Deac, P. Pirro, C. Adelmann, A. Anane, A. V. Chumak, A. Hirohata, S. Mangin, S. O. Valenzuela, M. C. Onbaşlı, M. D'Aquino, G. Prenat, G. Finocchio, L. Lopez-Diaz, R. Chantrell, O. Chubykalo-Fesenko, and P. Bortolotti, "Opportunities and challenges for spintronics in the microelectronics industry," *Nature Electronics*, vol. 3, pp. 446–459, aug 2020.

[228] D. Sanz-Hernández, M. Massouras, N. Reyren, N. Rougemaille, V. Schánilec, K. Bouzehouane, M. Hehn, B. Canals, D. Querlioz, J. Grollier, F. Montaigne, and D. Lacour, "Tunable stochasticity in an artificial spin network," oct 2020.

[229] G. S. Abo, Y.-K. Hong, J. Park, J. Lee, W. Lee, and B.-C. Choi, "Definition of Magnetic Exchange Length," *IEEE Transactions on Magnetics*, vol. 49, pp. 4937–4939, aug 2013.

[230] M. Tanaka, E. Saitoh, H. Miyajima, and T. Yamaoka, "Asymmetric field variation of magnetoresistance in Permalloy honeycomb nanonetwork," *Journal of Applied Physics*, vol. 99, p. 08G314, apr 2006.

[231] R. van den Boomgaard and R. van Balen, "Methods for fast morphological image transforms using bitmapped binary images," *CVGIP: Graphical Models and Image Processing*, vol. 54, pp. 252–258, may 1992.

[232] L. Vincent, "Morphological grayscale reconstruction in image analysis: applications and efficient algorithms," *IEEE Transactions on Image Processing*, vol. 2, pp. 176–201, apr 1993.

[233] J. M. Chambers, W. S. Cleveland, B. Kleiner, and P. a. Tukey, "Notched Box Plots," in *Graphical methods for data analysis* (P. Bickel, W. S. Cleveland, and R. Dudley, eds.), pp. 60–63, Wadsworth International Group and Duxbury Press, 1983.

[234] L. E. Moses, "Graphical Methods in Statistical Analysis," *Annual Review of Public Health*, vol. 8, pp. 309–353, may 1987.

[235] E. Puyoo, S. Grauby, J. M. Rampnoux, E. Rouvìre, and S. Dilhaire, "Scanning thermal microscopy of individual silicon nanowires," *Journal of Applied Physics*, vol. 109, no. 2, 2011.

[236] J. M. Bartell, D. H. Ngai, Z. Leng, and G. D. Fuchs, "Towards a table-top microscope for nanoscale magnetic imaging using picosecond thermal gradients," *Nature Communications*, vol. 6, pp. 1–7, 2015.

[237] A. Balčytis, M. Ryu, S. Juodkazis, and J. Morikawa, "Micro-thermocouple on nanomembrane: Thermometer for nanoscale measurements," *Scientific Reports*, vol. 8, no. 1, pp. 8–13, 2018.

[238] U. Martens, T. Huebner, H. Ulrichs, O. Reimer, T. Kuschel, R. R. Tamming, C.-L. Chang, R. I. Tobey, A. Thomas, M. Münzenberg, and J. Walowski, "Anomalous Nernst effect and three-dimensional temperature gradients in magnetic tunnel junctions," *Communications Physics*, vol. 1, no. 1, 2018.

[239] R. Iguchi, S. Kasai, K. Koshikawa, N. Chinone, S. Suzuki, and K. ichi Uchida, "Thermoelectric microscopy of magnetic skyrmions," *Scientific Reports*, vol. 9, no. 1, pp. 1–9, 2019.

[240] Y. Liu and Q. Shao, "Two-Dimensional Materials for Energy-Efficient Spin-Orbit Torque Devices," 2020.

[241] D. Nečas and P. Klapetek, "Gwyddion: An open-source software for SPM data analysis," *Central European Journal of Physics*, vol. 10, no. 1, pp. 181–188, 2012.

[242] S. Bhanja, D. K. Karunaratne, R. Panchumarthy, S. Rajaram, and S. Sarkar, "Non-Boolean computing with nanomagnets for computer vision applications," *Nature Nanotechnology*, vol. 11, no. 2, pp. 177–183, 2016.

[243] Y.-L. Wang, Z.-L. Xiao, A. Snezhko, J. Xu, L. E. Ocola, R. Divan, J. E. Pearson, G. W. Crabtree, and W.-K. Kwok, "Rewritable artificial magnetic charge ice," *Science*, vol. 352, pp. 962–966, may 2016.